
Dynamics of a Class of Vortex Rings

Karim Shariff, Anthony Leonard, and Joel H. Ferziger

December 1989

(NASA-TM-102257) DYNAMICS OF A CLASS OF
VORTEX RINGS Ph.D. Thesis - Stanford Univ.
(NASA) 291 p CSCL 200

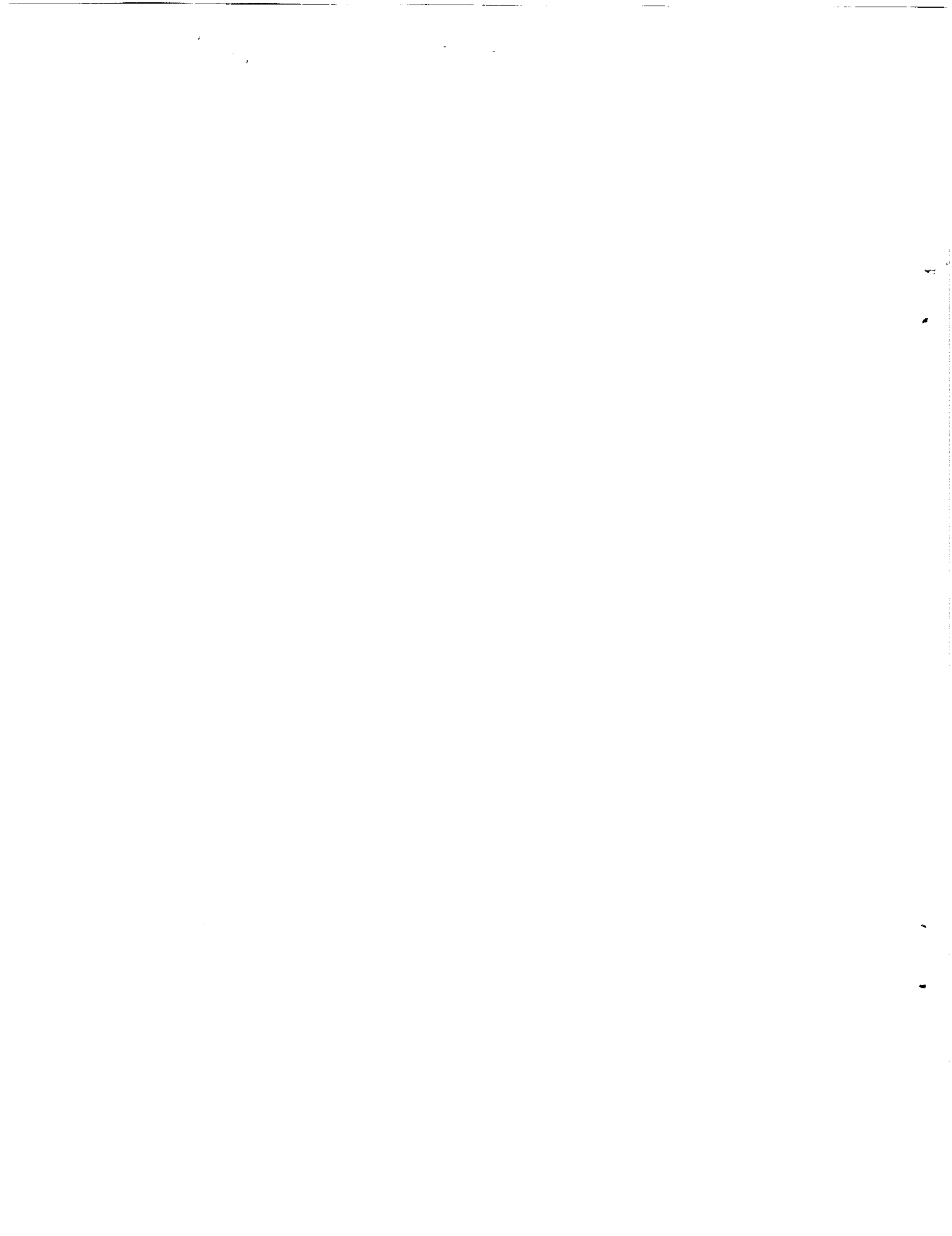
N90-19524

Unclass

63/34 0261692

NASA

National Aeronautics and
Space Administration



Dynamics of a Class of Vortex Rings

Karim Shariff, Ames Research Center, Moffett Field, California
Anthony Leonard, California Institute of Technology, Pasadena, California
Joel H. Ferziger, Stanford University, Stanford, California

December 1989

NASA

National Aeronautics and
Space Administration

Ames Research Center
Moffett Field, California 94035

ABSTRACT

A numerical method, based on the contour dynamics method for two-dimensional patches of uniform vorticity, is extended to axisymmetric regions that contain vorticity varying linearly from the axis of symmetry. Such a distribution remains invariant in time and only the motion of the *boundaries* of vorticity regions needs to be tracked, reducing the dimensionality of the problem by one. A simple model that retains only the elliptic degree of freedom in the core shapes is also developed to explain some of the features observed with contour dynamics. Passage and collision interactions of two identical rings are studied focusing on core deformation, sound generation and stirring of fluid elements.

With respect to core deformation it is found that not only the strain rate but how rapidly it varies is important and accounts for a greater susceptibility to vortex tearing than in two-dimensions. For slowly varying strain, core deformations are reversible in the sense that core shapes remain in equilibrium. For example, as a passage interaction is completed and the strain relaxes the cores return to their original shape. For sufficiently rapidly varying strain, permanent deformations remain. For collisions, if the strain changes slowly the cores migrate through the shapes of a known family of two-dimensional steadily translating vortex pairs up to the limiting member of the family. Thereafter the energy constraint does not allow the cores to maintain this or any other constant shape as the vortices stretch. For rapidly varying strain, core deformation is severe and a head-tail structure in good agreement with experiments is formed. The head has very nearly the shape of the two-dimensional limiting pair.

With respect to sound generation, good agreement with the measured acoustic signal for colliding rings is obtained and a feature that was thought to be due to viscous effects is shown to be an effect of inviscid core deformation alone. For passage interactions core pulsations lead to a component of high frequency and in certain cases high amplitude. Evidence for the presence and importance of this noise source in existing jet-rig noise spectra is provided.

Finally, transport of fluid elements in time periodic vortex flows is studied using techniques from non-linear dynamics. The processes of fluid engulfment and rejection for an isolated unsteady vortex ring are studied using the stable and unstable manifolds. Because fluid is drawn out along it, the unstable manifold shows excellent agreement with flow visualization experiments for leapfrogging rings suggesting that it may be a good tool for numerical flow visualization in time periodic flows.

ACKNOWLEDGMENTS

Apart from minor modifications, this work is a doctoral thesis submitted to Stanford University. I wish to express here my gratitude to my advisors and colleagues.

A thesis rarely embodies the work and ideas of a single individual and during writing I fondly recalled how a colleague helped me through a difficult point, corrected my faulty reasoning, suggested a fresh interpretation or struggled for me through a derivation. For their help I would like to thank Tanios Honein, Drs. Moon Joo Lee, Sanjiva Lele, Yen Liu, Nagi Mansour, Robert Moser, Eugene Pak, Ugo Piomelli, Bart Singer and Philippe Spalart. My understanding of dynamical systems theory benefited greatly from a study group with Marouhn Aboudi and Tanios Honein. Without the friendship and encouragement of Dr. Sharon Stanaway and Gary Coleman, completion of the manuscript would not have been possible.

I am extremely fortunate to have had two advisors. I am grateful to Prof. Joel Ferziger for his guidance in keeping this work focussed, for his encouragement during the wanderings and dry periods and for his careful editing of the manuscript. Prof. Anthony Leonard had the knack for taking my vague and confused ideas and sharpening them but still making it seem that I had known the answer all along. That encouragement really helped. I appreciate the unsung effort of Prof. Brian Cantwell in serving on my reading committee. Dr. Philippe Spalart not only launched the work in the direction that it took (see §1.5) but provided several ideas and critically reviewed the manuscript.

For its tonal quality and style, this work owes a lot to the work of Prof. Norman Zabusky. In addition, during his stay he provided several interpretations of the results, new diagnostics and tests which then led to further insight. I am indebted to Dr. Vered Rom-Kedar, Profs. Steve Wiggins and Anthony Leonard whose results and methods provided the inspiration for the work in Chapter 6. Profs. T. Matsui, Y. Oshima, B. Sturtevant and H. Yamada kindly sent me their experimental photographs whenever I requested them, many of them unpublished, or allowed their reproduction.

Financial support, computer and other resources were provided by NASA Ames Research Center under grant NCA 2-OR745-313 and the Co-op Program enabled

completion of coursework requirements. Partial support during my Masters year was provided by the Aga Khan Foundation.

I would like to dedicate this work to my parents Rajab and Nūr, to their love and sacrifice, to my father's love of learning and eclecticism and to my mother's hard work yet tender nurturance. Thornton Wilder has said that "the impulses of love return to the love that made them." Let this work be a token of that return.

K.S.

VORTEX IMAGERY

“When Strife had reached to the lowest depth of the whirl, and Love was in the middle of the eddy, under her do all these things come together so as to be one, not all at once, but congregating each from different directions at their will. And as they came together Strife began to move outwards to the circumference. Yet alternating with the things that were being mixed many other things remained unmixed, all that Strife, still aloft, retained; for not yet had it altogether retired from them, blamelessly, to the outermost boundaries of the circle, but while some parts of it had gone forth, some still remained within. And in proportion as it was ever running forth outwards, so a gentle immortal stream of blameless Love was ever coming in.” (Empedocles of Acragas, ca. 442 B.C. From Minahen (1983), p. 178.)

“The Nature of infinity is this: That every thing has its
Own Vortex, and when once a traveller thro’ Eternity
Has pass’d that Vortex, he perceives it roll backward behind
His path, into a globe itself infolding like a sun,
Or like a moon, or like a universe of starry majesty
While he keeps onwards in his wondrous journey on the earth,
Or like a human form, a friend with whom he liv’d benevolent.
As the eye of man views both the east and west encompassing
Its vortex, and the north and south with all their starry host,
Also the rising sun and setting moon he views surrounding
His cornfields and his valleys of five hundred acres square,
Thus is the earth one infinite plane, and not as apparent
To the weak traveller confin’d beneath the moony shade.
Thus is the heaven a vortex pass’d already, and the earth
A vortex not yet pass’d by the traveller thro’ Eternity.”
(William Blake, 1757–1827. From Minahen (1983), p. 288.)

“The center of the cyclone is that rising quiet central low-pressure place in which one can learn to live eternally. Just outside of this Center is the rotating storm of one’s own ego, competing with other egos in a furious high-velocity circular dance. As one leaves the center, the roar of the rotating wind deafens one more and more as one joins this dance. One’s centered thinking-feeling-being, one’s own Satoris, are in the center only, not outside. One’s pushed-pulled driven states, one’s anti-Satori modes of functioning, one’s self-created hells, are outside the center. In the center of the cyclone one is off the wheel of Karma, of life, rising to join the Creators of the Universe, the Creators of us.

Here we find that we have created Them who are Us.” (Lilly 1972, frontispiece)

CONTENTS

	<i>Page</i>
Abstract	iii
Acknowledgments	iv
Vortex Imagery	vi
Contents	ix
List of Figures	xi
Nomenclature	xvi
 <i>Chapter</i>	
1 General Introduction	1
1.1 The fascination of vortices	1
1.2 Objectives	4
1.3 Organization	6
1.4 Summary of main results	7
1.5 Evolution of the objectives and approach	11
2 Background on Axisymmetric Vortex Rings and their Stability	15
2.1 Introduction	15
2.2 The formation process	16
2.3 The structure of the core	20
2.4 Initially laminar vs. turbulent rings	22
2.5 The dynamics of laminar rings	23
2.6 Coaxial interactions	24
2.7 Theory of steadily translating inviscid vortex rings	30
2.8 Unsteady behavior and coaxial interactions of inviscid rings	39
2.9 Theory and numerical simulations of viscous vortex rings	41
2.10 Azimuthal instabilities of vortex rings	46
3 A Contour Dynamics Algorithm for Axisymmetric Flow	57
3.1 Introduction	57
3.2 Axisymmetric contour dynamics formulation	60
3.3 Numerical implementation	66
3.4 Tests of accuracy and convergence	68
3.5 A Qualitative illustration	69
<i>Appendices</i>	
3.A Contribution to the induced velocity from adjacent segments	70
3.B Contour formulation for the streamfunction	73
3.C Literature on two-dimensional patches of uniform vorticity	76

<i>Chapter</i>	<i>Page</i>
4 Simple Models	85
4.1 Dyson's (1893) model	85
4.2 Development of an elliptic model for axisymmetric vortices	96
4.3 Summary	116
5 Acoustics and Dynamics of Coaxial Interacting Vortex Rings	127
5.1 Passage cases	127
5.2 Collision cases	141
<i>Appendices</i>	
5.A Calculation of the energy and its spectrum	152
5.B Implementation of the vortex filament method to axisymmetric flow	158
6 Particle Motions due to Unsteady Vortex Rings	211
6.1 Introduction	211
6.2 Terminology	212
6.3 Literature survey	219
6.4 Results	222
7 Closing Remarks	245
6.1 Conclusions	245
6.2 Recommendations for future work	249
References	253

LIST OF FIGURES

<i>Figure</i>		<i>Page</i>
2.1	Initial topology of a magnetic field which leads to a magnetostatic state analogous to a steady vortex ring	55
3.1	Cylindrical coordinates	80
3.2	Surface oriented coordinates (n, s, ϕ) defined in the text	81
3.3	Integrand for the axial velocity along the chord of an arc between 25° and 75° on a Hill's vortex with unit radius	81
3.4	Axial velocity at node points on a Hill's vortex of unit radius and $\mathcal{A} = 1$	82
3.5	Error in velocities evaluated at the node points of a Hill's vortex with unit radius and $\mathcal{A} = 1$	82
3.6	History of the rms deviation of the Fourier coefficients of the core boundary from the initial Norbury (1973) shape for different number of segments N_s	83
3.7	Evolution of a vortex formed by removing a region of vortical fluid from a sphere	84
4.1	Schematic of the elements that comprise the elliptic model	118
4.2	Contours of the "composite" strain rate g due to a Helmholtz ring of unit circulation and radius	119
4.3	Phase portrait for the evolution of an elliptic vortex subjected to a fixed strain rate $g/\bar{\omega}_\phi = 0.11$. After Neu (1984)	119
4.4	Acoustic efficiency η_a for Moore's (1980) elliptic core vortex ring as a function of the core thickness parameter α' for several values of the aspect ratio λ	120
4.5	Motion of an initially elliptical core with an aspect ratio of 1.5 and $a/L_o = 0.3$	120
4.6	Core shapes at the instants A-G indicated in the previous figure	121
4.7	Variation of aspect ratio for an initially elliptical core with aspect ratio 1.5 and $a/L_o = 0.3$	122
4.8	Axial velocity of the shape centroid for an initially elliptical core with aspect ratio 1.5 and $a/L_o = 0.3$. t/T is the time normalized by the core rotation period	122
4.9	Acoustic signal for an initially elliptical core with aspect ratio 1.5 and $a/L_o = 0.3$	123
4.10	Trajectory of the shape centroid for an initially elliptical core with aspect ratio 1.5 and $a/L_o = 0.1$	123
4.11	Core shapes at the instants of Figure 4.10	124
4.12	Variation of aspect ratio for an initially elliptical core with aspect ratio 1.5 and $a/L_o = 0.1$	125
4.13	Acoustic signal for an initially elliptical core with aspect ratio 1.5 and $a/L_o = 0.1$	125

<i>Figure</i>	<i>Page</i>
5.1	Core shapes at equal time intervals for the passage of $\alpha = 0.1, \hat{d} = 1$ 170
5.2	Normalized acoustic signal for the passage of $\alpha = 0.1, \hat{d} = 1$ 170
5.3	Fourier amplitudes of the acoustic signal for four passage periods ($\alpha = 0.1, \hat{d} = 1$, elliptic model) 171
5.4	Evolution of aspect ratios (contour dynamics) for the passage of $\alpha = 0.1, \hat{d} = 1$ 171
5.5	Aspect ratios (elliptic model) for the passage of $\alpha = 0.1, \hat{d} = 1$ 172
5.6	Orientation angle (elliptic model) for the passage of $\alpha = 0.1, \hat{d} = 1$ 172
5.7	Contributions to the acoustic signal for the passage of $\alpha = 0.1, \hat{d} = 1$ (elliptic model) 173
5.8	Aspect ratios (elliptic model) for two passages of $\alpha = 0.1, \hat{d} = 1$ with equilibrium initial conditions 173
5.9	Acoustic signal (elliptic model) for two passages of $\alpha = 0.1, \hat{d} = 1$ with equilibrium initial conditions (compared with Dyson's model) 174
5.10	Core shapes for the passage of $\alpha = 0.2, \hat{d} = 1$ comparing contour dynamics with the elliptic model 175
5.11	Ratio of composite strain rate to vorticity at the centroid for the passage of $\alpha = 0.2, \hat{d} = 1$ (elliptic model) 176
5.12	Aspect ratios for the passage of $\alpha = 0.2, \hat{d} = 1$ 176
5.13	Acoustic signal for the passage of $\alpha = 0.2, \hat{d} = 1$ 177
5.14	Filament method passage of $\alpha = 0.2, \hat{d} = 1$ compared with the contours of Figure 5.10 at the same instants 178
5.15	Continuation from the previous figure, of the filament method pas- sage of $\alpha = 0.2, \hat{d} = 1$ 179
5.16	Acoustic signal for the entire filament calculation for passage of $\alpha =$ $0.2, \hat{d} = 1$ 180
5.17	Filament method passage of $\alpha = 0.2, \hat{d} = 1$ (peaked vorticity) 181
5.18	Continuation of filament method passage of $\alpha = 0.2, \hat{d} = 1$ from the previous figure (peaked vorticity) 182
5.19	Acoustic signal for filament method passage of $\alpha = 0.2, \hat{d} = 1$ (peaked vorticity) 183
5.20	Fourier amplitudes for the acoustic signal in Figure 5.19. The hor- izontal axis is the circular frequency normalized by the initial peak vorticity 183
5.21	Aspect ratio (elliptic model) for the rear vortex in the passage of $\alpha = 0.12, \hat{d} = 1$ compared with the equilibrium aspect ratio 184
5.22	Elliptic model phase plane trajectory of the initially rear vortex in the passage of $\alpha = 0.14, \hat{d} = 1$ 184

<i>Figure</i>	<i>Page</i>
5.23	Core shapes at equal time intervals for the passage of $\alpha = 0.14, \hat{d} = 1$ 185
5.24	Aspect ratio of the initially rear vortex for the passage of $\alpha = 0.14, \hat{d} = 1$ 185
5.25	Acoustic radiation for the passage of $\alpha = 0.14, \hat{d} = 1$ 186
5.26	Elliptic model phase plane trajectory of the initially rear vortex in the passage of $\alpha = 0.18, \hat{d} = 1$ 186
5.27	Core shapes at equal time intervals for the passage of $\alpha = 0.18, \hat{d} = 1$ 187
5.28	Aspect ratios for the passage of $\alpha = 0.18, \hat{d} = 1$ 187
5.29	Core shapes for $\alpha = 0.40$ passage compared with photographs from Oshima, Kambe & Asaka (1975) 188
5.30	Comparison of the normalized acoustic signal for the passage of $\alpha = 0.4, \hat{d} = 2$ 189
5.31	Passage of $\alpha = 0.4, \hat{d} = 2$. Comparison of calculations with the vortex filament method against contour dynamics. (a) Linear vorticity; (b) Peaked over-energetic vorticity; (c) Peaked vorticity with energy matched to (a) 190
5.32	Comparison of the acoustic signal from the three vortex filament passage cases and contour dynamics ($\alpha = 0.4, \hat{d} = 2$) 191
5.33	Initial vorticity normalized by Γ/L_o^2 for the two peaked vorticity passage cases ($\alpha = 0.4, \hat{d} = 2$). (a) Over-energetic; (b) Energy matched to the linear vorticity case 191
5.34	Speed of the vorticity centroid for the passage of $\alpha = 0.4, \hat{d} = 2$ 192
5.35	Core shapes for the collision of $\alpha = 0.2, \hat{d} = 8$ 193
5.36	(a) Shape at $U_o t/L_o = 5.57$ magnified from the previous figure; (b) $U_o t/L_o = 5.62$ 194
5.37	Rate of the radial shape centroid scaled on $\bar{\sigma}^{1/2}$ 194
5.38	Energies of states progressively stretched from the configuration at $U_o t/L_o = 5.57$ for the collision of $\alpha = 0.2, \hat{d} = 8$ 195
5.39	Rescaled core shapes (solid) for the collision of $\alpha = 0.2, \hat{d} = 8$ compared with two-dimensional translating pairs numbered 6-11 and 13 in Wu <i>et al.</i> (1984) 196
5.40	Core shapes for the collision of $\alpha = 0.5, \hat{d} = 8$ 197
5.41	Shape at $U_o t/L_o = 5.49$ magnified from the previous figure and compared with the Sadovskii (1971) pair 197
5.42	Rate of stretching of the centroid for the collision of $\alpha = 0.5$ 198
5.43	Rate of stretching of the head for the collision of $\alpha = 0.5$ as determined by the node point with maximum radius compared with the estimate given by Equation (5.2.19) 198

<i>Figure</i>	<i>Page</i>
5.44	Core shapes for the collision of $\alpha = 1.0, \hat{d} = 10$ 199
5.45	Magnified portion of the shape at $U_o t/L_o = 8.89$ from the previous figure compared with the Sadovskii (1971) eddy 200
5.46	Smoke visualization of the collision of two vortex rings by Oshima (1978a) 201
5.47	Transfer spectra for $\alpha = 1.0$ collision 202
5.48	Spectra of the total energy and sum of self-energies for selected frames in Figure 5.43 203
5.49	Energy for $\alpha = 1.0$ collision 203
5.50	Normalized version of Figure 17a in Kambe and Minota (1983) 204
5.51	Acoustic signal for the collision of $\alpha = 0.5, \hat{d} = 8$ compared with the experiment of Kambe & Minota (1983) 204
5.52	Orientation angle of the ellipse fitted to the moments of the core shape for the collision of $\alpha = 0.5, \hat{d} = 8$ 205
5.53	Acoustic signal for the collision of $\alpha = 0.2, \hat{d} = 8$ 205
5.54	Acoustic signal at early times for the collision of $\alpha = 0.2, \hat{d} = 8$ 206
5.55	Acoustic signal in a later time interval for the collision of $\alpha = 0.2, \hat{d} = 8$ 206
5.56	Acoustic signal for the collision of $\alpha = 1.0, \hat{d} = 10$ 207
5.57	Energy spectra for two members of the Norbury-Fraenkel family 207
5.58	Cell discretization of Hill's spherical vortex 208
5.59	Cell discretization for the $\alpha = 0.2$ Norbury-Fraenkel vortex used for the passage interaction of §5.1.2 208
5.60	Contours of normalized vorticity ($\omega_\phi/(\mathcal{A}L_o)$) for the discretization of the previous figure and using a core overlap factor, $f_c = 3$ 209
5.61	Vorticity distribution along the central radial slice for the previous figure compared with the desired distribution 209
5.62	Cell discretization of the unit disk for Fraenkel's (1972) peaked vorticity solution ($\alpha = 0.2$) 210
5.63	Contours of $\omega_\phi L_o^2/\Gamma$ corresponding to the discretization of the previous figure and using a core overlap factor, $f_c = 3$ 210
6.1	Sketch of streamlines for separated viscous flow over a solid wall 235
6.2	Sketch of streamlines for steady vortex rings illustrating some non-linear dynamics nomenclature 235
6.3	Smale's horseshoe map 236
6.4	Unstable manifold of the forward periodic point for an elliptical core ring. $\lambda = 2, \alpha' \equiv (a+b)/(2L_o) = 0.15$ 236
6.5	Abridged portions of the stable and unstable manifolds corresponding to the previous figure illustrating fluid engulfment and rejection 237

<i>Figure</i>	<i>Page</i>
6.6	Volume of fluid exchanged by elliptical core vortex rings per diameter translation as a function of the ellipticity. The volume is scaled using the mean toroidal radius L_o 238
6.7	Sketch of the motion of selected fluid regions bounded by the manifolds 238
6.8	Sketch of six Poincaré maps of a rectangle (dotted) leading to a the horseshoe map 239
6.9	Schlieren visualization of a shock-tube generated ring propagating to the left. <i>Courtesy of B. Sturtevant</i> 240
6.10	Poincaré section of regions of fluid permanently carried by an elliptical core ring with $\lambda = 2$ and $\alpha' \equiv (a + b)/(2L_o) = 0.15$ 241
6.11	Poincaré section of particle paths for Kirchhoff's two-dimensional elliptic vortex in a reference frame rotating with the vortex for aspect ratios 1.1 and 2 241
6.12	Poincaré section of particle paths for an elliptic vortex with a propagating wave on the boundary ($m = 4, \epsilon_a = 0.1, \lambda = 2$) 242
6.13	Close-up of the upper mound region in Figure 6.12 242
6.14	Poincaré section of particle paths for an elliptic vortex with a propagating wave on the boundary ($m = 3, \epsilon_a = 0.1, \lambda = 2$) 243
6.15	Same case as the previous figure showing one orbit started just outside the outermost torus 243
6.16	Unstable manifold at different phases for two leapfrogging rings compared with photographs from Yamada & Matsui (1978). <i>Reproduced with permission</i> 244

NOMENCLATURE

Roman Symbols

a	Length of semi-major axis of ellipse.
a_i	Quantity defined in Equation (5.B.15) pertaining to the calculation of the kinetic energy of the vortex filament method.
a_j, a'_j	Coefficients in the expansion of the contour dynamics integrand about the singularity (§5.A).
$\hat{a}_j, \delta\hat{a}_j$	Cosine coefficient of Fourier series description of core boundary and its deviation from the value given by Norbury (1973), respectively.
A	Similar quantities defined in several contexts: Equations (3.2.7), (4.1.2), (4.1.13), (5.B.12), (5.B.20).
\bar{A}	Core structure parameter in Equation (2.10.1); cryptic representation of the angular momentum vector in Equation (2.9.1).
A_0, A_1, \dots	Lobes in Figure 6.5.
$A_m(t)$	Amplitude for an eigenmode of the perturbation streamfunction $\delta\Psi$ for Love (1893) waves on the boundary of elliptic vortex (see Equation (6.4.5)).
A	Jacobian matrix of a system of ordinary differential equations linearized about a fixed point.
\mathcal{A}	Constant of proportionality for the linear variation of vorticity ω_ϕ with respect to σ .
\mathbf{A}	Vector potential of the velocity field.
A_ϕ, A_z	Azimuthal and z components of the vector potential \mathbf{A} , respectively.
b	Length of semi-minor axis of ellipse.
b_j, b'_j	Coefficients in the expansion of the contour dynamics integrand about the singularity (§5.A).
$\hat{b}_j, \delta\hat{b}_j$	Sine coefficient of Fourier series description of core boundary and its deviation from the value given by Norbury (1973), respectively.
B	Similar quantities defined in several contexts: Equations (3.2.7), (4.1.2), (4.1.13), (5.B.20).
B_0, B_1, \dots	Lobes in Figure 6.5.
$B_m(t)$	Amplitude for an eigenmode of the perturbation streamfunction $\delta\Psi$ for Love (1893) waves on the boundary of elliptic vortex (see Equation (6.4.5)).
\mathbf{B}	Jacobian matrix of a discrete map linearized about a fixed point.
\mathbf{B}, B_ϕ	Magnetic field intensity vector and its azimuthal component, respectively.
c	Plane contour; ellipse parameter $\equiv \sqrt{a^2 - b^2}$ (§6.4).
c_j, c'_j	Coefficients in the expansion of the contour dynamics integrand about the singularity (§5.A).
\bar{c}	Phase velocity (angular) of small amplitude waves on the boundary

	of a circular patch of constant vorticity.
c_o	Speed of sound in the medium at rest.
C	Amplitude of acoustic signal for a vortex ring with elliptical core defined in Equation (4.2.57); constant in the rate of stretching expression (5.2.19).
C_H	Multiplicative constant in the Hanning filter function.
C_i	Space curve for the i th vortex filament.
C	Coefficient in series expansion of contour dynamics integrand about the field point.
CS	Cross-section in a meridional plane of an axisymmetric vorticity containing domain.
d	Separation distance between two co-rotating two-dimensional vortex patches or the initial axial separation of two identical vortex rings.
\hat{d}	Initial axial separation of two identical vortex rings scaled on the mean toroidal radius L_o .
D	Diameter of pipe, orifice or jet.
D^2	Elliptic operator defined in Equation (2.7.2).
D_1, D_2	Constants in Equation (6.4.7).
$\mathcal{D}, \partial\mathcal{D}$	Vorticity containing domain and its boundary, respectively.
$\mathcal{D}+$	Any region containing \mathcal{D} .
D_o	Initial mean toroidal diameter of vortex ring ($\equiv 2L_o$).
e	Rate of plane strain.
E, \hat{E}	Kinetic energy with density set to unity and its normalized counterpart (see Equation (5.A.18)).
E_{2-D}	Kinetic energy per unit span (with density set to unity) of a two-dimensional vortex pair.
E_j^{self}	Energy of the velocity field induced by ring j in isolation.
$E(k), \hat{E}(\kappa)$	Radial energy spectrum function and its normalized counterpart (see Equation 5.A.18).
E_{ij}, \hat{E}_{ij}	Energy of interaction between vortex rings i and j and its normalized counterpart, respectively.
$E_{ij}(k), \hat{E}_{ij}(\kappa)$	Radial spectrum of the interaction energy and its normalized counterpart, respectively.
$E(\bar{r})$	Elliptic integral of the second kind as a function of modulus \bar{r} .
E_a	Radiated acoustic energy with density set to unity.
E^c, E^s, E^u	Center, stable and unstable eigenspaces, respectively.
f	Right hand side vector in a system of first order ordinary differential equations; segment geometry parameter in §3.A.
f as index	Refers to the "field" vortex.
$f(\psi)$	Azimuthal vorticity function ω_ϕ/σ for steady vortex rings.
f_c	Core overlap factor for the vortex filament method.
f_{jc}	Jet-column mode forcing frequency (Hz).
f_p	"Preferred" mode forcing frequency of a jet (Hz).
$f_H(t)$	Hanning filter function defined in Equation (5.1.1).

fs	Pair of indices used to denote quantities evaluated at the “field” vortex induced by the “source” vortex.
F	Front stagnation point in Figure 6.2 <i>b</i> ; front hyperbolic fixed point of the Poincaré map (§6.4).
g	Rate of “composite” strain in elliptic model defined in Equation (4.2.44); discrete map (§6.2).
$\bar{g}(x, \sigma)$	A non-negative bounded function in Benjamin’s variational statement (§2.7.3).
G	Integral defined in Equation (3.2.14).
\mathcal{G}	Green’s function for the Stokes’ streamfunction which is also the streamfunction of a ring of zero cross-section.
$\widehat{G}(\mathbf{k})$	Radial Fourier transform of the vortex filament method core function $\gamma(\mathbf{y})$.
h_n, h_s, h_ϕ	Metrics of the coordinate system (n, s, ϕ) conforming to the vortex ring boundary.
h_o	Quantity pertaining to elliptic coordinates (ξ, η) (defined in Equation (6.4.11)).
h	Axial width of a vorticity layer.
$h(x, y, t)$	Function such that $h = 0$ defines the boundary of an ellipse.
$\bar{h}(x, \sigma)$	“Rearrangements” of $\bar{g}(x, \sigma)$ (see §2.7.3).
H	Integral defined in Equation (3.2.14).
H_{ij}	Double line integral over vortex filaments i and j defined in Equation (5.B.16).
\bar{H}	Bernoulli head ($\equiv p/\rho + \frac{1}{2}\mathbf{u}^2$).
\bar{H}_o	Value of Bernoulli head in the potential flow exterior to a vortex.
\mathcal{H}	Hamiltonian for Dyson’s (1893) model.
$\mathcal{H}_i^{\text{self}}$	One vortex Hamiltonian for Dyson’s (1893) model.
$\bar{\mathcal{H}}_i$	Quantity defined in Equation (4.1.12).
\mathcal{H}_{ij}	Interaction Hamiltonian for Dyson’s (1893) model.
\mathcal{H}_e	Hamiltonian for an elliptic vortex patch in a strain field.
I_1, I_2, I_3	Integrals defined in Equation (3.B.14).
$I_4(\mu), I_5(\mu)$	Integrals defined in Equation (4.1.4).
$I_6(\mu), I_7(\mu)$	Integrals defined in Equation (4.2.30).
I_n	Integral with respect to the direction normal to the vortex boundary in Equation (3.B.9).
j_{ik}	Second order moments of the shape of a vortex core about its centroid (defined in Equation (4.2.10)).
$j_{0,1}$	First root of the Bessel function J_0 .
\mathbf{j}	Current density.
J_1	Bessel function of the first kind.
k	Magnitude of wave-number vector; parameter characterizing the peakiness of the vorticity for a class of two-dimensional circular vortex patches (§5.B.4).
k_z	Axial wave-number.

\mathbf{k}	Wave-number vector.
$K(\bar{r})$	Elliptic integral of the first kind as a function of modulus \bar{r} .
$\widetilde{K}(\psi)$	Azimuthal circulation on a streamsurface for a steady vortex ring with swirl.
K_1	Modified Bessel function of the second kind.
\mathbf{K}_1	Integrand for the jump contribution to the contour dynamics velocity field, defined in Equation (3.2.14).
\mathbf{K}_2	Integrand for the contribution to the contour dynamics velocity field from the continuous part of the vorticity, defined in Equation (3.2.24).
l	Length of a segment approximating a contour of integration.
l_{\max}	Length of the largest segment approximating a contour of integration.
l_x, l_σ	x and σ components of a vector directed along a segment in the direction of integration.
$\bar{l}_x, \bar{l}_\sigma$	x and σ components of a vector pointing in the direction of integration along the backward segment adjacent to the singularity.
l	Radial extent of a vortex layer.
L	Piston stroke.
\bar{L}	Unspecified vortex length scale.
\mathcal{L}	Length of closed vortex filament.
$L_m(z)$	Contribution to the line integral for two-dimensional contour dynamics by a segment from z_m to z_{m+1} in the complex plane.
L_o	Reference vortex ring length scale defined to be the mean toroidal radius.
m	Azimuthal wavenumber for Kelvin (1880 <i>b</i>) waves on a circular patch of uniform vorticity; wavenumber along the coordinate η for Love (1893) waves on an elliptic vortex (§6.4).
m_{ij}	Moments of vorticity distribution defined for planar flow in Equation (4.2.3) and Equation (5.A.19) for axisymmetric flow.
M	Mach number based on self-induced vortex ring translational velocity.
n	Curvilinear coordinate normal to the generator of the vortex boundary in a meridional plane (see Figure 4.2); frequency (number of cycles in the time record) in §5.1.1 and Figure 5.3.
n_s, n_u	Number of stable and unstable eigenvectors, respectively.
$\hat{\mathbf{n}}$	Unit vector, normal to a plane contour; unit vector normal to any surface surrounded by the vortex filament (after Equation 5.B.21).
N_w	Number of azimuthal waves on a vortex ring.
N_s	Number of segments used to represent a contour.
N_{st}, N_c	Parameters for the cell discretization of a Fraenkel (1972) vortex ring. Number of annular strips on the unit disk and number of these strips in the region of clustering, respectively (see §5.B.4).
O	Oval shaped region consisting of non-oscillating halves of the stable and unstable manifolds.
p	Hydrodynamic pressure; in §4.2, an element of the velocity gradient

	matrix defined in Equation (4.2.17) for planar flow and Equation (4.2.29) for axisymmetric flow; in §3.A, a segment geometry parameter.
p_a	Far-field acoustic pressure.
\mathbf{P}	Impulse vector per unit density.
P	Magnitude of the impulse vector per unit density.
P_i	Contribution to the impulse P from the i th ring.
\hat{P}	Normalized impulse defined in Equation (2.5.2).
\tilde{P}	Symbolic representation of the impulse vector in §2.9.1.
P_1^J, P_2^J	Polynomials of degree J with vector coefficients.
$P_{1/2}^{-1}$	Toroidal Legendre function.
q	Element of the velocity gradient matrix defined in Equation (4.2.17) for planar flow and Equation (4.2.29) for axisymmetric flow; segment geometry parameter in §3.A.
$q(r, \delta)$	Filament method core function in Equation (5.B.4) with the core size parameter δ .
$Q(t)$	Acoustic source function for axisymmetric flow defined in Equation (4.2.49).
Q'''	Third time derivative of the acoustic source function $Q(t)$.
Q_{ij}	Acoustic source tensor for 3-D flow.
$Q_1(\varrho)$	Function in the mapping (5.B.31) that defines Fraenkel's (1972) peaked vorticity rings.
\tilde{Q}	Symbolic representation of Phillips' (1956) quadrupole moment tensor in §2.9.1.
Q	$(1/2)\Delta$.
r	Radial distance in spherical polar coordinates.
\bar{r}	Modulus of elliptic integrals.
r^*	Complementary modulus of elliptic integrals ($\equiv \sqrt{1 - \bar{r}^2}$).
r_c	Geometric clustering factor for cell discretization of a Fraenkel (1972) vortex ring (see §5.B.4).
\mathbf{r}	Coordinate of a point on a space curve.
R	Impulse radius of a vortex ring ($\equiv \sqrt{P/(\pi\Gamma)}$); rear stagnation point in Figure 6.2.b; rear hyperbolic fixed point of the Poincaré map (§6.4).
R^n	n -dimensional Euclidean space.
Re	Reynolds number of vortex ring (defined where used).
Re_D	Reynolds number of vortex ring based on initial translational speed and the aperture diameter.
Re_m	Reynolds number of vortex ring based on initial translational speed and maximum diameter of dye bubble.
Re_p	Reynolds number of vortex ring based on average piston speed \bar{U}_p and aperture diameter D .
Re_j	Reynolds number of jet based on exit velocity U_e and diameter D .
s	Curvilinear coordinate around a plane contour; symmetric core func-

	tion in filament schemes 'C' and 'D' (see Equations (5.B.7) and (5.B.8)).
s as index	Refers to the "source" vortex.
S	Vortex core area; separation point (§6.2).
S_Λ	Area of the invariant set Λ .
St_D	Strouhal number based on jet exit velocity U_e and diameter D .
St_{θ_m}	Strouhal number based on jet exit velocity U_e exit shear layer momentum thickness θ_m .
S, S'	Contour integral defined in Equation (5.A.11) and its value for $\vartheta = \pi/2$, respectively.
S	Straining (linear) part of the velocity field in 2-D or in the meridional plane for axisymmetric flow.
t	Time; dummy variable of integration in Equation (5.B.4).
t'	Dummy variable of integration.
\hat{t}	Normalized time ($\equiv U_o t / L_o$).
$\hat{\mathbf{t}}$	Unit vector tangent to the boundary of a two-dimensional uniform vorticity region.
Δt	Time step.
T	Core rotation period of a vortex ring with an elliptical cross-section according to the asymptotic solution of Moore (1980).
T_1-T_9	Quantities defined in Equation (3.A.8).
T_c	Period between the creation of two vortex rings.
T_e	Ejection time of fluid slug in vortex ring formation.
T_p	Passage period of two vortex rings.
T_s	Period of time signal.
T_s	Local period between zero crossings of the integrand.
$T(k), \hat{T}(\kappa)$	Energy transfer rate spectrum and its normalized counterpart, respectively (5.A.17).
$T_{ij}(k), \hat{T}_{ij}(\kappa)$	Transfer rate spectrum of the energy of interaction between rings i and j and its normalized counterpart, respectively (see Equations (5.A.17) and (5.A.18)).
u	Velocity component in the x direction for planar flow; used for convenience in place of the axial velocity in cylindrical coordinates (u_x) in Chapter 4 and §5.B.2.
u_x, u_σ, u_ϕ	Velocity components in cylindrical coordinates.
$(u_x)_{2-D}$	Locally two-dimensional part of u_x .
$(u_\sigma)_{2-D}$	Locally two-dimensional part of u_σ .
$u_{,x}$	$\partial u / \partial x$ and similarly for other partial derivatives of u .
\mathbf{u}	Velocity vector.
\mathbf{u}_C	Contribution to the velocity from the continuous part of the vorticity.
\mathbf{u}_J	Contribution to the velocity from the jump in vorticity at the boundary.
$\hat{\mathbf{u}}$	Fourier transform of velocity vector.
$U(t)$	Time dependent speed of propagation of a vortex ring (centroid definition specified in each case).

U_e	Jet exit velocity.
$U_p(t)$	Time dependent piston speed.
\bar{U}_p	Average piston speed.
U_o	Speed of translation of a steady vortex ring in isolation.
U_i^{self}	Self-induced translational velocity of the i th ring in Dyson's model.
\mathcal{U}	Open set containing the fixed point \bar{x} .
v	Velocity component in the y direction; radial velocity in cylindrical coordinate system used in place of u_σ for convenience in Chapter 4.
$v_{,x}$	$\partial v / \partial x$ and similarly for other partial derivatives of v .
\bar{v}	Radial velocity evaluated at the centroid of the shape of the vortex core.
V_o	Speed of translation of a two-dimensional steady vortex pair.
$\text{Vol}(\psi)$	Volume distribution of regions bounded by streamsurfaces $\psi = \text{const}$.
V	Volume of vortical fluid.
\bar{V}	Non-dimensional speed of propagation of vortex ring defined in Equation (2.10.1).
V_j	Eigenvectors of the Jacobian matrix A .
w	Velocity component in the z direction.
$W(\chi)$	Flux of the azimuthal component of magnetic field through a flux tube $\chi = \text{const}$.
$W^c, W^s, W^u(\bar{x})$	Center, stable and unstable manifolds of the fixed point \bar{x} .
x	Axial position in cylindrical coordinate system; vector of independent variables in a system of ordinary differential equations (§6.2.5).
\bar{x}	x shape centroid of vortex core; fixed point of a system of ordinary differential equations or a discrete map (§6.2.5).
\tilde{x}	x position measured from the shape centroid of a two-dimensional vortex patch or vortex ring core.
\hat{x}	Non-dimensional axial coordinate x ($\equiv x / \bar{L}$).
x'	x position of source (integration) point; moving coordinate in Equations (4.2.51) and (4.2.52).
\hat{x}	Unit vector in the direction of coordinate x .
x''	Rotated Cartesian coordinate along principal strain direction.
\mathbf{x}	Space coordinate vector.
\mathbf{x}'	Space coordinate vector to the source (integration) point.
$\bar{\mathbf{x}}$	Position vector in the plane, to the centroid of a two-dimensional vortex patch.
$\dot{\bar{\mathbf{x}}}$	$d\bar{\mathbf{x}}/dt$.
$\tilde{\mathbf{x}}$	Position vector in the plane, measured from the centroid of a two-dimensional vortex patch.
X	Coordinate in the deformation phase plane of an ellipse ($\equiv \lambda \cos(\varphi - \varpi)$).
X'	Cartesian coordinate along the major axis of a rotating ellipse.
y	Cartesian coordinate; dummy argument or variable of integration in Equations (5.B.8) & (5.B.14).

\bar{y}	y shape centroid of vortex core.
\bar{y}	y position measured from the shape centroid of a two-dimensional vortex patch.
y'	y position of source (integration) point.
y''	Rotated Cartesian coordinate along principal strain direction.
y	Space coordinate vector used as a dummy variable of integration.
\hat{y}	Unit vector in the direction of coordinate y .
Y	Coordinate in the deformation phase plane of an ellipse $\equiv \lambda \sin(\varphi - \varpi)$.
Y'	Cartesian coordinate along the minor axis of a rotating ellipse.
z	Cartesian coordinate; complex variable $\equiv x + iy$ (§§3.1 & 6.4).
\hat{z}	Unit vector in the direction of coordinate z .
Z'	Point in the complex plane rotating with the ellipse ($\equiv X' + iY'$).

Greek Symbols

α	Ratio of area-effective core radius δ_s to mean toroidal radius L_o characterizing a steady vortex ring.
α'	Measure of the initial ratio of core size to toroidal radius of an elliptical core vortex ring ($\equiv (a + b)/(2L_o)$); defined to be $(a + b)/2R$ in Equation (4.2.62).
$\bar{\alpha}$	Orientation of principal strain axis relative to the x axis.
$\hat{\alpha}$	Constant of proportionality for the linear variation of azimuthal circulation $\bar{K}(\psi)$ with respect to ψ .
α_o	Free parameter in vortex filament method.
β	Angular coordinate in plane polar coordinates (ϱ, β) .
$\hat{\beta}$	Angular coordinate of plane polar coordinates $(\hat{\varrho}, \hat{\beta})$ having a different origin than (ϱ, β) coordinates.
β_1, β_2	Constants defined in Equations (6.4.8) and (6.4.9).
χ	Flux function of the magnetic field intensity \mathbf{B} .
δ	Radius of a circular vortex core; core size parameter in the vortex filament method (§5.B).
δ_o	Initial value of the core radius.
δ_c	Unspecified characteristic core size of a vortex ring.
δ_s	Area-effective core radius ($\equiv \sqrt{S/\pi}$).
$\delta\rho(\beta)$	Deviation of the vortex core boundary from the shape given by Norbury (1973).
$\delta\xi$	Difference in the value of the elliptic coordinate ξ between a point on the perturbed boundary of an elliptic vortex and the unperturbed boundary ξ_o .
$\delta\Psi$	Perturbation streamfunction for Love (1893) waves on the boundary of an elliptic vortex.
Δ	$ \mathbf{x} - \mathbf{x}' $, distance between the field point and source (integration) point; in some cases the two points are restricted to lie in a meridional plane; Δ is also used to denote increments.

Δz_m	$z_{m+1} - z_m$.
$\Delta(\xi, \xi')$	$\equiv \mathbf{r}_i(\xi) - \mathbf{r}_j(\xi') $, the distance between two points on vortex filaments i and j .
Δ	$\equiv \mathbf{r}_i - \mathbf{r}_j$, the vector between two points on vortex filaments i and j .
Δ_{ij}	Distance between the core shape centroids of rings i and j .
Δt	Time step.
$\epsilon, \epsilon', \epsilon''$	Small quantities with multiple usage (defined where used).
ϵ_a	Parameter, defined in Equation (6.4.13), characterizing the amplitude of Love (1893) waves on the boundary of an elliptic vortex.
ϵ_e	Ellipticity ($\equiv (\lambda - 1)/(\lambda + 1)$).
ϵ	Thickness of thin shell surrounding the boundary of the vortex.
η	Angular coordinate in elliptic coordinates (ξ, η) .
η_a	Acoustic efficiency.
γ	Core function for vortex filament method.
Γ	Vortex circulation.
κ	Wavenumber normalized with the mean toroidal diameter D_o .
λ	Ellipse aspect ratio $\equiv a/b > 1$; horizontal compression factor in Smale's horseshoe map (§6.2); (Beltrami) constant of proportionality between the vorticity and velocity vectors in Equation (6.3.2).
λ_j	Eigenvalues of the Jacobian matrix A .
$\tilde{\lambda}$	Constant of proportionality for the linear behavior of the Bernoulli function $\tilde{H}(\psi)$ for steady vortex rings of a certain class.
λ_e	Equilibrium value of the ellipse aspect ratio.
Λ	Invariant set for Smale's horseshoe map.
μ	Dummy argument for integrals I_4 - I_7 defined in Equation (4.1.4); dummy variable in Equations (4.1.15), (5.A.20), (5.B.3) and (5.B.17)-(5.B.19); vertical stretching factor in Smale's horseshoe map (§6.2).
μ^*	$\equiv \sqrt{\mu^2 - 1}$.
ν	Kinematic shear viscosity.
$\tilde{\nu}$	Eigenvalues (complex) for the motion of an elliptic uniform vortex in a strain field linearized about the equilibrium (see Equation (4.2.48)); eigenvalues for Love (1893) waves on the boundary of an elliptic vortex (see Equation (6.4.7)).
$\tilde{\nu}_1, \tilde{\nu}_2$	Quantities defined in Equation (6.4.7).
ω	Notation for azimuthal vorticity used in place of ω_ϕ between Equations (4.1.17) and (4.1.26); Frequency (radians/sec) in the acoustic spectrum shown in Figure (5.20).
ω_e	Frequency of the elliptic <i>azimuthal</i> mode for a thin vortex ring given in Equation (5.1.10).
ω_o	Value of vorticity inside a two-dimensional patch of uniform vorticity; uniform value of vorticity towards the positive normal vector (§3.1).
$\omega_x, \omega_\sigma, \omega_\phi$	Vorticity components in cylindrical coordinates.

ω_z	Vorticity component in the z direction.
$[\omega_z]$	Jump in vorticity, $\omega_0 - \omega_1$, across an interface between two regions of uniform vorticity, where ω_0 and ω_1 are the values towards the positive and negative normal directions, respectively.
ω_1	Uniform value of vorticity in the region towards the negative normal vector.
$\bar{\omega}_\phi$	Average azimuthal vorticity in the core ($\equiv \Gamma/S$).
$\hat{\omega}_\phi$	Non-dimensional azimuthal vorticity ($\equiv \omega_\phi L^2/\Gamma$).
$\hat{\omega}_{\phi k}$	Component of the Fourier transform of the vorticity in the azimuthal direction in wavenumber space.
ω	Vorticity vector.
$\hat{\omega}$	Fourier transform vorticity vector.
Ω	Angular rotation rate of a particle.
ϕ	Azimuthal angle in cylindrical or spherical coordinate system measured from the y Cartesian axis.
$\bar{\phi}$	Added direction in the phase space of a dynamical system; dummy integration variable introduced after Equation (5.A.8).
$\bar{\phi}_0$	Value of the phase space coordinate $\bar{\phi}$ defining the Poincaré map as being from $\bar{\phi}_0$ to $\bar{\phi}_0 + 2\pi$.
ϕ_k	Azimuthal position in cylindrical coordinate system in wavenumber space.
Φ	Complex velocity potential.
$\delta\Phi$	Perturbation potential (complex) for Love (1893) waves on the boundary of an elliptic vortex.
$\hat{\phi}$	Unit vector in the direction of increasing ϕ .
$\hat{\phi}_k$	Unit vector in the direction of increasing ϕ_k (in wavenumber space).
φ	Orientation angle of ellipse relative to the x -axis.
φ_e	Equilibrium value of ellipse orientation angle φ .
φ_0	Initial value of ellipse orientation angle φ .
ϖ	"Composite" straining angle in the elliptic model defined in Equation (4.2.45).
ψ	Streamfunction (Stokes') for axisymmetric incompressible flow.
Ψ	Streamfunction for two-dimensional flow.
Ψ_0	Value of the streamfunction on the boundary of a two-dimensional steadily translating vortex pair in a co-moving frame.
$\delta\Psi$	Perturbation streamfunction for Love (1893) waves on the boundary of an elliptic vortex.
ρ	Density.
ρ_0	Density of the acoustic medium at rest.
ϱ	Radial coordinate in plane polar coordinates (ϱ, β) .
$\hat{\varrho}$	Radial coordinate in plane polar coordinates $(\hat{\varrho}, \hat{\beta})$ having a different origin than (ϱ, β) coordinates.
$\varrho(\beta)$	Function which describes the shape of the vortex core boundary.
$\delta\varrho(\beta)$	Deviation of the vortex core boundary from the shape given by Nor-

	bury (1973).
σ	Radial position in cylindrical coordinate system (distance normal to the symmetry axis).
$\bar{\sigma}$	Radial position measured from the shape centroid of a vortex ring core.
$\hat{\sigma}$	Non-dimensional σ ($\equiv \sigma/L$).
σ_k	Same as σ but in wavenumber space.
σ'	Radial position of source (integration) point in cylindrical coordinates.
$\bar{\sigma}, \bar{\sigma}_0, \dot{\bar{\sigma}}$	Radial shape centroid of vortex ring core, its initial value and rate of change, respectively.
τ_1, τ_2	Time scales for internal rotation and variation of an externally imposed velocity field, respectively.
θ	Angle of lines of constant s relative to the x -axis in a fixed ϕ plane.
θ_m	Shear layer momentum thickness.
ϑ	Polar angle in spherical coordinates measured from the x -axis.
ϑ_k	Same as above but in wavenumber space.
Θ	Orientation of major axis of ellipse relative to principal strain direction ($\equiv \varphi - \bar{\alpha}$).
ξ	Parameter along a plane contour, space curve or segment of integration; the deviation $x - \bar{x}$ from the fixed point of a dynamical system (§6.2); "radial" elliptic coordinate (§6.4).
ξ'	Parameter along a plane contour, space curve or segment of integration.
ξ_0	Value of the elliptic coordinate ξ on the boundary of an elliptical vortex; initial condition for dynamical system linearized about a fixed point (§6.2).
ξ_1	A particular value of the parameter ξ on a segment of integration.
$\delta\xi$	Difference in the value of the elliptic coordinate ξ between a point on the perturbed boundary of an elliptic vortex and its value on the unperturbed boundary, ξ_0 .
ζ	Complex plane representation of elliptic coordinates ($\equiv \xi + i\eta$).

Other Symbols

!	Factorial.
,	Derivative with respect to the indicated argument.
\dot{q}	First time derivative of the quantity q .
*	Denotes complex conjugation.
	Scalar magnitude of a vector quantity; absolute value of a scalar.
\cap	Intersection.
\in	Belongs to.
$[a, b]$	Closed interval on the real line.
$\mathcal{O}(\)$	Order of.
$\Re\{q\}$	Real part of a complex quantity q .

Abbreviations

KAM	Kolmogorov-Arnold-Moser (theorem).
KM	Kambe & Minota (1983).
KdV	Korteweg-de Vries (equation).
M	Maxworthy (1974).
MZS	Melander, Zabusky & Styczek (1986).
NF	Norbury-Fraenkel (family of steadily translating vortex rings), see §2.7.
n	Used after a page number reference to indicate a footnote.
RLW	Rom-Kedar, Leonard & Wiggins (1988); also used for regularized long wavelength (equation).
RC	Rott & Cantwell (1988).
SCS	Stanaway, Cantwell & Spalart (1986, 1988 <i>a</i> , <i>b</i>).
WBT	Widnall, Bliss & Tsai (1974).
I	Zaman & Hussain (1980).
II	Zaman & Hussain (1984).
III	Hussain & Zaman (1980).
IV	Hussain & Zaman (1981).
V	Zaman (1985).

CHAPTER 1

GENERAL INTRODUCTION

1.1. The fascination of vortices†

We are fascinated by vortices because they appeal to both our imaginative (aesthetic) and deductive (noetic) faculties. With respect to the first, the dynamic power of wind and water has, from the earliest times, influenced rational and mythical attempts to come to terms with the mystery of the origin of the world, life, and their underlying forces. The whirl as a symbol for life, energy, ethical forces and states of higher (and lower) consciousness recurs in many ages, cultures and literatures. Yahweh speaks to Job from a whirlwind. According to von Kármán (1967) the vortex has also been “the ultimate symbol of danger to men. ‘Beware the eyes of the strange woman,’ says a translation from the Bible. ‘Her eyes are like a vortex.’” An almost identical association is made in the ancient Egyptian “Boulak Papyrus” (Minahen 1983, p. 158). Minahen (1983) devotes an entire thesis to the interpretation of the vortex symbol in the writings of Homer, pre-Socratic philosophers, Dante, William Blake and nineteenth century symbolists such as Edgar Allen Poe. Minahen gives many delightful quotes; two favorites appear on pages vi–vii together with a quote from a recent work by J. Lilly; we may not agree entirely, but we can be eclectic.

The vortex is a powerful primordial symbol in what Jungian psychologists call the “collective unconscious” of man and it has also surfaced in art and in scientific thought. In an article that deals with the role of computer generated images in stirring the intuition, Zabusky (1981) ends by quoting a statement by W. Pauli, a sober physicist. It states that new knowledge and understanding of nature is based on a matching of pre-existent inner primitive emotional images with external objects and their behavior.

Lugt (1983), in the first section of his book on vortex motion gives several examples of the appearance of the vortex motif in art and myth but as a personal and contemporary example of how internal images can surface in art and be in *accordance*

† The title of this section was inspired by Peregrine’s (1981) article entitled “The fascination of fluid mechanics.”

with *unseen* physical reality, there is the painting "Two macaques: mid-morning"†, in which the Kenyan born artist Jesse Allen depicts the sun in his imaginary world of fantasy with a pattern that evokes a sense of great but subdued power. Is it merely an accident that the pattern corresponds to the magnetic-force surfaces in the stellar model of Prendergast (1956)? Or, is it based on the type of intuition that Pauli describes? One teachers in graduate school here said that when people claim to be using intuition they are only recalling an argument they once learned or knew but simply could not trace through all the steps; in other words, intuition is knowing something to be true but forgetting why! We think that, while this is true in many circumstances, the testimonies given in Hadamard (1954) of the flashes of inspiration of many great mathematicians belong to a different category.

There are examples of the appearance of the vortex symbol in science. For a century preceding the acceptance of Newton's ideas on gravitation, the vortex theory of planetary motion published by Descartes in 1644 was propounded by his followers (Aiton 1972). They proposed that the planets must be carried in a fluid medium that was set into motion by the influencing body. The Cartesians rejected Newton's theory because the action at a distance concept was not compelling to them just as it is also not satisfying for us today.

It was a similar displeasure with unseen forces that led Kelvin to seek a theory of physical processes that used only the notions of matter and motion. Then in 1867, during its translation by Tait, Kelvin became enchanted with the 1858 paper of Helmholtz which laid the foundations of rotational motion. In fact, as an appendix to its translation, Tait published a letter by Kelvin in which he provided, without proof, the famous formula for the speed of translation of a vortex ring of circular cross-section. Vortex rings seemed ideal candidates for the essential constituents of the theory that Kelvin was seeking. In the same year in a paper entitled "On Vortex Atoms" Kelvin laid the beginnings of a theory that he was to proclaim until about 1880 (Buchwald 1976).

The topic set for the Adams Prize of 1882 was a "general investigation of the action upon each other of two closed vortices in a perfect incompressible fluid" (Heilbron 1976), a subject considered in this work. In his prize winning contribution "A Treatise on the Motion of Vortex Rings", J.J. Thomson (1883) went much further than required. He proceeded to explain many properties of matter: radiation, heat

† Vorpall Galleries, San Francisco.

conduction, chemical reactions by appealing to known facts about vortex rings and his own very original and still lasting deductions.

We turn next to the way in which vortices appeal to the logical and deductive side of our nature by providing us with a tool for explaining many fluid phenomena with only a little arm-waving and finger curling. Even though the aim of the early work towards a theory of atoms as being rotational motion in some postulated fluid possessing inertia (the æther) never materialized, the mathematical ideas and purely hydrodynamic results that were discovered are still used today. These authors have come to an appreciation that classical work has more relevance to the behavior of “real” vortex rings than one admits at first sight. With only minor additions to the classical line of inquiry, many experimentally observed features can be explained. In his inaugural lecture at the Imperial College, D.W Moore (1979) expresses a similar sentiment. He begins by stressing the “continuing vitality of the ideas contributed by the founders of the subject (of vortex motion), H. von Helmholtz and Lord Kelvin.” This vitality exists because many phenomena can be described by appealing to the concept of vorticity e.g. lift. It provides a powerful intuitive tool and increased knowledge and new examples of vortex behavior serves to sharpen it. Many facts known to us analytically can receive satisfying mechanical and geometric explanation in terms of vorticity. For example, Lighthill (1966) explains many phenomena in rotating fluids using vorticity “as the sole theoretical tool,” Hornung (1988) is able to quickly deduce without any mathematics that in a flow with a rotating lid, no steady solutions are possible at sufficiently high Reynolds number. Lin (1955, §4.4) explains the inflection point instability in terms of vorticity. The analogy between vorticity tilting and gyroscopic precession is used by Stuart (1967) to understand Rayleigh’s criterion for centrifugal instability and by Squire & Winter (1951) to understand the occurrence of secondary vorticity in wind-tunnel turning vanes.

Turbulence is often defined as “fluctuating vorticity.” Many find displeasure in statistical theories of turbulence and grope for physical or structural models. In the early seventies (Brown & Roshko 1974, Winant & Browand 1974) it came to be realized that many turbulent flows of engineering interest are not as chaotic as once thought but contain large scale vortex structures whose behavior is independent of Reynolds number when it is sufficiently large, which maintain their identity for long periods and between which recognizable interactions occur. Better understanding

of vortex dynamics is sure to lead to understanding of discrete events present in turbulent flows and, with it, an ability to control them.

1.2. Objectives

The motion of vortex rings has been the subject of longstanding inquiry. Most of the theoretical knowledge deals with the speed of translation of thin rings, interactions between vortices of such thin cores that their deformation may be neglected or, as in the case of Hill's spherical vortex and the Norbury-Fraenkel family of vortex rings, with inviscid steadily translating vortices (see §2.7 for a review). In referring to the latter, whose interactions are a primary subject of this work, Saffman (1981*b*) has said "The use of such vortex structures as models of the quasi-permanent coherent structures of a turbulent flow makes the study of their interactions and stability a matter of pressing interest." This work aims to provide a contribution in that direction.

Interest centers on the three issues related to the roles played by the inviscid dynamics of quasi-permanent structures in turbulent shear flows:

(i) *The permanence versus destruction of vortex rings when they interact and the generation of fine scale features.* It is known that two-dimensional vortices disintegrate when the strain they are subjected to by other vortices exceeds a critical value (Moore & Saffman 1971). How do these ideas apply to the axisymmetric case? Whether one vortex ring can pass through another has been the subject of a series of interesting exchanges in the literature (see §2.6.3 for a review). In the context of inviscid flow, what factors determine a successful passage?

(ii) *Generation of sound.* D. Küchemann (1965) referred to vortices as the "sinews and muscles" of fluid motion. Müller & Obermeier (1988) suggested that since, for small Mach number, vortex motion is practically the only source of aerodynamic sound, we might also call vortices the "voice of the flow." Indeed, according to Minahen (1983), "the words 'whirl' and 'whorl', associated with the vortex, for example, the breathy 'wh' in combination with the churning 'rl' indicates something more than a simply arbitrary relationship between the idea and its acoustical image..." In order to understand some basic sources of sound by vortex motions we shall study the sound generated by axisymmetric vortex dynamics. Kambe & Minota (1983) provide measurements of the acoustic radiation generated by two colliding rings and

the present simulations reproduce them well. In particular a feature in the signal they thought was due to viscous effects will be explained in terms of inviscid core deformation.

Winant & Browand (1974) suggested that pairing of vortex rings is the primary mechanism responsible for the generation of jet noise (under conditions in which pairing is in fact present, which it is not always). Since then, much experimental evidence has been gathered to favor this view. See Crighton (1980) for an excellent review. What particular aspects of the pairing process accounted for in the present analysis are important? In the so-called preferred mode of a jet, pairing does not occur and other mechanisms have to be sought. Hussain (1983) suggested that vortex line reconnection when vortex ring like structures break down is the dominant source of sound in this case. Is the sound due to purely axisymmetric degrees of freedom consistent in these cases with the observed noise characteristics?

(iii) *Stirring*. One of the properties of vortices is that they transport fluid. From the common experience of stirring cream into a cup of coffee we know that the motion of the two vortices causes complicated winding and folding of the interface before molecular mixing occurs. In the context of shear layers, one of their outstanding features is spatial growth of the width of the vortical region—the laminar mixing layer grows as the square-root of the downstream distance while the turbulent layer is observed to grow linearly. Dimotakis (1984) explains the manner in which a parcel of irrotational fluid from outside a shear layer or jet becomes endowed with vorticity as a two step process: engulfment by the Biot-Savart induced velocity followed by straining and molecular diffusion.

Chapter 6 addresses the first step for idealized and abstracted situations. A steady vortex ring carries with it a body of fluid. When the ring is unsteady it constantly rejects fluid and engulfs fresh fluid. How and at what rate does this occur? Tracers such as dye, smoke, air-bubbles, water-vapor, density or temperature often allow us to visualize fluid flow—indeed on a personal level, our immediate experience (equations and hot-wire traces aside) of fluid motion is mostly a visual one. How are tracers transported? In what ways might our inferences of the underlying vorticity field based on visualization be mistaken? What accounts for the layered filamentary patterns that dye often takes on? These certainly are broad questions but a brief attempt in this direction in the context of vortex rings is made in Chapter 6.

1.3. Organization

In the next chapter a review of the known facts about axisymmetric vortex rings is provided. The results are mostly experimental but some theoretical results and numerical simulations are included. Issues that receive attention in the present work are pointed out and some open questions are discussed. Most of the observed phenomena await deeper inquiry by more careful, systematic and sophisticated experiments and theoretical or numerical modeling. We hope that the reader will take up some of these challenges.

Axisymmetry is assumed throughout this work although there is an observed (and explained) instability which causes azimuthal waviness followed perhaps, by breakdown to turbulence. To understand what limitations this places on the current results, the chapter will be concluded by a discussion of the stability of axisymmetric rings.

In Chapter 3 we develop an inviscid numerical method that is suited for vortex rings of a particular class, namely, those in which the azimuthal vorticity varies linearly with respect to distance from the axis of symmetry. The vorticity of a circular vortex line increases linearly as it stretches so such a distribution is maintained for all time. Hence one needs to follow only the motion of the boundary between regions in which the ratio of vorticity to distance from the axis takes different constant values. The evolution of the boundary is formulated as a 1-D integro-differential equation which is solved numerically. The method is an extension to axisymmetric flow of the contour dynamics method developed for two-dimensions by Zabusky, Hughes & Roberts (1979). Tests of accuracy and convergence are provided.

Chapter 4 discusses some simple but restricted models for this class of rings. First, the classical model due to Dyson (1893) is reviewed and some of its properties are discussed. It assumes (a) that the core size is sufficiently small compared to the radius allowing circular cores to be steady in isolation; (b) that interacting vortices remain sufficiently distant so that one vortex influences the other only via the leading far-field term of its induced velocity, for which the vorticity may be considered to be concentrated on an infinitesimally thin circle, and (c) that deviations of the cores from being circular due to straining may be neglected.

Then a simple model is constructed which relaxes assumption (c) above by allowing the cores to be strained into ellipses; it was inspired by a model for two-dimensional vortices by Melander, Zabusky & Styczek (1986). Six ODEs govern the position and

shape of each vortex. The axisymmetric model incorporates Moore's (1980) elliptic core vortex ring solution to obtain the self-induced motion and Kida's (1981) solution of a two-dimensional elliptic patch of vorticity in a strain to obtain the core deformation due to plane strain. The elliptic model allows one to anticipate many of the features observed with contour dynamics and provides one with a terminology for explaining them.

Chapter 5 contains the main results of the simulations. The results deal with passage and head-on collisions of two initially identical rings and the accompanying generation of sound. Comparison with the flow visualization experiments of Oshima and her co-workers and the sound measurements of Kambe & Minota (1983) for colliding rings is provided. Wherever possible a connection is made with observations of axisymmetric shear-layers and jet-noise characteristics. Essential differences between two-dimensional and axisymmetric vortex behavior are pointed out. The differences in behavior presented by rings with a vorticity distribution that is more realistic than the linear distribution of the contour dynamics method is studied. To this end the vortex filament method (discussed in Appendix 6.B) is first tested for accuracy against the linear vorticity solutions and then applied to peaked vorticity distributions.

In Chapter 6 use is made of some basic notions from dynamical systems theory to study how unsteady vortex rings engulf and stir parcels of fluid. The main objective is to understand features observed in flow visualization experiments. Some of these features have been identified as being vortical whereas they may be due to stretching, winding and folding of smoke or dye in irrotational or weakly vortical regions. Two main cases are considered: first, a time periodic vortex ring to address some observations of "turbulent rings" and finally two rings alternately passing through each other to address a controversy concerning the interpretation of the flow visualization experiments of Yamada & Matsui (1978).

Chapter 7 states the conclusions and suggests specific sub-problems as extensions.

1.4. Summary of main results

We now provide a summary of the results of the numerical simulations in Chapters 5 and 6. Both overtaking or "passage" and "collision" (head-on) interactions are presented. The experimental literature on the subject is reviewed in §2.6. Acoustic signals are calculated using the low Mach number theory of Möhring (1978). The final

result of that theory, given in Equations (4.2.49) and (4.2.50), shows that to obtain the time behavior of the acoustic pressure requires merely the evaluation of the third time derivative of the centroid of the vorticity as defined by Helmholtz (1858, or see Lamb 1932, §162).

Unless otherwise specified, the initial core shapes are chosen from the steadily translating family of solutions computed by Norbury (1973). The initial shapes are parametrized by α , the ratio of area-effective core radius to toroidal radius L_o . The ratio of initial separation to L_o is denoted as \hat{d} .

Qualitative appreciation of the differences in the interactions of thin versus thick cores can be obtained from the elliptic model by considering the ratio of two time scales. On one hand there is the inverse of the vorticity, say τ_1 , which determines the natural period of perturbations of the core. On the other hand there is the time scale of the overall motion of the rings, say τ_2 , which determines how fast the field imposed by the other vortex is changing. Using Kelvin's speed formula (Equation 2.7.3) to estimate τ_2 one obtains

$$\frac{\tau_1}{\tau_2} \sim \alpha^2 \log(1/\alpha), \quad (1.4.1)$$

i.e. for thin cores, internal rotation is faster than translation. The effect of this ratio may be qualitatively understood in terms of a spring-mass system. The extension of the spring is analogous to the aspect ratio of the core while gravity is analogous to the varying strain-rate imposed by the other vortex. The analogy can be justified only in the context of the elliptic model. When a vortex is nutating or rotating, time varying strain appears as time-dependent forcing on a system with solutions that are periodic with a frequency set by the vorticity.

If the spring is initially in equilibrium and gravity changes sufficiently slowly in comparison with the natural frequency of the spring, the length will remain close to the equilibrium values corresponding to the instantaneous values of gravity. If the spring is initially oscillating and gravity changes slowly, subsequent oscillations will take place about the slowly varying equilibrium. However, if the value of gravity changes rapidly, the spring will overshoot the equilibrium. If the spring is linear and elastic, when the value of gravity is restored to its initial value, oscillations will occur about the equilibrium, but if it is non-linear, oscillations may occur about some other position or the spring may continue to stretch indefinitely if there is no equilibrium at large extensions. Similarly, for thin cores we shall observe that core shapes follow the instantaneous equilibrium and nearly return to the initial

shape when the strain relaxes. For fatter cores, there is deviation from equilibrium without a return to the initial shape when the strain relaxes. We shall refer to this as “permanent deformation” without any connotation of irreversibility.

1.4.1. *Summary of passage cases*

Four types of outcomes were encountered in contrast with the “leapfrogging” that is predicted by Dyson’s model. The determining parameters are α and \hat{d} . An exhaustive exploration of the parameter space was not undertaken; we merely suggest trends and sketch the relevant physical effects. The attempt of one vortex ring to slip through another represents the initial phase of pairing in jets subjected to jet-column excitation as seen in Hussain & Zaman (1980). The value of \hat{d} is unity for all cases but the last and corresponds roughly to that resulting from jet-column mode excitation (J. Bridges, private communication).

The four outcomes observed are as follows:

(i) The classical picture holds for only the thinnest cores; this is represented by the first case ($\alpha = 0.1$, §5.1.1). Core deformations are imperceptible to the eye with maximum aspect ratio 1.14 and nearly periodic with no permanent deformation. Yet, they induce acoustic oscillations with large frequency and amplitude superimposed on the circular-core result (Dyson’s model). These oscillations increase the total radiated power by a factor of 6.8 over the invariant core result. The elliptic model predicts the core deformation and acoustic signature very well.

Although Dyson’s model fails to predict the acoustic signal, it approximates the velocity field well in this case since the ellipticity is small. Using Dyson’s model, motion of passive particles is investigated in §6.4 with a view to establishing a connection with flow visualization experiments. This is done by calculating the unstable manifold, a concept from dynamical systems theory which is reviewed in §6.2. The manifold bears a striking resemblance to even fine scale features in the smoke visualizations of Yamada & Matsui (1978). The paper by Yamada & Matsui elicited the comment that classical models of vortex rings are of little use in understanding real flows. The present result suggests that the observed smoke pattern may in fact be due to complex motion of tracer, with vorticity behaving in an approximately classical manner.

(ii) For the previous case ($\alpha = 0.1$) the elliptic model shows that the cores pulsate about the equilibrium shape corresponding to the instantaneous strain rate, e.g. as

the rear vortex completes its passage and the strain rate to which it is subjected decreases, its aspect ratio also decreases to its initial value—recall the spring-mass analogy. However, in a case that has cores only slightly thicker than the previous case ($\alpha = 0.14$, §5.1.3), the elliptic model shows that even though the strain-rate is small, it *changes* sufficiently rapidly that each successive passage excites a permanent deformation in the passing vortex. The contour dynamics calculation exhibits the same feature.

(iii) For the third type of interaction involving even thicker cores ($\alpha = 0.20$, §5.1.2), it is observed that the rear vortex undergoes unabated elongation and part of it is captured by the leading one. The elliptic model represents the elongation process well and from it we learn that the elongation is not due to the fact that the strain rate induced by the other ring exceeds the axisymmetric analog of the critical value (set by Moore & Saffman (1971) for tearing, see §4.2.4), but rather that even though the strain is weak, it varies sufficiently rapidly in time that the core “overshoots” its equilibrium. This contrasts with the analogous interaction of a pair of like-signed vortices in two-dimensions which is more resilient because the strain rate does not vary.

(iv) In the fourth example ($\alpha = 0.40, \hat{d} = 2$, §5.1.4) the critical value of the strain rate is exceeded according to the elliptic model, the rear vortex is considerably elongated in the axial direction, and a thin wisp of it starts to roll-up around the leading vortex. The features are in agreement with the experimental photographs of Oshima, Kambe & Asaka (1975). In this experiment, electrolyte grains produced at the edge of the orifice were injected directly into the shear layer i.e. the vortical region. Hence, here the tracer is not prone to the effects of passive advection discussed above. However, the Schmidt number of the tracer is typically very large so that the vorticity may be considerably more diffused than tracer.

For passage cases the acoustic signals oscillate at a frequency of about half the vorticity which reflects elliptic mode core deformations. Section 5.1 will be concluded by demonstrating that peaks measured in jet-rig noise spectra correspond to half the peak phase averaged vorticity of the structures.

1.4.2. *Summary of collision cases*

In two-dimensions, collisions between vortex pairs have been studied by McWilliams & Zabusky (1983) for the quasi-geostrophic equivalent barotropic equation and

Overman & Zabusky (1982*a*) for the Euler equations. Axisymmetric collisions differ in two respects. First, vortex rings approach each other to an arbitrarily small distance, whereas vortex pairs asymptotically approach a finite separation. Second, whereas in two-dimensions the cores nearly attain a steady shape, in the axisymmetric case continual production of thin sheet-like regions must take place due to the energetics of the stretching process. For thin vortices ($\alpha = 0.2$, §5.2.1), the rate at which cores approach is much smaller than internal rotation so the shapes remain in equilibrium with respect to the instantaneous induced field of the other vortex. When the separation of the cores is smaller than their radius, the flow is nearly two-dimensional locally and the sequence of shapes follows the family of two-dimensional steadily translating pairs calculated by Pierrehumbert (1980) up to its touching member (Sadovskii 1971). Thereafter, energy conservation does not allow the core to retain this or any other constant shape and a thin tail is shed. This may be one mechanism by which self-stretching of paired vorticity leads to the formation of fine scales in turbulence.

For a collision of thick cores ($\alpha = 1$, §5.2.3), the strain changes rapidly so the cores deviate from equilibrium and attain a large aspect ratio before the cores make “contact”. However, the shape does not continue to flatten uniformly. It “fills-out” or thickens in one region to form a head, that has the shape of the Sadovskii eddy, and a long remnant tail. The head-tail structure agrees with the experimental photographs of Oshima (1978*a*).

With regard to the acoustic aspects of collisions (§5.2.4), comparisons will be made with the measurements of Kambe & Minota (1983) (henceforth KM). The agreement with experiment holds up to much later times than with Dyson’s model. In particular, a dip in the acoustic pressure signal which was thought by KM to be due to viscous effects is shown to be a manifestation of inviscid core deformation.

1.5. Evolution of the objectives and approach

The stated objectives of a work are usually formulated while it is performed, as capabilities and tools are developed. The goals expressed in §1.2 were no exception. Our own assimilation of the concerns expressed there was rather oblique. It was not as if we read Saffman’s statement and decided to come to the rescue. It is therefore perhaps of interest to discuss how the work actually developed the way it did.

In the initial phases of this research, the goal was to numerically simulate complex aerodynamic flows (separated unsteady wakes behind three-dimensional bluff bodies, in particular a slant-back car which experiments had shown produced a sharp increase in the drag coefficient at a particular slant angle). We expected to employ interacting computational vortex elements. The fact that at high Reynolds numbers the vorticity is confined to small regions and, for incompressible flows, the entire flow field can be computed from it and boundary conditions, means that the vorticity provides an economical representation of the flow. Thus storage is a computer resource one seldom needs to worry about in vortex methods. The vorticity was to be discretized into vorticity bearing elements which were to be convected with the flow velocity averaged over the element, neglecting the deformation of the elements. Leonard (1985) provides a review of such methods. However, it was suggested by P. Spalart at NASA Ames that, despite the existence of mathematical proofs of convergence to solutions of the inviscid equations as the number of computational elements is increased, of at least one such method, these methods had never been subjected to tests in three-dimensions against either analytic solutions or those which had been obtained by more accurate though less general computational techniques. All the demonstrations of the efficacy of this modeling technique for three-dimensions were qualitative in nature. The Hill's spherical vortex solution (see Lamb 1932, §165), and the family of axisymmetric steadily translating vortex ring solutions studied by Norbury (1973) and Fraenkel (1972) were considered good but restricted test cases. Good in the sense that vortex stretching, one of the distinguishing features of three-dimensional flows was present but restricted because (i) the stretching is purely geometric, (ii) the solutions can be made steady in a translating frame in an Eulerian description and (iii) the accuracy of the method in treating variations along the computational vortex filaments could not be studied.

In initial studies it became clear that the overall properties of the Norbury-Fraenkel vortices, for example their speed of translation, could be easily reproduced with only a small number of filaments and that a more demanding study of unsteady behavior was needed. No exact unsteady solutions were available except for the linear stability analysis of Hill's spherical vortex by Moffatt & Moore (1978) and Moore's (1980) asymptotic solution of a slender elliptical core vortex ring. Moore's solution was reproduced well by the method as were the general features of the Hill's

vortex instability. The behavior encountered (for example the shedding of tails, entrainment of irrotational fluid) was deemed interesting and perhaps relevant to jets. It was suggested that if these physical processes was what interested us then they ought to be investigated rather by the more accurate, though specialized, technique of contour dynamics, if it could be extended to axisymmetric flow. This approach was developed and exploited by Zabusky and co-workers for two-dimensional vortex patches of constant vorticity. Since, in two dimensions, vorticity is convected with the fluid the patches maintain a constant vorticity and only the shape of these boundaries evolves. An integro-differential equation for the motion of the boundary can be obtained. This approach was extended to the axisymmetric case and the objectives stated in §1.2 evolved. In relation to the original concerns, however, accurate unsteady solutions which could be used as a better benchmark for the vortex filament method were obtained. After the vortex filament method was qualified for the linear vorticity case it could be used to study the behavior of rings with a peaked vorticity distribution which better represents real vortex rings.

So, this is how our attention was diverted to vortex rings.

CHAPTER 2

BACKGROUND ON AXISYMMETRIC VORTEX RINGS AND THEIR STABILITY

2.1. Introduction

Instead of reviewing only those results which have a direct bearing upon this work, a broader perspective will be taken. It may seem pointless to review experimental and theoretical work since the assumptions of inviscid flow and confined linear vorticity made in most of this work are too idealized. However, we are able to reproduce flow visualizations of interacting rings and to obtain the measured acoustic signature of colliding vortex rings. These are exceptions. There are many experimentally observed phenomena whose mechanisms remain unclear and they provide a challenge for theoretical and numerical models. The purpose of this chapter is to pose challenges for both this work and others; only a small subset of these challenges is met in this work. This chapter will also serve to indicate the degree to which our results are relevant to experimental vortex rings. To avoid confusion a clear distinction will be made between questions that are given attention here and those we would like to see addressed.

An excellent and concise introduction to vortex rings is provided in pp. 157-164 of the review article by Widnall (1975).

Saffman (1981a), in encapsulating the vortex ring problem, said that "the formation of vortex rings is a problem of vortex sheet dynamics, the steady state is a problem of existence, their duration is a problem of stability, and if there are several we have a problem of vortex interactions." We shall do our best to follow this paradigm in organizing this chapter but sometimes we are forced to make a division along experimental/theoretical/numerical and viscous/inviscid lines.

In the first three sections we focus on the problem of formation by discussing how rings are generated naturally or in the laboratory, the resulting structure and, finally, what factors determine whether the formed rings are laminar or turbulent.

Section 5 discusses observations of laminar rings and simple models which have been proposed. We then take up the issue of coaxial interactions. The discussion

is mostly experimental. In Chapters 5 and 6 we shall attempt to address, using the inviscid assumption, some of the issues raised here.

The flavor then changes sharply towards theory beginning with a discussion concerning the existence and properties of steadily translating inviscid rings (§2.7). Then we discuss unsteady inviscid behavior including coaxial interactions, which are the main topics of the present work. The next section reviews theoretical and numerical work on viscous vortex rings. Finally we take up the subject of azimuthal instabilities, an area in which theory has been reasonably successful in accounting for experimental observation.

2.2. The formation process

2.2.1. *Introduction*

In his book, Sommerfeld (1950) concludes an exposition of the classical theory of vortex rings with a note of dissatisfaction: the theory had to be left incomplete with respect to one essential point, the uncertainty about the assumed vorticity distribution in the core. He states that this uncertainty could be removed by investigation of the vortex formation process. Since that statement was made, understanding of how vortex rings form in various circumstances has increased. The next subsection reviews methods for producing vortex rings. In the laboratory, the most common technique is to push a slug of fluid through a circular pipe or orifice. Models which address the characteristics of rings produced in this way are discussed in §2.2.3.

2.2.2. *Techniques for producing vortex rings*

The simplest “home-brew” way of producing a vortex ring is to allow a drop of water, lightly colored with milk or food dye, to fall from an eye dropper or pipette into a glass of water. A variation that provides consistency and repeatability is to hold a partially formed drop at the tip of the dropper, slowly lowering it until it makes contact with the surface of the water. Surprisingly a vortex ring is also formed without the drop having any initial kinetic energy, indicating that there is another source for the energy of the rotational motion. It is entertaining to toy with different conditions. For example, increasing the concentration of coloring produces a negatively buoyant

ring which cascades into many smaller rings. For a realization of this with heavy smoke in air see Chen & Chang (1972).

In any case, upon entering the water the spherical drop quickly deforms to a toroidal shape. This phenomenon was reported by W.B. Rogers (1858, the founder of M.I.T.), studied in greater detail by Thomson & Newall (1885) and photographed by Okabe & Inoue (1961); some of the pictures have been reproduced in Batchelor (1973, Plate 21).

The process by which the toroidal shape forms remains unclear. Chapman & Critchlow (1967) provide an explanation based upon conversion of surface energy into kinetic energy as the drop surface disappears. A thorough study of the characteristics of the rings produced and even the derivation of qualitative estimates needed to confirm this mechanism are tasks that await doing.

Rayfield & Reif (1963) showed that nearly inviscid vortex rings may be produced in superfluid helium by subjecting it to helium ions from a radioactive source. A ring becomes tagged with an ion which allows a determination of its energy and speed of translation. The measured values are fit extremely well by the corresponding relationship for Kelvin's (Tait 1867) thin core ring. The rings have one quantum unit of circulation ($.998 \times 10^{-3} \text{cm}^2/\text{sec}$) and effective core size to radius ratios down to 10^{-4} .

Another interesting method can be found in the May 1976 issue of *National Geographic* (p. 602). A beautiful photograph shows a diver blowing air rings in water. The rings become remarkably large in radius due to buoyancy forces which increase the momentum of the ring. The phenomenon has been studied by Walters & Davidson (1963). Initially spherical air bubbles acquire a distribution of surface vorticity due to buoyancy. The vorticity causes the spherical volume to deform into a torus after which, experiments suggest, the circulation remains nearly constant. We shall henceforth limit the discussion to flows with a single fluid.

An alternative, but lesser known and studied scheme for generating vortex rings is to let a shock-wave emerge at the open end of a cylindrical tube. Two types of apparatus have been used. The first method is documented in Elder & De Haas (1952) and references therein, Sturtevant & Kulkarny (1978) and Sturtevant (1981). It consists of a circular tube with a compression chamber filled with helium or nitrogen. This gas is separated by a diaphragm from an open expansion chamber. After the diaphragm is ruptured, a shock propagates into the expansion chamber trailed by a

slower moving contact surface which separates the fluid initially in the two chambers. The contact surface may be thought of as a piston which drives the fluid between itself and the shock. An expansion wave propagates into the compression chamber, reflects off the end wall and as it propagates, brings to rest fluid behind it. The tube is long enough that it catches up with the contact discontinuity, thus preventing the helium or nitrogen from exiting. The length of the ejected slug and hence the core size of the produced vortex are determined by the length of the compression chamber. Plate 78 in Van Dyke (1982) shows a Schlieren visualization of a ring produced in this way by Sturtevant. The core radius is quite small. In some cases Sturtevant found that the volume of fluid transported with the vortex becomes "turbulent" even before the core exhibits azimuthal instability. In §6.4 we will suggest that this may be due to core unsteadiness causing chaotic particle paths in the irrotational fluid carried along with the vortex i.e., the vortex is in fact not turbulent.

The second type of apparatus has been used by Kambe & Minota (1983) to study the acoustic radiation when two vortex rings collide head-on. We will simulate this case and compare our calculated results with theirs in §5.2.4. In their technique, the shock passes through a second diaphragm without rupturing it and bifurcates through two pipes which turn to face each other. The length of the ejected slug is limited by the second diaphragm.

The advantages of using a shock-tube is that vortices approaching the idealized ring may be produced i.e. they have large Reynolds numbers and thin cores. Also, as the vortex sound is proportional to some power of the propagation velocity, high speed rings produce measurable acoustic signals making possible fundamental studies into the nature of vortex sound. Moreover, shadowgraph and Schlieren visualization techniques, when used to visualize the different density of the core, are not affected by history of the motion as is dye. On this basis, Sturtevant (1981) proposed a different scenario of events leading to breakdown of vortex rings which will be discussed further in §2.10. Sturtevant also employs the technique of thermally tagging the fluid initially in the shock tube by cooling its walls, in which case, history effects are important. A disadvantage of shock-tubes is that no velocimetry technique has yet been devised to provide detailed flowfield information. LDV is not possible because there is insufficient time for seed particles to begin to move with the rapidly accelerated fluid, and, being heavy, they move outward and away from the region of interest in a rotational flow.

We would like to suggest that a greater variety of studies of vortex dynamics should be done with shock tubes. For example the “cut and connect” process which Hussain (1983) believes is the dominant source of jet noise could be studied by creating several vortex rings in tandem analogous to the low speed experiments of Oshima & Asaka (1977).

2.2.3. Models of ring formation at an edge

The technique most often employed to produce vortex rings is to push a slug of fluid, through a pipe or the orifice of a chamber, using a piston with stroke L . If the history of the piston velocity scaled by the average piston velocity (\bar{U}_p) as a function of time normalized by the ejection time (T_e) remains fixed as these two parameters are varied, then the character of the ring depends upon the piston velocity curve, $Re_p \equiv \bar{U}_p D / \nu$ and D/L where D is the diameter of the aperture. The boundary layer inside the pipe separates at the sharp edge of the opening and rolls-up into a vortex spiral. Didden (1979, 1982) has studied this process experimentally for a pipe, focusing on how the vortex attains its circulation via a flux of vorticity from inside and outside the pipe. Some of his flow visualization photographs are contained in Van Dyke (1982, Plate 76). In the 1982 paper a comparison is made of the measured growth of circulation in the spiral against the predictions of a slug flow model and a model (due to Pullin 1979) which relies upon known similarity solutions for the rolling up of a vortex sheet in two-dimensional impulsively started flow past a wedge. The slug flow model is often employed in vortex simulations of jets to determine the circulation of the numerical vortex elements released. The latter type of model has been used by Saffman (1975, 1978) to estimate the overall properties of the rings.

Both models ignore the production of vorticity of sign opposite to the main spiral required to maintain a slip free wall. This secondary vorticity is ingested into the spiral and, for one set of experimental conditions in Didden's paper, was about a quarter of the main vorticity. Another drawback of the self-similar roll-up model is that its validity rests upon the absence of a length scale which is true only in two-dimensions. In other words, the diameter of the spiral is assumed small compared with the diameter of the pipe so that the latter does not enter as a length scale. This is satisfied only during the initial stages of roll-up but at this stage the thickness of the vorticity layer is comparable to the dimensions of the spiral and similarity assumptions fail once again. These factors account for the poor agreement of the

model with experiments. Considering this state of affairs, a numerical study of the roll-up of axisymmetric vortex sheets using the techniques recently developed by Krasny (1987) to evolve vortex sheets in two-dimensions, would be a worthwhile venture.

In the slug flow model, the piston velocity $U_p(t)$ alone governs the rate of growth of vortex strength Γ . It is assumed that the velocity external to the pipe boundary layer at the exit plane is the piston velocity so that the flux of vorticity is

$$\frac{d\Gamma}{dt} = \int \omega_\phi u_z d\sigma \approx \int -\frac{\partial u_z}{\partial \sigma} u_z d\sigma \approx \frac{1}{2} U_p^2(t). \quad (2.1.1)$$

The integrals extend over the boundary layer; the first approximation sign means boundary layer assumptions are being invoked and the second, that the boundary layer edge velocity is the piston speed. In reality, the velocity external to the boundary layer at early times is determined by the local potential flow past the edge with the velocity imposed only at the piston. The sharp turn of the potential flow past the edge does not occur because a small bubble, surrounding the small piece of vortex sheet that has been shed, serves to smooth the turning of the flow. The boundary layer edge velocity is higher than the piston speed. As noted by Glezer (1981) this would be more pronounced for a tube without a backplane than in his apparatus, in which an exit is formed by the intersection of a cylindrical cavity with a plane wall, in which the flow turns through a smaller angle. At later times, the maximum velocity relaxes toward the piston velocity but remains slightly higher due to a slight constriction caused by the displacement thickness. Thus the overall effect is that the slug flow model underestimates the total circulation of the vortex, the error being larger for shorter pulses. The slug model is often used in vortex simulations of jets where it is probably adequate because there is no start-up transient and rings form due to a shear layer instability.

2.3. The structure of the core

In spite of its shortcomings, the model of self-similar roll-up together with considerations of the effect of viscosity does suggest the form of the vorticity distribution in the core and its dependence on the parameters of the generating process. In the analysis of Moore & Saffman (1973) for the structure of aircraft trailing vortices, which has been applied to vortex rings by Pullin (1979), the core has three regions.

An inner viscous subcore has radius $\mathcal{O}(\nu t)^{1/2}$. In the outer two regions, the growth is governed by inviscid self-similar roll-up and proceeds as a power of time determined by the interior angle of the edge and the assumed power law of the piston velocity history. The need to regard this region as composed of two parts arises because in the inner portion the radial distance between successive turns of the sheet is smaller than the thickness of the sheet determined by viscous diffusion. In this intermediate region the distribution of vorticity is smooth. In the outermost region the shear layer is rolled up in a tightly wound spiral whose discrete structure is not lost. The size of the intermediate region may be overestimated because the total length of the vortex sheet is much larger than the emitted slug length so a large amount of stretching takes place and diminishes the width of the diffused layer. The rapid stretching also stabilizes the spiral against Kelvin-Helmholtz instabilities (Moore & Griffith-Jones 1974).

Based on this model, Moore & Saffman (1973) obtained the velocity distribution for the core of the aircraft trailing vortex (Pullin extended the result to vortex rings) by matching a solution for the inner viscous subcore to the solution for the intermediate region. The result is expressed in terms of a confluent hypergeometric function. A comparison of this result to experiments still needs to be made. In any case, the vorticity is highly peaked at the center of the core and decays algebraically.

Experiments qualitatively confirm this distribution. Maxworthy (1972) used the distortion of a line of hydrogen bubbles to infer that the vorticity was not confined to a thin core as assumed by classical models but spread throughout the volume of fluid it transports. Furthermore, the vorticity was not distributed linearly with radial distance. Sullivan, Widnall & Ezekiel (1973) used LDV to study rings formed in air by pulsing fluid through a sharp edged orifice using a loudspeaker. Figure 9 of their paper shows that the vorticity distribution has a bell shape. In their rings, which were less viscous than Maxworthy's, the vorticity was concentrated in a thin core and they concluded that Maxworthy's findings were probably peculiar to low Reynolds number vortices. In 1977 Maxworthy studied high Reynolds number rings and essentially recovered the results of Sullivan, Widnall & Ezekiel but thought it significant that even though the vorticity at the edge of the moving volume is more than two orders of magnitude less than the maximum in the core, it was measurable. The presence of this weak vorticity is important in Maxworthy's conception of laminar vortex rings at any Reynolds number. We will describe his ideas in §2.5. The fact that

real vortex rings do not resemble the class of vortex rings we are able to study with contour dynamics will motivate us to study the differences in passage interactions when the distribution is closer to experiments (Chapter 5).

2.4. Initially laminar vs. turbulent rings

Depending on the parameters of the generation process, the behavior immediately after the ejection may be either laminar or turbulent. The Reynolds number is not the only governing parameter; the details of the piston motion, because they affect the core structure are also important. In Saffman (1975, p. 267) it is hypothesized that if the piston velocity history is such that the strength (circulation per unit length) of the produced sheet is maximum at its leading edge then it will roll-up as a single spiral, which is presumably stable, but if the maximum strength occurs at some other point then the sheet rolls up as a double spiral which may be unstable and lead to a ring which appears turbulent from the outset. However Glezer (1981, Figure 2) reproduces some data from Didden's (1977) thesis which shows that two piston velocity histories, one which slug flow reasoning suggests would produce a monotonically decreasing sheet strength, and another with a bump shaped distribution which should roll-up as a double spiral, both result in laminar rings. Thus the role of the piston velocity history in determining the character of the ring remains unclear. Another factor in producing initially unstable rings is the ingestion of negative vorticity into the core. This would make it susceptible to Rayleigh's centrifugal instability. To demonstrate this, Maxworthy (1972) enhanced the creation of negative vorticity by placing a centerpiece protruding from the hole along the axis of symmetry. The resulting vortex ring was violently unstable. Two points are in order. First, the Rayleigh stability criterion is valid for inviscid two-dimensional flow with circular streamlines and may be invoked for sufficiently thin cores. It states that if the sense of local rotation (vorticity) is anywhere opposite to the direction of overall rotation (angular velocity), then the flow is unstable to three-dimensional disturbances (this version is due to Coles 1965, p. 386*n*). It would be interesting to study the most unstable mode for a given profile and the effects of finite core and viscosity. Second, Maxworthy's demonstration is somewhat artificial in that his apparatus would cause a negative layer of vorticity around the periphery of the core whereas without the centerpiece the negative vorticity is wound with the sheet vorticity and it is possible

that viscous cancellation occurs before nearly circular streamlines are established in the core. Clearly there must be some explanation for the fact that the pipe geometry produces stable rings.

2.5. The dynamics of laminar rings

In this section we present what is known about the behavior of laminar vortex rings. As pointed out by Maxworthy (1972) it was O. Reynolds (1876) who seems to have observed that contrary to Kelvin's picture, vortex rings realized in the laboratory do not have a permanent form. The volume of fluid transported along with a ring continually increases due to entrainment of external fluid and its velocity decreases because its momentum has to be shared with a greater mass of fluid. Maxworthy's measurements for rings with $Re \approx 600$ based on translation speed and maximum diameter showed that growth of this mass proceeded roughly as $t^{1/3}$ and the speed of propagation as t^{-1} . He was able to construct a theory based on order of magnitude estimates to account for this dependence. We hope that accurate simulations with schemes such as that developed by Stanaway, Cantwell & Spalart (1986) will be able to provide a refined picture.

The increase in volume was explained with the aid of a physical picture based on the high Reynolds number spherical drop solution of Harper & Moore (1968). Maxworthy's argument has three ingredients: a hypothesis of entrainment, conservation of impulse and self-similarity. With respect to the first, the fact that measurable vorticity extends up to the edge of the volume carried with the vortex (called the bubble) is crucial in Maxworthy's view. Irrotational fluid is contaminated with vorticity by diffusion as it flows along the surface of the bubble. Due to an associated loss in total pressure, this fluid is unable to traverse the surface of the bubble and it is entrained into the bubble at a volumetric rate proportional to the speed of propagation and the area of the diffused layer normal to the flow.

With respect to the second, the linear momentum of the fluid in the entire flow domain (assumed to be unbounded) is an invariant even in the presence of viscosity in the absence of body forces. Its definition for axisymmetric flow reads (with density set to unity)

$$P = \pi \int \omega_{\phi} \sigma^2 dx d\sigma, \quad (2.5.1)$$

where the integral is taken over a meridional half-plane. If Γ is the circulation and \bar{L} some length scale of the vortex then

$$P = \hat{P}\Gamma\bar{L}^2, \quad (2.5.2)$$

where

$$\hat{P} = \pi \int \hat{\omega}_\phi \hat{\sigma}^2 d\hat{x} d\hat{\sigma}. \quad (2.5.3)$$

The hats represent values normalized using Γ and \bar{L} . If, as the vortex expands, its shape *as well as the vorticity distribution* remains similar then \hat{P} is a constant. So, to maintain P constant, the observed increase in \bar{L} must be accompanied by a decay in circulation. We return to this point later. At the same time the speed of propagation, $U(t)$, decreases because the impulse is proportional to the speed per unit volume. The entrainment hypothesis and conservation of impulse with self-similarity give the following power laws

$$\begin{aligned} \bar{L} &\sim t^{1/3} \\ U &\sim t^{-1} \\ \Gamma &\sim t^{-2/3}. \end{aligned} \quad (2.5.4)$$

The first two agree well with dye visualization. A difficulty occurs with the last relationship. In the context of the given model, loss in circulation can occur only due to viscous cancellation at the axis of symmetry. However an analysis of this process yields a slower rate of decay than that given above. Thus one has an inconsistent model. This is remedied by allowing vorticity to be lost to a wake. Of course neither the assumption of self similar growth nor of constant bubble impulse is now true. The model remains valid only at small times when the wake is small. In a subsequent paper (Maxworthy 1974) the analysis is improved to account for the loss of impulse from the bubble.

2.6. Coaxial interactions

2.6.1. Introduction

Here we give a review of the known experimental facts and classical explanations concerning the interaction of two vortex rings initially placed a certain distance apart on a common axis of symmetry. A detailed numerical study of such interactions will be the subject of Chapter 5. The treatment there is based on the assumption of

inviscid flow. Nevertheless, one is able to reproduce many of the experimental tracer visualizations and the radiated acoustic signal. The only known inviscid model, that due to Dyson (1893), is not equipped to predict the variety of observational data. Its inability to predict core distortion and merging has encouraged the view that inviscid models have little application in understanding the behavior of real vortex rings. The model we will develop extends Dyson's by allowing deformation of vortex cores and finite size. Some of the observations discussed below can then be reproduced and understood.

The experiments to be described were performed at a time when the effect of apparatus parameters on the characteristics of the rings had not been appreciated. Thus as one parameter of the generation process is varied, all the characteristics of the vortex change. The precise characteristics of experimental vortices, for example the circulation and vorticity distribution are difficult to measure. But, with some of the knowledge one now has about the formation process, it is hoped that these characteristics will be controlled in future experiments. At present therefore it is difficult to precisely place each experiment in the space of dimensionless parameters that govern the interaction. All experimental studies have been qualitative, focusing on flow visualization. It should be remembered that smoke, dye and hydrogen bubbles have very large Schmidt numbers (ratio of momentum to tracer diffusivity) so that tracer does not mark all of the vorticity containing region. Thus when we say below, "vortex", "core" or "ring" in describing the experiments we mean simply the "region of tracer". Thermal tagging is less prone to misinterpretation by Schmidt number effects (since the Prandtl number of air ≈ 1) and has been utilized by Sturtevant and his co-workers (1978, 1979, 1981) for isolated ring experiments by cooling the walls of the shock tube. We are not aware of any interaction experiment which utilizes it. Thermal tagging would still be prone to the effects of passive advection, a subject taken up in Chapter 6.

2.6.2. *Motivation*

There are two kinds of interactions. If the vortices have the same sense of rotation, they travel in the same direction and, under certain conditions, the rear vortex will attempt to pass through the front one. The motivation for studying such interactions is that they are observed in the jet column mode of a round jet near the exit where

they play important role in sound generation and mixing (Hussain & Zaman 1980, Zaman 1985). Here, we will concern ourselves with just two isolated vortices.

If the vortices have opposite senses of rotation, they travel towards each other i.e., a head-on collision takes place. The reasons for studying collisions are indirect. Firstly, they shed light on what happens when two counter-rotating sections of three-dimensional vortex tubes interact closely. Intense stretching occurs locally. In free turbulence, this would lead to energy transfer to small scales. Siggia & Pumir (1987) studied three-dimensional collisions with a filament model in order to understand possible finite-time singularities of the Euler equations resulting from a succession of such collisions. Based on our preliminary results, they concluded that the largest uncertainty in their model is “inviscid core deformation which would turn the cores into ribbons as they stretch.” Pumir & Kerr (1987) studied such interactions using a spectral method in a periodic domain and the pattern of core deformation in a plane of symmetry resembles both the experimental and the present results for colliding vortex rings. Secondly, collision has been used by Kambe and his co-workers primarily to test theories of vortex sound generation, but they too have recognized that the collision may be representative of a fundamental process in turbulence. Finally, McWilliams (1983) studied collisions between vortex solutions to the plane quasigeostrophic equations. He suggested that studying vortex collisions may lead to similar achievements as for colliding particles. Just as particle collisions have led to the discovery of new types of particles, “this may also prove to be true for isolated vortices; the appropriate apparatus in this case is the computer used to solve the governing equations.” We think that this motivation is not too fanciful. For example in Chapter 5, from a vortex ring collision, there emerges a structure with the shape of a known two-dimensional translating pair.

2.6.3. *Passage Interactions*

In his original memoir on vortex motion, Helmholtz (1858) describes the motion of two vortex rings having the same axis and circulation. Due to the velocity induced by the rear vortex, the leading vortex widens and travels more slowly because its self induced velocity decreases with increasing radius. Similarly, “the pursuer shrinks and travels faster, till finally, if their velocities are not too different, it overtakes the first and penetrates it. Then the same game goes on in opposite order, so that the rings pass through each other alternately” (Tait’s 1867 translation). Later, Dyson (1893)

carried out a formal study using a model based on the assumptions of widely separated vortices having slender circular cores. The details of his model are given in §4.1. He obtained criteria that determine which of the two possible outcomes occurs: the rings continue to revolve about each other or they separate with time.

The notion that this description applies to real rings has permeated into textbooks and has led to controversy. Sommerfeld (1950, pp. 164-166) states that the "leapfrogging" can be observed several times in succession for rings generated by drops penetrating a free-surface. In an earlier printing of Batchelor (1967, pp. 523-524) there is the statement: "it is possible to demonstrate in the laboratory one or two such passages of one vortex through the other before they decay." The remark was deleted from the first paperback edition of 1973 presumably because Maxworthy (1972) questioned whether the process could be realized experimentally after an unsuccessful attempt at reproducing it. Instead, for rings with Reynolds numbers less than 600 (based on initial translatory velocity and maximum ring diameter) he found that the two rings merged into one. Only when the rear ring is sufficiently stronger than the forward one does it pass through, and even then it gains some of the vorticity of the front vortex. Oshima, Kambe & Asaka (1975) tried harder. They varied several parameters: orifice diameter, ejection period and time between ejections, but were never able to obtain a clean passage. The Reynolds number of the produced rings based on initial propagation speed and orifice diameter ranged from 200 to 300. They report that the observed outcomes could be classified into three categories depending on the relative magnitudes of the initial translation velocities. However, inspection of the three cases they consider as being representative of each range of velocities shows that the core sizes and separation distance also varied widely. Hence we will discuss each of the cases as unique rather than as a member of a larger set. In the first case, the leading ring had a higher velocity and, as the initial separation was large, the rear ring was unable to slow it down and distance between the two continued to increase. In the second case, the rear ring is stronger by about 10% in terms of initial speed. It is considerably distorted as it attempts to pass through and begins to roll-up around the core of the first. Both rings had the same ejection time so we suspect that the two rings had nearly identical strength. The higher velocity of the rear ring is probably due to the fact that as it is produced, the first ring is close enough to influence it. In Chapter 5 the core deformation in a simulation compares well with the photographs for this case. The authors describe the rolling-up as eventually leading to merging.

In the third case, the ejection period of the rear ring is larger and it has speed greater than 50% compared to the first vortex. The rings are observed to merge, leaving behind a portion of the *foremost* vortex in the shape of a flared skirt.

Finally in 1978, Yamada & Matsui were the first to provide proof that a successful passage could be achieved in the laboratory. Their photographs are reproduced in Van Dyke (1982, Plate 79). In some cases, a second passage occurred and in others, in particular for the photographs contained in Van Dyke, the interpretation of Yamada & Matsui of their photographs is that the first vortex was so distorted after the other had passed through it that it merged during its own passage, leaving some residual smoke. The fact that it is the passed that appears to suffer deformation is contrary to the results of contour dynamics (Chapter 5) which predict that the passing vortex is subjected to a larger strain. The study of particle motions in §6.4 suggest in the experiments it is only smoke in the irrotational region that appears to distort.

Yamada & Matsui attribute their success to higher Re_D (≈ 1600). In addition, we believe that the fact that the rings were produced by the impact of a pendulum must have resulted in a short piston stroke and hence smaller cores which would suffer weaker deformation. However, in comments upon this work, Maxworthy (1979) doubts that a successful passage characterized by the vorticity remaining distinct had indeed occurred. Arguing that smoke does not track vorticity, he suggested that the vorticity of the two rings diffuses together at the first passage and that smoke appears distinct only because at high Reynolds number the peaks of the vorticity distribution remain distinct. He believes that the subsequent pairing of the two rings is merely a delayed manifestation (due to slower diffusion) of the same process he had reported in 1972. Our view is this: First, the outcome of the interaction (assuming that two identical rings are produced) must depend on the shape of the vorticity distribution which has as one parameter the ratio of the initial effective core size to mean toroidal radius L_o , the reduced initial separation d/L_o , and the Reynolds number. The experimental work has focussed on the Reynolds number as the most important parameter while our inviscid study is defined by the first two parameters. Second, in §6.4, we will apply concepts of non-linear dynamics to show that a classical inviscid model with thin, circular and non-deforming cores gives almost identically the same smoke pattern as the photographs of Yamada & Matsui. Hence one ought to be very careful in interpreting tracer visualizations. Our view therefore is that

the truth lies between our inviscid calculations and Maxworthy's reliance on diffusion arguments. A synthesis of the two views will lead to a more balanced picture.

In Oshima (1978*b*), the Re_D , d/D plane was surveyed to identify regimes of successful passage for two identical rings. We will focus on the air experiments since the rings in water were not reproducible. d/D was varied by the interval between puffs. Re_D was varied between 500 and 1600 by changing orifice diameters as well the displacement and speed of a driving speaker diaphragm. Hence the core size varied. Oshima found that the only effect of separation distance (other parameters fixed) was that if it is too small, the rings are not distinct initially and there is no passage. If it is too large the second ring does not catch up to the first. In intermediate cases, clean passages occurred. Our results suggest greater influence of the separation distance. It affects the history of strain that each vortex encounters which in turn determines the amount of core distortion during the interaction. Indeed, the case from Oshima, Kambe & Asaka (1975), in which there is considerable deformation followed by a partial merger, does not fall into either of the above descriptions of failed passage. The effect of changing the initial propagation velocity (both Re_D and core size to radius ratio change) is that, for small values, the circulation was too weak to cause an interaction (the interaction was so slow that either the length of the apparatus was too short or the rings dissipated by loss of circulation at the symmetry axis). If the translational speed was too large, an instability along the circumference occurred before a passage could be completed.

2.6.4. *Head-on collisions*

Next we consider collisions of oppositely signed rings. With perfect symmetry, each vortex can be regarded as the image of the other with respect to a slip wall, for example a free liquid surface at Froude numbers so small that the surface does not deform. Experiments on collision of rings against a solid surface have also been performed but do not represent the desired situation well at late times, the production of secondary vorticity leading to a rebound of the ring. We do not consider such interactions here.

Owing to their self-induction the rings approach and due to mutual induction their radii grow and they decelerate. According to Dyson's model, which regards the vortices as having zero cross-section for the *mutual* interaction, the cores overlap at some point and the model becomes invalid. In Chapter 5, deviations from Dyson's

model in the late stages of collision will be studied. Oshima (1978a) carried out experimental collisions at Re_D between 260 and 400. The size of the orifice was held fixed; Re_D was increased by increasing the level of d.c. current to a speaker. Apparently the displacement of the driving speaker also increases since thicker cores are formed. For small cores, the smoke cross-sections deform from a circular to an aerofoil shape as they collide. For thicker cores the core deformation is stronger. The dye forms a head with a long trailing tail. These features are reproduced well and explained by the simulations to be discussed in Chapter 5. Subsequently, the head pinches-off and continually increases in radius. At larger radii, an azimuthal waviness occurs and the filaments of dye in the head intertwine. The ejected tail possibly grows another head.

Kambe & Minota (1983) studied the acoustic signal resulting from the collision of high speed rings ($Re_D = 3.6 \times 10^4$). They present an acoustic theory which assumes that the Mach number, based on the maximum velocity in the vortical region, is small. The theory predicts that the far-field acoustic pressure has a quadrupole and a monopole part. The latter depends on second time derivatives of the kinetic energy and is absent in inviscid flow. Kambe & Minota (1983) separate the two parts in the measured signal using their predicted angular dependence. Shadowgraph pictures are given in Kambe & Murakami (1979) but because they represent an integrated view, the core deformations discussed above are not discernible. Nevertheless, the quadrupole part of the measured acoustic signature compares well with the present inviscid simulations and a particular feature of the signal will be shown to be a result of core distortion, rather than viscous effects as previously believed.

2.7. Theory of steadily translating inviscid vortex rings

2.7.1. Problem statement

We begin this section with a review of the theory of steadily translating axisymmetric vortex rings without an azimuthal velocity component (called swirl) and then discuss effects of swirl. For inviscid swirl-free axisymmetric flow the equation for the azimuthal vorticity is (Batchelor 1973, p. 508)

$$\frac{D(\omega_\phi/\sigma)}{Dt} = 0, \quad (2.7.1)$$

where σ is the cylindrical radial coordinate. The equation describes the convection of vortex lines and the purely geometric stretching of the vorticity. We consider flows which are steady in a reference frame translating with the vortex. The speed of the frame is determined as part of the solution. The condition for steadiness is that ω_ϕ/σ be constant on streamlines, that is $\omega_\phi/\sigma = f(\psi)$ where ψ is the Stokes streamfunction and $f(\psi)$ is an arbitrary function. Then the streamfunction-vorticity relation

$$D^2\psi \equiv \frac{\partial^2\psi}{\partial x^2} + \frac{\partial^2\psi}{\partial \sigma^2} - \frac{1}{\sigma} \frac{\partial\psi}{\partial\sigma} = \sigma^2 f(\psi), \quad (2.7.2)$$

together with the condition of uniform flow at infinity defines the elliptic problem to be solved. Note that the operator D^2 is not the Laplacian due to the sign of the last term. One is usually interested in solutions in which the vorticity vanishes at infinity. The known axisymmetric solutions are exclusively those in which the vorticity is confined i.e. where $f(\psi)$ vanishes outside some region \mathcal{D} . One then has to solve (2.7.2) separately in the interior and exterior of \mathcal{D} subject to the condition that $\psi = \text{constant}$ on the boundary of \mathcal{D} . An additional condition that in two instances is not employed is the continuity of tangential velocity across the boundary. When it is not imposed, the resulting solutions have a vortex sheet on the boundary and $f(\psi)$ has a delta-function on the boundary. This is inconsistent with the form assumed for $f(\psi)$. In this category are the ellipsoidal ‘‘extensions’’ of Hill’s vortex obtained by O’Brien (1961) and the family of toroidal rings obtained using finite-differences by Durst & Schonung (1982).

The problem outlined above is difficult because the shape of the boundary is unknown. The difficulty of free-boundary value problems is nicely illustrated in a simple one-dimensional example by Berger & Fraenkel (1975).

2.7.2. *The case $f(\psi) = \text{const}$*

We now give an exposition of the case in which $f(\psi) = \text{const}$ in \mathcal{D} and zero everywhere else. This has been a favorite for over a century; our understanding of it is quite thorough. This is also the case referred to in the Prandtl-Batchelor theorem (Batchelor 1956) for the form of a steady recirculating eddy behind axisymmetric bodies at vanishingly small but non-zero viscosity. For example, Fornberg (1988) numerically found that the steady recirculating eddy behind a sphere at sufficiently large Reynolds number has very nearly $f(\psi) = \text{const}$ and resembles Hill’s spherical vortex.

Kelvin (Tait 1867) considered steady behavior in the limit of thin cores. In this case, to leading order, the core dynamics in a frame moving with the core are the same as for a rectilinear vortex with uniform vorticity. A steady solution in two-dimensions is the circular (Rankine) vortex; a circular core is also steady to leading order in the axisymmetric case. The speed of the reference frame or equivalently the speed of translation of the vortex relative to a frame in which the velocity vanishes at infinity is given by the celebrated formula presented by Kelvin without proof as an appendix to Helmholtz (1858):

$$U = \frac{\Gamma}{4\pi L_o} \left[\log \left(\frac{8L_o}{\delta} \right) - \frac{1}{4} + \mathcal{O}(\alpha, \alpha \log \alpha) \right], \quad (2.7.3)$$

where Γ is the circulation, δ the radius of the core, L_o the toroidal radius and α is the slenderness parameter, δ/L_o . After Kelvin published it, this formula was the source of much controversy. Various authors presented their own derivations and, in place of $-1/4$, J.J. Thomson is said to have favored -1 and Lichtenstein's method gives $-3/16$ (Fraenkel 1970). It turned out that Kelvin's value is correct though we can only guess how he obtained it.

The discrepancies are due to lack of care in keeping the orders of neglected terms straight. One obtains simply, using the Biot-Savart law, the leading order streamfunction in the vicinity of the core. Then, to get the axial velocity, one differentiates with respect to σ a quantity in which σ variations have been neglected; errors of $\mathcal{O}(1)$ are thereby introduced. Clearly, higher order terms in α for the shape of the core and the streamfunction are needed. These are formidable to obtain but Fraenkel (1970, 1972) has succeeded.

In his textbook, Lamb (1932, §162–163) presents an ingenious and simple method of circumventing the difficulty. It is referred to as “Lamb's transformation” by Saffman (1970) and Moore (1980) but can be traced to Helmholtz (1858) although he does not carry to completion the calculation of the speed. The trick is that for a steady ring, all the axial centroids of the vorticity, no matter how they are defined, have the same speed. The idea is to choose a convenient definition. Helmholtz and Lamb define an axial centroid of the vorticity weighted by σ^2 without telling the reader why. Then they evaluate its speed and use the expression for the energy and conservation of impulse to eliminate a term which would otherwise require knowledge of the streamfunction beyond the zeroth order in α . The result is given as Equation (9b) in Helmholtz (1858) after correcting for a slight algebraic error that originates

in Equation (8a). We shall refer to it as Helmholtz's transformation. In article 163, Lamb obtains the streamfunction and then the energy to zeroth order to complete the calculation of the speed. Presumably, this is also the method used by Kelvin starting from Equation (9b) in Helmholtz.

The choice of the centroid is immaterial in the steady case. This leads one to expect that the terms that dropped out would do so regardless of the centroid definition. Indeed, Saffman (1970, §2) finds that they do so as a consequence of the *equations of motion* regardless of the choice of centroid. What Helmholtz stumbled upon was a centroid whose speed could be easily evaluated even in the *unsteady* case. This fact is used by Saffman (1970) to evaluate the speed of a viscous ring in which the vorticity is Gaussian and spreads as $\sqrt{\nu t}$.

A more physically appealing way of obtaining the speed of translation is by a force balance. The method has been used by Widnall & Bliss (1971) and Moore & Saffman (1972) and by Moore (1985) in which he obtains a compressibility correction to Kelvin's formula. The idea is that the velocity around the vortex core is increased from its two-dimensional value on the concave side due to contraction of area and decreased on the convex side. This contributes to a pressure difference, called "vortex line tension", which would tend to shrink the radius. However, this would violate conservation of momentum—the momentum of a ring is the product of its circulation and frontal area. Hence the force must be balanced by a Kutta lift from forward translation. Hicks (1884, p. 162) states the argument without invoking Kutta lift and conservation of momentum. The force balance method has also been applied to curved vortex tubes in general. The nice thing is that, as in the Helmholtz method, one does not need to know how the streamlines are distorted from the rectilinear vortex—the required pressure can be obtained from the zeroth order (basically two-dimensional) solution. Lundgren & Ashurst (1988) have, on the basis of a force balance, formulated model equations for the motion of a three-dimensional vortex tube which allow the core radius to vary along the tube and in time. Gray (1914) gives yet a different method for obtaining Kelvin's speed formula that yields the correct answer.

A general deduction about the speed of rings was made by Roberts (1972). He found, regardless of core thickness and the form of the vorticity distribution $f(\psi)$, that for steady rings the speed of translation is the derivative of the energy with respect to the impulse holding circulation and volume of vortical fluid fixed.

Hicks (1885) obtained the speed of translation of hollow rings—ones in which fluid has circulation without any rotational fluid; the fluid in the core can be thought of as having velocity but zero density. The hollow vortex idealization has served well to illustrate some mechanisms or the mathematical structure of a problem, for example it is used by Moore & Saffman (1974) to gain insight into the azimuthal stability of vortex rings. From a practical viewpoint the hollow ring is an approximation for cavitating rings if surface tension is neglected. An expression for the speed of translation of vapor rings including the effects of surface tension has been derived by Chahine & Genoux (1983).

We now consider thicker core members of the $f(\psi) = \text{const}$ family. Dyson (1893), in an extraordinary paper that Fraenkel (1972) called “bewildering to modern eyes,” investigated, among many other things, corrections to the circular shape up to fourth order in $\alpha = \delta_s/L_o$, the ratio of area-effective core radius to toroidal radius. At the opposite extreme, Hill (1894) discovered that a spherical core was also steady. In this case, (2.7.2) is amenable to solution by separation of variables although it appears that Hill found the solution by trial. These solutions led Batchelor (1967, p. 526) to expect that a continuous family of steady rings ranging from a ring of zero cross-section to Hill’s vortex may exist. Fraenkel (1970) indeed was able to prove existence for a wider class of vorticity distributions than $f(\psi) = \text{const}$ for small α . In ignorance of Dyson’s work he obtained specific solutions with $f(\psi) = \text{const}$ providing the core shapes and the properties of the vortex to lower order than Dyson. Fraenkel (1972) also provides a specific solution valid to first order in α for rings with a *peaked* vorticity distribution. Because a peaked vorticity is more representative of rings generated in the laboratory we consider also their interactions in Chapter 5. A more complete discussion of these peaked vorticity solutions is given in Appendix 5.B. Norbury (1972) proved existence and obtained specific $f(\psi) = \text{const}$ solutions in the neighborhood of Hill’s vortex. Norbury (1973) wrote down the formal solution of (2.7.2) in terms of the Green’s function of the D^2 operator. The problem is thus recast as an integral equation, the unknown being the region over which the integral is performed. He solved the problem numerically, approximating the integral by plane quadratures and exhibited specific solutions in the entire range for $f(\psi) = \text{const}$. In Appendix 3.B we reduce the area integral to a line integral, i.e., a 1-D integral equation. We hope it will be useful in finding other steady solutions, for example those in which $f(\psi)$ is a different constant in different bands.

Finally, throughout this work, we shall refer to the class of rings with $f(\psi) = \text{const}$ as the Norbury-Fraenkel (NF) family.

2.7.3. *Global existence proofs for general $f(\psi)$*

In 1974 Fraenkel & Berger used a variational technique to prove existence of steady vortex rings for a large class of vorticity distributions in the entire range of α . Benjamin (1976) poses a simpler and more natural variational form of the problem of steady confined vortex rings of a broad class as follows. Consider all possible bounded vorticity distributions with a given axial centroid with specified impulse in which the vorticity distributions (divided by σ) are rearrangements of a prescribed non-negative bounded function $\bar{g}(x, \sigma)$ defined on a connected core. Within this class of rings, steady solutions maximize the kinetic energy.

The rearrangements $\bar{h}(x, \sigma)$ of a function $\bar{g}(x, \sigma)$ can be visualized by imagining \bar{h} to be a passive scalar with initial distribution $\bar{g}(x, \sigma)$ that is convected by stream-functions that are more or less arbitrary functions of space and time. We include this technicality to emphasize the fact that in Benjamin's formulation one does *not* maximize the energy over vorticity distributions that have a prescribed vorticity function $f(\psi)$. Rather, if the variational problem has a solution, to every specified $\bar{g}(x, \sigma)$ there will correspond a certain $f(\psi)$ that is unknown beforehand. The variational formulation of Fraenkel & Berger (1974) is more cumbersome but has the advantage that $f(\psi)$ is prescribed. Benjamin uses his formulation to establish existence of a steady solution within the stated class; note again that it does answer the question of existence for a given $f(\psi)$. The formulation is ideally suited to establish non-linear stability with respect to axisymmetric disturbances in the sense that a positive definite functional of the perturbation remains bounded in terms of its initial value. Two points are in order. First, Benjamin (p. 20) ostensibly takes this functional to be the difference in energy between the perturbed motion and the stationary flow rather than a norm of the perturbation (for example the energy of the difference motion) which is the usual practice in establishing Lyapunov stability (Arnol'd 1965). Second, even Lyapunov stability does not preclude behavior such as the growth of wavy perturbations or the shedding of tails which are instabilities by other definitions. Friedman & Turkington (1981) give a variational formulation similar to Benjamin's with yet different technicalities. From a practical point of view, the greatest value

of variational statements is that they lead to efficient numerical schemes for finding steady solutions; one example is given below.

A less mathematical, more geometric, and remarkably simple method for demonstrating the existence of steady rings is due to Moffatt (1986). It is a constructive argument and suggests a procedure for finding them. Moffatt exploits the analogy between the steady inviscid equations and the equations for magnetostatics in a fluid with infinite magnetic conductivity. The idea is to consider the relaxation to magnetostatic equilibrium of the magnetohydrodynamic equations which are the Navier-Stokes equations with a Lorentz force term and an equation which expresses the fact that the magnetic field lines are convected and stretched with the fluid. If the initial condition is such that the velocity field is zero but the Lorentz force is non-conservative (it can otherwise be absorbed into the pressure) then motion will ensue i.e. magnetic energy is transferred to kinetic energy where it dissipated by viscosity. Now the lines of the magnetic field intensity \mathbf{B} , like vortex lines, follow the fluid hence the magnetic energy which is the integral of the square of \mathbf{B} has the interpretation of the length of magnetic field lines. Both therefore continually decrease as long as the Lorentz force is non-conservative. Now consider how this decrease would affect a flux-tube of \mathbf{B} (the analog of a streamtube). Lines on the surface of the tube contract but the volume of the tube must remain constant because it follows the fluid, so the tube fattens. Thus process will continue until it is impeded by a non-trivial topology of the \mathbf{B} field. For example a cylindrical tube can shrink indefinitely in surface area with volume remaining constant but two linked doughnuts cannot. Thus to obtain non-trivial solutions one imagines situations like this in which the magnetic energy has a lower bound. Kinetic energy will eventually dissipate to zero leaving the Lorentz force to be balanced by pressure gradient:

$$\mathbf{j} \times \mathbf{B} = \nabla p, \quad \mathbf{j} = \nabla \times \mathbf{B}, \quad (2.7.4)$$

where \mathbf{j} is the current density and units are chosen such that the magnetic permeability is unity. Equations (2.7.4) are analogous to the steady Euler equations:

$$\boldsymbol{\omega} \times \mathbf{u} = -\nabla \tilde{H}, \quad \boldsymbol{\omega} = \nabla \times \mathbf{u} \quad (2.7.5)$$

Hence a certain of class of steady Euler flows correspond to magnetic equilibria arrived at by the process of relaxation. Moffatt (1985) discusses many 3-D possibilities and vortex rings (Moffatt 1986, pp. 297-300). To obtain vortex rings one considers an

initial axisymmetric \mathbf{B} field whose flux tubes are nested tori inside some closed region containing the axis and infinite surfaces of revolution outside (see Figure 2.1). As the relaxation proceeds the tori follow the fluid and maintain the same volume $\text{Vol}(\chi)$ where χ is the streamfunction of \mathbf{B} which identifies each tube. In the relaxed state χ is analogous to ψ and one has realized a vortex ring with the corresponding $\text{Vol}(\psi)$, the volume of the streamsurfaces which Moffatt calls the signature of the vortex. Like Benjamin's variational statement this has the disadvantage that it does not allow one to specify the vorticity distribution $f(\psi)$; indeed the relation between $\text{Vol}(\psi)$ and $f(\psi)$ may be quite complicated.

2.7.4. *Steady axisymmetric vortex rings with swirl*

We now discuss steady solutions in which there is present a velocity component in the azimuthal direction. Interest in them partly stems from the occurrence of nearly axisymmetric breakdown bubbles in leading edge vortices over delta wings. We shall however limit ourselves here to discussing isolated ring-like solutions in which swirl is confined to the same region as the azimuthal vorticity whereas for the breakdown problem there is swirl present upstream of the bubble.

The problem of existence has been addressed by Turkington (1986) and Moffatt (1988) generalized his magnetic relaxation method to vortex rings with swirl. In addition to the signature function referred to earlier, one also specifies the flux $W(\chi)$ of the azimuthal component of the magnetic field B_ϕ . $W(\chi)$ remains invariant during relaxation and in the magnetostatic state becomes analogous to the volumetric flux through a streamtube $\psi = \text{const}$.

What is the effect of swirl on the speed of translation of thin rings? Since centrifugal force helps to balance vortex line tension, less Kutta lift is required and the speed of translation is reduced (Bliss 1973, p. 76). For a more complete description one solves the vorticity streamfunction equation that remains identical to Equation (2.7.2); the streamfunction now describes the projection of the velocity vector in an azimuthal plane. Only the condition for steadiness changes. It can be deduced by formal manipulation of the equations of motion (Batchelor 1973, p. 545) or from the basic physics and geometry of the problem (Benjamin 1962, pp. 623–625). Due to axisymmetry, any initially circular material line will remain circular as it moves on a streamsurface ($\psi = \text{const}$). By Kelvin's theorem the circulation $\widetilde{K} = 2\pi\sigma(x, \sigma, t)u_\phi$

will remain constant following the line. Hence $\widetilde{K} = \widetilde{K}(\psi)$. The steady vorticity equation is

$$\mathbf{u} \times \boldsymbol{\omega} = \nabla \widetilde{H}, \quad (2.7.6)$$

where $\widetilde{H} = p/\rho + \frac{1}{2}\mathbf{u}^2$ is the Bernoulli head. Hence velocity vectors lie on surfaces of $\widetilde{H} = \text{const}$ so that streamsurfaces coincide with surfaces of constant \widetilde{H} , i.e., $\widetilde{H} = \widetilde{H}(\psi)$. Benjamin, using a vector diagram similar to that used for turbomachinery, expresses the azimuthal vorticity in terms of the two arbitrary functions \widetilde{H} and \widetilde{K} as

$$\omega_\phi = \frac{\widetilde{K}(\psi)\widetilde{K}'(\psi)}{\sigma} - \widetilde{H}'(\psi)\sigma, \quad (2.7.7)$$

where primes denote differentiation with respect to the argument. When substituted into (2.7.2) this gives the so-called Squire-Long equation. It is subject to the same conditions stated earlier and the line of inquiry is the same: try different forms for $\widetilde{H}(\psi)$ and $\widetilde{K}(\psi)$. To our knowledge confined vortex solutions have been obtained only when $\widetilde{H}(\psi) = \widetilde{H}_o + \widehat{\lambda}\psi$ in the core and $\widetilde{H} = \widetilde{H}_o$ in the exterior potential flow and $\widetilde{K}(\psi) = \pm\widehat{\alpha}\psi$ in the core and zero in the exterior swirl free region. Now, the swirl free limit $\widehat{\alpha} = 0$ corresponds to the linear vorticity distribution and solutions exist i.e. the NF family and, in particular, Hill's vortex. What happens as the swirl parameter $\widehat{\alpha}$ is increased? It turns out, rather nicely, that the modified Hill's vortices remain spherical. The solutions are given by Moffatt (1969) and can be obtained via separation of variables. The force balance argument does not apply for such a thick core and the speed of translation of Hill's vortices with small swirl is larger than in the swirl-free case. Swirling extensions of toroidal members of the NF family have been obtained by Eydeland & Turkington (1988) using a variational approach geared to efficient numerical solution. They found that for all solutions the angular impulse was bounded by a constant times the linear impulse suggesting that steady solutions are possible only up to a critical level of swirl. This seemed consistent with experimental results communicated to them by D. Bergerud. Vortex lines lie on toroidal streamsurfaces and are helically wound around them. For almost all streamsurfaces the number of times that a vortex line winds around the core for every one turn around the azimuth will be irrational and the line will continue to fill the surface without closing.

The limit $\widehat{\lambda} = 0$ gives flows (called Beltrami) in which the vorticity is parallel to the velocity: $\mathbf{u} = \pm\widehat{\alpha}\boldsymbol{\omega}$ and streamlines coincide with vortex lines. The confined

sphere solution in this limit had been obtained earlier in the context of magnetic fields in which the Lorentz force is zero (Moffatt 1978, p. 29 and the references therein).

Due to the enormous variety of steady inviscid solutions there naturally arises the question of what determines the selection of solutions in particular situations. Some clues are provided by specific examples. In shear layers the structure may be chosen from the unstable eigenmodes of the shear profile which saturate and thereby become finite amplitude extensions of neutral modes (of perhaps a different basic shear profile). For example, the Stuart (1967*b*) vortices in two-dimensions represent finite amplitude extensions of the neutral wave of the $\tanh y$ profile, but how they arise from an instability of perhaps a different profile remains to be investigated. Then there is the selective decay hypothesis (see Appendix 5.B for examples) by which a bit of viscosity may affect one invariant of inviscid flow more than another thus leading to the selection of solutions in which the less robust invariant is minimized while others remain fixed. We may also finally mention the Prandtl-Batchelor hypothesis (Batchelor 1956) for the form of the vorticity in steady separation bubbles at high Reynolds number, of course they are probably unstable.

2.8. Unsteady behavior and coaxial interactions of inviscid rings

All the results reviewed in this section are valid in certain asymptotic limits. The aim of the present work is to add to the repertoire of unsteady inviscid behavior by calculating numerical solutions.

A model for interacting vortex rings was proposed by Dyson (1893). It assumes (i) that vortices are sufficiently far apart compared to their core sizes that the velocity field induced by one ring on another is the same as if all its vorticity were concentrated on a line of zero thickness, (ii) that this velocity field does not deform the core, and (iii) that the cores are thin and circular so that, for the linear vorticity case, their self-induced velocity is given by Kelvin's formula. The model does not appear to be a consistent asymptotic limit to the equations of motion, but we suggest in Chapter 4 that it may be one in the sense of an average over the fast time scale of core deformations. The elliptic model of Chapter 4 extends Dyson's model to allow core deformation. Further discussion about Dyson's model and its applications appears in Chapter 4.

Moore (1980) considered a vortex ring with thin elliptical cross-section with linear vorticity. When the core is thin compared to its radius, the flow is locally two-dimensional and given by Kirchhoff's elliptic vortex (Lamb §159) which rotates at constant angular velocity. Only the self-induced motion remains to be determined. Moore uses Helmholtz's method to obtain the motion of Helmholtz's centroid and relates it to the centroid of the shape. The calculation of the energy required in this method is performed by obtaining the local streamfunction using an asymptotic matching procedure; however a simple expansion also suffices (Chapter 4). Moore finds that the translational speed oscillates in time, with a period equal to half the core rotation period; the average speed is obtained from Kelvin's result by replacing the core radius with the mean of the major and minor axis dimensions. The radial centroid of the core also oscillates. This solution is an element of the elliptic model in Chapter 4.

Moffatt & Moore (1978) studied the linear stability of Hill's spherical vortex to perturbations of the boundary. They found that if the vortex is squashed so that initially its long side is along the axis of symmetry, it sheds a tail of volume proportional to the disturbance amplitude from its rear stagnation area. If the vortex is squashed the other way, irrotational fluid enters through a spike from the rear. Bliss (1973) also studied the problem less completely and argues for the presence of a short wave instability. Pozrikidis (1986) independently developed a contour dynamics formulation for the linear vorticity case and used it to study the non-linear stability of Hill's vortex. He found (as did we) that when a tail is shed the remnant vortex is very nearly spherical, even for large perturbations i.e. a perturbed Hill's vortex returns to a Hill's vortex by shedding a tail. When a spike of irrotational fluid is entrained, the spike travels towards the front stagnation point, forming a thin spherical cap. Aside from the thin cap, the resultant vortex is toroidal i.e. if the thin cap is neglected, a hole has been punched through the vortex. Pozrikidis concluded that the resulting vortex was a member of the NF family; we do not agree because the core shapes are not fore-aft symmetric. His point is based on resultant core shapes having a similar energy-impulse relationship as the NF family. In our calculations there appeared a high wavenumber sawtooth instability as suggested by Bliss (1973) but Pozrikidis' calculations are free of them. In the rest of this work, we shall not present results which overlap with Pozrikidis'. Rather, we shall concentrate on thinner core vortices and coaxial interactions.

2.9. Theory and numerical simulations of viscous vortex rings

2.9.1. Final period of decay

We have already mentioned Saffman's (1970) viscous solution for a diffusing Gaussian core ring. It remains valid so long as the core remains thin i.e. for small times. We now discuss the large time limit. The total momentum of the fluid is constant. As the core diffuses, the momentum has to be shared with more fluid and velocities decrease. Eventually the Stokes flow limit is reached. Phillips (1956) showed that any unbounded flow that has net linear momentum decays to a vortex ring solution of the Stokes equations. Basically, the idea is to consider the evolution of the Fourier transform of the velocity expanded in the powers of the wavenumber k :

$$\hat{\mathbf{u}}(t) \sim \bar{\mathbf{P}} + (\bar{\mathbf{Q}}(t) + \bar{\mathbf{A}})k + \dots \quad (2.9.1)$$

The expansion is written symbolically so as to bring out the salient points. Here $\bar{\mathbf{P}}$ and $\bar{\mathbf{A}}$ represent the conserved linear and angular impulse respectively (the latter is zero for swirl-free axisymmetric flow), and $\bar{\mathbf{Q}}$ is the quadrupole moment, a quantity that is a function of time. Assume that subsequent to some instant t_o the non-linear terms in the Navier-Stokes equation can be neglected, so the solution is given by the inverse Fourier transform

$$\mathbf{u}(\mathbf{x}, t) \sim \int (\bar{\mathbf{P}} + (\bar{\mathbf{Q}}(t_o) + \bar{\mathbf{A}})k + \dots) e^{-\nu k^2(t-t_o)} e^{i\mathbf{k}\cdot\mathbf{x}} d\mathbf{k}. \quad (2.9.2)$$

We are interested in an asymptotic expansion for large $(t - t_o)$. By Laplace's method, the dominant contribution to the integral will come from a small sphere of radius ϵ near $\mathbf{k} = 0$. This allows one to use only a finite number of terms in the series for $\hat{\mathbf{u}}$, say the first two. More terms lead to higher order expansions valid earlier in time (for the Stokes equations only). Next one argues that the contribution to the integral from outside the small sphere is exponentially small which allows us to once again integrate over all of \mathbf{k} . This incongruous looking step is nicely explained in Bender & Orszag (1978, p. 261). Phillips (p. 141) himself never invokes Laplace's method; instead he keeps only the first term in the expansion of $\hat{\mathbf{u}}$ *before* doing the integral.

In any case, performing the integral one obtains the first two terms in the long time expansion. The first term describes a self-similar vortex ring for which translational motion has ceased, velocities decay as $[\nu(t - t_o)]^{-\frac{3}{2}}$, lengths increase as $[\nu(t - t_o)]^{\frac{1}{2}}$ and the strength is the conserved impulse. This behavior can also be argued dimensionally

(assuming self-similarity) since the only relevant parameters at large times are \tilde{P} , ν and t . Phillips exhibits the solution explicitly. If the angular impulse is zero, the second term represents a ring together with its image of the opposite vorticity, for which velocities decay as $[\nu(t - t_o)]^{-2}$, lengths increase as $[\nu(t - t_o)]^{\frac{1}{2}}$ and where the strength is the value of the quadrupole moment $\tilde{Q}(t_o)$ at the termination of the non-linear phase of the evolution which depends on the entire history of the non-linear evolution. By substituting the expansion for \hat{u} into the transform of the Stokes equation one sees that \tilde{Q} is an invariant for Stokes flow so \tilde{Q} asymptotes to some value at the end of the non-linear evolution. Lack of knowledge of $\tilde{Q}(t_o)$ precludes a closed higher order expansion to earlier times even within the Stokes limit. In some situations, for example that of two colliding vortex rings, the net linear impulse is zero, the first term vanishes and one is left with the second term as the large time solution but with an undetermined strength $\tilde{Q}(t_o)$.

2.9.2. *Improvement of the Stokes solution*

The Stokes vortex ring does not propagate, however, one might expect that large time solutions of the Navier-Stokes equations would continue to drift at an ever decreasing speed. How does one obtain this asymptotic drift? We shall first describe some heuristic ideas and then describe an alternate point of view developed in Rott & Cantwell (RC, 1988). A similar analysis for the two-dimensional pair is to be found in Cantwell & Rott (1988) and, due to the simpler geometry, provides a good introduction to the vortex ring situation.

The Stokes ring does have net momentum, fluid does drift forward, indeed the motion of fluid particles is interesting (Allen 1984), but, due to the absence of convection terms particles do not transport any vorticity. Suppose one did calculate this transport from the full Navier-Stokes equations and expressed the answer in terms of the motion of Helmholtz's definition of the centroid. Kambe & Oshima (1975) perform this exercise and find that the speed of the centroid U has the same power law decay ($U(t) \sim (t - t_o)^{-\frac{3}{2}}$) as the velocity field of the Stokes solution. We shall refer to this result as the Stokes drift. RC have given it meaning but, before discussing it, some historical remarks are in order.

Kambe & Oshima (1975) attempted to obtain the second term in the expansion in terms of inverse powers of time (for the Navier-Stokes equation). In the second order problem, the Stokes operator acting on the second order solution is equal to forcing

terms consisting of the non-linear operator acting on the first order solution (the pressure gradient of the first order solution is zero in the present case). On solving this, they encounter a non-uniformity in which the second-order solution becomes arbitrarily large compared to the first order solution at large distances from the origin. A similar situation occurs in the improvement of Stokes flow past a sphere (Whitehead's paradox). Kambe & Oshima attempt to resolve the difficulty by means of matched asymptotic expansions but the analysis is left incomplete.

RC show that a *uniformly valid* second approximation *can* be obtained after impressing a uniform drift on the first order solution. The value of the drift is obtained by solving for the second order pressure and equating it to its value at infinity. The resulting drift velocity is the same as that obtained from evaluating the speed of Helmholtz's centroid using the Navier-Stokes equations as explained above. The result is

$$U(t) = 0.0037038 \frac{P}{[\nu(t - t_o)]^{\frac{3}{2}}}, \quad (2.9.1)$$

where P is the impulse with density set to unity. In numerical simulations of viscous rings using a spectral method described below, Stanaway, Cantwell & Spalart (1988a,b) discovered that, from a variety of initial conditions, the speed $U(t)$ of the centroid had this behavior in the final stages of decay. Hence, the Stokes drift does have meaning for the decay of a vortex ring proceeding from the Navier-Stokes equations. RC obtain the second order solution which contains an undetermined constant which reflects loss of information about the non-linear part of the evolution.

In bringing the theoretical part of the discussion to a close we should like to mention for completeness that Tung & Ting (1967) have studied the thin diffusing ring using matched asymptotic expansions and Batishchev & Srubshchik (1971) studied the diffusion of Hill's spherical vortex at small times with small viscosity.

2.9.3. Numerical solutions of viscous vortex rings

We now turn to a discussion of numerical solutions for viscous vortex rings. Some preliminary attempts are included here for completeness.

Kambe & Mya Oo (1982, 1984) solve the axisymmetric vorticity equation using ADI splitting of both the centrally differenced viscous and convective terms. A uniform cartesian grid with 136×121 points is used. The Poisson equation for streamfunction is inverted using successive over-relaxation and the velocities are calculated

from the streamfunction by a fourth-order implicit formula. The conditions $\omega_\phi = 0$ and $\psi = 0$ are applied on a finite boundary. Collisions of vortex rings with $Re = 50$ - 500 based on initial translation speed and toroidal radius are presented. The size of the domain (inferred from the figures) in the quarter plane is 8×8 initial toroidal radii in the axial and radial directions. The decay of energy and circulation are studied. For the highest Re case the circulation remains nearly constant initially and then decays as the cores "make contact" and gradients intensify at the collision plane. On the other hand, the energy decreases throughout. For the low Re cases the vorticity dissipates rapidly before the cores stretch very much. For the highest Re case, the cores stretched to $2\frac{1}{2}$ radii at the latest time shown and the cores deformed into a head and diffuse tail. Accuracy was judged by comparing the value of the kinetic energy dissipation rate, obtained from an integral expression, versus the rate of energy decay. At the latest time for which this accuracy check is provided the cores have stretched to $1\frac{1}{2}$ radii and the rate of energy decay exceeds the dissipation by 22%. The calculated quadrupole part of the acoustic signal at the highest Re agrees very well with the experimental measurements of Kambe & Minota (1983) at a much higher $Re = 20,000$. They find that the dip in the experimentally measured signal, which we shall claim in Chapter 5 is due to inviscid core deformation, is coincident with the beginning of circulation decay and hence is taken as confirming the hypothesis in Kambe & Minota (1983) of its viscous origins. On the other hand, the monopole part of the signal which arises from kinetic energy dissipation is very much underpredicted.

Kambe & Oshima (1975) use a similar method except that the Crank-Nicolson (implicit) method is used. They study the generation of a vortex ring resulting from applying a velocity profile at the computational boundary for a certain period of time. The vortex propagates and collides with the right boundary on which inviscid boundary conditions are applied. Qualitative comparison with the experimentally measured speed of propagation is provided.

One of the difficulties of simulating these flows with finite difference methods is that boundary conditions have to be applied at a finite distance. Liu & Ting (1982) developed a strategy in which they employ far-field expansions to supply boundary data. The head-on collision of vortex rings is considered. Numerical details are not presented in the paper cited. The information we present is obtained partially from Chamberlain & Liu (1984) in which a three-dimensional example for obliquely interacting and reconnecting rings is given. The vorticity equation is advanced using

the Dufort-Frankel scheme (explicit). The velocity is obtained from the vorticity by the curl of the vector potential which is related to the vorticity via a Poisson equation. It is solved, using a second-order direct solver, in a smaller subdomain with boundary data for the vector potential supplied using a multipole expansion with three terms. This expansion contains coefficients which are integrals of the vorticity and they are calculated using Simpson's rule. The vector potential outside the subdomain is calculated with the far-field expansion. The velocity field is then calculated from the vector potential by taking its curl using second-order central differences. Results are provided for a vortex ring collision with a Reynolds number ($\equiv \Gamma_o/\nu$) equal to 201, a very small initial separation equal to 0.2 of the toroidal radius and a core radius of 0.05 times the toroidal radius. Results are presented for a short time during which the rings have stretched to only 1.6 the initial radius.

Stanaway, Cantwell & Spalart (1986, 1988*a,b*, hereafter SCS) developed a numerical method which is attractive in several respects. A spectral method was employed and it was verified to converge exponentially. The Navier-Stokes equation is solved in spherical coordinates in an unbounded domain using basis functions chosen to give the proper decay of velocity at infinity. A weak formulation of the Navier-Stokes equations is used in which inversion of a Poisson equation is not required. The time-stepping algorithm is second-order with the Crank-Nicolson (implicit) scheme for the viscous terms and Adams-Bashforth (explicit) for the convective terms. Several physical insights have been obtained:

(i) Fraenkel (1970, 1972) in his higher order treatment of inviscid steady rings found that the formal error estimate for the ring speed, obtained using the Helmholtz method, is too conservative. SCS found that this is also true for Saffman's (1970) formula for a diffusing ring and study the behavior for fatter cores. Maxworthy's (1972) model of laminar rings in which vorticity is deposited in a wake and his model estimates should be amenable to testing by the method.

(ii) The large time behavior in the decay of a vortex ring was studied and, as mentioned earlier, it is shown that the Stokes drift has a physical meaning.

(iii) With respect to leapfrogging interactions, we shall see in Chapter 5 that one important inviscid effect is the unequal strain rates experienced by the two vortices. This causes the passing vortex to undergo a permanent deformation at the end of the passage. The simulations of SCS reveal another important asymmetry when viscosity is present. The initially rear vortex undergoes compression of vortex lines followed

by extension whereas the opposite happens for the rear vortex. The stretching versus compression affects the rate of diffusion. For example see Lundgren (1982) or Kambe (1984) who show how a rectilinear vortex that is axially strained diffuses as if it were unstrained with only spatial and time scales modified. One might therefore expect the two rings to undergo not only different deformation but different diffusion. SCS find that the initially forward ring undergoes more diffusion and weakening of vorticity. Therefore during its passage which follows, it is more susceptible to being torn and merged.

2.10. Azimuthal instabilities of vortex rings

2.10.1. *Introduction*

Although this work deals with the axisymmetric dynamics of vortex rings, one needs to be aware of three-dimensional effects which arise in practice. Three-dimensionality may influence the emitted sound. For example, Hussain (1983) suggested that reconnection of vortex lines when vortex ring-like structures breakdown near the end of the potential core of a jet may be a dominant source of jet noise. In this section we focus primarily on the breakdown of an isolated vortex ring. The breakdown of jet vortices is qualitatively similar but straining due to other vortices must be accounted for. We will discuss experimental observations and the mechanisms which have been proposed to explain them. The unfolding of the problem and the history of ideas is an interesting case study in the process of scientific dialogue. It is noteworthy that the problem was finally resolved when a *spurious* instability was being investigated. In the recent history of the problem, a denouement seems to have occurred with the work of Widnall & Tsai (1977). There remain several unresolved issues, some were recognized by the original participants in the saga and others were suggested by subsequent experiments.

2.10.2. *Early theoretical work*

The story begins with Kelvin and as the reader will discern, finds temporary shelter, a hundred years later, in ideas that are minor extensions of his. This is not to say that convincing proof of these ideas has been a simple achievement; the analysis presented in Widnall & Tsai (1977) is formidable. In 1880 Kelvin published

an article entitled "Vortex Statics" which treats helical waves on vortex rings, as is apparent from the title, as static; the definition of "static" includes stable oscillations. There is ample recognition of the tentative nature of the discussion and as a first step in rigorously demonstrating stability, a month later Kelvin (1880*b*) showed that a rectilinear vortex with an initially circular core containing uniform vorticity could support a spectrum of neutrally stable modes of vibration. According to Widnall & Sullivan (1973), in 1867 he described the analogous calculation for the modes of oscillation of a vortex ring. He did not complete the calculation (the analysis is not trivial) but expressed the conviction that like the straight vortex, the situation would be stable. Early work reinforced Kelvin's beliefs. J.J. Thomson (1883) studied the stability of infinitesimal sinusoidal perturbations on a vortex ring but considered the limit of very small core size and a small number of waves, N_w . To the order of the analysis, all modes are neutrally stable with a definite frequency of oscillation. Pocklington (1895) provided a solution for waves on a hollow vortex ring of small cross-section. A hollow vortex ring is an idealization in which the rotational core is a vacuum permitting the surface of the core to be held at constant pressure. This simplification allows one to investigate mathematical properties of the general problem. The solution was valid to linear order in α , the ratio of core and ring radii. It was found that all modes are stable.

2.10.3. *Early experimental work*

The necessity to reconcile classical theoretical results suggesting stability with experimentally observed instability, has motivated much of the theoretical work of the past decade. The first photographs of the instability of vortex rings produced by ejecting a slug of fluid from an orifice were presented by Kruttsch (1939). He observed between 5 and 12 waves as the parameters of the generation (slug length, etc.) were varied. But, instead of suggesting that Kelvin might have been mistaken, he attributed the phenomenon to foreign matter acquired from the region outside the orifice during the generation of the ring. Maxworthy (1972) reported the appearance of an azimuthal waviness with 5 peaks for "energetic" rings (those for which the Reynolds number based on propagation speed and maximum diameter of the bubble exceeded 600). He posited that the ingestion of secondary vorticity of the opposite sign during the generation process was responsible; this would make the core unstable

by Rayleigh's criterion (strictly speaking, the condition is applicable for disturbances to two-dimensional flow with circular streamlines).

2.10.4. Analysis using the filament approximation

From the experimental observations, one is tempted to conclude that the type of ring studied in the classical analyses, namely one with a thin core with uniform vorticity, has little in common with the behavior of real vortex rings. But not discouraged and perhaps spurred by the success of Crow (1970) in explaining the wavy instability of aircraft trailing vortices via a filament approximation, Widnall & Sullivan (1973) undertook an analysis for vortex rings in which they treated the vortex ring as a filament in which variations of the core structure (in time and along the filament) are ignored; the motion of the filament is governed by the Biot-Savart law. First a filament of zero cross-section is considered. The singularity of the Biot-Savart integral is treated by the cut-off approximation suggested by Hama (1962) and used with remarkable success by Crow (1970). In this method the Biot-Savart integral is "cut-off" at a certain arc length on either side of the point where the velocity is evaluated. For thin cores (compared to the radius of curvature), the cut-off distance can be rigorously related to the local structure of the core. Filament models assume an invariant core structure and apply to a vortex tube only for variations along the tube which have a wavelength much larger than the size of the core, a condition which needs to be checked *a posteriori*. In any case, Widnall & Sullivan considered perturbations which distort the filament into a helical shape. They predicted the spatial amplification rate for each value of N_w ; it is strongly dependent on a single parameter \tilde{V} , a non-dimensional velocity of propagation:

$$\tilde{V} = \log(8L_0/\delta_c) - 1/2 + \tilde{A}, \quad (2.10.1)$$

where L_0 is the toroidal radius, δ_c is a characteristic core size and \tilde{A} is a constant that depends on the distribution of swirl velocity in the core and the way in which δ_c is defined. Each value of N_w has a narrow range of \tilde{V} for which it is amplified. For larger values of N_w , larger values of \tilde{V} (hence smaller core sizes, with fixed shape of the velocity profile) are required. This feature is exhibited in the experiments of Widnall & Sullivan. However, quantitative agreement with experiment could not be obtained. The theory underpredicts the number of waves; the error increases with \tilde{V} . The ratio of unstable wavelength to core diameter for a linear vorticity distribution

is about 2 and led the investigators to question the applicability of their filament treatment for such short waves.

In a reply, Moore & Saffman (1974) cast doubts on even the qualitative correctness of the theory by showing that the instability predicted by the filament approximation is spurious. The question of why it is spurious which Widnall and her co-workers must have asked, enabled thinking to get on the track to where it currently stands. Moore & Saffman started with Pocklington's (1895) solution for the period of vibrations (all of which are stable) on the hollow core vortex ring which is valid to linear order in core size to radius ratio but unrestricted as to wavelength. They found that a Biot-Savart formulation for this case gave a spurious instability. However they emphasized that Pocklington's result does not prove the stability of even a hollow vortex. One could not, and this turned out to be crucial, rule out that a higher order expansion of the vibration frequency in terms of α might contain imaginary (growth) terms. Nevertheless they concluded by expressing the belief that the instability of experimental vortices was to be accounted for by Maxworthy's explanation based on the generation process rather than an inherent instability of the ideal vortex ring. Things seemed to regress back to Kelvin's notion about the indestructibility of ideal vortex rings.

2.10.5. *A proposal for the mechanism of the azimuthal instability*

The next contribution (Widnall, Bliss & Tsai 1974, hereafter WBT) is a result of a search for the cause of the erroneous instability of the filament approximation. After finding the mechanism they propose that the *same* physical process may apply to the actual situation. Their ideas lead to predictions for the number of waves that are in much closer agreement with experiment than those of Widnall & Sullivan. Furthermore, their explanation accounts for the effect of the detailed distribution of vorticity in the core.

The chronological progress of thought probably occurred in the following sequence. When Crow's (1970) work on trailing vortices was reexamined they noted that, in addition to a long wave instability which matches observations, he found a short wavelength instability which is not observed in practice and which is incompatible with the assumptions of the filament approximation. Crow, however, not realizing this (a systematic derivation of the cut-off approximation and the conditions for its validity came later with the work of Moore & Saffman 1972) states that "nothing in

the stability theory precludes their appearance” and goes on to suggest that atmospheric agitation favors the long-wave mode. Crow did realize, and this is crucial, that the band of unstable short waves was centered about the wave whose self induced rotation rate is zero according to the cut-off theory. Such a wave would diverge under the induced strain of the other vortex. Wavelengths whose rotation rates are smaller than the imposed strain rate would also diverge. Yet when WBT plot the self induced rotation rate for small amplitude bending waves for an isolated uniform core columnar vortex as studied by Kelvin (1880*b*), they find that short waves always have a finite rate of rotation. Therefore, the filament approximation is erroneous in predicting instability of these waves. Incidentally, in numerical calculations via the filament method, the size of segments must be chosen larger than the numerical core size to keep the spurious mode outside the resolvable range. Winkelmanns & Leonard (1986, private communication) developed an improved core function that reproduces the behavior of short waves of pure bending.

If the same mechanism is also responsible for the instability of real vortex rings, then the mode involved cannot be a pure bending wave. There are other bending modes for which the rotation rate is zero. These have a more complex radial structure of the eigenfunction for the perturbation velocity, having at least one node at some radius in the core. WBT postulate that it is the mode with the least radial structure that appears. For the constant vorticity case, it is found from Kelvin’s (1880*b*) formulae that this mode attains a zero self induced rotation at $(k_z \delta)_{\text{crit}} = 2.5$ (k_z is the axial wavenumber and δ is the core radius). Then together with the requirement that an integer number of waves exist on the ring ($k_z = N_w/L_o$), this gives the discrete values of the ratio of core size to radius which would result in the amplification of a given number of waves.

Experimental evidence provides credence to the WBT proposal. Maxworthy (1977) confirmed that during the small amplitude phase, stagnant (non-rotating and non-propagating) waves grow at 45° relative to the direction of ring propagation. At large amplitudes, the waves begin to rotate and the core fluid is mixed and becomes turbulent. That it is the second radial mode of bending that appears is seen in Plate 114 of Van Dyke (1982). Focusing on a cross-section at which the inner core (the darkest portion of dye) moves outward, one observes that the outward portions of the core are displaced inward so that a profile of the eigenfunction for radial velocity has one nodal line within the core.

2.10.6. *Mathematical justification of the WBT mechanism*

In their next two contributions, Tsai & Widnall (1976, Widnall & Tsai 1977) place their theory on a firm mathematical footing for the case of a uniform vorticity distribution. In particular, the hypothesis put forward in WBT is deficient in the following respects. First, one cannot speak of the instability of a circular core in a straining field because the cross-section is deformed into an ellipse. Second, there is no support for the contention that among all the bending modes of Kelvin (1880*b*) which have zero rotation rate, it is the one with the least radial structure that should appear. Third, as pointed out by Moore & Saffman (1975*b*), it is insufficient to consider the individual stagnated eigenmodes as the only candidates for instability; two modes of the same wavenumber but different radial structure and sense of twist, can have the same direction and value for the rotation rate. When superposed these produce a standing wave that propagates in the axial direction but maintains the same angular orientation so it too can be unstable under an imposed strain. Fourth, WBT demonstrated that one of the effects of curvature was to produce a quasi-stagnation point flow in the vicinity of the core but there are other effects of curvature of the same order which may be stabilizing.

The first three issues are addressed in the 1976 paper dealing with the stability of a rectilinear vortex with constant vorticity under a weak straining field in which the basic state has an elliptical cross-section. They show that the unstable wavenumbers lie in bands whose width is proportional to the imposed strain rate. The growth rate is maximized locally at wavenumbers corresponding to the center of the band. These wavenumbers are of two kinds. The first group corresponds to non-rotating waves in the unstrained circular vortex. The second group consists of some but not all of those wavenumbers at which two bending modes with the same rotation rate but different radial structure can exist simultaneously, in agreement with the assertion of Moore & Saffman (1975*b*). These modes are referred to as being degenerate. There does not appear to be a general rule to decide whether a given degenerate pair of modes leads to instability, each has to be tested on a case by case basis. For some cases treated numerically the former class had maximum growth rates an order of magnitude larger than the latter class and, among these, the second radial mode, which was conjectured to occur on vortex rings, had the largest growth rate. Unfortunately, the third radial mode has a growth rate only 0.2% smaller so the second objection is not met satisfactorily. It is possible that under the influence of

viscosity, the higher radial mode is damped. It has wavelength which is 60% smaller. Maxworthy (1977) reported experimental observations of what he calls a "bimodal" type of instability in which two modes, one exactly twice the wavelength of the other, are observed simultaneously in a certain range of Reynolds number. It is possible that these are the second and third radial modes but Saffman (1978) doubts this for reasons that are not made explicit. Saffman & Robinson (1984) numerically studied the same problem for finite strains and find that the asymptotic analysis of Tsai & Widnall provides fairly accurate predictions for even large values of strain; the main difference is a slight decrease in the most amplified wavenumber with strain rate. For large strains, the bands widen and eventually overlap. Thus there is little selectivity of a preferred mode indicating sensitivity to the properties of the external disturbance. This would be an important consideration for turbulent shear flows where each vortex lies in the straining field of others. It might also prevent the emergence of a distinct number of waves on vortex rings with thicker cores. It is important to keep in mind, however, that for long waves, a mechanism does exist for mode selection. This comes from the realization that perturbations on the influencing vortex can have an effect of the same order as the strain induced by that vortex were it unperturbed. This is suggested by the fact that for an isolated rectilinear vortex in a strain field, sufficiently long waves such that the strain rate exceeds the rate of rotation are all unstable; the growth rate increases with wavelength until it asymptotes to the strain rate for infinitely long waves. Hence there is no preferred mode. If one accounts for the velocity field caused by waviness of the influencing vortex a preferred mode does emerge. This is precisely the long wave mode for aircraft trailing vortices identified by Crow.

The final objection of the WBT proposal which regards the effects of curvature is met in Widnall & Tsai (1977) in which a rigorous stability analysis is performed for a vortex ring with vorticity varying linearly from the axis of symmetry. The results are obtained as a perturbation expansion to $\mathcal{O}(\alpha^2)$ for the frequencies of oscillation, the zeroth order solutions being identical to those for the uniform rectilinear vorticity obtained by Kelvin (1880*b*). Recall that Pocklington's (1895) analysis for the hollow ring predicted stability. The reason is that in the expansion of the basic state with respect to the same parameter, at $\mathcal{O}(\alpha)$ deviations from local two-dimensionality of the flow simply make the streamlines non-concentric. Indeed, Widnall & Tsai find no correction to the frequency at this order for their case also. Destabilizing

strain like terms appear first only at $\mathcal{O}(\alpha^2)$. It is found that the coupling of this strain to the zeroth order bending waves of Kelvin (1880*b*) is the dominant effect of curvature. The analysis is carried to completion only for the second and third radial modes, the former being only slightly more unstable. Thus the mechanism of WBT is shown to be correct at least for the uniform vorticity distribution and for thin cores and observations are explained by appealing only to the *classical* picture of the vortex ring. Hence Kelvin was incorrect in believing the ideal vortex ring to be “indestructible.” Also proved to be too pessimistic were those who believed that the behavior of the ideal vortex ring had little to do with the behavior of “real” vortex rings.

The work to be described now was anti-climactic but still necessary. It attempted to address the fact that the vorticity distribution measured for rings generated by a piston or orifice apparatus tends to be peaked (Sullivan, Widnall & Ezekiel 1973) unlike the linear distribution used in the Widnall & Tsai (1977) analysis.

In WBT it was shown that if the analysis of Kelvin is used to determine the wavenumber of the stagnant second radial mode for a particular peaked distribution of vorticity, the prediction for the number of waves agrees slightly better with experiments. Saffman (1978) carried this further by analyzing distributions derived from careful consideration of the process of generation of the vortex. The experiments of Leiss & Didden (1976) show that if the translational velocity is held fixed over successive realizations of various rings (this fixes the speed-effective core size), but the Reynolds number of generation Re_p (based on piston velocity and orifice diameter) is allowed to vary, then the number of waves changes significantly. This indicates that the character of the vorticity is altered so that $(k\delta)_{\text{crit}}$ for the stagnant mode also changes (δ now represents the speed-effective core size of the vorticity distribution). Saffman used his vortex sheet roll-up model to predict the form of the vorticity and hence the value of $(k\delta)_{\text{crit}}$ as a function of Re_p . The agreement for the number of waves compared with the experiments of Leiss & Didden was excellent thus lending support to the applicability of the WBT mechanism to non-uniform vorticity distributions.

2.10.7. *Unresolved issues*

There remain several unresolved issues that deserve further investigation:

- 1) What is the precise nature and dynamical significance of flow along the axis of the core that experiments show is set-up in the later stages, after the waves break about 10 diameters downstream of the exit? Maxworthy (1977) observed that regions of non-uniform dye concentration tended to rotate *intermittently* about the axis through several wavelengths of the primary instability accompanied by a pulsation in core diameter. The axial flow velocity was quite rapid, about half of the maximum swirl velocity. It is conjectured that the axial flow occurs because waves do not break at different azimuthal locations at the same time, creating an azimuthal pressure gradient. It is believed that the axial flow is accompanied by a solitary bulge wave. The axial flow profile is reversed at the periphery of the core to give zero net momentum. It has been suggested that axial flow prevents further instability since the resulting turbulent vortex is apparently stable. There has been no theoretical justification of this. Only Krutzsch (1939) has observed a repeat of the wavy instability.
- 2) What is the sequence of events leading to a turbulent vortex ring? In contrast to the above observations of Maxworthy, the experiments of Sturtevant (1981) using Schlieren visualization of shock-tube generated rings show a different scenario. The waves never grow and break, instead they simply decay and vanish! Sturtevant is unsure whether the difference is due to the unreliability of dye visualization or because in previous studies the cores have been thicker with a Reynolds number an order of magnitude smaller. Compressibility effects may also play a role. Moreover, Sturtevant observes "turbulent vortex rings" even before the occurrence of waviness. However, the phrase "turbulent vortex ring" as used by Sturtevant very likely has a different meaning than as used by Maxworthy. The term is attached to observations in the following experiment. The walls of the shock tube are cooled to aid in visualization. As the vortex ring is formed, the rotational core consists of both fluid from the tube and ambient fluid. The irrotational fluid surrounding the core but carried with it is mostly cold fluid. The interface between it and ambient fluid flowing past appears as a line in the Schlieren photographs. Initially it is sharply defined but before the wavy instability occurs, it becomes irregular. Disturbances on this interface "protrude into the surrounding fluid and after being convected along the boundary to the rear of the ring, seem to grow almost explosively outward from the rearward surface." It is only later that instability waves develop on the core. In §6.4 we will provide

results which suggest that a similar process occurs for a non-turbulent core; a simple form of core unsteadiness (periodic rotation of an elliptic core at constant angular velocity) can produce complicated particle paths and distortions of the interface similar to those described by Sturtevant. However, in the experiments, irregular azimuthal variations in the distortion of the interface are also noted and this we are unable to account for. In any case, the first observation of Sturtevant seems to stand.

- 3) What is the status of the bimodal instability? Is it a non-linear effect or the concurrent appearance of the second and third radial modes?
- 4) What are the effects of viscosity in the initial mode selection process? Can one verify the inhibition of the third radial mode which has an inviscid growth rate nearly identical to the second radial mode?
- 5) Finally, in the context of an inviscid model, would a thicker core have a broadband amplification spectrum to preclude the appearance of a definite number of waves? This statement can be checked by a simulation via the filament method.

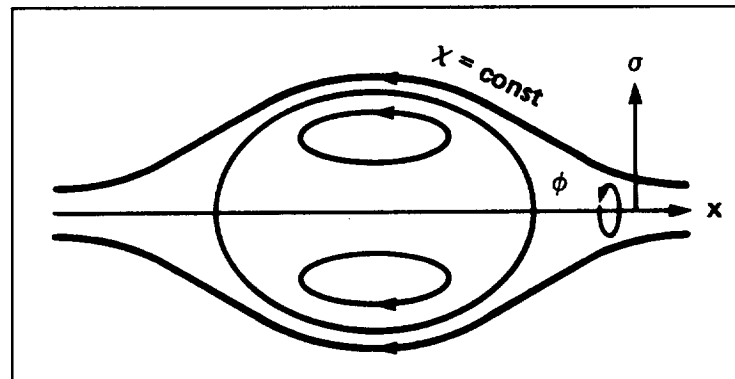


FIGURE 2.1. Initial topology of a magnetic field which leads to a magnetostatic state analogous to a steady vortex ring.

CHAPTER 3

A CONTOUR DYNAMICS ALGORITHM FOR AXISYMMETRIC FLOW

3.1. Introduction

In this chapter, the method of contour dynamics developed for two dimensions by Zabusky, Hughes & Roberts (1979) is extended to axisymmetric flows for vorticity distributions that vary linearly with normal distance from the symmetry axis. We will discuss the derivation and implementation of the scheme, verify its accuracy and convergence, and present a qualitative illustration. A detailed study of interacting vortex rings of this class will be presented in Chapter 5.

In two dimensions, the contour dynamics approach has made possible the study of the inviscid motion of vortex patches containing piecewise constant vorticity. Since vorticity follows the fluid, such a distribution remains unaltered in time and only the contours surrounding the regions have to be tracked as they convect with the fluid velocity. The velocity can be expressed as a line integral along the contours, thus reducing the dimensionality of the problem by one. In principle, arbitrary distributions may be approximated by region-wise constant ones, but to date most of the work has focussed on vortices containing single regions. Some exceptions to this are listed in Appendix 3.C which also provides an annotated list of works for various categories of uniform vorticity flows. These studies have yielded mathematical insight into the nature of solutions of the Euler equations as well as understanding of physical processes in shear layers and two-dimensional turbulence. As a highlight of the first, we mention the work of Dritschel (1985, 1986) who elucidated the role of energetics in the merger and fission of vortices and in more general topological changes that occur during their long time evolution. Specifically, perturbations of equilibrium solutions tend asymptotically to different equilibrium states which are energetically compatible with the original state. With respect to the second, Moore & Saffman (1975) studied the stability of an array of uniform elliptical vortices. Their work stimulated them to propose "tearing" as one mechanism in the growth of mixing layers. Melander,

Zabusky & McWilliams (1988) used an elliptical core model to provide explicit criteria for the convective pairing of two like signed uniform vortices. Their predictions agree well with the results of spectral simulations. Neu (1984), motivated to explain the genesis of streamwise braid vortices in mixing layers, showed that highly flattened uniform vorticity cores “collapse” to a circular shape with concentrated vorticity when subjected to a three-dimensional strain which models the influence of spanwise rollers and neighboring streamwise vortices. Lin & Corcos (1984), using finite-difference calculations of the two-dimensional Navier-Stokes equations with out of plane strain confirmed the mechanism for an array consisting of counter rotating pairs. Pullin & Jacobs (1986) provided further evidence with contour dynamics simulations of vortex arrays employing multiple contours. Recently M.M. Rogers & R.D. Moser (1988, private communication) at NASA Ames have shown the relevance of Neu’s collapse mechanism to the fully three-dimensional time developing mixing layer.

In this chapter we generalize the method of contour dynamics to vortex rings in the hope that it may play a similar role in providing insight for axisymmetric flow that contour dynamics has for planar flows. The extension to axisymmetric flow provides the possibility of expanding the repertoire of possible vortex behavior by allowing an important effect lacking in planar flow, namely vortex stretching. It is expected and demonstrated in Chapter 5 that vortex stretching, which inevitably arises when vortices interact, leads to qualitatively different behavior than one finds in two dimensions. In particular, we will see that the energetics of stretching necessitates the generation of smaller scales in vortex ring collisions.

In §3.2 we give a derivation of the evolution equations for the case in which ω_ϕ/σ (the ratio of vorticity to cylindrical radius) is constant within each vorticity region. This form of the vorticity has been studied for over a century; the focus has mainly been on steadily translating core shapes and interacting rings in the limit of thin cores and large separations in which core dynamics is neglected. That work was reviewed in more detail in §§2.7 and 2.8.

In §3.3 we discuss the numerical implementation of the algorithm. Care is required to maintain accuracy; we stress proper handling of the local contribution to the velocity field resulting from those portions of the contour which neighbor the point at which the velocity is evaluated. In §3.4 we verify the accuracy and convergence of the numerical scheme.

Finally, in §3.5 we present a qualitative illustration of the method for the behavior of an annular vortex layer.

During the course of this work, Pozrikidis (1986) independently developed a contour dynamics algorithm for axisymmetric flow. We will remark on the significant differences between the two formulations where appropriate.

Before proceeding to the axisymmetric case, let us briefly review the contour dynamics formulation for two dimensions. Barotropic (or uniform density), incompressible ($\nabla \cdot \mathbf{u} = 0$) and inviscid flow is governed by:

$$\frac{D\omega_z}{Dt} \equiv \frac{\partial\omega_z}{\partial t} + \mathbf{u} \cdot \nabla\omega_z = 0, \quad (3.1.1a)$$

$$\omega_z \hat{\mathbf{z}} = \nabla \times \mathbf{u}. \quad (3.1.1b)$$

The first equation expresses the fact that vorticity is convected with the fluid. Hence piecewise uniform vorticity remains so, and only the boundaries between regions have to be tracked as they follow the fluid. To obtain the velocity take the curl of (3.1.1b) and use incompressibility ($\nabla \cdot \mathbf{u} = 0$):

$$\nabla^2 \mathbf{u} = \hat{\mathbf{z}} \times \nabla\omega_z. \quad (3.1.2)$$

For free space, this has the solution

$$\mathbf{u}(\mathbf{x}) = \frac{1}{2\pi} \int (\hat{\mathbf{z}} \times \nabla\omega_z) \log |\mathbf{x} - \mathbf{x}'| d\mathbf{x}'. \quad (3.1.3)$$

The gradient for piecewise constant vorticity is a Dirac δ concentrated on the boundary and points in the direction $\hat{\mathbf{n}}$ normal to it (choose either sense). Denote by ω_o and ω_1 the value of the vorticity towards the positive and negative normal directions, respectively. Divide up the interfaces into pieces c_i across which the jump in vorticity, $[\omega_z]_i \equiv \omega_o - \omega_1$, is uniform. Then after integration with respect to the normal direction (3.1.3) becomes

$$\mathbf{u}(\mathbf{x}) = \frac{1}{2\pi} \sum_i [\omega_z]_i \int_{c_i} \hat{\mathbf{t}}(s) \log |\mathbf{x} - \mathbf{x}'(s)| ds, \quad (3.1.4)$$

where $\hat{\mathbf{t}} \equiv \hat{\mathbf{z}} \times \hat{\mathbf{n}}$ is the unit tangent.

For numerical implementation each c_i is represented by a discrete set of node points which are usually convected as material particles. For flows in which the fluid velocity is dominated by the component tangent to the boundary, shape changes are slow yet the former scheme requires that the time step be some fraction of the

period of revolution of a particle. In such cases it is better to evolve node points by the component of velocity normal to the boundary, however, the projection of the velocity on to the normal may be inaccurate if the boundary is not defined sufficiently smoothly. Two other choices have to be made: the interpolation scheme to obtain $\mathbf{x}'(s)$ between node points and the quadrature rule to compute the integral over the interpolated boundary. Item (2) in Appendix 3.C provides several references that discuss numerical procedures, including higher order schemes and specialized techniques for obtaining steady solutions. If he or she wishes, the reader can quickly begin experimenting with linear interpolation; in this case the contribution, from each linear segment can be obtained exactly. To this end it is convenient to write (3.1.4) in complex notation (and to use complex arithmetic on the computer):

$$u(z) + iv(z) = \frac{1}{2\pi} \sum_i [\omega_z]_i \int_{c_i} \Re \{ \log(z - z') \} dz'. \quad (3.1.5)$$

The contribution, say $L_m(z)$, to the line integral from a segment defined by

$$\begin{aligned} z' &= z_m + \xi \Delta z_m, \quad 0 \leq \xi \leq 1, \\ \Delta z_m &\equiv z_{m+1} - z_m, \end{aligned} \quad (3.1.6)$$

is

$$\begin{aligned} L_m(z) &\equiv \Delta z_m \Re \left\{ \int_0^1 \log(z - z_m - \xi \Delta z_m) d\xi \right\} \\ &= \Delta z_m \Re \left\{ \frac{1}{\Delta z_m} [(z_{m+1} - z) \log(z - z_{m+1}) + (z - z_m) \log(z - z_m)] - 1 \right\}. \end{aligned} \quad (3.1.7)$$

3.2. Axisymmetric contour dynamics formulation

In this section we derive the equations of motion for contours which bound regions in which the vorticity is a linear function of the cylindrical radius, σ . The reason for using this distribution will be explained below.

Consider cylindrical polar coordinates (x, σ, ϕ) as shown in Figure 3.1; x and σ measure distance along and normal to the axis of symmetry respectively and ϕ is the azimuthal angle. Let the vorticity ω be entirely azimuthal and independent of ϕ :

$$\omega = (0, 0, \omega_\phi(x, \sigma)). \quad (3.2.1)$$

The velocity field is

$$\mathbf{u} = (u_x(\mathbf{x}, \sigma), u_\sigma(\mathbf{x}, \sigma), 0). \quad (3.2.2)$$

Then for inviscid and incompressible flow of constant density the vorticity obeys the dynamical equation (Batchelor 1973, p. 508)

$$\frac{D(\omega_\phi/\sigma)}{Dt} = 0. \quad (3.2.3)$$

The inclusion of the metric σ in (3.2.3) is a consequence of the fact that a circular vortex line which moves from a radius σ_1 to a radius σ_2 undergoes a change in vorticity proportional to σ_2/σ_1 , i.e. according to the relative change in its circumference. If, in some region \mathcal{D} , we initially have

$$\omega_\phi = \mathcal{A}\sigma, \quad (3.2.4)$$

where \mathcal{A} is a constant for the region, then this distribution is maintained for all time. Then to solve (3.2.3) it is necessary to follow only the interfaces between such regions which are advected according to the local fluid velocity.

We now seek a representation of the velocity field in terms of line integrals along the generators of the bounding surfaces of the vortical regions. Several vortex structures may be present and there may be several nested regions within each structure, but, for brevity of the presentation and notation we will only consider the case of a single contour. Nested regions can be treated by superposition. A kinematic relation between the velocity and vorticity is the Poisson equation

$$\nabla^2 \mathbf{u} = -\nabla \times \boldsymbol{\omega}, \quad (3.2.5)$$

whose inversion for an unbounded fluid yields the Biot-Savart expression

$$\mathbf{u}(\mathbf{x}) = \frac{1}{4\pi} \int_{\mathcal{D}} \frac{\nabla \times \boldsymbol{\omega}(\mathbf{x}')}{\Delta} d\mathbf{x}'. \quad (3.2.6)$$

Here, $\Delta \equiv |\mathbf{x} - \mathbf{x}'|$ is the distance between the source and field points. In his numerical study of steadily translating rings, Norbury (1973) used a formulation based on the Stokes streamfunction which is more convenient than a velocity formulation for calculating steady shapes. Reduction to contour integrals was not made and this necessitated costly plane quadratures. In Appendix 3.B we obtain this reduction for the Stokes streamfunction which might prove useful in studying steady solutions more complicated than the Norbury-Fraenkel (NF) family including ones with nested regions.

For future use we note that in cylindrical polar coordinates

$$\begin{aligned}\Delta^2 &= A - B \cos(\phi - \phi'), \\ A &\equiv (x - x')^2 + \sigma^2 + \sigma'^2, \quad B \equiv 2\sigma\sigma'.\end{aligned}\tag{3.2.7}$$

For an axisymmetric distribution of vorticity $\omega_\phi = \omega_\phi(x, \sigma)$, $\omega_x = \omega_\sigma = 0$, the curl of the vorticity which appears in the integrand of (3.2.6) is

$$\nabla \times \boldsymbol{\omega}(\mathbf{x}) = \frac{1}{\sigma} \frac{\partial(\omega_\phi \sigma)}{\partial \sigma} \hat{\mathbf{x}} - \frac{\partial \omega_\phi}{\partial x} \hat{\boldsymbol{\sigma}}.\tag{3.2.8}$$

The vorticity suffers jumps at the boundary of the vortical region so the derivatives above must be interpreted in the sense of distributions. In two-dimensional flow with uniform vorticity, $\nabla \times \boldsymbol{\omega}$ is non-zero only where jumps in vorticity occur and so a formulation in terms of contour integrals is almost immediate. In the present situation $\nabla \times \boldsymbol{\omega} = 2\mathcal{A} \hat{\mathbf{x}}$ inside \mathcal{D} and a Dirac δ "function" concentrated on the boundary, $\partial\mathcal{D}$, due to the discontinuity. Hence, it is convenient to decompose the velocity field, as given by (3.2.6), into a contribution due to the continuous vorticity distribution and another due to the jump across the interface:

$$\mathbf{u} = \mathbf{u}_c + \mathbf{u}_j.\tag{3.2.9}$$

3.2.1. *Jump contribution to the velocity field*

One way of obtaining \mathbf{u}_j is to evaluate the Biot-Savart integral over a shell of thickness 2ε surrounding $\partial\mathcal{D}$ and then pass to the limit of zero ε . This is best accomplished by transforming to an orthogonal surface oriented coordinate system (n, s, ϕ) as shown in Figure 3.2. To ensure unit metrics let n and s measure arc length along the respective coordinate lines. The metric for the ϕ coordinate lines is σ . If θ is the angle, with respect to the axis of symmetry, of the normal direction, then these coordinates are described by the transformation

$$\begin{pmatrix} dn \\ ds \\ d\phi \end{pmatrix} = \begin{pmatrix} \cos \theta(s, n) & \sin \theta(s, n) & 0 \\ -\sin \theta(s, n) & \cos \theta(s, n) & 0 \\ 0 & 0 & 1 \end{pmatrix} \begin{pmatrix} dx \\ d\sigma \\ d\phi \end{pmatrix}.\tag{3.2.10}$$

On the surface of the vortex, $n = 0$, one has $\theta(s, n) = \theta(s)$, the orientation of the outward pointing normal relative to the axis of symmetry. Expressing (3.2.8) in this

system, we obtain

$$\begin{aligned} \nabla \times \boldsymbol{\omega}(\mathbf{x}) = & \left(\frac{\partial \omega_\phi}{\partial n} \sin \theta(s, n) + \frac{\partial \omega_\phi}{\partial s} \cos \theta(s, n) + \frac{\omega_\phi}{\sigma} \right) \hat{\mathbf{x}} \\ & - \left(\frac{\partial \omega_\phi}{\partial n} \cos \theta(s, n) - \frac{\partial \omega_\phi}{\partial s} \sin \theta(s, n) \right) \hat{\boldsymbol{\sigma}}. \end{aligned} \quad (3.2.11)$$

Upon insertion of this expression into the Biot-Savart equation (3.2.6), the contributions of the tangential derivatives, being finite, vanish in the limit as ε tends to zero, as will the last term in the first parenthesis. This leaves only normal derivatives of the vorticity; each becomes the jump in vorticity, $-\mathcal{A}\sigma'$, after integration over the direction normal to the surface. Thus we are left with

$$\mathbf{u}_j = \frac{\mathcal{A}}{4\pi} \oint_c \sigma'^2 d\sigma' \int_0^{2\pi} \frac{-\sin \theta' \hat{\mathbf{x}} + \cos \theta' \hat{\boldsymbol{\sigma}}'}{\Delta} d\phi', \quad (3.2.12)$$

where the contour c is the generator of the surface in the meridional plane. The numerator of the inner integrand is the unit vector tangent to the surface in this plane. The unit vector $\hat{\boldsymbol{\sigma}}'$ in the radial direction depends on the integration variable and must be retained inside the integration ($\hat{\boldsymbol{\sigma}}' = \cos \phi' \hat{\mathbf{y}} + \sin \phi' \hat{\mathbf{z}}$ from Figure 3.1). Substituting this into (3.2.12), choosing to evaluate the velocity on the xy plane ($\phi = 0$), and identifying $\hat{\mathbf{y}}$ with $\hat{\boldsymbol{\sigma}}$ on this plane, gives

$$\mathbf{u}_j = \mathcal{A} \oint_c \mathbf{K}_1(s') ds', \quad (3.2.13)$$

where

$$\begin{aligned} \mathbf{K}_1(s') &= \sigma' [-G(s') \sin \theta' \hat{\mathbf{x}} + H(s') \cos \theta' \hat{\boldsymbol{\sigma}}], \\ G(s') &= \frac{\sigma'}{4\pi} \int_0^{2\pi} \frac{1}{\Delta} d\phi', \quad H(s') = \frac{\sigma'}{4\pi} \int_0^{2\pi} \frac{\cos \phi'}{\Delta} d\phi'. \end{aligned} \quad (3.2.14)$$

The integrals G and H are (Gradshteyn & Ryzhik 2.571.4; Bierens De Haan, Table 68, item 25, respectively)

$$\begin{aligned} G(s') &= \frac{\sigma'}{\pi \sqrt{A+B}} K(\bar{r}), \\ H(s') &= \frac{1}{2\pi\sigma} \left(\frac{A}{\sqrt{A+B}} K(\bar{r}) - E(\bar{r}) \sqrt{A+B} \right), \\ \bar{r} &\equiv \sqrt{\frac{2B}{A+B}}, \end{aligned} \quad (3.2.15)$$

in which K and E are the complete elliptic integrals of the first and second kind respectively, \bar{r} is their modulus and A and B are defined in (3.2.7).

3.2.2. Contribution due to the continuous part of the vorticity

After substituting the fact that $\nabla \times \boldsymbol{\omega} = 2\mathcal{A} \hat{\mathbf{x}}$ inside \mathcal{D} into the Biot-Savart expression (3.2.6) one obtains

$$\mathbf{u}_c = \left(\frac{\mathcal{A}}{2\pi} \int_{\mathcal{D}} \frac{1}{\Delta} d\mathbf{x}' \right) \hat{\mathbf{x}}. \quad (3.2.16)$$

The volume integral is transformed to a surface integral by use of Green's second identity:

$$\int_{\mathcal{D}} [\psi \nabla^2 \varphi - \varphi \nabla^2 \psi] d\mathbf{x}' = \int_{\partial \mathcal{D}} [\psi \text{grad } \varphi - \varphi \text{grad } \psi] \cdot \hat{\mathbf{n}}' dS. \quad (3.2.17)$$

Choosing $\psi = 1$ and $\varphi = (1/2)\Delta$ we find that $\nabla^2 \varphi = 1/\Delta$ where the Laplacian is taken with respect to the source point. Thus we obtain

$$\mathbf{u}_c = \left(\frac{\mathcal{A}}{4\pi} \int_{\partial \mathcal{D}} \text{grad } \Delta \cdot \hat{\mathbf{n}}' dS \right) \hat{\mathbf{x}}. \quad (3.2.18)$$

The use of Green's identity is valid provided $\nabla^2 \varphi = 1/\Delta$ is regular. This holds for field points exterior to \mathcal{D} but fails otherwise. However one can apply the identity to a region which excludes a spherical region of radius ϵ about the singularity for interior field points and excludes a similar hemispherical region for field points on the surface. It can then be shown that the volume and surface integrals arising from the excluded region vanish in both cases as $\epsilon \rightarrow 0$. This renders (3.2.18) valid everywhere in the flow domain.

For an axisymmetric surface the integrand in (3.2.18) can be simplified as follows. First, write the quantity $\text{grad } \Delta$ in Cartesian coordinates.

$$\text{grad } \Delta = -\frac{1}{\Delta} [(x - x') \hat{\mathbf{x}} + (y - y') \hat{\mathbf{y}} + (z - z') \hat{\mathbf{z}}]. \quad (3.2.19)$$

Next put $y = \sigma$ and $z = 0$, our previous choice of the azimuthal location of the field point, $y' = \sigma' \cos \phi'$ and $z' = \sigma' \sin \phi'$. From Figure 3.2, we observe that the normal vector can be expressed as

$$\begin{aligned} \hat{\mathbf{n}}' &= \cos \theta' \hat{\mathbf{x}} + \sin \theta' \hat{\boldsymbol{\sigma}}' \\ &= \cos \theta' \hat{\mathbf{x}} + \sin \theta' \cos \phi' \hat{\mathbf{y}} + \sin \theta' \sin \phi' \hat{\mathbf{z}}. \end{aligned} \quad (3.2.20)$$

Substituting (3.2.19) and (3.2.20) into (3.2.18) and expressing the resulting integral in terms of the quantities, G and H defined previously we obtain

$$\mathbf{u}_c = \mathcal{A} \oint_c \mathbf{K}_2(s') ds', \quad (3.2.21)$$

where

$$\mathbf{K}_2(s') = \{G(s')[(x' - x) \cos \theta' + \sigma' \sin \theta'] - H(s')\sigma \sin \theta'\} \hat{\mathbf{x}}. \quad (3.2.22)$$

3.2.3. Summary of the formulation

Finally, combining the two contributions to the velocity field and invoking the dynamical fact that the boundary is convected with the fluid, the contour dynamics formulation for axisymmetric flow reads

$$\frac{d\mathbf{x}(s)}{dt} = \mathcal{A} \oint_c \mathbf{K}(s') ds', \quad (3.2.23)$$

where

$$\mathbf{K}(s') = [(x' - x)G(s') \cos \theta' - \sigma H(s') \sin \theta'] \hat{\mathbf{x}} + \sigma' H(s') \cos \theta' \hat{\boldsymbol{\sigma}}. \quad (3.2.24)$$

The formulation of Pozrikidis (1986) differs from ours in the following respects. The radial component of the velocity arises from the jump contribution only. For it, Pozrikidis' formulation is analogous to ours and the two-dimensional case. The difference lies in the treatment of the axial component of the velocity. Pozrikidis expresses the velocity potential external to the vortex as an integral over the core of the potential due an elemental vortex filament, which can be written in terms of elliptic integrals of the third kind. To obtain the axial velocity this expression is differentiated with respect to x and Green's theorem in the plane is used to secure a contour integral for the velocity. Because the formulation relies on a velocity potential a branch cut needs to be introduced to make it single valued. His final expression involves the elliptic integral of the third kind which can be written in terms of complete and incomplete elliptic integrals of the first and second kind. The latter can be computed iteratively. The present formulation is in terms of the complete elliptic integrals which are calculated explicitly by a log-polynomial approximation.

3.3. Numerical implementation

Equation (3.2.23) is a non-linear integro-differential equation for motion of the boundaries of the vortex cores. For numerical purposes, the contours are represented

by a discrete set of node points which are convected as material particles. The integrals are approximated by connecting the points with straight line segments. In the planar case, the segment integrals are carried out in closed form. However, quadrature is sometimes used to save computing time. This requires that the singularity be removed with integration by parts. In the axisymmetric case, neither of these approaches is possible. Instead just the contribution to the integrals from segments not adjacent to the field point is evaluated by two-point Gaussian quadrature. The elliptic integrals are calculated using the approximations of Cody (1965); the formula which is accurate to 10^{-8} is being used. Due to the logarithmic singularity of the integrand as the modulus $\bar{r} \rightarrow 1$, the contribution from segments neighboring the field point is evaluated by expanding the terms in (3.2.24) in a series of powers and logarithms about the singularity along an adjacent segment. This series is then integrated exactly term by term. The expansions obtained using MACSYMA have the form

$$K(\xi) = P_1^J(\xi) + P_2^J(\xi) \log\left(\frac{8\xi}{l}\right), \quad (3.3.1)$$

where P_i^J denotes a polynomial of degree J with vector coefficients, l is the length of the segment and ξ is a parameter along the segment such that $0 \leq \xi \leq l$. The coefficients of the polynomials depend upon the segment geometry and are listed in Appendix 3.A.

To assess the number of terms in the expansion necessary for accuracy and to check the analysis we compared the values of the integrand for several J against the kernels obtained using the approximations of Cody. This comparison is meaningful because Cody's expressions have the proper analytic behavior of the elliptic integrals in the limits $\bar{r} \rightarrow 0$ and $\bar{r} \rightarrow 1$. For example Figure 3.3 shows the approximations for the case of a segment for Hill's vortex spanning an arc between polar angles $\vartheta = 25^\circ$ and $\vartheta = 75^\circ$ measured from the forward stagnation point. This length is much larger than any we used in the simulations yet the representation using five terms is accurate throughout the segment.

Figure 3.4 compares the exact and computed axial velocity on the surface of Hill's vortex using only 15 segments of identical length. It serves as a check of the overall formulation and underscores the care with which the logarithmic contribution to the velocity must be treated. The results are excellent, the error at the point of maximum velocity being 4%. The dashed curve shows the result obtained when the

contribution of adjacent segments is deleted. One observes that away from the axis the contribution from adjacent segments is substantial.

There is a standard approach for treating singular kernels which arise frequently in potential theory (see for example the book by Jawson & Symm 1977). This technique was adopted by Pozrikidis (1986). Here, one subtracts out just the singular part of the kernel. In our formulation this would be the constant term in $P_2^N(\xi)$ times the log term. The contribution of this term over the entire contour may then be computed exactly for the segment or circular arc discretization. This contribution is then added to the result of the non-singular integration. In order to also accurately integrate terms like $\xi \log \xi$, $\xi^2 \log \xi$ etc near the singularity which cannot be integrated accurately enough with polynomial quadrature rules, we chose not to follow this approach. Rather we exactly integrate terms up to $\xi^4 \log \xi$.

The time integration was performed using the fourth order Runge-Kutta scheme. In initial tests it was found that too large a time step resulted in a shrinking volume of vortical fluid. The time step Δt was chosen to satisfy

$$\Omega \Delta t < \epsilon, \quad (3.3.2)$$

where Ω is half the vorticity at the center of the core and represents the magnitude of the eigenvalues of the ODE system for a particle undergoing solid body rotation at angular velocity Ω . Numerical tests indicated that a constraint in volume change of $\Delta V/V < 0.01\%$ over one eddy turnover period dictated that $\epsilon < 0.05$.

The program halves the length of segments which have stretched beyond a specified tolerance (currently $0.016L_o$) and removes nodes when segments become too short ($< 0.004L_o$) provided the curvature is sufficiently small. Here L_o is the initial mean toroidal radius of the vortex rings. It is also essential that the length of segments close to the axis of symmetry be kept proportional to the distance of the segment from the axis. This is because the expansion of the elliptic integrals proceeds in powers and logarithms of the complementary modulus, $r^* = \sqrt{1 - \bar{r}^2}$ (see Appendix 3.A). Now, the first term in the expansion for r^* itself is proportional to $(l/\sigma)\xi$ so we want $l/\sigma = \mathcal{O}(1)$ or better. The node insertion routine ensures that $l/\sigma < 0.15$ if this condition is more stringent than previous criteria.

The amount of insight that one may obtain from a contour dynamics run and ones confidence in it are increased by extensive diagnostics. To gauge the accuracy of a calculation we monitor the flow invariants: volume, circulation, impulse and

energy together with its radial spectrum. The overall motion of the vortices was obtained by calculating the positions of the centroids of the core shape and of the vorticity distribution. Their corresponding time-rates were also monitored. It is not enough to merely visually observe the core shape. This remark also applies to vortex calculations via finite difference or spectral methods. Even very weak strains caused by the presence of another vortex result in the excitation of small but complex deformation modes. Hence the overall features of the core deformation were obtained by fitting an ellipse to the core shape. The dimensions and orientation of the ellipse are related to the eigenvalues and eigenvectors of the matrix of second order moments.

3.4. Test of accuracy and convergence

Figure 3.5 shows the convergence in the discrete L^2 norm of the axial and radial velocity as a function of the number of segments in the case of Hill's vortex. The slope is close to -2 , consistent with the second order accuracy of the segment discretization. There is a slight decrease in the slope as we approach machine round-off (single precision on a VAX for this test). This represents a static test of the algorithm. A good dynamic test (suggested to us by Prof. Zabusky) is to ensure that for Norbury's (1973) equilibrium shapes, the core remains steady up to the accuracy of the Fourier coefficients in his paper. Adopting the mean toroidal radius L_o as a reference length, we specify the boundary by

$$\frac{\varrho(\beta)}{L_o} = \hat{a}_o + \sum_{j=1}^J (\hat{a}_j \cos j\beta + \hat{b}_j \sin j\beta). \quad (3.4.1)$$

The initial shapes are symmetric in x , about $x = 0$ say, ϱ is measured from the point $x = 0$, $\sigma = L_o$ and β runs counterclockwise from the point of maximum σ on the line $x = 0$. We studied the excursions of the coefficients from the values supplied by Norbury for the duration of three revolutions of a particle on the boundary for an $\alpha = 0.6$ vortex. Here α is the ratio of area-effective core radius ($\sqrt{\text{Area}/\pi}$) to L_o . The observed deviations must have two parts. The first reflects inherent unsteadiness due to errors in the initial shape; a 'cautious' estimate of the error in the initial coefficients is ± 0.0001 according to Norbury. The second is due to inaccuracies in the present method; runs with 200, 400, 800, and 1200 segments were made to check

that it converged to zero. An overall measure of the departure from the initial shape is the quantity

$$\text{rms deviation} = \left(2(\delta\hat{a}_0)^2 + \sum_{j=1}^J (\delta\hat{a}_j)^2 + (\delta\hat{b}_j)^2 \right)^{1/2}, \quad (3.4.2)$$

which is equal, by Parseval's identity, to

$$\left(\frac{1}{\pi L_o^2} \int_0^{2\pi} (\delta\varrho(\beta))^2 d\beta \right)^{1/2}, \quad (3.4.3)$$

where δ signifies the difference from the Norbury value and $J = 11$, the number of coefficients furnished by Norbury.

The results are shown in Figure 3.6. Time has been normalized using L_o and the translation speed U_o . By 1200 segments the behavior has visually converged and nearly repeats every particle revolution; individual coefficients exhibit the same periodicity. A small but otherwise arbitrary disturbance on a two-dimensional circular vortex with uniform vorticity is also periodic according to Kelvin's analysis because the period of particle revolution is an integer multiple of the period required for any Fourier mode to advance one wavelength. A power law fit to the rms deviations at the last instant produced an order of convergence of 2.3, consistent with the segment discretization. The amplitude of the rms deviation for 1200 nodes is less than that obtained by applying Norbury's bound to every coefficient. The maximum variation was observed in \hat{a}_2 with an amplitude of 0.00008, close to Norbury's estimate.

3.5. A qualitative illustration

As a qualitative illustration of the method, we simulated a Hill's spherical vortex with a region of vortical fluid removed. The removed region has as its initial boundary, one of the interior streamsurfaces of Hill's vortex. The time evolution is shown in Figure 3.7 where the shading indicates the vorticity containing region. Time \hat{t} has been normalized using the mean toroidal radius and speed of translation of a Hill's vortex without the hole. A violent instability occurs during the time that the centroid of the outer boundary has propagated $2\frac{1}{2}$ radii. Irrotational fluid pushes through the rear, forming a thin cap. The vortex layer at the outer radii thickens in spots as it rolls-up. This illustrates that distinct vortex patches can form from vortex layers by

a fast convective action without the intervention of the mechanisms of roll-up into a spiral followed by viscous smoothing across the turns of the spiral. A direct and detailed study of this phenomenon for two-dimensional layers was made by Shelley (1985, private communication) who was also the first to observe it. The final state in Figure 3.7 is composed of patches connected by thin sheets and a distorted region of vorticity. The total number of node points increased from 400 to 806 during the calculation. Up to the third frame, the circulation and impulse decreased by 0.1% but subsequently more inaccuracy resulted from the closeness of non-adjacent nodes. The integrand behaves logarithmically and polynomial quadrature is no longer accurate. Accurate computation of the integrals requires that the distance between quadrature points be smaller than the distance between non-adjacent nodes. At the last frame, these invariants have decreased by 1%.

Appendix 3.A. Contribution to the induced velocity from adjacent segments

The purpose of this appendix is to obtain the contribution to the velocity at a given node point from segments which are adjacent to it. We proceed by expanding the kernel $K(s')$ in a series of powers and logarithms. The series is then integrated exactly term by term.

Let the field point be the n th node located at (x_n, σ_n) . Let (l_x, l_σ) be the axial and radial components of the vector with length l , pointing in the direction of integration along the forward adjacent segment. Then along this segment we have

$$x' = x_n + \xi l_x, \quad \sigma' = \sigma_n + \xi l_\sigma, \quad (3.A.1)$$

where ξ is a parameter which runs from 0 to 1 on the segment. The quantities A and B defined in (3.2.7), are along the segment

$$A = f\xi^2 + p\xi + q, \quad B = p\xi + q, \quad (3.A.2)$$

where

$$f = l^2, \quad p = 2\sigma_n l_\sigma, \quad q = 2\sigma_n^2. \quad (3.A.3)$$

The coefficients f , p and q above are functions of the segment geometry and the expansions of the kernels depend only on them. The contribution to the velocity at the n th node due to the segment is

$$\begin{aligned}\Delta u_\sigma &= \mathcal{A} l_\sigma \int_0^1 \sigma' H d\xi, \\ \Delta u_x &= \mathcal{A} \left[-l_\sigma \int_0^1 (x_n - x') G + l_x \int_0^1 \sigma_n H d\xi \right].\end{aligned}\tag{3.A.4}$$

We provide expansions for each of the integrands which appears above. They are obtained with the aid of the expansions of the elliptic functions $K(\bar{r})$ and $E(\bar{r})$ about $\bar{r} = 1$ given in Byrd & Friedmann (1971). We write these out up to

$$\mathcal{O} \left[\log \left(\frac{4}{r^*} \right) r^{*4} \right],\tag{3.A.5}$$

where r^* is the complementary modulus $\sqrt{1 - \bar{r}^2}$. The leading term in the expansion of r^* is $\mathcal{O}(\xi)$ so for consistency the highest power in ξ that may be retained in any term is four. Each of the kernels in (3.A.4) assumes the following form

$$C \left[\log \left(\frac{8\sigma_n}{l\xi} \right) \sum_{j=0}^J c_j \xi^j + \sum_{j=0}^J c'_j \xi^j \right].\tag{3.A.6}$$

For $\sigma' H$ and $\sigma_n H$, $J = 4$ but for $(x - x') G$ it is consistent to go up to $J = 5$. Each of the coefficients in (3.A.6) has the structure

$$\begin{aligned}c_j &= a_j l_\sigma + b_j \sigma_n, \\ c'_j &= a'_j l_\sigma + b'_j \sigma_n.\end{aligned}\tag{3.A.7}$$

The following combination of terms recur often so it is convenient to define them at the outset.

$$\begin{aligned}T_1 &= fpq^2, & T_2 &= p^3q, & T_3 &= f^2q^2, \\ T_4 &= fp^2q, & T_5 &= p^4, & T_6 &= fq^3, \\ T_7 &= p^2q^2, & T_8 &= pq^3, & T_9 &= q^4.\end{aligned}\tag{3.A.8}$$

For $\sigma'H$, $J = 4$ and

$$\begin{aligned}
a_4 &= 288T_1 - 96T_2, & b_4 &= 90T_3 - 216T_4 + 60T_5, \\
a'_4 &= -384T_1 + 224T_2, & b'_4 &= -93T_3 + 360T_4 - 152T_5, \\
a_3 &= -576T_6 + 192T_7, & b_3 &= a_4, \\
a'_3 &= 192T_6 - 384T_7, & b'_3 &= a'_4, \\
a_2 &= -768T_8, & b_2 &= a_3, \\
a'_2 &= -a_2, & b'_2 &= a'_3, \\
a_1 &= -1536T_9, & b_1 &= a_2, \\
a'_1 &= 3072T_9, & b'_1 &= a'_2, \\
a_0 &= 0, & b_0 &= a_1, \\
a'_0 &= 0, & b'_0 &= a'_1, \\
C &= -\frac{1}{2\pi} \frac{1}{1536q^4}.
\end{aligned} \tag{3.A.9}$$

After the entries for $\sigma'H$ have been generated, to obtain the corresponding entries for $\sigma_n H$ simply zero out the a_j and a'_j above.

For $(x_n - x')G$, $J = 5$ and

$$\begin{aligned}
a_5 &= 288T_1 - 480T_2 & b_5 &= 54T_3 - 360T_4 + 420T_5 \\
a'_5 &= -384T_1 + 736T_2 & b'_5 &= -63T_3 + 552T_4 - 704T_5 \\
a_4 &= -192T_6 + 576T_7 & b_4 &= a_5 \\
a'_4 &= 192T_6 - 768T_7 & b'_4 &= a'_5 \\
a_3 &= -768T_8 & b_3 &= a_4 \\
a'_3 &= -a_3 & b'_3 &= a'_4 \\
a_2 &= 1536T_9 & b_2 &= a_3 \\
a'_2 &= 0 & b'_2 &= a'_3 \\
a_1 &= 0 & b_1 &= a_2 \\
a'_1 &= 0 & b'_1 &= 0 \\
a_0 &= 0 & b_0 &= 0 \\
a'_0 &= 0 & b'_0 &= 0 \\
C &= -\frac{1}{2\pi} \frac{t_x \sigma_n}{768q^5}
\end{aligned} \tag{3.A.10}$$

Finally, each integral is obtained by integrating (3.A.6) for $0 \leq \xi \leq 1$:

$$C \left\{ \log \left(\frac{8\sigma_n}{l} \right) \sum_{j=0}^J \frac{c_j}{j+1} + \left[\sum_{j=0}^J \frac{c_j}{(j+1)^2} + \frac{c'_j}{j+1} \right] \right\}. \tag{3.A.11}$$

For the segment behind the node, if $(\bar{l}_x, \bar{l}_\sigma)$ are its components (in the direction of integration) then the expansions are identical except that $(-\bar{l}_x, -\bar{l}_\sigma)$ replace (l_x, l_σ) in forming f, p and q .

Appendix 3.B. Contour formulation for the streamfunction

An expression for the velocity field has been derived in terms of contour integrals. We now attempt to do the same for the Stokes streamfunction, ψ .

In calculating the shapes of steadily translating vortex rings, the condition that the streamfunction be constant on the surface of the vortex (in a steadily translating frame whose velocity is determined as part of the solution) is easier and more accurate to impose than one requiring that the velocity be tangent to the surface. Using the formulation one could compute the Prandtl-Batchelor eddy behind an axisymmetric body or calculate steady shapes more complicated than the NF family, for example rings with nested contours. In his work, Norbury (1973) did not have available a contour formulation for the streamfunction and this necessitated costly and less accurate plane quadratures for the solution of the integral equation for steadily translating rings.

The vector potential, \mathbf{A} is defined as

$$\mathbf{u} = \nabla \times \mathbf{A}, \quad (3.B.1)$$

$$\nabla \cdot \mathbf{A} = 0. \quad (3.B.2)$$

Given a certain \mathbf{u} , \mathbf{A} is defined up to the gradient of a scalar function. The condition (3.B.2) is a convenient choice that makes \mathbf{A} unique. Writing (3.B.1) in cylindrical coordinates and comparing it with the definition of the Stokes streamfunction one finds

$$\psi = \sigma A_\phi. \quad (3.B.3)$$

Hence it is enough to calculate the vector potential. Equations (3.B.1) and (3.B.2) together imply

$$\nabla^2 \mathbf{A} = -\boldsymbol{\omega}, \quad (3.B.4)$$

whose solution for an unbounded fluid is

$$\mathbf{A} = \frac{1}{4\pi} \int_{\mathcal{D}} \frac{\boldsymbol{\omega}(\mathbf{x}')}{\Delta} d\mathbf{x}', \quad (3.B.5)$$

where \mathcal{D} is the vorticity containing region. The goal is to transform this equation into a form in which the integrand is concentrated on the boundary. First, as noted previously $1/\Delta = \nabla^2 Q$ where $Q = (1/2)\Delta$ so that

$$\mathbf{A} = \frac{1}{4\pi} \int_{\mathcal{D}} \boldsymbol{\omega}(\mathbf{x}') \nabla^2 Q d\mathbf{x}'. \quad (3.B.6)$$

Next, applying Green's second identity for any region $\mathcal{D}+$ containing \mathcal{D} in order to make boundary terms vanish leads to the desired form:

$$\int_{\mathcal{D}+} \omega(\mathbf{x}') \nabla^2 Q \, d\mathbf{x}' = \int_{\mathcal{D}+} Q \nabla^2 \omega(\mathbf{x}') \, d\mathbf{x}'. \quad (3.B.7)$$

Decompose the right hand side into two parts, one for the interior of $\mathcal{D}+$ and another for a thin shell of width 2ε which surrounds $\partial\mathcal{D}$. Then take the limit as $\varepsilon \rightarrow 0$. The first part vanishes because the Laplacian of the linear vorticity is zero.*

To work out the second part, introduce orthogonal curvilinear coordinates (n, s, ϕ) such that the surfaces $n = -\varepsilon, 0, \varepsilon$ coincide with the inner boundary of the shell, the surface of the vortex and the outer boundary of the shell, respectively. If s and n are chosen to be the arc lengths on the lines along which they vary then the metrics are $(h_n, h_s, h_\phi) = (1, 1, \sigma)$. With these metrics the Laplacian becomes

$$\begin{aligned} \nabla^2 \omega(\mathbf{x}) &= \nabla^2 [\omega_\phi(s, n) \hat{\phi}] = \frac{\partial}{\partial n} \left[\frac{1}{\sigma} \frac{\partial(\sigma \omega_\phi)}{\partial n} \right] \hat{\phi} + \mathcal{O}(\varepsilon), \\ \hat{\phi} &= -\sin \phi \hat{\mathbf{y}} + \cos \phi \hat{\mathbf{z}}, \end{aligned} \quad (3.B.8)$$

where $\mathcal{O}(\varepsilon)$ denotes terms which disappear upon integration as $\varepsilon \rightarrow 0$. These arise from s derivatives of the vorticity. As before, let us choose the field point to be on the $\phi = 0$ plane where $A_\phi = A_z$ and $\Delta = \sqrt{A - B \cos \phi'}$ with A and B as defined in (3.2.7). Then

$$A_\phi(x, \sigma) = \frac{1}{8\pi} \lim_{\varepsilon \rightarrow 0} \int_0^{2\pi} d\phi' \cos \phi' \oint ds' \int_{-\varepsilon}^{+\varepsilon} dn' \sigma' \Delta \frac{\partial}{\partial n'} \left[\frac{1}{\sigma'} \frac{\partial(\sigma' \omega_\phi)}{\partial n'} \right]. \quad (3.B.9)$$

Denote the innermost integral by I_n . Applying integration by parts twice gives

$$I_n = \sigma' \Delta \left[\frac{\partial \omega_\phi}{\partial n'} \right]_{-\varepsilon}^{+\varepsilon} - \sigma' \frac{\partial \Delta}{\partial n'} [\omega_\phi]_{-\varepsilon}^{+\varepsilon} + \mathcal{O}(\varepsilon). \quad (3.B.10)$$

In the limit as $\varepsilon \rightarrow 0$

$$\begin{aligned} [\omega_\phi]_{-\varepsilon}^{+\varepsilon} &\rightarrow -A\sigma', \\ \left[\frac{\partial \omega_\phi}{\partial n'} \right]_{-\varepsilon}^{+\varepsilon} &\rightarrow -A \sin \theta'. \end{aligned} \quad (3.B.11)$$

* At this point, one might think that the formulation could be used to obtain steady vortex rings for more general vorticity distributions with vanishing Laplacian in \mathcal{D} . Such steady flows are called "controllable" by the Truesdell school of mechanics. Unfortunately, however, Marris & Aswani (1977) have provided a long and complicated proof that the only non-rectilinear controllable axisymmetric motions are those in which $\omega_\phi/\sigma = \text{constant}$.

Finally,

$$\psi(x, \sigma) = \frac{A\sigma}{8\pi} \oint ds' \left(\sigma'^2 \int_0^{2\pi} \frac{\partial \Delta}{\partial n'} \cos \phi' d\phi' - \sigma' \sin \theta' \int_0^{2\pi} \Delta \cos \phi' d\phi' \right). \quad (3.B.12)$$

The two integrals with respect to ϕ' can be expressed explicitly in terms of tabulated integrals denoted as I_1, I_2 and I_3 below. The first is obtained after substituting for $\partial \Delta / \partial n'$ from (3.2.19) and (3.2.20) and the second after an integration by parts:

$$\begin{aligned} \int_0^{2\pi} \frac{\partial \Delta}{\partial n'} \cos \phi' d\phi' &= 2[(x' - x)I_2 \cos \theta' - \sigma I_3 \sin \theta' + \sigma' I_2 \sin \theta'], \\ \int_0^{2\pi} \Delta \cos \phi' d\phi' &= B(I_3 - I_1), \end{aligned} \quad (3.B.13)$$

where

$$\begin{aligned} I_1 &\equiv \int_0^\pi \frac{d\phi'}{\sqrt{A - B \cos \phi'}} = \frac{2}{\sqrt{A + B}} K(\bar{r}), \\ I_2 &\equiv \int_0^\pi \frac{\cos \phi'}{\sqrt{A - B \cos \phi'}} d\phi' = \frac{2A}{B\sqrt{A + B}} K(\bar{r}) - \frac{2}{B} \sqrt{A + B} E(\bar{r}), \\ I_3 &\equiv \int_0^\pi \frac{\cos^2 \phi'}{\sqrt{A - B \cos \phi'}} d\phi' = \frac{2}{3B^2 \sqrt{A + B}} [(2A^2 + B^2)K(\bar{r}) - 2A(A + B)E(\bar{r})], \\ \bar{r} &= \sqrt{\frac{2B}{A + B}}. \end{aligned} \quad (3.B.14)$$

This formulation was checked numerically against the exact expression for Hill's spherical vortex given in Batchelor (1973, Equation 7.2.18) relative to a reference frame travelling with the vortex. For example, at the point where the streamfunction has a peak, the errors with 15, 30 and 60 segments were -2.4%, -0.61% and -0.15%, respectively, indicating the second order convergence of the segment discretization.

Appendix 3.C. Literature on two-dimensional patches of uniform vorticity

(1) *Reviews*

- Saffman (1982): Review of steady solutions including single patches, corotating pairs and arrays.
- Aref (1983): A general review of plane vortex motion, including patches of uniform vorticity.
- Melander, Overman & Zabusky (1987): Review of steady solutions, the elliptic model, axisymmetrization, convective merger and interactions between pairs.
- Saffman (1988): Brings Saffman (1982) up to date and includes an overview of three-dimensional instabilities.

(2) *Numerical procedures*

- Zabusky, Hughes & Roberts (1979): Contour dynamics algorithm.
- Saffman & Schatzman (1981, Appendix A): Comment on the formal infinite order accuracy achieved when using singularity subtraction and trapezoidal rule.
- Zabusky & Overman (1983): Filtering to allow longer time simulations.
- Wu, Overman & Zabusky (1984): Higher order discretization of the contour integral.
- Pozrikidis & Higdon (1985): Circular arc discretization.
- Meiron, Saffman & Schatzman (1984), Kamm (1987): Method of Schwarz functions.
- Dritschel (1988*b*): Contour surgery to allow long time simulations.
- Zou, Overman, Wu & Zabusky (1988): Curvature controlled initial node placement.

(3) *Isolated steadily rotating vortices*

(a) *m*-fold symmetric vortices

(i) $m = 2$

- Kirchhoff (see Lamb 1932, §159): Uniform ellipses.
- Love (1893): Stability of elliptical vortex.
- Dritschel (1988*f*): Steady states with multiple contours and their stability.

(ii) $m > 2$

- Kelvin (1880*b*, see in addition Lamb 1932, §158): Linear waves on a circular vortex.

- Deem & Zabusky (1978): First finite amplitude examples.
 - Su (1979): Analytic solution for small but finite deviation from circularity.
 - Burbea & Landau (1982): Steady shapes and linear stability.
 - Wu, Overman & Zabusky (1984): Steady shapes with local analysis and corrections to Burbea & Landau (1982) for shapes near the limiting members.
- (b) *Steadily rotating vortices not symmetric under rotation*
- Kamm (1987): Bifurcations from ellipses at points of stability exchange.
- (4) *Corotating configurations of n vortices (invariant under rotation by $2\pi/n$) and annular vortex layers*
- (a) $n = 2$
- Saffman & Szeto (1980): Steady shapes & Kelvin's energy stability argument.
 - Overman & Zabusky (1982b): Calculations of convective merger and transitions to ellipses.
 - Dritschel (1985): Steady shapes, linear stability and energetically compatible transitions to ellipses.
 - Melander, Zabusky & McWilliams (1988): Explicit criteria for convective merger using the elliptic model.
- (b) $n > 2$
- Thomson (1883), Havelock (1931): Point vortex limit including stability.
 - Dritschel (1985): Steady shapes for arbitrary area, linear stability and non-linear evolution.
- (c) *Annular layers*
- Baker (1980, p. 216): Linear stability of the sheet limit.
 - Snow (1978): Linear stability of finite layers.
 - Dritschel (1986): Non-linear development of perturbed finite layers and possible transitions to non-symmetric corotating configurations.
 - Dritschel (1988e): Stabilization of finite layers by adverse shear.
- (5) *Steadily translating counter rotating pairs*
- Sadovskii (1971): Calculation of limiting member.
 - Deem & Zabusky (1978): Calculation of intermediate member.

- Pierrehumbert (1980, 1981): Calculation of several members and corrigendum for limiting member, respectively.
- Saffman & Tanveer (1982): Analysis of the shape of the limiting member near the symmetry line.
- Wu, Overman & Zabusky (1984): Careful recomputation of several members and local analysis of limiting member.

(6) *Spatially periodic configurations*

(a) Finite thickness layers

- Rayleigh (1945, §367): Linear stability.
- Pullin (1981): Vorticity layer adjacent to a slip wall.
- Pozrikidis & Higdon (1985), Shelley (1985): Non-linear development of the Kelvin-Helmholtz instability for finite vortex layers.
- Dritschel (1988e): Stabilization by adverse shear.

(b) Single arrays (model of developed shear layers)

- Moore & Saffman (1975): Tearing mechanism. Stability according to static elliptic model with point vortex far-field.
- Pierrehumbert & Widnall (1981): Steady shapes.
- Saffman & Szeto (1981): Steady shapes and Kelvin's energy stability argument.
- Kamm (1987): Steady shapes using Schwarz functions.

(c) Double arrays (model of wakes)

- von Kármán (1912, see Lamb 1932): Point vortex limit and its stability.
- Kochin (1939, see Kochin, Kibel' & Roze (1964), §5.21): Higher order instability of the single linearly stable point vortex configuration.
- Saffman & Schatzman (1981): Steadily propagating shapes with finite core.
- Saffman & Schatzman (1982): Stabilization of subharmonic disturbances by finite core.
- Kida (1982): Analysis for small core area and disturbances not restricted to the subharmonic.
- Meiron, Saffman & Schatzman (1984): Persistence of an isolated marginally stable configuration for finite cores.
- Jimenez (1986a): Uses Hamiltonian formalism to provide an analytical basis of the Meiron, Saffman & Schatzman (1984) result for translative modes of vortex arrays "close" to the Kármán model.

- Jimenez (1986b), Kamm (1987): Lack of stabilization by two rows having unequal area.

(7) *Vortices subjected to strain*

- Moore & Saffman (1971): Steady ellipses in an external strain field and their stability to elliptic and non-elliptic modes.
- Burbea (1980), Burbea (1981), Burbea (1983): Steady shapes under higher order strain and their stability.
- Kida (1981), Neu (1984): Unsteady behavior of ellipses subjected to strain.
- Jacobs & Pullin (1985): Convective merger of two vortices in the presence of stretching along their axes.
- Pullin & Jacobs (1986): Evolution of streamwise braid vortices in a mixing layer.
- Kamm (1987): Bifurcations from the steady ellipses.

(8) *Filamentation and breaking of the boundary*

- Deem & Zabusky (1978).
- Dritschel (1988d): Repeated filamentation and the development of complexity of the interface.

(9) *Elliptic model: formalism and applications*

- Saffman (1979): Quasi-steady elliptic model.
- Melander, Styczek & Zabusky (1984), Melander, Zabusky & Styczek (1986): Hamiltonian elliptic model.
- Melander, Zabusky & McWilliams (1988): Conditions for convective merger.

(10) *Motion of vortex pairs with a common axis*

- Love (1894): Point vortex limit.
- Saffman (1979): Collision of identical pairs using a quasi-steady elliptic model.
- Overman & Zabusky (1982a): Passage and collision interactions of pairs using contour dynamics.

(11) *Misc.*

- Hebert (1983): Infinite dimensional Hamiltonian and Lagrangian formulation.
- Tang (1985): Lyapunov stability for circular and elliptical vortex patches.
- Dritschel (1988c), Kimura (1988, Appendix B): Contour dynamics on a sphere.

- Dritschel (1988a): Lyapunov stability for states with rotational or translational symmetry and with monotonic vorticity.

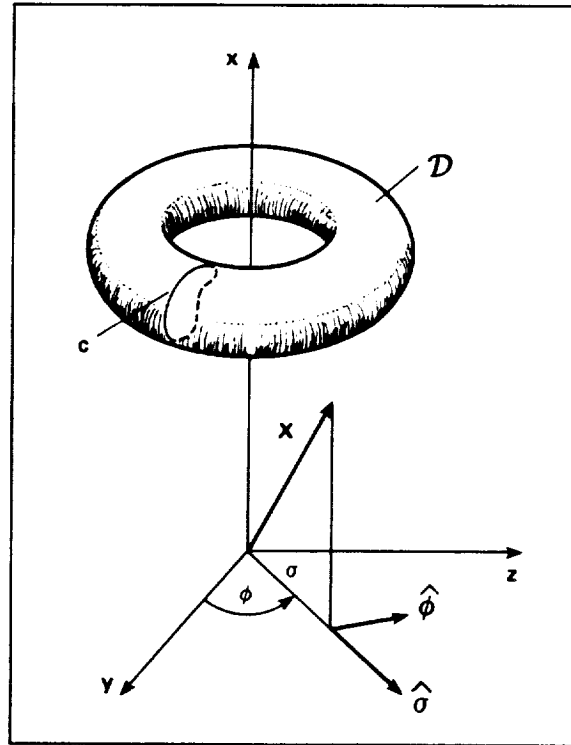


FIGURE 3.1. Cylindrical coordinates.

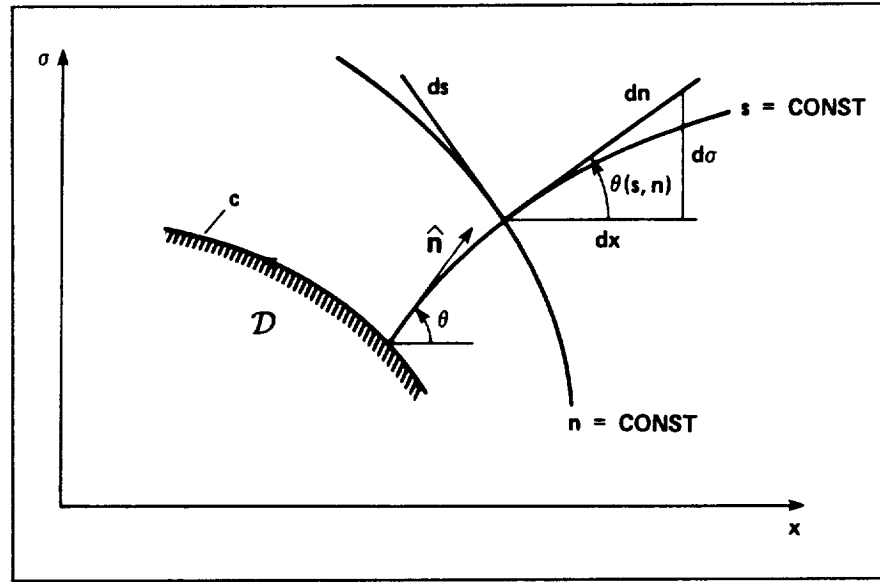


FIGURE 3.2. Surface oriented coordinates (n, s, ϕ) defined in the text.

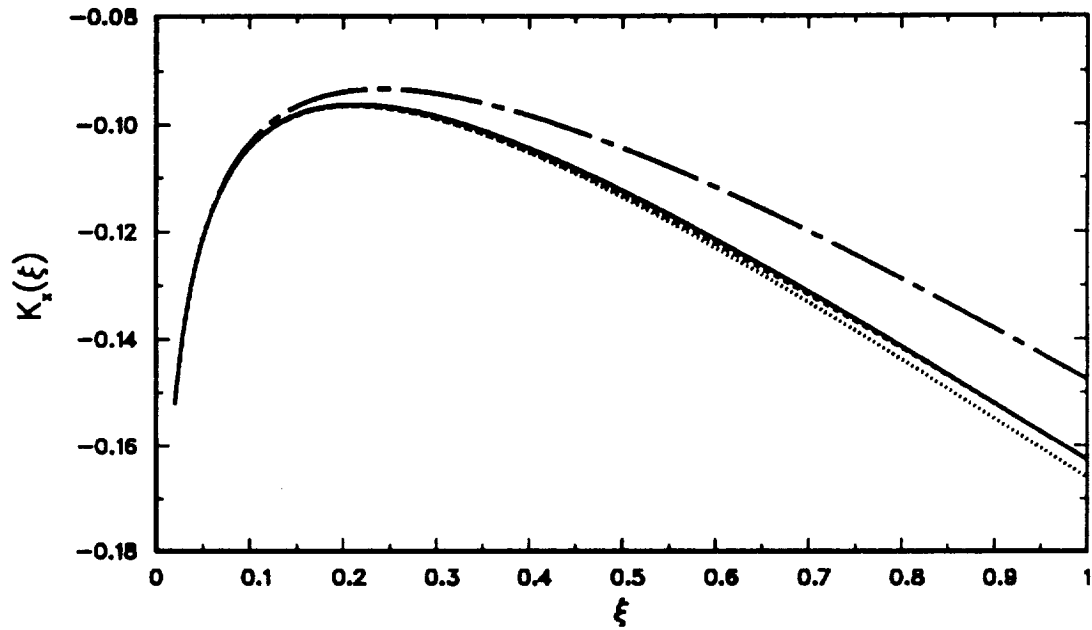


FIGURE 3.3. Integrand for the axial velocity along the chord of an arc between 25° and 75° on a Hill's vortex with unit radius. —, exact; ----, 5 term expansion; , 3 terms; — · — , 2 terms.

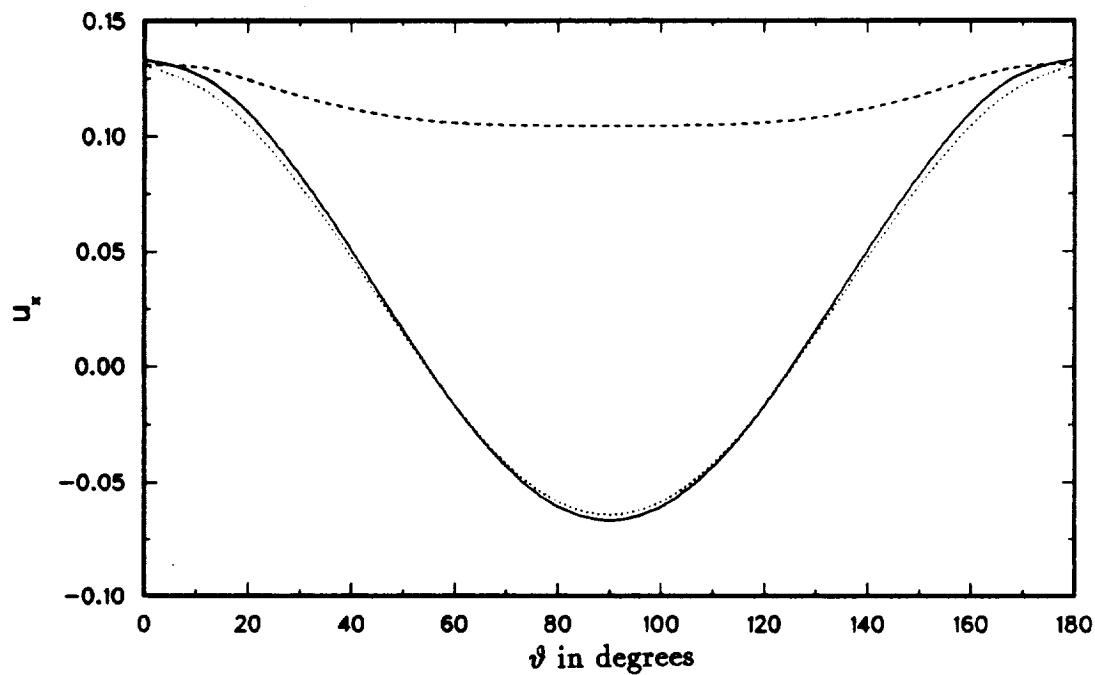


FIGURE 3.4. Axial velocity at node points on a Hill's vortex of unit radius and $\mathcal{A} = 1$. —, exact; ·····, computed with 15 segments; ----, deleting the contribution from adjacent segments.

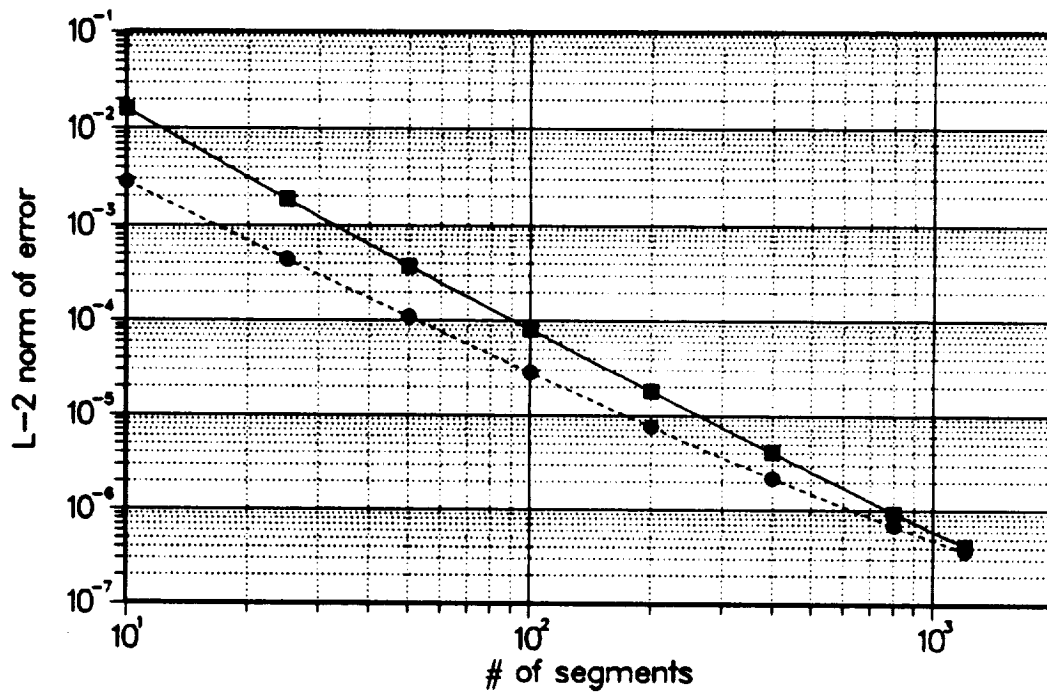


FIGURE 3.5. Error in velocities evaluated at the node points of a Hill's vortex with unit radius and $\mathcal{A} = 1$. ■, ●, for the axial and radial component, respectively.

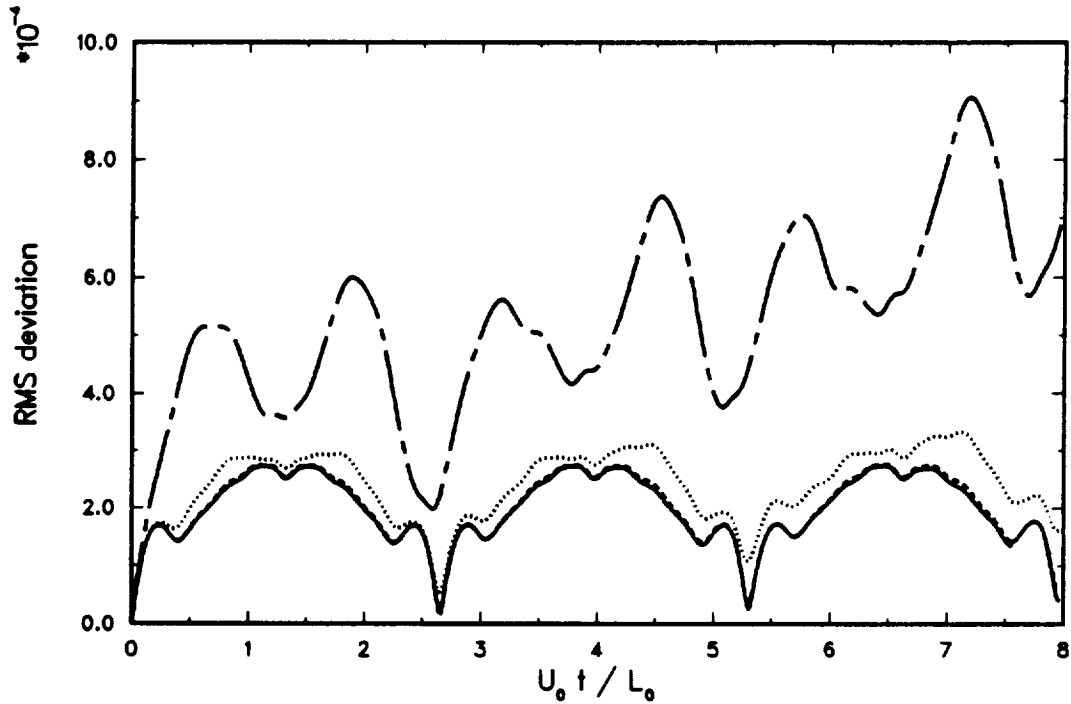


FIGURE 3.6. History of the rms deviation of the Fourier coefficients of the core boundary from the initial Norbury (1973) shape for different number of segments N_s . ———, $N_s = 200$; ·····, $N_s = 400$; -·-·-, $N_s = 800$; ———, $N_s = 1200$. The ordinate values are multiplied by 10^{-4} not the axis title.

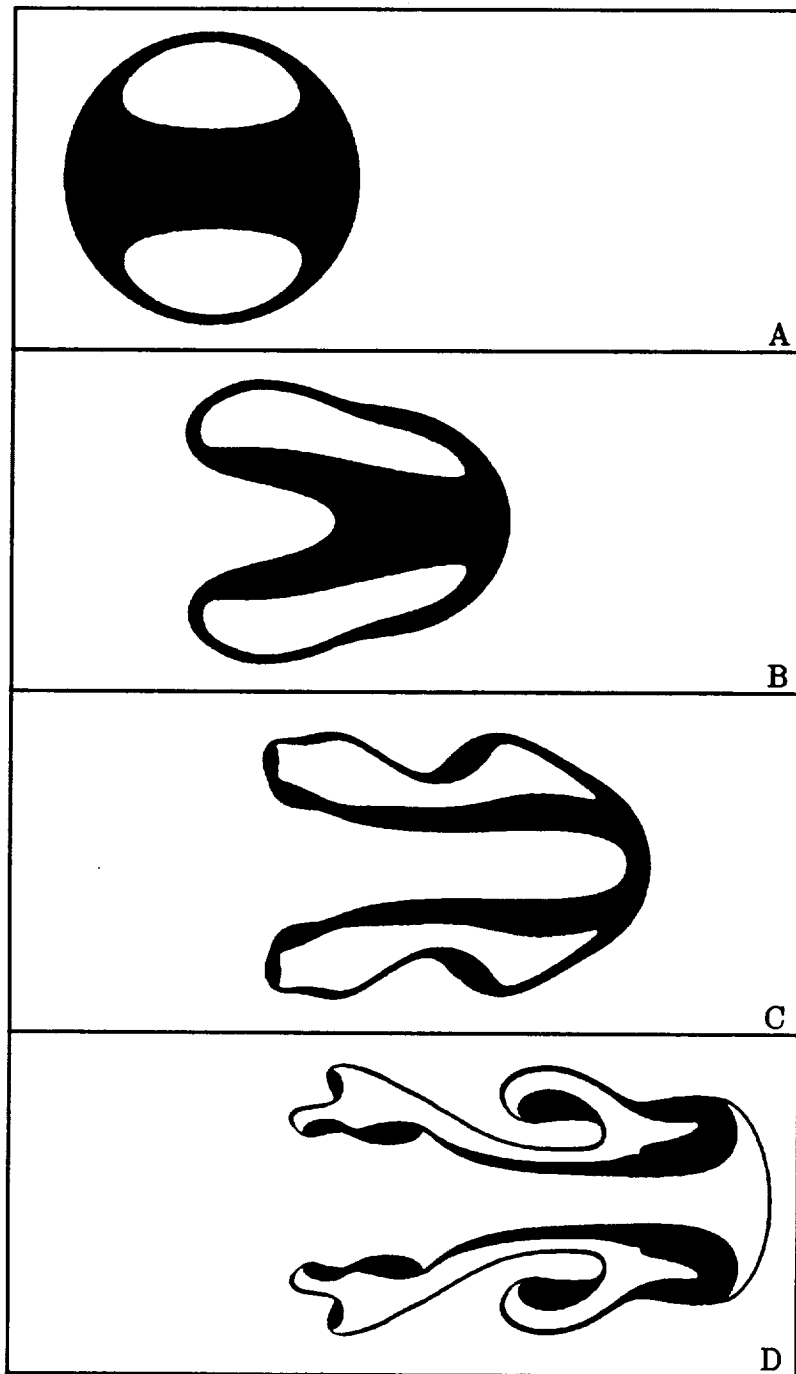


FIGURE 3.7. Evolution of a vortex formed by removing a region of vortical fluid from a sphere. Times normalized using the mean toroidal radius and the speed of translation of the vortex without the hole: A, 0; B, 4.27; C, 8.53; D, 12.80.

CHAPTER 4

SIMPLE MODELS

In this chapter, we present two simple models for the interaction of vortex rings belonging to the class we are studying. They are valid for cores which are thin compared to toroidal radii and separations distances. The first model is due to Dyson (1893) in which core deformations are neglected. It has been used to study the acoustic signal of vortex ring interactions (Kambe & Minota 1981, 1983) and for simulating round jets (Acton 1980, Kitaplioglu & Kibens 1980) in which many discrete rings are used to represent a vortex structure. In the second model to be presented, corrections for core deformation are made by allowing the cores to be strained into ellipses. The elliptic model will be used in Chapter 5 to predict and gain physical understanding of core deformations and accompanying acoustic radiation observed in the contour dynamics runs.

4.1. Dyson's (1893) model

4.1.1. *Evolution equations*

In two dimensions, the simplest model of vortex motion is based on point vortices. Its validity stems from both physical and mathematical considerations. From the mathematical perspective, the motion of point vortices constitutes a weak solution to the Euler equations, in a sense that has been recently clarified by Greengard & Thomann (1988). The issue of whether the trajectories of many point vortices converge to the particle trajectories of smooth solutions of the Euler equations has received attention in the mathematics and statistical mechanics literature; however, it is not pertinent here since we do not intend to use such models to represent arbitrary distributions of vorticity. Rather our purpose is to represent vortices by *single* elements and the following physical considerations are therefore more relevant: If one has vorticity containing regions which are distant from each other compared to their core sizes then (i) the velocity induced by one region on another is well approximated by that due to a point vortex located at the vorticity centroid; thus point vortices

are useful kinematic replacements, (ii) the vorticity centroid of each patch is not displaced by its own velocity; thus point vortices also provide a valid dynamic model in the limit of large separations.

In three dimensions, vortex lines are curved and the same physical notions cannot be transplanted without modification. Even though the model of a line vortex (zero cross-section) is the kinematic limit at large distances, the displacement of a vortex tube is influenced by the local structure of the core. In Dyson's model, the assumptions about the core structure are that the vorticity varies linearly with distance from the axis of symmetry, that the core is thin compared to the radius, that it is initially circular and remains so. Then, the self-induced motion is a translation at a uniform velocity given by Kelvin's celebrated formula (Lamb 1932, §163)

$$U_i^{\text{self}} = \frac{\Gamma_i}{4\pi\bar{\sigma}_i} \left[\log \left(\frac{8\bar{\sigma}_i}{\delta_i} \right) - \frac{1}{4} + \mathcal{O}(\alpha_i^2, \alpha_i^2 \log \alpha_i) \right], \quad (4.1.1)$$

for the i th vortex say, with core and toroidal radii δ_i and $\bar{\sigma}_i$, respectively; α_i is the ratio of these radii. The error term is based on Fraenkel's (1972) higher order treatment rather than the formal error term expected from Lamb's derivation. For the mutual induction, the velocity that the j th vortex induces in the far-field is the same as that due to a circular line vortex (also called a Helmholtz ring (1858)) placed at the centroid of the circular shape. For thin cores, this choice guarantees that, for the core being modeled, both the far-field of the quasi two-dimensional flow in the vicinity of the core and the far-field relative to the toroidal radius, in which the impulse is the coefficient of the leading term, are identical to those for the Helmholtz ring. The axial and radial velocities induced by the Helmholtz ring at the i th vortex are, according to the Biot-Savart law,

$$\begin{aligned} u(\bar{x}_i, \bar{\sigma}_i; \bar{x}_j, \bar{\sigma}_j) &= -\frac{\Gamma_j}{4\pi} \int_0^{2\pi} \frac{\bar{\sigma}_i \bar{\sigma}_j \cos \phi - \bar{\sigma}_j^2}{(A - B \cos \phi)^{3/2}} d\phi, \\ v(\bar{x}_i, \bar{\sigma}_i; \bar{x}_j, \bar{\sigma}_j) &= -\frac{\Gamma_j}{4\pi} \int_0^{2\pi} \frac{(\bar{x}_j - \bar{x}_i) \bar{\sigma}_j \cos \phi}{(A - B \cos \phi)^{3/2}} d\phi, \end{aligned} \quad (4.1.2)$$

$$A = (\bar{x}_i - \bar{x}_j)^2 + \bar{\sigma}_i^2 + \bar{\sigma}_j^2,$$

$$B = 2\bar{\sigma}_i \bar{\sigma}_j.$$

The integrals can be expressed in terms of K and E , the complete elliptic integrals of the first and second kind:

$$\begin{aligned} u(\bar{x}_i, \bar{\sigma}_i; \bar{x}_j, \bar{\sigma}_j) &= -\frac{\Gamma_j}{4\pi\sqrt{B}} \left[I_5(\mu) - \frac{\bar{\sigma}_j}{\bar{\sigma}_i} I_4(\mu) \right], \\ v(\bar{x}_i, \bar{\sigma}_i; \bar{x}_j, \bar{\sigma}_j) &= -\frac{\Gamma_j}{4\pi\sqrt{B}} \frac{(\bar{x}_j - \bar{x}_i)}{\bar{\sigma}_j} I_5(\mu), \end{aligned} \quad (4.1.3)$$

where

$$\begin{aligned} I_4(\mu) &\equiv \int_0^\pi \frac{d\phi}{(1 + \mu - \cos \phi)^{3/2}} = \frac{2/\mu}{\sqrt{2 + \mu}} E(\bar{r}), \\ I_5(\mu) &\equiv \int_0^\pi \frac{\cos \phi d\phi}{(1 + \mu - \cos \phi)^{3/2}} = \frac{2}{\sqrt{2 + \mu}} \left[\frac{1 + \mu}{\mu} E(\bar{r}) - K(\bar{r}) \right], \\ \bar{r} &= \sqrt{\frac{2}{2 + \mu}}, \\ \mu &= A/B - 1. \end{aligned} \quad (4.1.4)$$

The integrals were obtained from Bierens de Haan (1939), Table 67, item 3 and the book of corrections by Lindman (1944), Table 67, item 4, respectively. For a system of vortex rings, the complete system of ODEs for the motion of the rings is

$$\begin{aligned} \frac{d\bar{x}_i}{dt} &= U_i^{\text{self}} + \sum_{j \neq i} u(\bar{x}_i, \bar{\sigma}_i; \bar{x}_j, \bar{\sigma}_j), \\ \frac{d\bar{\sigma}_i}{dt} &= \sum_{j \neq i} v(\bar{x}_i, \bar{\sigma}_i; \bar{x}_j, \bar{\sigma}_j). \end{aligned} \quad (4.1.5)$$

These equations need to be supplemented with the requirement of "volume conservation" that

$$\delta_i^2 \bar{\sigma}_i = \text{constant}, \quad (4.1.6)$$

which may also be considered as an assumption about the nature of the local straining process. The deformation matrix evaluated at the center of the core can be split as

$$\begin{pmatrix} u_{,x} & u_{,\sigma} \\ v_{,x} & v_{,\sigma} \end{pmatrix} = \begin{pmatrix} u_{,x} + v/2\sigma & u_{,\sigma} \\ u_{,\sigma} & -u_{,x} - v/2\sigma \end{pmatrix} + \begin{pmatrix} -v/2\sigma & 0 \\ 0 & -v/2\sigma \end{pmatrix}, \quad (4.1.7)$$

on account of the incompressibility and irrotationality conditions

$$\begin{aligned} u_{,x} + v_{,\sigma} + \frac{v}{\sigma} &= 0, \\ u_{,\sigma} - v_{,x} &= 0. \end{aligned} \quad (4.1.8)$$

The first part of (4.1.7) represents a plane strain which preserves area but not volume and the second, an isotropic compression of the core (for $v > 0$). Condition (4.1.6) respects only the second of these which seems inconsistent. The first part is not smaller than the second. To neglect it is to presume something about its long-term dynamical effect, namely, that variations in self-induced translation due to core deformations occur on a fast time scale and average to zero over the slower time scale of variations caused by the isotropic term.

For the acoustic signal, small core deformations, even when their effect on the overall motion averages to zero, can radiate considerable power. Furthermore, even when the overall motion is periodic, core deformations may not be—the first term in (4.1.7) may induce permanent deformations of the core. It is these considerations that motivate the elliptic model of §4.2 in which explicit treatment is given to the first term.

4.1.2. Conserved quantities

Dyson's model is known to possess at least two invariants of the motion. They are useful for checking the accuracy of the numerical procedure for time advancement and they provide trajectories for the case of two rings. The two quantities are most readily observed after writing the evolution equations (4.1.5) in Hamiltonian form, using as conjugate variables the positions \bar{x}_i and linear impulses $P_i = \pi\Gamma_i\bar{\sigma}_i^2$.

First, one sees from (4.1.1) that

$$U_i^{\text{self}} = \frac{\partial \mathcal{H}_i^{\text{self}}}{\partial P_i}, \quad (4.1.9)$$

where

$$\mathcal{H}_i^{\text{self}} = \frac{\Gamma_i^2 \bar{\sigma}_i}{2} \left[\log \left(\frac{8\bar{\sigma}_i}{\delta_i} \right) - \frac{7}{4} \right], \quad (4.1.10)$$

provided $\delta_i^2 \bar{\sigma}_i = \text{constant}$. If one wishes to hold δ_i fixed (as is done in certain vortex methods) then the 7/4 in (4.1.10) should be replaced by 5/4. The quantity $\mathcal{H}_i^{\text{self}}$ (with 7/4) is the kinetic energy (with density set to unity) of the flow induced by the ring as shown in Lamb §163. The fact that Kelvin's speed is the derivative of the energy with respect to the impulse, keeping circulation and volume fixed, exemplifies a general result due to Roberts (1972) for steadily translating inviscid rings of arbitrary core structure and thickness.

Next one writes the velocities in the summation of (4.1.5) in terms of the streamfunction of Helmholtz rings to obtain

$$\begin{aligned}\frac{d\bar{x}_i}{dt} &= \frac{\partial \widehat{\mathcal{H}}_i}{\partial P_i}, \\ \frac{dP_i}{dt} &= -\frac{\partial \widehat{\mathcal{H}}_i}{\partial \bar{x}_i},\end{aligned}\tag{4.1.11}$$

where

$$\begin{aligned}\widehat{\mathcal{H}}_i &= \mathcal{H}_i^{\text{self}} + \sum_{j \neq i} 2\mathcal{H}_{ij}, \\ \mathcal{H}_{ij} &= \pi \Gamma_i \Gamma_j \mathcal{G}(\bar{x}_i, \bar{\sigma}_i; \bar{x}_j, \bar{\sigma}_j)\end{aligned}\tag{4.1.12}$$

The streamfunction \mathcal{G} due to a Helmholtz ring of unit strength located at $(\bar{x}_j, \bar{\sigma}_j)$ is obtained by evaluating the Biot-Savart integral explicitly (Helmholtz 1858, p. 506, Lamb §161)

$$\begin{aligned}\mathcal{G}(x, \sigma; \bar{x}_j, \bar{\sigma}_j) &= \frac{(\sigma \bar{\sigma}_j)^{\frac{1}{2}}}{2\pi} \left[\left(\frac{2}{\bar{r}} - \bar{r} \right) K(\bar{r}) - \frac{2}{\bar{r}} E(\bar{r}) \right], \\ \bar{r} &= \sqrt{\frac{2B}{A+B}}, \\ A &= (x - \bar{x}_j)^2 + \sigma^2 + \bar{\sigma}_j^2, \\ B &= 2\sigma \bar{\sigma}_j.\end{aligned}\tag{4.1.13}$$

Due to the symmetry of \mathcal{H}_{ij} under interchange of i and j (4.1.11) can be written in the canonical form

$$\begin{aligned}\frac{d\bar{x}_i}{dt} &= \frac{\partial \mathcal{H}}{\partial P_i}, \\ \frac{dP_i}{dt} &= -\frac{\partial \mathcal{H}}{\partial \bar{x}_i}, \\ \mathcal{H} &= \sum_k \mathcal{H}_k^{\text{self}} + \sum_{\substack{j,k \\ j \neq k}} \mathcal{H}_{jk}.\end{aligned}\tag{4.1.14}$$

It follows that $d\mathcal{H}/dt = 0$. The quantity $P = \sum_i P_i$ corresponding to the total impulse is also conserved since

$$\frac{dP}{dt} = -\sum_i \frac{\partial \mathcal{H}}{\partial \bar{x}_i} = 0.\tag{4.1.15}$$

The last equality holds because \mathcal{H} depends only on differences of axial positions. The Hamiltonian representation for vortex rings bears a closer analogy to the motion of point masses in their mutual potentials than does the two-dimensional motion of point vortices where the conjugate variables are related to the x and y positions

(Lamb §157). A similar analogy probably holds for two-dimensional vortex dipoles however.

Dyson's model is frequently applied outside its range of validity. The limitations arising from the distant-interaction assumption are often ignored on the basis of the argument that if the energy is conserved the results cannot be too far from the truth. Let us attempt to make this statement more precise. We begin by making a distinction between the assertion that a model or vortex method possesses a conserved energy function \mathcal{H} and that it conserves energy. By the latter we mean that the fluid energy E of the hydrodynamic field predicted by the model is conserved. As an example of when the two statements are not equivalent, suppose δ_i is kept constant. A conserved Hamiltonian still exists but it does not correspond to E if δ_i is interpreted as the core radius of an actual vortex; in fact E would change in time.

We shall see presently that, for Dyson's model, \mathcal{H} and E are equivalent for thin rings as long as cores do not overlap. One concludes that an attempt to make near-field corrections to the interaction Hamiltonian of the model would not be successful—the model would remain unchanged. Whether the model can be corrected to prevent overlap, or, if overlapped configurations may be interpreted in some way that does conserve E are questions that are yet to be answered.

Direct calculation of E is not possible for all cases because of the complicated form of the integrals. Rather we shall proceed by showing the equivalence of E and \mathcal{H} for two limits. First, as expected the equivalence holds for interactions in which vortices are separated by distances much larger than their core radii. Second, it also holds for close interactions in which the separation distance is small compared to the toroidal radii, provided the cores do not overlap. This is surprising since the assumptions of the model are violated. Because the two limits share a common range the equivalence holds uniformly.

The kinetic energy for an axisymmetric distribution of vorticity is (Lamb §162)

$$E = \pi \int \omega_\phi(x, \sigma) \psi(x, \sigma) dx d\sigma, \quad (4.1.16)$$

provided the additive constant in ψ is chosen to make ψ vanish at the symmetry axis and $|\psi u|$ decays faster than $1/r$ at large distances; both conditions are satisfied in what follows. For the time being we shall drop the ϕ subscript on the azimuthal vorticity but will revert to it again when the distinction with the two-dimensional

vorticity needs to be emphasized. If the vorticity is non-zero in regions \mathcal{D}_j (not necessarily disjoint):

$$\omega(\mathbf{x}, \sigma) = \sum_j \omega_j(\mathbf{x}, \sigma), \quad (4.1.17)$$

then

$$\psi(\mathbf{x}, \sigma) = \sum_j \psi_j(\mathbf{x}, \sigma), \quad (4.1.18)$$

where $\psi_j(\mathbf{x}, \sigma)$ represents the flow induced by $\omega_j(\mathbf{x}, \sigma)$ alone. We substitute (4.1.17) and (4.1.18) into (4.1.16) and separate the double sum into self-energies E_j^{self} and interaction energies $E_{jk}, j \neq k$, where

$$E_{jk} = \pi \int \omega_j(\mathbf{x}, \sigma) \psi_k(\mathbf{x}, \sigma) d\mathbf{x} d\sigma. \quad (4.1.19)$$

We have already stated that Lamb has shown the equivalence of the self-energy with the one-vortex Hamiltonian so it suffices to establish that $E_{jk} = \mathcal{H}_{jk}$. Notice that \mathcal{H}_{jk} corresponds to the interaction energy of two Helmholtz rings. We shall see that it also corresponds to the interaction energy of two finite circular core vortices.

It is because the integral in (4.1.19) cannot be evaluated for arbitrary configurations of two circular cores that we now consider two independent limits. In all that follows we shall, consistent with the model, neglect terms of linear order in α , the quotient of core size to radius. To this order the vorticity in (4.1.19) is uniform.

For the case in which Δ_{jk} , the distance between the centers of j and k , is large compared to core radii, ψ_k becomes the Helmholtz ring streamfunction and may be Taylor expanded to linear order about the center of j . The linear terms vanish upon integration and one is left with

$$E_{jk} = \pi \Gamma_j \Gamma_k \mathcal{G}(\bar{\mathbf{x}}_j, \bar{\sigma}_j; \bar{\mathbf{x}}_k, \bar{\sigma}_k) + \mathcal{O}(\alpha_j) + \mathcal{O}\left(\frac{\delta_j + \delta_k}{\Delta_{jk}}\right), \quad (4.1.20)$$

which is the same as \mathcal{H}_{jk} as expected.

The limit of small Δ_{jk} compared to toroidal radii is more involved. First introduce the small parameter

$$\epsilon = \frac{\Delta_{jk}}{2(\bar{\sigma}_j \bar{\sigma}_k)^{\frac{1}{2}}}. \quad (4.1.21)$$

The argument of the elliptic integrals is in terms of ϵ ,

$$\tilde{r}^2 = \frac{1}{1 + \epsilon^2}. \quad (4.1.22)$$

With the aid of expansions of the elliptic integrals about $\bar{r} = 1$ (Byrd & Friedman 1971) we get

$$\mathcal{H}_{jk} = \frac{\Gamma_j \Gamma_k}{2} (\bar{\sigma}_j \bar{\sigma}_k)^{\frac{1}{2}} \left[\log \left(\frac{8 (\bar{\sigma}_j \bar{\sigma}_k)^{\frac{1}{2}}}{\Delta_{jk}} \right) - 2 + \mathcal{O}(\epsilon^2, \epsilon^2 \log \epsilon) \right]. \quad (4.1.23)$$

Next we evaluate E_{jk} for finite circular cores in the same limit. Whereas \mathcal{H}_{jk} represents the interaction energy of two Helmholtz rings, E_{jk} is the interaction energy of the *distribution* of elemental Helmholtz rings in two circular core regions. The streamfunction due to the vorticity in region k is

$$\psi_k(x, \sigma) = \int \omega_k(x', \sigma') \mathcal{G}(x, \sigma; x', \sigma') dx' d\sigma'. \quad (4.1.24)$$

After expanding \mathcal{G} for field points in the vicinity of the vortex, this becomes

$$\psi_k(x, \sigma) = (\sigma \bar{\sigma}_k)^{\frac{1}{2}} \left\{ \Psi(x, \sigma) + \frac{\Gamma_k}{2\pi} \left[\log 8 (\sigma \bar{\sigma}_k)^{\frac{1}{2}} - 2 \right] + \mathcal{O}(\epsilon'^2, \epsilon'^2 \log \epsilon') \right\} + \mathcal{O}(\alpha_k), \quad (4.1.25)$$

where

$$\Psi(x, \sigma) \equiv -\frac{1}{2\pi} \int \omega_k(x', \sigma') \log \left[(x - x')^2 + (\sigma - \sigma')^2 \right]^{\frac{1}{2}} dx' d\sigma', \quad (4.1.26)$$

is the two-dimensional streamfunction of a vortex *cylinder* with the arbitrary additive constant chosen so that $\Psi \sim -\Gamma/2\pi \log \rho$, at a large distance ρ from the center of the core. The two small parameters which appear in (4.1.25) are defined as

$$\epsilon' = \frac{\rho}{(\sigma \bar{\sigma}_k)^{\frac{1}{2}}}, \quad \alpha_k = \frac{\delta_k}{\bar{\sigma}_k}. \quad (4.1.27)$$

Care is required in not confusing these parameters. It is too restrictive to say that because the ratios of core size to radius and distance to radius are small that both are of the same order. This is true only in the interior or small neighborhood of the core. We want to leave a range of validity that is shared by (4.1.20), viz, $\delta_j + \delta_k \ll \Delta_{jk} \ll (\bar{\sigma}_j \bar{\sigma}_k)^{1/2}$. Equation (4.1.25) has the useful interpretation that the flow in the vicinity of thin cores is a simple modification of two-dimensional flow. This fact will be used again in Chapter 5. Equation (4.1.25) invites comparison with Moore's (1980) derivation for the streamfunction for a thin vortex ring of elliptic cross-section. In this case Ψ is the streamfunction for the Kirchhoff elliptic vortex (Lamb §159) with the additive constant adjusted to give the required behavior at infinity. The result agrees with Moore's which is obtained by a matching argument.

For the present case, substituting the Rankine vortex solution

$$\Psi = \begin{cases} -\frac{\Gamma_k}{2\pi} \left[\log \delta_k - 1/2(1 - \rho^2/\delta_k^2) \right], & \rho \leq \delta_k; \\ -\frac{\Gamma_k}{2\pi} \log \rho, & \rho \geq \delta_k; \end{cases} \quad (4.1.28)$$

into (4.1.25) gives that $\psi_k(x, \sigma)$ equals

$$\begin{cases} \frac{\Gamma_k(\sigma\bar{\sigma}_k)^{\frac{1}{2}}}{2\pi} \left[\log \left(\frac{8(\sigma\bar{\sigma}_k)^{\frac{1}{2}}}{\delta_k} \right) - \frac{3}{2} - \frac{1}{2} \frac{\rho^2}{\delta_k^2} + \mathcal{O}(\epsilon'^2, \epsilon'^2 \log \epsilon') \right] + \mathcal{O}(\alpha_k), & \rho \leq \delta_k; \\ \frac{\Gamma_k(\sigma\bar{\sigma}_k)^{\frac{1}{2}}}{2\pi} \left[\log \left(\frac{8(\sigma\bar{\sigma}_k)^{\frac{1}{2}}}{\rho} \right) - 2 + \mathcal{O}(\epsilon'^2, \epsilon'^2 \log \epsilon') \right] + \mathcal{O}(\alpha_k), & \rho \geq \delta_k. \end{cases} \quad (4.1.29)$$

Next, consider the interaction energy between ψ_k and the vorticity of core j which is assumed not to overlap with core k so that the streamfunction exterior to k is used. The only variable part of the integrand is $\log \rho$. Its integral is evaluated in polar coordinates $(\hat{\rho}, \hat{\beta})$ with origin at the center of j and $\hat{\beta}$ measured counterclockwise from the line joining the centers of cores j and k :

$$\int_{\mathcal{D}_j} \log \rho \, dx \, d\sigma = \frac{1}{2} \int_0^{\delta_j} \hat{\rho} \, d\hat{\rho} \int_0^{2\pi} \log [\hat{\rho}^2 + \Delta_{jk}^2 + 2\hat{\rho}\Delta_{jk} \cos \hat{\beta}] \, d\hat{\beta} \quad (4.1.30)$$

The angular integral is tabulated (Gradshteyn & Ryzhik 4.224.14) as

$$\begin{cases} 4\pi \log \Delta_{jk}, & \hat{\rho} \leq \Delta_{jk}; \\ 4\pi \log \hat{\rho}, & \hat{\rho} \geq \Delta_{jk}. \end{cases} \quad (4.1.31)$$

The first case is appropriate when \mathcal{D}_j does not contain the center of \mathcal{D}_k and is certainly true when there is no overlap:

$$\begin{aligned} E_{jk} &= \frac{\Gamma_j \Gamma_k}{2} (\bar{\sigma}_k \bar{\sigma}_j)^{\frac{1}{2}} \left[\log \left(\frac{8(\bar{\sigma}_j \bar{\sigma}_k)^{\frac{1}{2}}}{\Delta_{jk}} \right) - 2 + \mathcal{O}(\epsilon''^2, \epsilon''^2 \log \epsilon'') \right] + \mathcal{O}(\alpha_j, \alpha_k), \\ \epsilon'' &= \frac{\Delta_{jk}}{(\bar{\sigma}_j \bar{\sigma}_k)^{\frac{1}{2}}}, \end{aligned} \quad (4.1.32)$$

which is the same as \mathcal{H}_{jk} given in (4.1.23).

The equivalence breaks down when the cores overlap. One must then use the interior streamfunction in $\mathcal{D}_j \cap \mathcal{D}_k$. When core j does not contain the center of k the difference between E_{jk} and \mathcal{H}_{jk} is

$$E_{jk} - \mathcal{H}_{jk} = \frac{\Gamma_j \Gamma_k}{\pi} \frac{(\bar{\sigma}_j \bar{\sigma}_k)^{\frac{1}{2}}}{\pi \delta_j^2} \int_{\mathcal{D}_j \cap \mathcal{D}_k} \left[\log \left(\frac{\rho}{\delta_k} \right) + \frac{1}{2} \left(1 - \frac{\rho^2}{\delta_k^2} \right) \right] dx \, d\sigma + \mathcal{O}(\alpha_j, \alpha_k). \quad (4.1.33)$$

The integral in the overlap region appears intractable, however, since $0 < \varrho/\delta_k \leq 1$ the integrand is everywhere ≤ 0 and the error non-zero.

In summary, the interaction energy E_{jk} of two thin circular core rings is equivalent to the interaction energy \mathcal{H}_{jk} of two Helmholtz rings in the following ranges:

- (i) $(\delta_j + \delta_k) \ll \Delta_{jk}$
- (ii) $\Delta_{jk} \ll (\bar{\sigma}_j \bar{\sigma}_k)^{\frac{1}{2}}$, provided the cores do not overlap.

The second range contains a portion of the first so that $E_{jk} = \mathcal{H}_{jk}$ is uniformly true. This means that Dyson's model conserves energy for thin non-overlapping cores.

4.1.3. *The final period of collision according to Dyson's model*

Now, based upon constancy of the Hamiltonian we shall note, for reference in Chapter 5, some facts about the behavior of Dyson's model for the head-on collision of a vortex ring pair at large times.

Consider the collision of two identical but oppositely signed vortices with $\bar{x}_2 = -\bar{x}_1 \equiv \bar{x}$, $\bar{\sigma}_1 = \bar{\sigma}_2 \equiv \bar{\sigma}$, $\Gamma_1 = -\Gamma_2 \equiv \Gamma$. In the final stage of collision $\epsilon \equiv \bar{x}/\bar{\sigma}$ is small and the Hamiltonian becomes

$$\mathcal{H} = \Gamma^2 \bar{\sigma} \left[\log \left(\frac{2\bar{x}}{\delta} \right) + \frac{1}{4} \right] + \mathcal{O}(\epsilon^2, \epsilon^2 \log \epsilon). \quad (4.1.34)$$

Setting this equal to its value when the vortices are well separated so that the interaction energy is zero gives the asymptotic trajectory as

$$\log \left(\frac{2\bar{x}}{\delta} \right) + \frac{1}{4} = \frac{\bar{\sigma}_o}{\bar{\sigma}} \left[\log \left(\frac{8\bar{\sigma}_o}{\delta_o} \right) - \frac{7}{4} \right]. \quad (4.1.35)$$

With $\bar{\sigma}/\bar{\sigma}_o \rightarrow \infty$ this has an asymptote for which

$$\bar{x} \rightarrow 0.389\delta. \quad (4.1.36)$$

For initially thinner cores, this happens at larger values values of $\bar{\sigma}/\bar{\sigma}_o$. Thus the cores approach a self-similar configuration in which axial motion is balanced by shrinking core area. The fact that \bar{x} becomes arbitrarily small contrasts with the collision of vortex pairs in two-dimensions in which the pairs never come closer than a finite distance (Lamb §155). Since the cores have overlapped, (4.1.33) shows the true energy to be larger than the Hamiltonian. Even if it were possible to concoct an interaction

Hamiltonian to give instead of (4.1.36) the hard-core asymptote $\bar{x} \rightarrow \delta$ the energy would be from (4.1.10) and (4.1.32)

$$E \rightarrow 0.943\Gamma^2\bar{\sigma}, \quad (4.1.37)$$

which is still not conserved.

When the distance between the vortices is smaller than their radii, the radial motion will be the same as that for a pair of translating line vortices separated by distance $2\bar{x}$:

$$\dot{\bar{\sigma}} = \frac{\Gamma}{4\pi\bar{x}}, \quad (4.1.38)$$

which can also be shown from the equations of motion. Substituting (4.1.36) into this we get

$$\frac{\dot{\bar{\sigma}}}{\bar{\sigma}^{\frac{1}{2}}} \rightarrow 0.909\frac{\Gamma}{V^{\frac{1}{2}}} = \text{constant}, \quad (4.1.39)$$

where $V = 2\pi^2\delta^2\bar{\sigma}$ is the volume. For later comparison with contour dynamics, note that

$$\Gamma = \int \omega_\phi(x, \sigma) dx d\sigma = \mathcal{A} \int \sigma dx d\sigma = \mathcal{A}V/2\pi, \quad (4.1.40)$$

so that

$$\frac{\dot{\bar{\sigma}}}{\bar{\sigma}^{\frac{1}{2}}} \rightarrow 0.363\sqrt{\Gamma\mathcal{A}} = \text{constant}. \quad (4.1.41)$$

In contrast, the contour dynamics simulations to be presented in Chapter 5 show that because cores do not overlap the peak rate of stretching attained even for thin cores is considerably smaller, viz

$$\frac{\dot{\bar{\sigma}}}{\bar{\sigma}^{\frac{1}{2}}} = 0.164\sqrt{\Gamma\mathcal{A}}. \quad (4.1.42)$$

4.2. Development of an elliptic model for axisymmetric vortices

4.2.1. Introduction

The contour dynamics equations are exact but have infinite degrees of freedom. The elliptic model permits a limited number of degrees of freedom. As with Dyson's model, the approximations become more accurate as the distance between interacting cores becomes large compared to their sizes and as the ratios of core size to toroidal radius become small.

The present treatment was inspired by a similar model for two-dimensional vortices by Melander, Zabusky & Styczek (1986, hereafter MZS). They constructed a consistent truncation of the kernel in the evolution equation for the shape of the boundaries of the vortices, keeping moments of the core shape up to second order, which define an ellipse. In the axisymmetric case, the complexity of the kernels precludes such a rigorous approach. Even if the task were possible, moments arise which cannot be related to the shape of an ellipse. We therefore chose a heuristic approach not based on expansion of the contour dynamics equations. Rather one considers the flow induced locally at one vortex by the others i.e., we expand the induced velocity field about the centroid of the vortex and retain only the linear terms. To obtain the velocity field induced by other vortex rings, the Helmholtz ring representation is used as in Dyson's model.

Elliptic core models have been used quite successfully in two dimensions. Saffman (1979) followed this approach in dealing with the motion of a translating vortex pair towards a plane slip surface. Saffman & Szeto (1980) used it to study equilibrium shapes of co-rotating pairs of vortices and found excellent agreement with exact solutions. Saffman, in unpublished work, used the model to study the existence of steady configurations of a von Kármán street in which the vortex rows have unequal strengths. We will describe the differences between Saffman's approach and that of MZS after background material has been furnished.

In §4.2.2 it is demonstrated how the heuristic approach works for two dimensions. It yields evolution equations for the centroids, the orientation angles of the ellipses and the lengths of their major and minor axes which are identical to those obtained in MZS. In the derivation, we will try to convey a physical understanding of each term in their equations. Next, in §4.2.3 the methodology will be applied to the axisymmetric case. In §4.2.4 a correspondence of variables between the two-dimensional and axisymmetric cases will be made. This makes Neu's (1984) phase plane portraits of the deformations of an elliptic vortex in a plane strain relevant to the axisymmetric case and provides one with a language for discussing the core deformations observed with contour dynamics. Finally, in §4.2.5, departures to be expected from the elliptic model will be discussed.

4.2.2. Background for an elliptic model for two-dimensions

(i) *The far-field of an elliptic vortex.* Consider several interacting patches of vorticity. Points inside the patches are convected by the combined influence of vorticity in the same patch (the near-field) and by the influence of other patches (the induced field). For the latter assume that the patches are distant relative to their sizes. Then we ask: What is the influence of a distant vortex patch? The streamfunction due to the vortex is

$$\Psi(\mathbf{x}) = -\frac{1}{2\pi} \int \log |\mathbf{x} - \mathbf{x}'| \omega_z(\mathbf{x}') d\mathbf{x}'. \quad (4.2.1)$$

If $\rho \equiv |\mathbf{x}|$, the distance from the origin to the point of evaluation, is large compared to $|\mathbf{x}'|$ then a Taylor series expansion about \mathbf{x} gives

$$\begin{aligned} \log |\mathbf{x} - \mathbf{x}'| &= \log \rho - \frac{\mathbf{x}\mathbf{x}'}{\rho^2} - \frac{\mathbf{y}\mathbf{y}'}{\rho^2} \\ &+ \frac{1}{2\rho^4} (x'^2 y'^2 - x^2 x'^2 - 4xx'y'y' - y^2 y'^2 + x^2 y'^2) + \mathcal{O}\left(\frac{1}{\rho^3}\right). \end{aligned} \quad (4.2.2)$$

When this is substituted into (4.2.1), the moments, m_{ij} of the vorticity distribution appear:

$$m_{ij} = \int x'^i y'^j \omega_z(x', y') dx' dy'. \quad (4.2.3)$$

In terms of them, the far-field expansion of the streamfunction is

$$\begin{aligned} \Psi(x, y) &= -\frac{1}{2\pi} \left\{ \Gamma \log \rho - \frac{x}{\rho^2} m_{10} - \frac{y}{\rho^2} m_{01} \right. \\ &\left. + \frac{1}{2\rho^4} [(y^2 - x^2)(m_{20} - m_{02}) - 4xy m_{11}] + \mathcal{O}\left(\frac{1}{\rho^3}\right) \right\}. \end{aligned} \quad (4.2.4)$$

Thus, in the far-field the vorticity distribution can be represented in terms of a few overall properties. The first term in equation (4.2.4) is the streamfunction generated by a point vortex at the origin whose circulation is that of the patch. If we locate the vorticity centroid of the patch at the origin, the terms of $\mathcal{O}(1/\rho)$ vanish and the point vortex approximation is valid up to $1/\rho^2$. The last retained terms involve second order moments about the vorticity centroid. For an ellipse with uniform vorticity,

area S , aspect ratio $\lambda = a/b$, and orientation angle φ relative to the x axis these moments are

$$\begin{aligned} m_{20} &= \frac{\Gamma S}{4\pi\lambda} [\lambda^2 + (1 - \lambda^2) \sin^2 \varphi], \\ m_{02} &= \frac{\Gamma S}{4\pi\lambda} [\lambda^2 + (1 - \lambda^2) \cos^2 \varphi], \\ m_{11} &= -\frac{\Gamma S}{8\pi\lambda} (1 - \lambda^2) \sin 2\varphi. \end{aligned} \quad (4.2.5)$$

Using these in (4.2.4), the velocities can be obtained from the streamfunction after differentiation:

$$\begin{aligned} u &= \frac{\Gamma}{2\pi} \left[-\frac{\sin \beta}{\rho} + \frac{S(1 - \lambda^2)}{4\pi\lambda\rho^3} \sin(3\beta - 2\varphi) + \mathcal{O}\left(\frac{1}{\rho^4}\right) \right], \\ v &= \frac{\Gamma}{2\pi} \left[\frac{\cos \beta}{\rho} - \frac{S(1 - \lambda^2)}{4\pi\lambda\rho^3} \cos(3\beta - 2\varphi) + \mathcal{O}\left(\frac{1}{\rho^4}\right) \right], \end{aligned} \quad (4.2.6)$$

where β is the angle, relative to the x axis, of the line directed from the centroid to the field point.

(ii) *Induced motion of the centroid.* We now consider a “field” vortex (denoted by the index f) under the influence of the far-field of another vortex (denoted by index s for “source”) whose centroid is at the origin. The velocity at the field vortex due to the source vortex may be expanded to second order about its centroid ($\bar{\mathbf{x}}_f$) as

$$\mathbf{u}_{f,s} = \mathbf{u}_{s}(\bar{\mathbf{x}}_f) + \begin{pmatrix} u_{,x} & u_{,y} \\ v_{,x} & v_{,y} \end{pmatrix} \begin{pmatrix} \bar{x} \\ \bar{y} \end{pmatrix} + \frac{1}{2} \begin{pmatrix} \bar{x}^2 u_{,xx} + 2\bar{x}\bar{y}u_{,xy} + \bar{y}^2 u_{,yy} \\ \bar{x}^2 v_{,xx} + 2\bar{x}\bar{y}v_{,xy} + \bar{y}^2 v_{,yy} \end{pmatrix}. \quad (4.2.7)$$

The double index fs above should be read “at f due to s .” All velocity derivatives are evaluated at the centroid of vortex f and $\bar{\mathbf{x}} \equiv \mathbf{x} - \bar{\mathbf{x}}_f$. The effect of the first term is to rigidly translate the vortex with the velocity evaluated at its centroid. The second term corresponds to plane strain. We will see later that it preserves the elliptical shape of the vortex but alters its aspect ratio and orientation.

The last term distorts the shape from ellipticity, an effect we neglect. However, it has a non-negligible effect on the motion of the centroid. This can be seen as follows. By its definition, the centroid moves with the average induced velocity over the core i.e.,

$$\dot{\bar{\mathbf{x}}}_f = \frac{1}{S_f} \int_f \mathbf{u}_{f,s}(\bar{\mathbf{x}}) d\bar{\mathbf{x}}. \quad (4.2.8)$$

Substituting the expansion (4.2.7) into this gives

$$\dot{\bar{\mathbf{x}}}_f = \mathbf{u}_s(\bar{\mathbf{x}}_f) + \frac{1}{2S_f} \begin{pmatrix} j_{20}u_{,xx} + 2j_{11}u_{,xy} + j_{02}u_{,yy} \\ j_{20}v_{,xx} + 2j_{11}v_{,xy} + j_{02}v_{,yy} \end{pmatrix}. \quad (4.2.9)$$

The moments of the core shape about the centroid are

$$j_{ik} = \int \bar{x}^i \bar{y}^k d\bar{x} d\bar{y}. \quad (4.2.10)$$

The highest order term contained in the far-field expansion of the first term in (4.2.9) is $\mathcal{O}(1/\rho^3)$. The second part of (4.2.9) yields a term of the same order from the point vortex part of the far-field which we cannot ignore. This represents a correction to the velocity evaluated at the centroid that must be included in order to obtain equations for the centroid motion that are consistent with the expansion (4.2.6). Due to the constraints of continuity and irrotationality there are two independent second derivatives, say, $u_{,xx}$ and $u_{,xy}$. Then (4.2.9) becomes

$$\dot{\bar{\mathbf{x}}}_f = \mathbf{u}_s(\bar{\mathbf{x}}_f) + \frac{1}{2S_f} \begin{pmatrix} (j_{20} - j_{02})u_{,xx} + 2j_{11}u_{,xy} \\ (j_{20} - j_{02})u_{,xy} - 2j_{11}u_{,xx} \end{pmatrix}. \quad (4.2.11)$$

For the point vortex part of the far-field, these second derivatives are

$$u_{,xx} = \frac{\Gamma_s}{2\pi} \left(-\frac{2 \sin 3\beta_{,f}}{\rho_{,f}^3} \right); \quad u_{,xy} = \frac{\Gamma_s}{2\pi} \left(\frac{2 \cos 3\beta_{,f}}{\rho_{,f}^3} \right), \quad (4.2.12)$$

where $\beta_{,f}$ is the angle of the line, relative to the x axis, from the center of s to the center of f and $\rho_{,f}$ is its length. When (4.2.12) is substituted into (4.2.11) together with the relationships between moments and ellipse parameters given in equation (4.2.5) we obtain three terms in the equation for the centroid motion. These are:

A. Centroid motion due to leading order far-field velocity evaluated at the centroid:

$$\dot{\bar{\mathbf{x}}}_f = \frac{\Gamma_s}{2\pi\rho_{,f}} \begin{pmatrix} -\sin \beta_{,f} \\ \cos \beta_{,f} \end{pmatrix} \quad (4.2.13)$$

B. Centroid motion due to second order far-field evaluated at the centroid:

$$+ \frac{\Gamma_s S_f (1 - \lambda_s^2)}{2\pi 4\pi\lambda_s \rho_{,f}^3} \begin{pmatrix} \sin(3\beta_{,f} - 2\varphi_s) \\ -\cos(3\beta_{,f} - 2\varphi_s) \end{pmatrix} \quad (4.2.14)$$

C. Centroid motion due to second derivatives of the point vortex part of the far-field:

$$+ \frac{\Gamma_s S_f (1 - \lambda_s^2)}{2\pi 4\pi\lambda_s \rho_{,f}^3} \begin{pmatrix} \sin(3\beta_{,f} - 2\varphi_f) \\ -\cos(3\beta_{,f} - 2\varphi_f) \end{pmatrix}. \quad (4.2.15)$$

This expression may be compared with equation (3.24) in MZS. The similar form of the last two terms is not fortuitous. It leads to antisymmetry of $\Gamma, \dot{\bar{x}}_f$, with respect to permutation of the indices f and s which assures conservation of the global centroid of the system, equivalent to conservation of linear impulse. This is another indication that in a higher order far-field treatment, vortices must not be convected by the velocity induced at the centroid.

(iii) *Induced evolution of the ellipse shape.* Here we are interested in the effect upon the shape of the ellipse of the straining component of the velocity field (4.2.7) about the centroid of a field vortex. It is here that our treatment differs from that of MZS. We make use of the solution of an elliptic vortex subjected to strain (Kida 1981) rather than a formal expansion. Due to continuity and irrotationality the strain term is

$$\mathbf{S} = \begin{pmatrix} p & q \\ q & -p \end{pmatrix} \begin{pmatrix} \bar{x} \\ \bar{y} \end{pmatrix}, \quad (4.2.16)$$

where

$$p = u_{,x} = -v_{,y}; \quad q = u_{,y} = v_{,x}, \quad (4.2.17)$$

evaluated at the centroid. The orientation, $\tilde{\alpha}$, of the principal strain directions is obtained from

$$\tan 2\tilde{\alpha} = \frac{q}{p}, \quad (4.2.18)$$

which have a maximum rate of extension given by

$$e = p \sec 2\tilde{\alpha}. \quad (4.2.19)$$

$e > 0$ corresponds to extensive strain along that direction and vice-versa. When p and q are computed as derivatives of the far-field velocity, it is consistent to keep only the strain arising from the leading (point vortex) term:

$$\begin{pmatrix} p \\ q \end{pmatrix} = \frac{\Gamma_s}{2\pi \rho_{s,f}^2} \begin{pmatrix} \sin 2\beta_{s,f} \\ -\cos 2\beta_{s,f} \end{pmatrix}. \quad (4.2.20)$$

From this (4.2.18) gives the well known result that, for point vortices, the principal axis of strain is at 45° from the line joining their centers. Kida (1981) has studied the response of an elliptic vortex to a straining field which does not change in time and his results can be applied to determine the influence of \mathbf{S} . However, before doing so, one must realize that in general, the strain axes may rotate arbitrarily and

Kida's analysis needs slight generalization. *A priori* one can say that because rotation of the strain axes does not involve rotation of the fluid, no additional rotation is imparted to the ellipse so that one should merely replace the orientation angle by the orientation relative to the instantaneous strain axes without making the corresponding replacement for the *rate* of the orientation. In other words, the rate of change of the ellipse shape should only depend on the instantaneous velocity field. To convince ourselves of this the following formal reasoning may be applied.

Let us define new cartesian axes (x'', y'') with origin at the centroid of vortex f and the x'' axis along one of the principal strain directions. Then the equation for the boundary of the ellipse is

$$h(x, y, t) = \frac{(x'' \cos \Theta(t) + y'' \sin \Theta(t))^2}{a^2(t)} + \frac{(-x'' \sin \Theta(t) + y'' \cos \Theta(t))^2}{b^2(t)} - 1 = 0, \quad (4.2.21)$$

where $\Theta(t) = \varphi(t) - \tilde{\alpha}(t)$. The deformation of the ellipse due to strain is obtained by imposing, in a *fixed set of coordinates*, the kinematic condition that the boundary is a material line

$$\frac{Dh}{Dt} = \left(\frac{\partial h}{\partial t} \right)_{xy} + \mathbf{S} \cdot \nabla h = 0 \text{ on } h = 0, \quad (4.2.22)$$

where for emphasis we have indicated that the time derivative be evaluated holding x and y fixed i.e., using the chain rule

$$\left(\frac{\partial h}{\partial t} \right)_{xy} = \frac{\partial h}{\partial x''} \frac{\partial x''}{\partial t} + \frac{\partial h}{\partial y''} \frac{\partial y''}{\partial t} + \frac{\partial h}{\partial a} \dot{a} + \frac{\partial h}{\partial b} \dot{b} + \frac{\partial h}{\partial \Theta} \dot{\varphi} - \frac{\partial h}{\partial \Theta} \dot{\tilde{\alpha}}. \quad (4.2.23)$$

Using the equation of the ellipse (4.2.21) we find that the sum of the first, second and last terms vanishes. This means that the rate, $\dot{\tilde{\alpha}}$, at which the strain axis rotates does not enter into the solution, only its instantaneous orientation relative to the ellipse is important. Then after substitution of (4.2.16) for \mathbf{S} and transformation to strain axes coordinates (4.2.22) becomes

$$\frac{\partial h}{\partial a} \dot{a} + \frac{\partial h}{\partial b} \dot{b} + \frac{\partial h}{\partial \Theta} \dot{\varphi} + ex'' \frac{\partial h}{\partial x''} - ey'' \frac{\partial h}{\partial y''} = 0, \quad (4.2.24)$$

The rates of change of ellipse parameters, \dot{a} , \dot{b} and $\dot{\varphi}$ are obtained by carrying out the required differentiations of $h(x, y, t)$ and setting the coefficients of the three monomials x''^2 , y''^2 and $x''y''$ separately to zero. This leads to a linear system of equations for the three unknowns. Kida (1981) has done this for the case of an isolated vortex

in a fixed straining field in which case the equation to be solved is identical to the one above except with $\dot{\varphi}$ replaced by $\dot{\Theta}$. His solution with $\dot{\varphi}$ replacing $\dot{\Theta}$ and $\varphi - \bar{\alpha}$ replacing Θ is

$$\begin{aligned}\dot{a} &= ea \cos 2(\varphi - \bar{\alpha}), \\ \dot{b} &= -eb \cos 2(\varphi - \bar{\alpha}), \\ \dot{\varphi} &= -e \frac{a^2 + b^2}{a^2 - b^2} \sin 2(\varphi - \bar{\alpha}).\end{aligned}\tag{4.2.25}$$

Note that the area $\sim ab$ of the vortex is constant. Substituting in the values for the strain rate and the straining direction for the point vortex part of the far field and calculating the evolution of the aspect ratio $\lambda = a/b$ we obtain:

D. Evolution of aspect ratio due to strain of leading far-field behavior:

$$\dot{\lambda}_f = \frac{\lambda_f \Gamma_f}{\pi \rho_{fj}^2} \sin 2(\beta_{fj} - \varphi_f).\tag{4.2.26}$$

E. Ellipse rotation due to strain of leading far-field behavior:

$$\dot{\varphi}_{fj} = -\frac{1 + \lambda_f^2}{2} \frac{1 - \lambda_f^2}{1 - \lambda_f^2} \frac{\Gamma_f}{\pi \rho_{fj}^2} \cos 2(\beta_{fj} - \varphi_f).\tag{4.2.27}$$

These expressions are the same as equations (3.19) and (3.20) in MZS.

(iv) *Self-induced evolution of the ellipse shape.* The solution for the self induced motion is Kirchhoff's elliptic vortex (Lamb §159) which rotates with constant angular velocity without changing shape:

F.

$$\dot{\varphi}_f = \frac{\Gamma_f}{\pi (a_f + b_f)^2}\tag{4.2.28}$$

(v) *Comments.* Items A–F represent the effects that comprise the elliptic model for two-dimensions. For several interacting vortices a summation over the index s excluding the $s = f$ term is implied. When A–F are superposed, they give the model developed in MZS.

We are now in a position to comment on an elliptic model for two-dimensions introduced in Saffman (1979) to treat the approach of a vortex pair to a plane slip surface and used in Saffman & Szeto (1980) for a stationary problem. It has the following differences with the approach MZS: (a) The velocity and strain induced by one vortex on another is calculated from Kirchhoff's elliptic vortex rather than a far-field expansion as in MZS. This may seem advantageous but is not consistent

in view of the fact that, (b) The core centroids are moved according to the velocity induced there rather than by the average of the induced velocity over the core. When the vortices are well separated, the error incurred would be the effect represented by equation (4.2.15). Since this term is comparable to higher order terms in the far-field expansion, it is not consistent to use the exact Kirchhoff solution; it does not ensure conservation of the global centroid. In Saffman (1979), however, the centroid is conserved trivially due to symmetries of the problem considered. (c) The evolution equations for the ellipse parameters are complicated and require numerical solution. Saffman did not have these evolution equations which were developed later by Kida (1981). Instead, he used an algebraic equation for the equilibrium value of the aspect ratio as a function of the instantaneous strain rate. In other words he knew only of the fixed points in the evolution equations and used this information to obtain an *algebraic* expression for the variation of the aspect ratio along the trajectory of the vortex pair. Implicit in this is the assumption that the shape follows the equilibrium as it migrates towards larger aspect ratios with increasing strain. Hence Saffman's approach may be termed quasi-steady. In reality, because the equilibrium point in a phase plane is a center (as long as the strain rate is below a certain critical value) the aspect ratio will tend to either oscillate about the equilibrium if the strain rate varies very slowly, or, as we will observe in particular cases in Chapter 5, if the strain rate changes sufficiently rapidly the shape will overshoot the equilibrium aspect ratio and undergo permanent deformation or tearing at strain rates below the critical value.

4.2.3. *Elliptic model for axisymmetric vortices*

We shall now incorporate the ideas set forth in the preceding subsection into a derivation of an elliptic model for the axisymmetric case. The development is an assembly of the effects identified previously; for each one there is an available solution in the literature which can be used. The content of each roman numeral item parallels that for the corresponding item in §4.2.2.

(i) *The far-field of a ring vortex.* As in two dimensions, assume that the vortices initially have cores of elliptical cross-section and remain well separated. In two dimensions the notion of separation was based on core size. However, for a vortex ring with a finite core, the presence of two reference lengths, namely, the core dimension and the toroidal radius lead to two definitions of the far-field. The

expansion of the induced velocity in a manner similar to that employed to derive equation (4.2.4) would be valid for points distant according to the more restrictive criterion. It yields a multi-pole expansion in which the coefficients of the various inverse powers of the distance are moments of the vorticity distribution. Even for linearly varying vorticity these are not second order moments of the core shape. The main reason for not using this expansion is that one based on the core size allows for closer interactions. However, only the leading term is expressible in closed form. This term represents the velocity induced by a vortex ring of zero cross-section i.e., a Helmholtz ring located at the shape centroid. From the Biot-Savart law the axial and radial velocities it induces are given by equations (4.1.2)-(4.1.4).

For later use we will also require the strain in the far-field. Differentiating the kernels of (4.1.2) we have

$$\begin{aligned} p \equiv u_{,x} &= \frac{3\Gamma(x - \bar{x})}{2\pi} \int_0^\pi \frac{\sigma \bar{\sigma} \cos \phi - \bar{\sigma}^2}{(A - B \cos \phi)^{5/2}} d\phi, \\ q \equiv u_{,\sigma} &= -\frac{\Gamma}{4\pi} \left[\int_0^\pi \frac{-\bar{\sigma} \cos \phi}{(A - B \cos \phi)^{3/2}} d\phi + \int_0^\pi \frac{3(x - \bar{x})^2 \bar{\sigma} \cos \phi}{(A - B \cos \phi)^{5/2}} d\phi \right]. \end{aligned} \quad (4.2.29)$$

The integral with the 3/2 exponent in the denominator has already been dealt with previously in connection with the velocity field itself and can be expressed in terms of $I_4(\mu)$ and $I_5(\mu)$ defined in (4.1.4). The integrals with a 5/2 exponent can also be expressed in terms of I_4 and I_5 as follows using an identity in Gradshteyn & Ryzhik (2.554.1):

$$\begin{aligned} I_6(\mu) &\equiv \int_0^\pi \frac{d\phi}{(A - B \cos \phi)^{5/2}} = \frac{1}{(A^2 - B^2) B^{3/2}} \left[AI_4(\mu) + \frac{1}{3} BI_5(\mu) \right], \\ I_7(\mu) &\equiv \int_0^\pi \frac{\cos \phi d\phi}{(A - B \cos \phi)^{5/2}} = \frac{1}{(A^2 - B^2) B^{3/2}} \left[BI_4(\mu) + \frac{1}{3} AI_5(\mu) \right]. \end{aligned} \quad (4.2.30)$$

Then (4.2.29) becomes

$$\begin{aligned} p &= \frac{3\Gamma(x - \bar{x})}{2\pi} \left[\frac{1}{2} BI_7(\mu) - \bar{\sigma}^2 I_6(\mu) \right], \\ q &= \frac{\Gamma}{2\pi} \left[\frac{\bar{\sigma} I_5(\mu)}{B^{3/2}} - 3(x - \bar{x})^2 \bar{\sigma} I_7(\mu) \right]. \end{aligned} \quad (4.2.31)$$

(ii) *Induced motion of the centroid.* In the discussion for two-dimensions it was noted that, if a higher-order term in the far-field is retained, a correction term must

be added to the velocity induced at the centroid. Since we keep only the leading term in the far-field, this correction is not applied here. Hence the model for the axisymmetric case is less accurate by one order in the ratio of core size to separation distance and only item A is required:

A. Centroid motion due to the leading-order far-field velocity evaluated at the centroid:

$$\begin{aligned}\dot{\bar{x}}_j &= u(\bar{x}_j, \bar{\sigma}_j; \bar{x}_s, \bar{\sigma}_s) \\ \dot{\bar{\sigma}}_j &= v(\bar{x}_j, \bar{\sigma}_j; \bar{x}_s, \bar{\sigma}_s),\end{aligned}\tag{4.2.32}$$

where u and v denote expressions (4.1.3).

(iii) *Induced evolution of the ellipse shape.* The induced velocity expanded about the centroid of the field vortex is the same as (4.2.7) with y replaced by σ , but, because the conditions of continuity and irrotationality are now, respectively

$$\begin{aligned}u_{,x} + v_{,\sigma} + \frac{v}{\sigma} &= 0, \\ u_{,\sigma} - v_{,x} &= 0,\end{aligned}\tag{4.2.33}$$

the analog of the strain term (4.2.16) takes the form

$$\mathbf{S} = \begin{pmatrix} p & q \\ q & -p \end{pmatrix} \begin{pmatrix} \bar{x} \\ \bar{\sigma} \end{pmatrix} + \begin{pmatrix} 0 & 0 \\ 0 & -\frac{\bar{v}}{\bar{\sigma}} \end{pmatrix} \begin{pmatrix} \bar{x} \\ \bar{\sigma} \end{pmatrix},\tag{4.2.34}$$

where \bar{v} denotes $v(\bar{x}, \bar{\sigma})$. The first term represents plane strain; the contributions to p and q from a single vortex are given in equation (4.2.31). The second term serves to preserve volume in the presence of stretching. It has the form of a unidirectional stretch (for $\bar{v} < 0$) and will be referred to as an ‘‘extra strain.’’ The motion of the boundary is determined from the kinematic condition (4.2.22) which retains the same form with y replaced by σ . Because of its linearity, the effect of the two straining components can be evaluated separately. The first part gives the same evolution equations as in two-dimensions. For the second part, the kinematic constraint becomes

$$\begin{aligned}\frac{\partial h}{\partial t} - \frac{\bar{v}}{\bar{\sigma}} \sigma' \frac{\partial h}{\partial \sigma'} &= 0 \\ \text{on } h(x, \sigma, t) &= \frac{(\bar{x} \cos \varphi(t) + \bar{\sigma} \sin \varphi(t))^2}{a^2(t)} + \frac{(-\bar{x} \sin \varphi(t) + \bar{\sigma} \cos \varphi(t))^2}{b^2(t)} - 1 = 0.\end{aligned}\tag{4.2.35}$$

Carrying out the required differentiations of h and setting each of the coefficients of the monomials \bar{x}^2 , $\bar{\sigma}^2$ and $\bar{x}\bar{\sigma}$ on the left hand side to zero provides a system of three

linear equations for $\dot{a}(t)$, $\dot{b}(t)$ and $\dot{\varphi}(t)$. We display the answer together with the solution for plane strain:

B. Induced evolution of ellipse shape due to plane strain:

$$\begin{aligned}\dot{a}_{f_s} &= e_{f_s} a_f \cos 2(\varphi_f - \bar{\alpha}_{f_s}), \\ \dot{b}_{f_s} &= -e_{f_s} b_f \cos 2(\varphi_f - \bar{\alpha}_{f_s}), \\ \dot{\varphi}_{f_s} &= -e_{f_s} \frac{a_f^2 + b_f^2}{a_f^2 - b_f^2} \sin 2(\varphi_f - \bar{\alpha}_{f_s}).\end{aligned}\tag{4.2.36}$$

C. Induced evolution of ellipse shape due to extra strain:

$$\begin{aligned}\dot{a}_{f_s} &= \frac{\bar{v}_{f_s}}{\bar{\sigma}_f} a_f \sin^2 \varphi_f, \\ \dot{b}_{f_s} &= -\frac{\bar{v}_{f_s}}{\bar{\sigma}_f} b_f \cos^2 \varphi_f, \\ \dot{\varphi}_{f_s} &= \frac{(a_f^2 + b_f^2) \sin \varphi_f \cos \varphi_f}{(b_f^2 - a_f^2)} \left(\frac{\bar{v}_{f_s}}{\bar{\sigma}_f} \right).\end{aligned}\tag{4.2.37}$$

Note that volume (hence circulation) is conserved for the induced evolution.

(iv) *Self-induced motion.* Moore (1980) studied the self-induced motion of a vortex ring with a thin elliptical cross-section. In this limit the core dynamics are locally two-dimensional so the core rotates with the constant angular velocity of the plane Kirchhoff vortex:

D. Self-induced rotation:

$$\dot{\varphi}_f = \frac{\Gamma_f}{\pi (a_f + b_f)^2}\tag{4.2.38}$$

Unlike in two dimensions, however, the core rotation influences the motion of the centroid thus:

E. Self-induced centroid motion:

$$\begin{aligned}\dot{\bar{x}}_f &= \frac{\Gamma_f}{4\pi R_f} \left[\log \left(\frac{8R_f}{\frac{1}{2}(a_f + b_f)} \right) - \frac{1}{4} - \frac{3(a_f - b_f)}{2(a_f + b_f)} \cos 2\varphi_f \right], \\ \dot{\bar{y}}_f &= \frac{\Gamma_f}{4\pi R_f} \left[-\frac{3(a_f - b_f)}{2(a_f + b_f)} \sin 2\varphi_f \right].\end{aligned}\tag{4.2.39}$$

R_f is the impulse radius which is conserved for a vortex in isolation:

$$R_f = \sqrt{\frac{P_f}{\Gamma_f \pi}},\tag{4.2.40}$$

where P_f the impulse of the vortex is

$$P_f \equiv \pi \int_f \omega_\phi(x, \sigma) \sigma^2 dx d\sigma, \quad (4.2.41)$$

which evaluates to

$$P_f = \pi \Gamma_f \left\{ \bar{\sigma}_f^2 + \frac{3}{4} \left[(b_f^2 - a_f^2) \cos^2 \varphi_f + a_f^2 \right] \right\}. \quad (4.2.42)$$

Note that the axial velocity oscillates about a mean value which is less than that given by Kelvin's formula for a circular core with the same area in which case the geometric mean of a_f and b_f replaces their arithmetic mean in the argument of the logarithm in equation (4.2.39).

The interpretation of Moore's solution and its use in a model of interacting rings requires care. First consider an isolated vortex. Since $\mathcal{O}(a/R)$ variations in the shape have been neglected, the explicitly computed volume, circulation and impulse integrals correspond to their conserved counterparts to within error terms of the same order. The Γ_f and R_f in Equation (4.2.39) represent the conserved variables so, for example, R_f should be computed using (4.2.40) and (4.2.42) at the *initial* instant. For interacting rings, R_f changes due to the induced effect of other rings and one must be careful to evaluate it in a manner that would exactly yield the isolated vortex solution in the limit of no induction. For this purpose, rather than evaluate (4.2.40) and (4.2.42) at each instant, we differentiate these expressions and enforce the fact that the self-induced motion does not alter the impulse:

$$\dot{R}_f = \sum_{s \neq f} \frac{\bar{\sigma}_f \dot{\bar{\sigma}}_{fs}}{R_f} + \frac{3}{4R_f} \left[(b_f \dot{b}_{fs} - a_f \dot{a}_{fs}) \cos^2 \varphi_f + (b_f^2 - a_f^2) \dot{\varphi}_f \sin \varphi_f \cos \varphi_f + a_f \dot{a}_{fs} \right]. \quad (4.2.42a)$$

Equation (4.2.42a) represents an additional evolution equation, giving a total of six for each vortex.

Superposition of items A-C (with summation over the index s ($s \neq f$)) together with items D-E for the self-induced motion gives the complete equations for the model. Each is illustrated schematically in Figure 4.1.

4.2.4. The deformation phase plane

The two contributions for the evolution of the aspect ratio and orientation angle due to plane and extra strain can be combined into one which has the appearance

of the former. This makes the analyses of Kida (1981) and a certain phase plane representation introduced by Neu (1984) for two dimensions directly relevant to this study. Including the self rotation term these equations for any vortex become

$$\begin{aligned}\dot{\lambda} &= 2\lambda g \cos 2(\varphi - \varpi), \\ \dot{\varphi} &= g \frac{1 + \lambda^2}{1 - \lambda^2} \sin 2(\varphi - \varpi) + \frac{\bar{\omega}_\phi \lambda}{(\lambda + 1)^2},\end{aligned}\quad (4.2.43)$$

where $\bar{\omega}_\phi$ is the average vorticity ($\Gamma/\pi ab$). These are identical to the deformation equations in two-dimensions (4.2.25) except that the rate of plane strain e is replaced by

$$g \equiv \sqrt{e^2 + \frac{1}{4} \frac{\bar{v}^2}{\bar{\sigma}^2} + \frac{e\bar{v}}{\bar{\sigma}} \cos 2\bar{\alpha}},\quad (4.2.44)$$

which is a “composite” strain rate. The straining angle $\bar{\alpha}$ is replaced by a composite angle

$$\varpi \equiv \frac{1}{2} \tan^{-1} \left(\frac{e \sin 2\bar{\alpha}}{\frac{1}{2} \frac{\bar{v}}{\bar{\sigma}} + e \cos 2\bar{\alpha}} \right).\quad (4.2.45)$$

Figure 4.2 shows contours of $g(x, \sigma)$ for a Helmholtz ring with $\Gamma = 1$. To avoid crowding, contours near the core are not shown. The effect of the axisymmetric geometry is that for the same distance from the core, points with radial location smaller than the vortex radius have higher strain rates than those with a larger radius. In two dimensions, a point vortex induces a radially symmetric strain field. It will be argued in Chapter 5 that the spatial variation of strain rate in the axisymmetric geometry leads to greater susceptibility to tearing in the passage of one vortex ring through another than in the case of two co-rotating vortices in two-dimensions.

Equations (4.2.43) are coupled to and externally forced by the equations of centroid motion via $g(t)$ and $\varpi(t)$. In turn, core deformation affects the motion of the centroid via (4.2.39). If g and ϖ are constant (set $\varpi = 0$ without loss of generality) one recovers the equations analyzed by Kida (1981) and Neu (1984). Consideration of their results, apart from being suitable when g and ϖ vary sufficiently slowly, leads to a useful terminology for describing what is observed in the general situation.

We now review some of the known features of solutions to equations (4.2.43) under fixed strain. First, to find equilibrium shapes (λ_e, φ_e) set the right hand side of the system to zero. The first equation implies

$$\varphi_e = (2n + 1) \frac{\pi}{4}, \quad n = 0, 1, 2, 3.\quad (4.2.46)$$

When this is substituted into the second

$$\frac{\lambda_e (\lambda_e - 1)}{(1 + \lambda_e)(\lambda_e^2 + 1)} = \frac{g(-1)^n}{\bar{\omega}_\phi}. \quad (4.2.47)$$

To proceed, we need to be clearer about how λ and φ are defined. We shall insist that $\lambda \geq 1$ which allows φ to jump abruptly by $\pi/2$ when an ellipse strained along the minor axis transits through a circle. Then the left hand-side of (4.2.47) is positive. For $g/\bar{\omega}_\phi > 0$, n must be even which restricts the equilibria to lie in second and fourth quadrants; conversely for $g/\bar{\omega}_\phi < 0$ equilibria lie in the first and third quadrants. Hence the ellipse is oriented so that its vorticity opposes the strain. The maximum value of the left hand side occurs when $\lambda_e \approx 2.89$ and is ≈ 0.15 , so for values of $|g/\bar{\omega}_\phi|$ greater than this no steady elliptical solutions are possible. As will be shown later, when this happens the vortex will eventually elongate indefinitely. This is the Moore & Saffman (1971) criterion for tearing and quoting them, it says "that a cylindrical vortex has only a finite strength to resist deformation by an imposed strain." For $|g/\bar{\omega}_\phi| < 0.15$ the cubic equation (4.2.47) has two real roots for $\lambda_e \in [1, \infty]$, one on each side of $\lambda_e = 2.89$. To track the migration of the stable root as the strain rate varies is the approach of the quasi-steady elliptic model of Saffman.

To determine the stability of the stationary states, linearize (4.2.43) about them and calculate the eigenvalues, $\tilde{\nu}$, of the system:

$$\frac{\tilde{\nu}^2}{g^2} = \frac{4}{(1 + \lambda_e)^2} \left[\lambda_e^2 + 1 - \frac{4\lambda_e^2}{(1 - \lambda_e)^2} \right]. \quad (4.2.48)$$

For $\lambda_e < 2.89$ the term in brackets is negative; the eigenvalues are purely imaginary implying a neutrally stable center in the (λ, φ) plane, with closed periodic orbits about it. Hence a small perturbation leads to small fluctuations in orientation angle and aspect ratio which is called *nutaton* or *libration*. The frequency of nutation is the imaginary part of the eigenvalues. For $\lambda_e > 2.89$ the eigenvalues are purely real implying an unstable saddle with perturbations leading locally to irreversible elongation.

Both Kida (1981) and Neu (1984) have studied the global behavior of equations (4.2.43) but we prefer to discuss the more graphical and visual presentation of Neu. He considers trajectories in the phase plane $(X, Y) \equiv (\lambda \cos \varphi, \lambda \sin \varphi)$. The equations possess a conserved energy function $\mathcal{H}_e(\lambda, \varphi)$ whose level curves are possible trajectories. For the cases of time varying strain in Chapter 5 the plane

$(X, Y) \equiv (\lambda \cos(\varphi - \varpi), \lambda \sin(\varphi - \varpi))$ will be used to display the pattern of deformation. To acquaint the reader with its interpretation we reproduce Neu's plot for $g/\bar{\omega}_\phi = 0.11$ in Figure 4.3. The dotted lines represent the regime of nutation; solid lines, full rotation and dashed lines, irreversible elongation. The empty areas consist of elongating trajectories which have been omitted for clarity. The thick lines are separatrices which bound the three regimes. Since we have defined $\lambda \geq 1$, trajectories inside the unit circle are not shown. An orbit on the separatrix of the nutating and rotating regions jumps abruptly by $\pi/2$ when it encounters the unit circle. The direction of the jump does not affect the shape of the ellipse.

For other values of $g/\bar{\omega}_\phi$ we shall only describe the features. From the previous discussion, as $g/\bar{\omega}_\phi$ increases, the saddle and center approach each other thus shrinking the region of rotation to narrower annular bands until it disappears altogether at $g/\bar{\omega}_\phi = 0.1227$. At $g/\bar{\omega}_\phi = 0.15$ the center and saddle coalesce and there are no initial conditions (apart from an exceptional set of measure zero) which will not eventually lead to unabated elongation.

4.2.5. *Expected deviations from the elliptic model*

Here we shall discuss the deviations to be expected from the elliptic model arising from more complex core dynamics. If we suppose that the vortex rings are well separated then assumptions about core structure are the most critical, especially for the acoustic signal. The only place where core structure is essential in the elliptic model is in the self-induced motion for which Moore's solution (1980) was used. We consider Moore's (1980) solution and first calculate the acoustic signal it generates. In Chapter 6 this will provide a useful estimate for interacting rings if one of the vortices is in the rotation regime in Neu's phase plane. Then we discuss deviations that may arise in practical situations. Finally we use contour dynamics to assess deviations from Moore's solution for thicker cores.

Of interest first are the time behavior of the acoustic signal and the acoustic efficiency which we define to be the fraction of the total energy of the flow which is radiated during one complete rotation of the core boundary.

According to M6hrring's (1978) theory of vortex sound, the acoustic source function for the axisymmetric case is

$$Q(t) = \int \omega_\phi(x, \sigma, t) x \sigma^2 dx d\sigma. \quad (4.2.49)$$

In terms of $Q(t)$, the acoustic pressure (in the far-field) is

$$p_a(\vartheta, r, t) = \frac{\rho_o}{4c_o^2 r} \left(\cos^2 \vartheta - \frac{1}{3} \right) Q'''(t - r/c_o), \quad (4.2.50)$$

where c_o and ρ_o are the speed of sound and density in the medium at rest, and ϑ is the polar angle.

Next, introduce an axial coordinate x' which moves with velocity $U(t)$ parallel to the x -axis:

$$x' = x - \left(x_o + \int_0^t U(t') dt' \right). \quad (4.2.51)$$

In terms of this coordinate

$$Q(t) = \int \omega_\phi(x', \sigma, t) x' \sigma^2 dx' d\sigma + \left(x_o + \int_0^t U(t') dt' \right) \int \omega_\phi(x, \sigma, t) \sigma^2 dx d\sigma. \quad (4.2.52)$$

The first integral is constant if $U(t)$ is chosen to be Helmholtz's (1858) definition for the speed of an unsteady vortex ring. Saffman (1970) calculated $U(t)$ for a viscous vortex ring, and later Moore (1980) calculated it for the situation we are considering. It can be computed without knowledge of the deviations of the dynamics from local two-dimensionality. Thus, as we shall see, even when the core departs from ellipticity due to curvature effects, the prediction of the acoustic signal remains good. For this velocity, Moore (1980) obtained

$$U(t) = \frac{\Gamma}{4\pi R} \left[\log \left(\frac{16R}{a+b} \right) - \frac{1}{4} + \frac{3(a-b)}{2(a+b)} \cos 2\varphi \right], \quad (4.2.53)$$

$$\varphi(t) = \varphi_o + \frac{\Gamma t}{\pi(a+b)^2},$$

Here R is the "impulse radius" of the core defined by

$$R = \sqrt{\frac{P}{\pi\Gamma}}, \quad (4.2.54)$$

where P the impulse is

$$P = \pi \int \omega_\phi(x, \sigma, t) \sigma^2 dx d\sigma, \quad (4.2.55)$$

which is also the integral in the second term in (4.2.52). The acoustic signal is proportional to the third time derivative of (4.2.52), hence

$$Q'''(t) = \frac{P}{\pi} U'''(t). \quad (4.2.56)$$

The acoustic signal is thus related to the motion of a particular centroid of the vortex. Substitution of (4.2.53) into (4.2.56) gives

$$-\frac{Q''(t)}{C} = \cos 2\varphi, \quad (4.2.57)$$

$$C = \frac{3P^{1/2}\Gamma^{7/2}(a-b)}{2\pi^{7/2}(a+b)^5}.$$

The acoustic signal is thus sinusoidal at twice the frequency of the core rotation.

Since it may be of interest to check this result in the laboratory we shall now discuss possible deviations from it. Consider an experiment in which the core is distorted into an elliptical shape by passing it through a converging section. If the vortex ring is perturbed to an aspect ratio of 1.2 and has a core size to radius ratio of 0.3, the value Kambe & Minota (1983) estimate their apparatus produces, then (4.2.57) together with (4.2.50) predicts an amplitude of 1 Pa. for a Mach number based on translational speed of 0.2. This amplitude is about a fifth of the peak value they measured for colliding vortex rings and is certainly detectable. One may be concerned about the fact that the core structure may evolve during the course of several core rotations. For example, Melander, McWilliams & Zabusky (1987), using a spectral simulation in two dimensions, found that an elliptical vortex with a peaked vorticity distribution, which is closer to the experimental situation, tends to become nearly circular in just two eddy turnover times. Hence Moore's solution may not apply. Nevertheless, if changes of the core structure occur they should be detectable acoustically.

To estimate the effect of viscosity, if we now substitute the expression for the velocity of a viscous vortex ring obtained by Saffman (1970) into (4.2.56) we get

$$Q''(t) = \frac{\Gamma^2 R}{8\pi t^2}, \quad (4.2.58)$$

which is independent of the viscosity. Here t is measured from a virtual origin when the vortex is a Helmholtz ring. Equation (4.2.58) holds so long as the assumptions in Saffman's theory remain valid, namely, that the core is so slender that the vorticity diffuses in a two-dimensional fashion and viscous cancellation of circulation at the axis of symmetry is negligible. Equation (4.2.58) represents the quadrupole part of the noise; according to the formulation of Kambe & Minota (1983) there is also a monopole contribution due to energy dissipation which is negligible in Saffman's theory.

The energy per unit density radiated during the interval $[0, T]$ through a sphere of radius r in the far-field is

$$E_a = \frac{2\pi r^2}{\rho_o c_o} \int_0^T dt \int_0^\pi p_a^2(r, \vartheta, t) \sin \vartheta d\vartheta. \quad (4.2.59)$$

Putting (4.2.50) into this and then setting T to the period of core rotation one obtains

$$E_a = \frac{1}{20c_o^5} \frac{\Gamma^7 R^2 (a-b)^2}{\pi^3 (a+b)^8}, \quad (4.2.60)$$

whereas, from Moore's paper the energy of the hydrodynamic flow is

$$E = \frac{1}{2} \Gamma^2 R \left[\log \left(\frac{16R}{a+b} \right) - \frac{7}{4} \right]. \quad (4.2.61)$$

Let us define the radiation efficiency, η_a , as the ratio E_a/E :

$$\eta_a = \frac{8\pi^2 \epsilon_e^2}{5\alpha'^6 \left[\log \left(\frac{8}{\alpha'} \right) - \frac{1}{4} \right]^5 \left[\log \left(\frac{8}{\alpha'} \right) - \frac{7}{4} \right]} M^5, \quad (4.2.62)$$

where α' , is a measure of the thickness of the core and is defined as

$$\alpha' \equiv \frac{a+b}{2R}. \quad (4.2.63)$$

M is Mach number associated with the average translation velocity, and ϵ_e is a measure of the eccentricity:

$$\epsilon_e \equiv \frac{\lambda - 1}{\lambda + 1}. \quad (4.2.64)$$

For any fixed non-zero value of ϵ_e , as the core shrinks to a point, η_a blows up. However, the acoustic theory remains valid only if the energy radiated away by the sound does not deplete a significant portion of the total energy. Hence, as the core size becomes thin, one must place a limit on the maximum Mach number. Figure 4.4 plots the acoustic efficiency as a function of α' for various aspect ratios for a vortex Mach number of 0.2 which is typical for the vortex rings produced in Kambe's apparatus.

We now describe how the acoustic signal was numerically evaluated for many interacting rings in the elliptic model. In this case, the right hand side of (4.2.52) is to be summed over individual rings, using separate coordinates, each chosen to move at the speed $U_i(t)$ of the Helmholtz centroid of the ring in order to make the first integral in (4.2.52) a constant:

$$Q(t) = \text{constant} + \sum_i (x_o)_i \Gamma_i R_i^2 + \sum_i \Gamma_i R_i^2 \int_0^t U_i(t') dt'. \quad (4.2.64a)$$

The second term above is proportional to the total impulse and is also constant. The speed of the Helmholtz centroid is the speed of the shape centroid minus the speed of the shape centroid relative to the Helmholtz centroid. The latter is provided by Moore (Equation 3.5) so that after substitution Equation (4.2.64a) becomes

$$Q(t) = \sum_i \left(\Gamma_i R_i^2 \bar{x}_i + \frac{3}{8} \Gamma_i R_i (a_i^2 - b_i^2) \sin 2\varphi_i \right) + \text{constant}. \quad (4.2.64b)$$

We shall now study how the acoustic signal of Moore's vortex deviates from solutions computed with contour dynamics for thick cores. These runs constitute a test of the effects of curvature on local two-dimensionality. Two cases were run with the same aspect ratio of 1.5 but different thickness. In the first case, the initial major-axis to radius ratio $a/L_o = 0.30$ which is out of the range of the applicability of Moore's solution. The contour was represented by 300 segments. The initial and final states are displayed in Figure 4.5. The total translation is about 2 radii during which time a particle on the boundary undergoes $3\frac{1}{2}$ revolutions. The core does not remain elliptical; a fine wisp has broken from the surface. The dotted line is the trajectory of the vorticity centroid exaggerated by a factor of 15 for clarity. It undergoes small radial oscillations at twice the frequency of the core rotation in accord with Moore's prediction. The letters A-H indicate centroid positions every half of a particle rotation and Figure 4.6 shows the corresponding core shapes. As your eye follows the top row of frames (A, C, E & G) which correspond to the same phase, observe steepening of the contour at the rightmost point, the formation of a cusp and breaking against the direction of rotation as required by conservation of angular momentum. In the lower row of figures (also at equal phase) note the flattening in the left regions of the boundary, the formation of an indentation, and finally the shedding of a filamentary region. Aside from this wisp, frames F and H have nearly identical shapes. The main difference is that the bump-like region has receded inwards whereas the flattened portion has bulged outward giving the core a rounder appearance. This tendency is depicted quantitatively in Figure 4.7 showing the variation of aspect ratio (of the ellipse fit by moments) with time. The maxima correspond with the upper frames in Figure 4.6 and the minima with the lower ones. Note the secular decline of the mean level of the fluctuations. It is tempting to conjecture that the vortex is approaching a steady state close to a member of the NF family if the shed wisps are ignored. Another possibility is that the core is tending towards a periodic orbit more complicated than a rotating shape. An interesting study would be to numerically determine the family

of periodic orbits from the axisymmetric contour dynamics equations. When the core thickness parameter is increased from zero, one family of solutions would bifurcate from Moore's solution and other families from the two-dimensional rotating solutions of Wu, Overman & Zabusky (1984).

The determination of which, if any, of the two outcomes will prevail is not possible at present because the algorithm loses accuracy when two non-adjacent portions of contours come close together. For example in the above calculation, the relative change in circulation and impulse was -0.05% ; about 60% of this change took place in the last few time steps when the wisp began to thin.

Figure 4.8 shows the axial velocity of the shape centroid (solid) compared with Moore's solution. The theory overpredicts the actual amplitude with an increasing error. One would then expect the acoustic radiation to be overpredicted also. That this is so is shown in Figure 4.9. The amplitude is about 65% of the asymptotic result with a secular decrease and phase drift.

The next case is for a thinner core ($a/L_o = 0.10$) which is better approximated by the theory. Figure 4.10 shows the trajectory of the shape centroid for just over six particle rotations. The letters identify frames in Figure 4.11. Compared to the thick core case they show that a finer wisp is shed after roughly twice as many periods. Figure 4.12 shows that again the aspect ratio oscillates as it decreases. Figure 4.13 shows that the acoustic signal (solid) compared with the prediction (dashed) is excellent.

Studies in connection with azimuthal instabilities (Widnall & Tsai 1977) have shown that to second order in core thickness the effect of curvature is the appearance of strain-like terms. This accounts for the oscillations observed in aspect ratio as follows. Saffman (1978, Equation 4.2) provides an estimate for the strain rate due to curvature. For our case his expression becomes

$$\frac{e}{\bar{\omega}_\phi} = \frac{3ab}{16\bar{\sigma}^2} \left[\log \left(\frac{16\bar{\sigma}}{a+b} \right) - \frac{17}{12} \right], \quad (4.2.65)$$

and evaluates to 0.0023 and 0.039 for the thin and thick core cases. From (4.2.25) the amplitude of small aspect ratio oscillations can be estimated after using the fact that when the aspect ratio is not close to unity and the strain rate to vorticity ratio is small, the self-rotation term dominates and $\dot{\varphi}$ can be taken to be its unstrained value. We obtain

$$\lambda_{\text{amp}} \approx (\lambda + 1)^2 \frac{e}{\bar{\omega}_\phi}, \quad (4.2.66)$$

from which $\lambda_{\text{amp}} = 0.025$ and 0.14 for the thin and thick core cases respectively. This compares well with the observed amplitudes of 0.023 – 0.026 and 0.13 .

The reason for the non-ellipticity and secular decrease in aspect ratio is less clear. Love (1893) showed that an unstrained elliptical vortex is stable to non-elliptical perturbations if $\lambda < 3$. The presence of the weak strain due to curvature is therefore important. The analysis of Moore & Saffman (1971) shows that a strained *steady* elliptical vortex in two-dimensions is stable to non-elliptic perturbations for the present values of $e/\bar{\omega}_\phi$. Thus the conjecture is that unsteadiness in the presence of strain is important and therefore what needs to be considered (as a problem that we would like to suggest) is the stability to non-elliptic perturbations of a two-dimensional elliptical vortex undergoing periodic motion on one of Neu's closed integral curves. The periodic unsteadiness allows the possibility of parametric excitation of non-elliptic modes.

4.3. Summary

We began this chapter by reviewing Dyson's (1893) model for interacting vortex rings. The model assumes that cores are thin, widely separated and always circular. Equations of motion (§4.1.1) were provided and then cast into Hamiltonian form (§4.1.2) in order to discern two conserved quantities. These quantities are the sum of the generalized momenta which corresponds to the linear impulse and the Hamiltonian which corresponds to the total energy for thin non-overlapping cores. The invariants were used to obtain the trajectories at large times for the collision of two identical vortex rings, and, for later comparison with contour dynamics, the asymptotic rate of stretching was given (§4.1.3).

In §4.2, an elliptic model which allows cores to be deformed into ellipses, but which retains the assumptions of thinness and large separation, was assembled from known solutions. An elliptic model for two dimensions has been developed in Melander, Zabusky & Styczek (1986, MZS) by formal expansion of the contour dynamics equations. A similar technique appeared intractable for the axisymmetric case so a simpler approach was followed. The approach was first shown to be valid for two-dimensions in §4.2.2 and was then applied to the axisymmetric case in §4.2.3. It made use of Kida's (1981) analysis for the behavior of an elliptic two-dimensional vortex subjected to strain and Moore's (1980) solution for the self-induced motion of a thin

vortex ring of elliptical cross-section. Section 4.2.4 considered the case of fixed strain, and the terminology of nutation, rotation and tearing was reviewed. Finally, the acoustic signal that Moore's solution generates was studied and the departure from Moore's solution for thick cores were investigated using contour dynamics (§4.2.5). Two deviations were observed. The aspect ratio oscillates with an amplitude that can be accounted for by self-induced strain due to curvature. In addition, the aspect ratio underwent a secular decline accompanied by an instability of a non-elliptic mode, possibly due to parametric excitation by the primary oscillations.

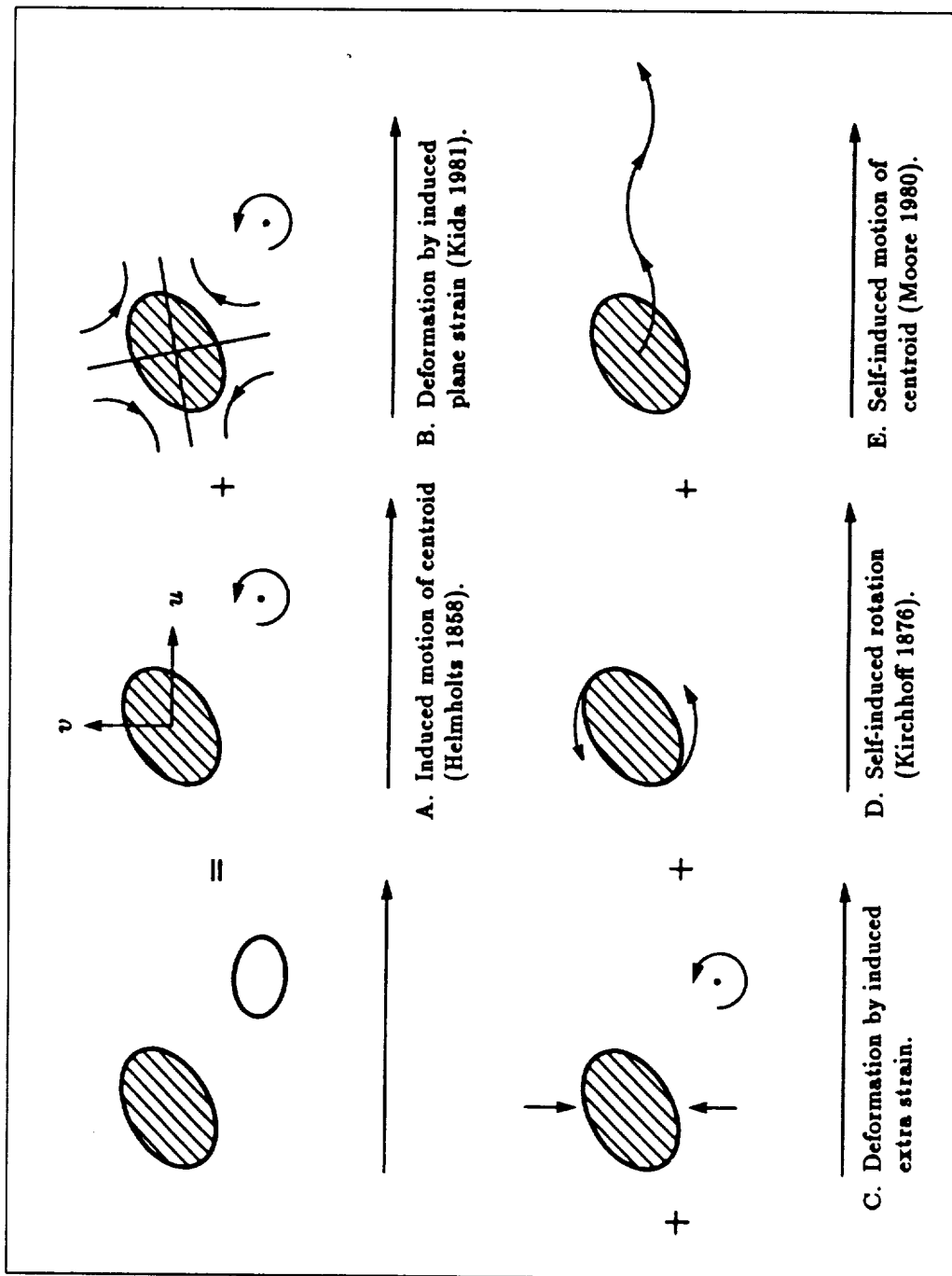


FIGURE 4.1. Schematic of the elements that comprise the elliptic model. The motion of the shaded vortex is of interest. The unshaded ellipse is the inducing vortex, idealized as having zero cross-section for items A-C.

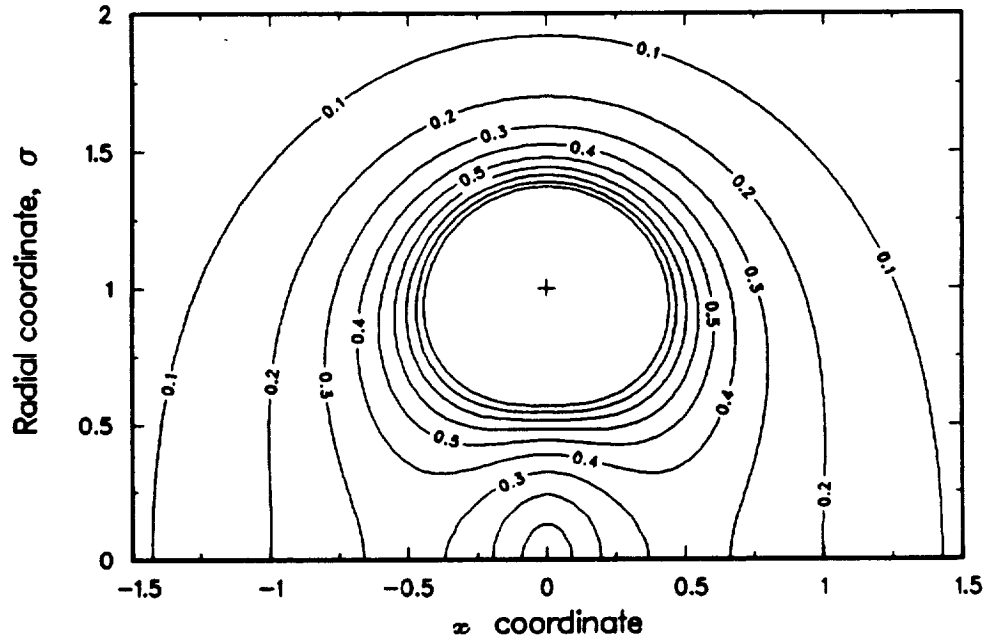


FIGURE 4.2. Contours of the "composite" strain rate g due to a Helmholtz ring of unit circulation and radius.

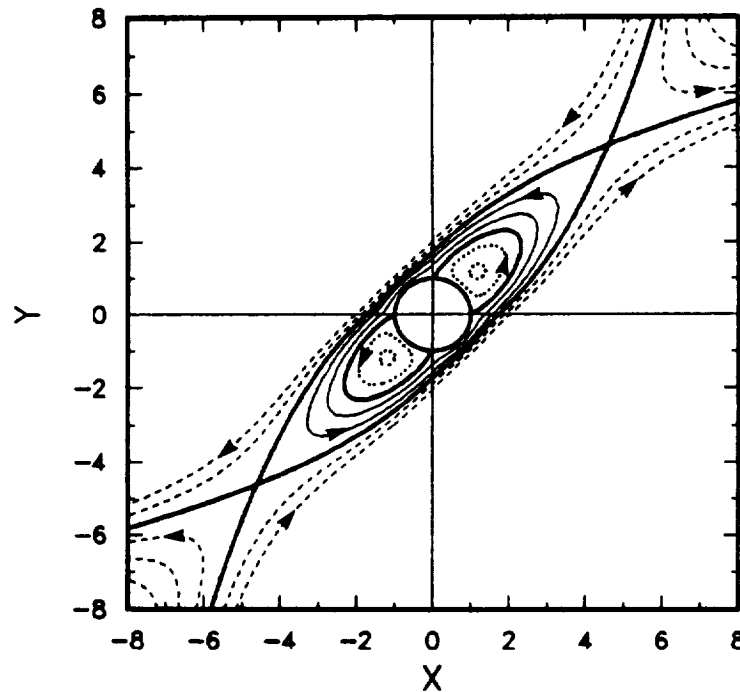


FIGURE 4.3. Phase portrait for the evolution of an elliptic vortex subjected to a fixed strain rate $g/\bar{\omega}_\phi = 0.11$, nutation; —, rotation; ----, elongation; ———, separatrices. After Neu (1984).

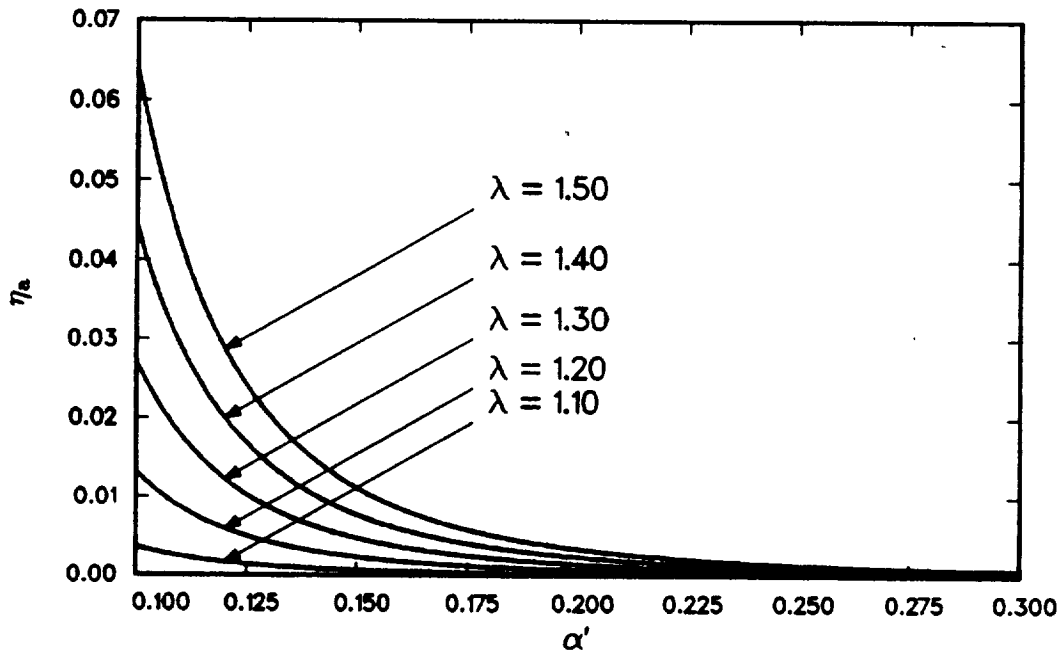


FIGURE 4.4. Acoustic efficiency η_a for Moore's (1980) elliptic core vortex ring as a function of the core thickness parameter α' for several values of the aspect ratio λ .

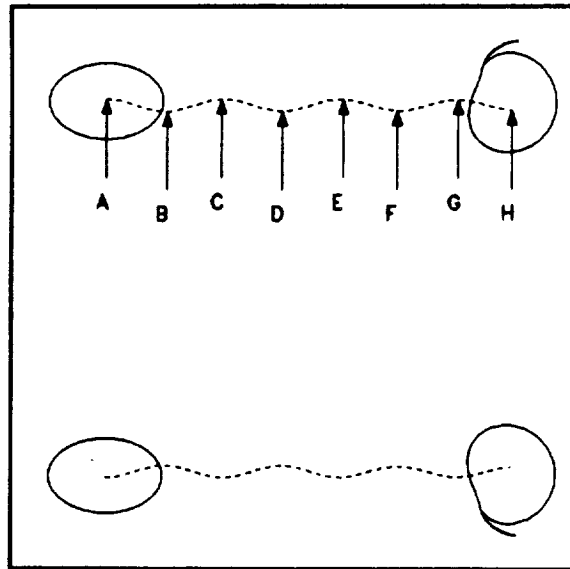


FIGURE 4.5. Motion of an initially elliptical core with an aspect ratio of 1.5 and $a/L_o = 0.3$. ----, trajectory of the vorticity centroid with amplitude *exaggerated* by a factor 15; A-H, indicate instants for which the core shapes are plotted in the next figure.

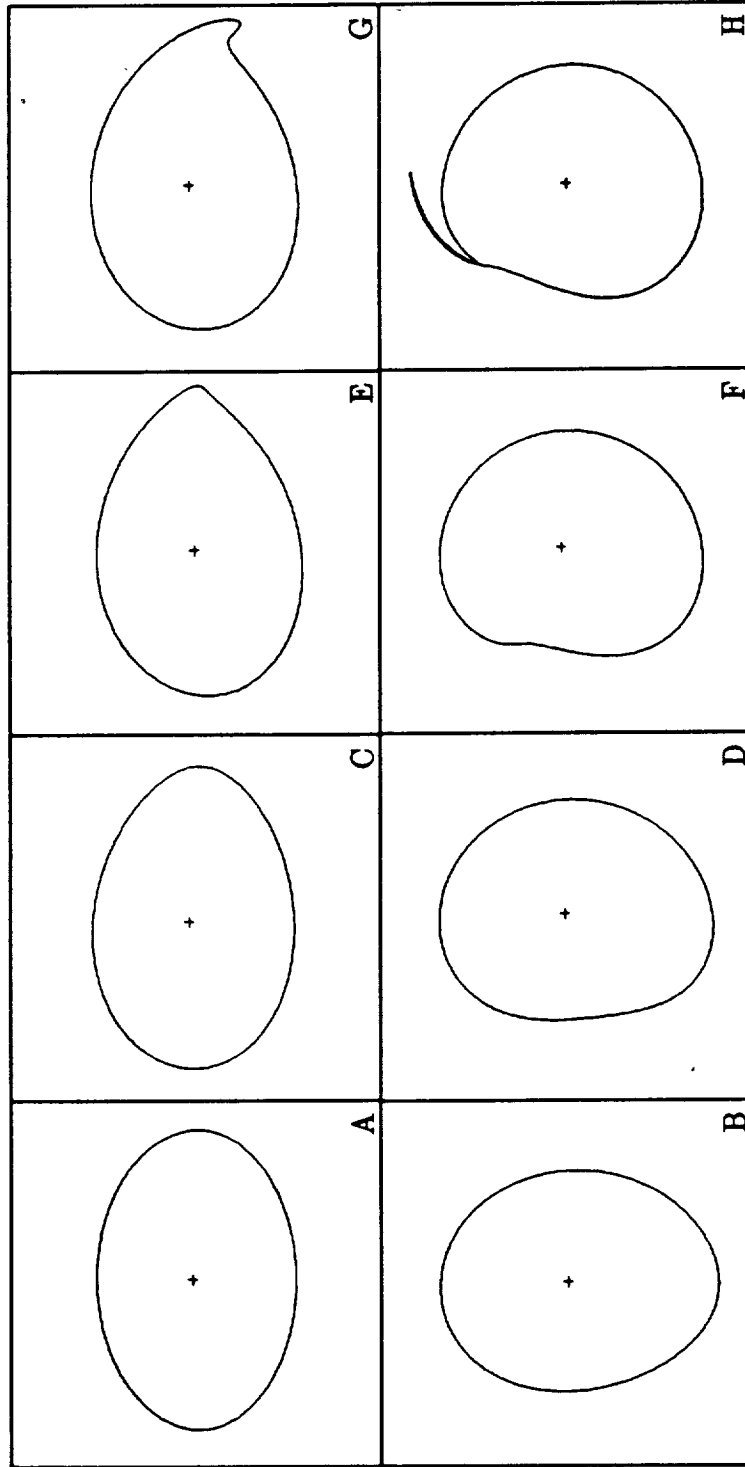


FIGURE 4.6. Core shapes at the instants A-H indicated in the previous figure. The symmetry axis is horizontal across the page. A,C,E,G, shapes at instants of maximum radial centroid; B,D,F,H, shapes at instants of minimum radial centroid. +, vorticity centroid.

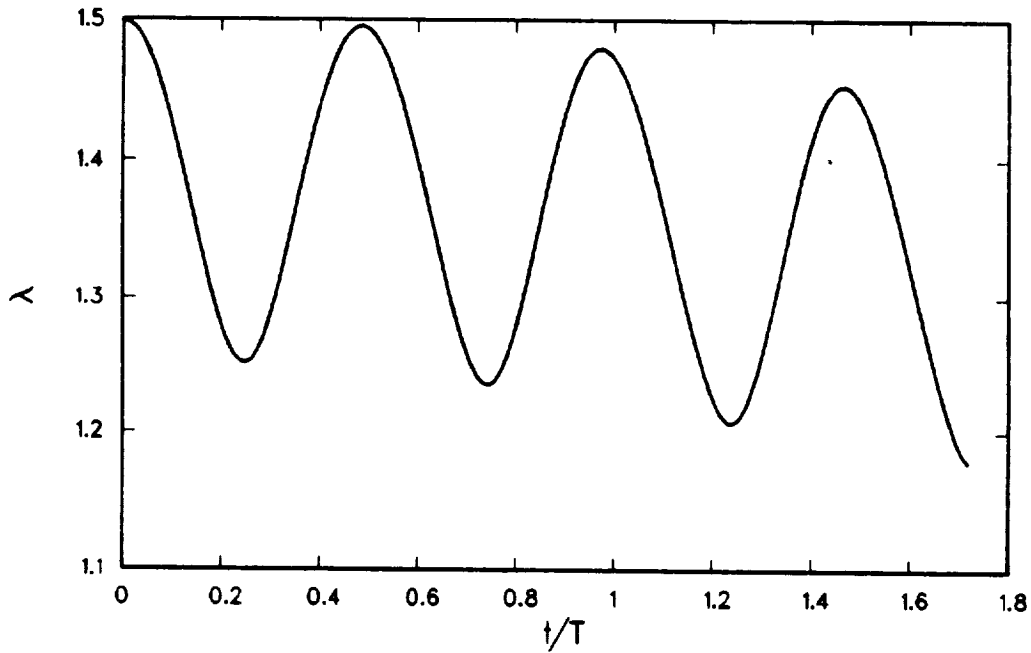


FIGURE 4.7. Variation of aspect ratio for an initially elliptical core with aspect ratio 1.5 and $a/L_o = 0.3$. t/T is the time normalized by the core rotation period.

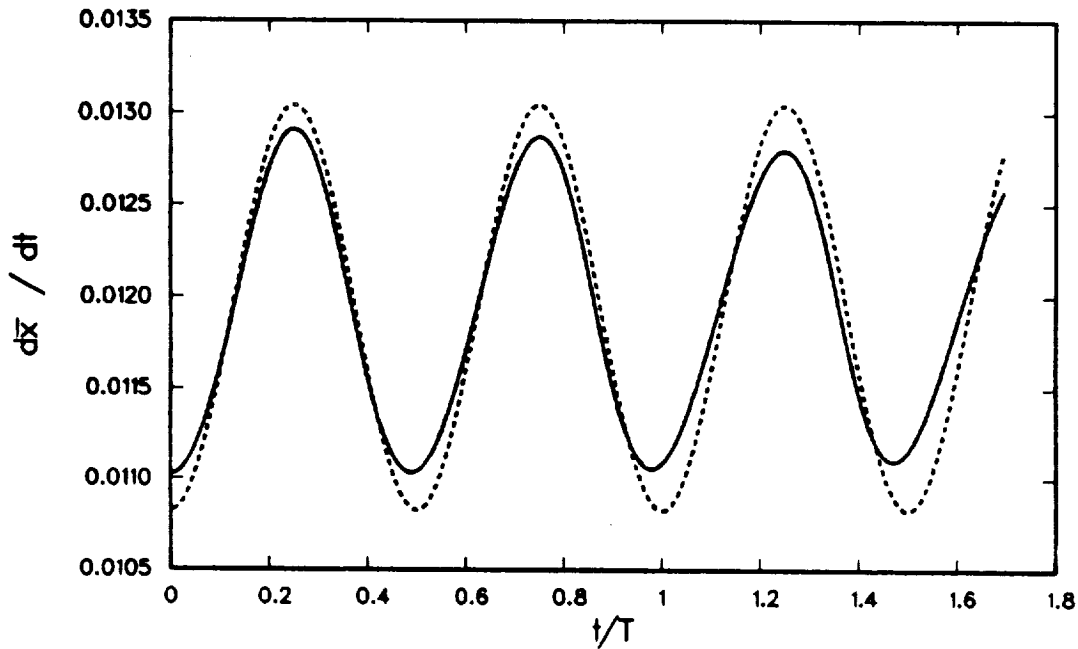


FIGURE 4.8. Axial velocity of the shape centroid for an initially elliptical core with aspect ratio 1.5 and $a/L_o = 0.3$. t/T is the time normalized by the core rotation period. —, contour dynamics; ----, Moore's solution, Equation (4.2.39).

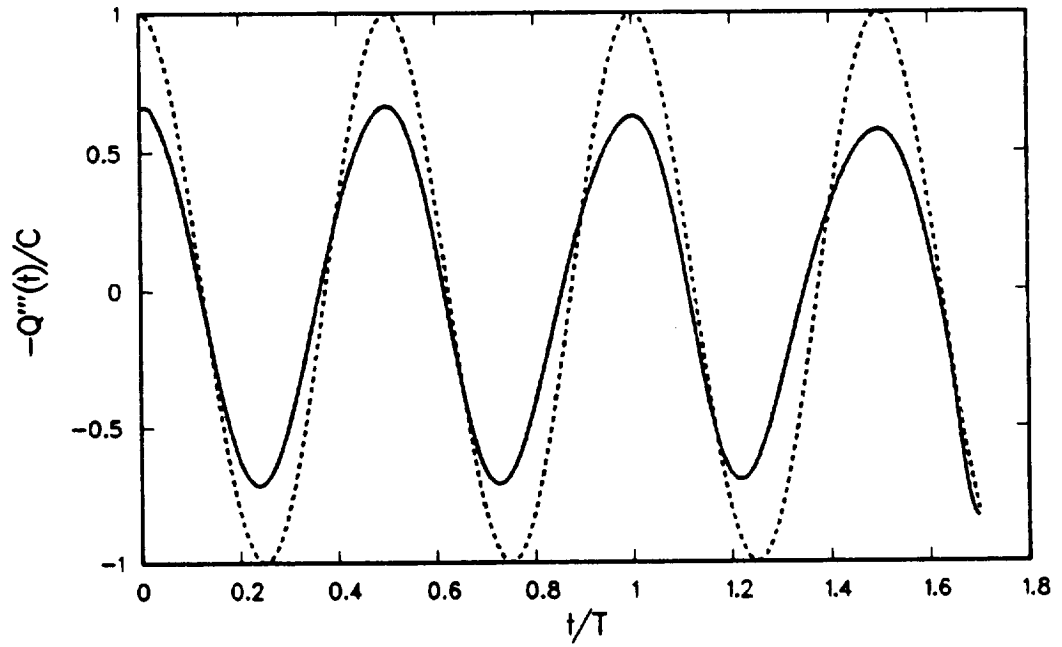


FIGURE 4.9. Acoustic signal for an initially elliptical core with aspect ratio 1.5 and $a/L_o = 0.3$. t/T is time normalized by the core rotation period. —, contour dynamics; ----, asymptotic result, Equation (4.2.57).

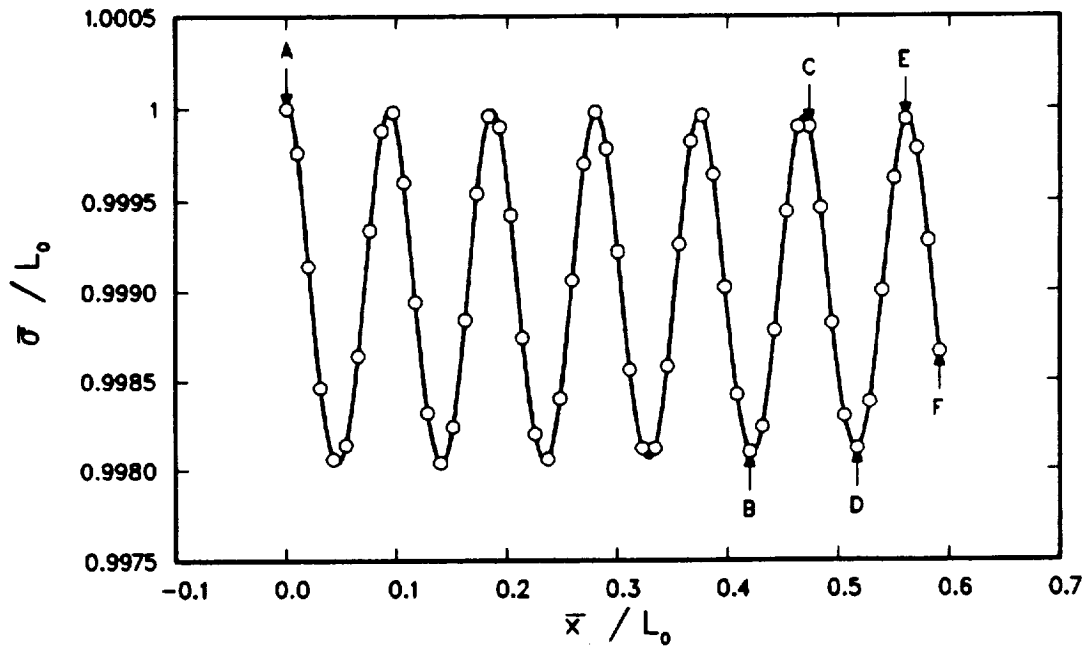


FIGURE 4.10. Trajectory of the shape centroid for an initially elliptical core with aspect ratio 1.5 and $a/L_o = 0.1$. The letters A-F indicate the points for which the core shapes are given in Figure 4.11.

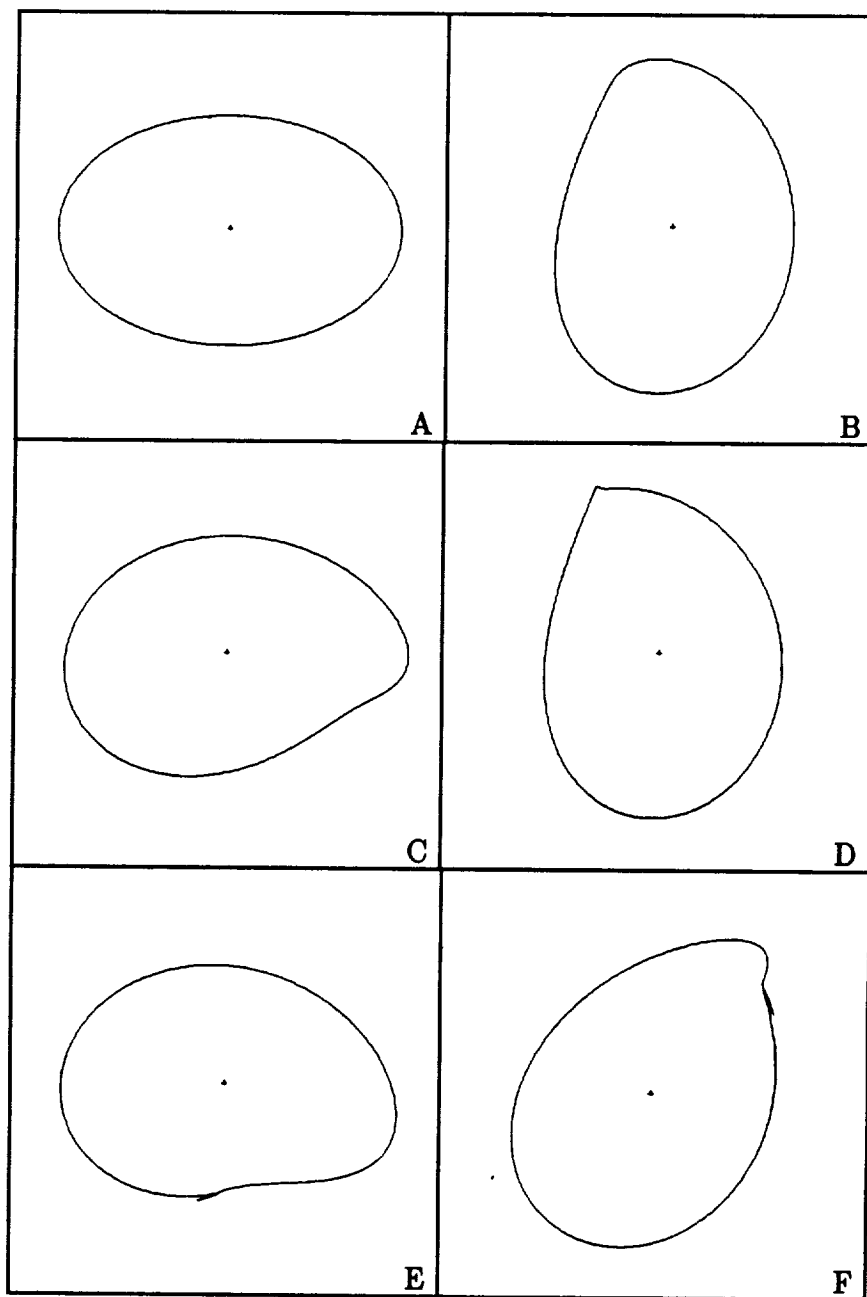


FIGURE 4.11. Core shapes at the instants A-F indicated in the previous figure. The symmetry axis is horizontal across the page. +, vorticity centroid.

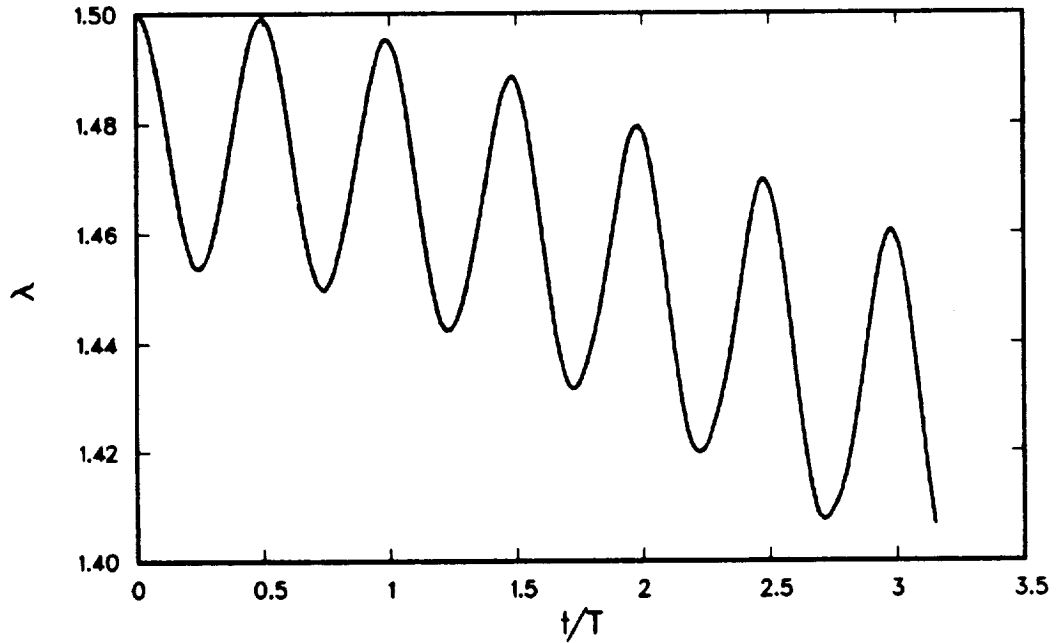


FIGURE 4.12. Variation of aspect ratio for an initially elliptical core with aspect ratio 1.5 and $a/L_o = 0.1$. t/T is the time normalized by the core rotation period.

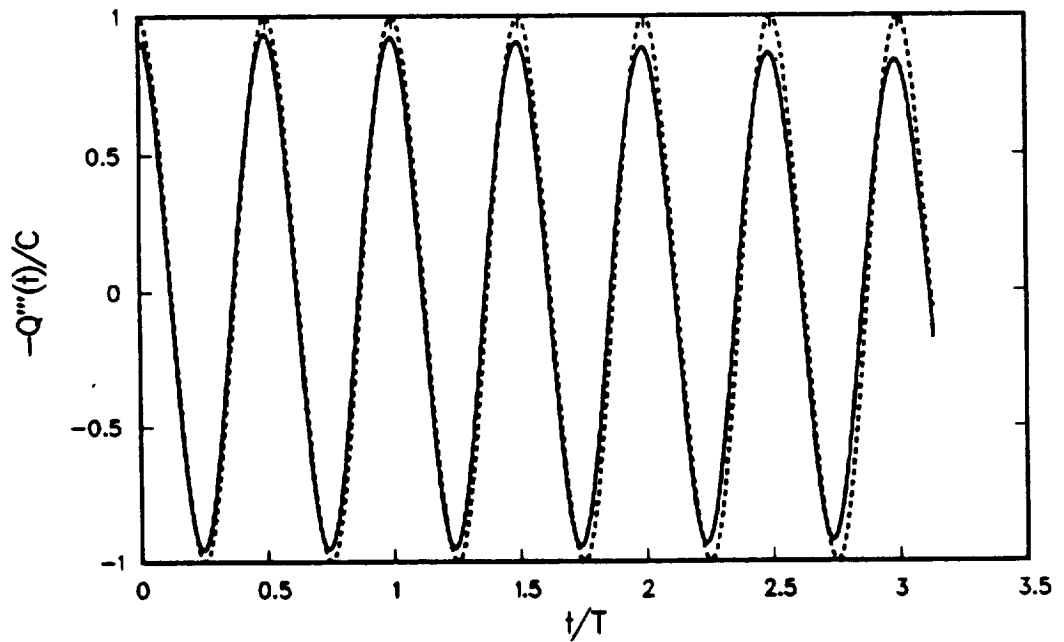


FIGURE 4.13. Acoustic signal for an initially elliptical core with aspect ratio 1.5 and $a/L_o = 0.1$. t/T is time normalized by the core rotation period. —, contour dynamics; ----, asymptotic result, Equation (4.2.57).

ACOUSTICS AND DYNAMICS OF
COAXIAL INTERACTING VORTEX RINGS

Using the contour dynamics method for inviscid axisymmetric flow developed in Chapter 3, we examine the effects of core deformation on the dynamics and acoustic signatures of two coaxial interacting vortex rings. Both "passage" and "collision" (head-on) interactions are studied for initially identical vortices. Good correspondence with experiments is obtained. A simple model developed in Chapter 4 which retains only the elliptic degree of freedom in the core shape is also used to explain some of the calculated features.

Acoustic signals are calculated using the low Mach number theory of Möhring (1978). The final result was given in Equations (4.2.49) and (4.2.50). As these expressions show, to obtain the time behavior of the far-field acoustic pressure requires merely the evaluation of the third time derivative of the centroid of the vorticity as defined by Helmholtz (1858). The time factor of the acoustic pressure is denoted as $Q'''(t)$ in the figures.

Unless otherwise specified, the initial core shapes were chosen from the steadily translating family of solutions computed by Norbury (1973). The initial shapes are parametrized by α which is the ratio of area-effective core radius to toroidal radius L_o . The ratio of initial separation to L_o is denoted as \hat{d} .

5.1. Passage cases

5.1.1. A weak passage interaction ($\alpha = 0.1, \hat{d} = 1$)

Figure 5.1 shows the successful passage of one ring through another. Since Norbury (1973) does not provide them, properties required for normalization were obtained from Fraenkel's (1972) asymptotic analysis. The cores hardly distort and remain slender. One may therefore expect Dyson's model to predict the acoustics well. However, Figure 5.2 shows this not to be the case. Dyson's model (chain-dashed) predicts a minimum when the vortex centers are coplanar and symmetry about this

point. The contour dynamics result (solid) is similar but has superimposed oscillations of unexpectedly large amplitude. These are due to core deformations excited by the straining field of each vortex on the other as we discuss below. The dashed curve is the prediction of the elliptic model.

The acoustic efficiency η_a is the ratio of the energy radiated during the simulation to twice the energy of each vortex in isolation. Dyson's model gives $\eta_a = 2.04M^5$, where M is the Mach number based on the initial self-induced velocity of each vortex. For contour dynamics, η_a is 6.8 times larger. The literature often points to bulk core motion as the source of sound without regard for small variations in that motion. This case demonstrates that, because the signal is proportional to the third time derivative of the centroid, even very small variations in the motion can be significant noise sources.

The frequency of core oscillations scales with the vorticity which, for thin cores and large separations, is larger than the passage frequency. Figure 5.3 plots the spectrum of the acoustic signal calculated for four passages with the elliptic model. The number of data points is 4804 so the highest frequencies shown are well below the sampling frequency. The signal was truncated using the Hanning function

$$f_H(t) = C_H \left(\frac{1}{2} - \frac{1}{2} \cos \frac{2\pi t}{T_s} \right) \quad 0 \leq t \leq T_s, \quad (5.1.1)$$

where T_s is length of the signal and the constant C_H was chosen to give the same energy as the top-hat truncated signal. The passing frequency (about $n = 4$) is not dominant; the peak of the first band occurs at about three times this frequency. This is because overall motion, as represented by Dyson's model, does not produce a sinusoidal signal but rather a peak that is localized about the midpoint of the passage. The second band is due to core deformations. The frequency corresponding to half the initial vorticity is $n = 76$. The dominant frequency is about 25% larger.

Next we discuss the core deformations which produce the high frequency part of the signal. Figure 5.4 shows aspect ratios of the ellipses fit to the moments of the core shapes predicted by contour dynamics. The solid line is for the initially trailing vortex which undergoes compression. This is manifested as a decrease in the frequency of the oscillations. The oscillations occur about a level which increases as the strain experienced by the core increases. The behavior for the initially leading vortex is shown by the dashed line. As it stretches, the frequency of oscillations increases. The level about which oscillations occur varies weakly because the ratio of strain rate to

vorticity varies little: the effect of smaller separation is compensated by the reduced strain at larger radii (see Figure 4.2) as well as increased vorticity.

The above interpretations were suggested by the elliptic model whose results we display in Figure 5.5. The overall features are reproduced. A notable difference is the absence of a dip in the aspect ratio of the compressed vortex halfway through the interaction. This is probably due to the combined effect of thickening of the core and proximity of the cores which violate assumptions of the model. The dotted and chain-dashed lines correspond to the stable fixed point as the strain rate varies. In this case, the oscillations follow the fixed points, however, in the next case the strain rate varies sufficiently rapidly that there is a marked excursion. Notice the aperiodicity of the deformations; both contour dynamics and the elliptic model show a phase lag at the end of the passage for the initially front vortex.

The ellipse orientation (Figure 5.6) shows that the initially forward vortex executes rotations while the rear vortex nutates. The number of peaks in the acoustic signal is twice the number of peaks in the orientation angle of the stretched vortex. At these small aspect ratios the nutation frequency from (4.2.47) and (4.2.48) is

$$\bar{\nu} \approx \frac{1}{2}\bar{\omega}_\phi, \quad (5.1.2)$$

while the rotation frequency is half this. For rotation at fixed strain, the shape repeats every half a rotation as should the acoustic signal. Therefore at small fixed strain, both nutation and rotation produce an acoustic signal with frequency given by (5.1.2). Figure 5.7 shows individual contributions to the acoustic signal for the elliptic model. It is surprising that the self-acoustic-energy for the front vortex which rotates at smaller aspect ratio is 34% larger than for the nutating rear vortex.

The elliptic model is used to consider the effect of equilibrium initial conditions. The NF shapes are perturbed initially by the presence of the other vortex. In the "tamest" initial conditions, the core shapes are in equilibrium with the field induced by the other vortex. We shall not attempt to say if this is more realistic *vis à vis* experiments. The question has to do with the effect on the rolling-up process at the lip of the orifice by the presence of another vortex. A similar situation occurs in the roll-up of aircraft trailing vortices where two halves of the sheet, evolving in the presence of an image, form non-circular spirals.

Figure 5.8 shows the aspect ratio for two passage periods. The initial (equilibrium) value is about 1.025. Small amplitude oscillations are excited on the passing

vortex after the mid-point of the first passage. The increase in efficiency of the acoustic signal (Figure 5.9) over Dyson's model is 1.71 in the first passage, much smaller than for "perturbed" initial shapes.

5.1.2. *A moderately strong passage interaction* ($\alpha = 0.2, \hat{d} = 1$)

For the case shown in Figure 5.10 the core sizes were doubled from the previous case. The solid line was calculated using contour dynamics and the dashed line with the elliptic model. As before, the deformation of the stretched vortex is comparatively weak but the compressed vortex undergoes unabated elongation. Until $\hat{t} \equiv U_o t / L_o = 1.35$ the elliptic model describes the elongation process well. Thereafter a thin filament torn from the trailing vortex begins to wrap around the leading vortex. The vorticity centroid shown as the '+' sign lies outside the vortex and the elliptic model cannot be expected to work well. To continue the calculation beyond $\hat{t} = 1.49$, thinned leading portions of the filament were removed. At $\hat{t} = 1.89$ the core pinches. Subsequently, a thin umbilical sheet connects the captured region and the region that moves away. This umbilical sheet was also removed. 60% of the circulation of the vortex is captured, 24% resides in the sheet-like structure that propagates away and 16% is lost in the removal of thinned regions.

In the two-dimensional case, the analogous interaction is a pair of co-rotating patches. Due to symmetry, moderately strong interactions are characterized by an exchange (Overman & Zabusky 1982*b*) rather than capture of vortical fluid. The asymmetry in the axisymmetric case is due to unequal strain rate histories experienced by the vortices. To realize the two-dimensional outcome would require small core sizes *and* separations compared to the radius. Capture has also been observed in jet shear layers by Hussain (1980): "Evolution of large-scale structures occurs not primarily through complete pairing as widely believed, but frequently through 'fractional pairing' when substructures torn from larger structures pair up, or 'partial pairing' when one structure captures only a part of another."

One may think that the tearing occurs because the strain rate exceeds the axisymmetric equivalent of the critical value above which no stable equilibrium exists (Moore & Saffman 1971). In §4.2.4 we saw that for $g/(\Gamma/\pi ab) > 0.15$ a vortex subjected to fixed strain will elongate for any initial condition. Figure 5.11 shows that the strain-rate at the passing vortex remains well below the critical value. The reason for the elongation is that the strain-rate and its orientation vary sufficiently rapidly that

the core shape overshoots the equilibrium and finds itself in a regime of elongation. This is depicted in Figure 5.12 where the solid line shows the aspect ratio for the elongating vortex and the dotted line is the stable equilibrium value corresponding to the strain rate of the previous figure. The deviation from equilibrium is marked.

The two-dimensional analog is two co-rotating vortices. Compare equivalent elliptic models for the axisymmetric and two-dimensional cases. By equivalent we mean that in the two-dimensional model only the point vortex part of the far-field is considered in determining the strain rate and the motion of the centroids. Such a model has been considered by Moore & Saffman (1971). For the two-dimensional model, the strain is constant in time so whether tearing occurs is determined by the initial conditions and the Moore & Saffman criterion applies. Further, it is known (Moore 1979) that for two circular vortices to tear according to the elliptic model, they must initially overlap! Two-dimensional vortices tear due to the larger strain on the major axis side than the point vortex value given by the elliptic model. Roberts & Christiansen (1972) found that for initially circular vortices, d/δ , the separation to core radius ratio had to be less than 3.4 for (convective) merging; Saffman & Szeto (1980) found no steady co-rotating solutions to be possible for $d/\delta_s < 3.16$, where δ_s is the area-effective core radius. The present case has $d/\delta_s = 5$, yet tearing occurs. Variation of strain is therefore important in the axisymmetric case.

Consider plane shear layers. The Moore & Saffman criterion does account for tearing because, in a linear array of vortices, the strain can be supercritical if the spacing is small enough (Moore & Saffman 1975a). Consider however a *pairing* interaction in which the condition for tearing is not met but vortices in the array co-rotate due to the sub-harmonic instability. The strain-rate does vary and deviation from equilibrium may occur, a dynamic (non-linear) effect not accounted for in the stability analyses. In axisymmetric arrays additional strain variations occur due to curvature and this may be one reason (in addition to azimuthal instabilities) why axisymmetric shear layers exhibit less organization than planar ones. According to Zaman & Hussain (1984), Clark's (1979) flow visualization experiments reveal enhanced tearing and fractional pairing in jets compared to plane mixing layers. It is likely that overshoot due to strain variation accounts for this.

We now discuss the acoustic signal shown in Figure 5.13 up to $\hat{t} = 1.49$ when the wisps were cut. In addition to oscillations, there is a large dip associated with local elongation, viz the rolling up of the wisp. Uniform elongation prior to this time

does not result in a significant deviation from Dyson's model (chain-dashed) nor does the uniform elongation of the elliptic model. The acoustic efficiencies are $4.62M^5$ for Dyson's model and $23.6M^5$ for contour dynamics.

The long-dashed curve in Figure 5.12 shows the aspect ratio for the rear vortex corresponding to equilibrium initial conditions. Elongation is not prevented and the long-dashed curve in Figure 5.13 shows that apart from a phase lag resulting from a smaller self-induced velocity (see the remark following Equation 4.2.42) the acoustic signal is almost identical to Dyson's model. We conclude that the acoustic signal is sensitive to small changes in initial conditions but whether elongation occurs is not affected. Uniform elongation does not yield a significant contribution to the acoustic signal.

Next, a passage interaction with the same circulation and core size as the present case but a peaked vorticity distribution is studied using the vortex filament method described in Appendix 5.B. The rings employed are due to Fraenkel (1972) and are discussed further in §5.B.4. Relative to the linear vorticity case, the vorticity is stronger in the inner region but weaker in an outer band. Specifically, in units of Figure 5.63, the linear vorticity varies between 6.37 and 9.56. Is this distribution more or less resilient to being strained?

First the filament method is benchmarked for the linear vorticity case. The initial discretization is documented in Appendix 5.B. Figure 5.14 compares the location of filaments (dots) with the contour dynamics result (solid line). The agreement is excellent until sheet-like regions form and resolution degrades. In particular, note the clumping of filaments in the sheet-like regions in a manner suggestive of Kelvin-Helmholtz instability. This is not present in the contour dynamics result. Figure 5.15 shows the filament calculation beyond the final instant possible with contour dynamics. It shows that the thin region which initially avoided being captured is eventually captured. The acoustic signal is the chain-dotted curve in Figure 5.13. It is almost identical to the contour dynamics result until the latter has a sharp dip. The signal for the entire calculation is provided separately in Figure 5.16.

Figure 5.17 shows a passage for peaked vorticity. Except for a fine wisp that is captured by the front vortex the passage is successful! A spiral arm forms, similar to that which is later observed for the $\alpha = 0.18$ linear vorticity case. The second passage shown in Figure 5.18 is also successful. The passing vortex again forms a spiral arm and there is an exchange of filaments between the vortices.

The acoustic signal is shown in Figure 5.19; note the higher frequency of the initial oscillations and the production of higher harmonics. To obtain an indication of the dominant frequency, a spectrum (Figure 5.20) was calculated but, as the length of the record here is not long and fine scales are unresolved, we urge caution in its interpretation. The peak frequency is 0.47 of the initial maximum vorticity and corresponds to 16 oscillations in the record.

5.1.3. Behavior in the range $0.1 < \alpha < 0.2$, $\hat{d} = 1$

Because the differences between the $\alpha = 0.1$ and $\alpha = 0.2$ cases proved to be so dramatic, the elliptic model was used to probe intermediate values of α at intervals $\Delta\alpha = 0.02$. The purpose of the study was to identify the significant qualitative differences that occur as α changes, and to examine the extent to which contour dynamics also exhibits these differences. For the contour dynamics simulations, because Norbury (1973) did not provide the steady core shapes in this range, the asymptotic solution of Fraenkel (1972) valid for small α was used.

First the $\alpha = 0.1$ case for the elliptic model was extended to give 8 passages of the initially rear vortex and the near-periodic behavior of the deformation was verified. Attention will focus mainly on the initially rear vortex and to avoid repetition it will be referred to as 'the vortex.'

Figure 5.21 shows the aspect ratio for $\alpha = 0.12$ during 6 passages. The dashed line is the equilibrium value corresponding to the instantaneous strain rate. The largest value of strain occurs when the vortex is almost directly below its partner. The strain remains relatively small and constant during those periods in which the vortex is being stretched and passed. During the first passage there is nutation about the equilibrium. An overshoot occurs when the strain changes rapidly but then the oscillations follow the equilibrium and there is no permanent deformation. In the second passage, the overshoot is larger and the mean of the oscillations fails to relax to equilibrium. The orientation angle shows that this is accompanied by a transition from nutation to rotation. In the first four passages, the aspect ratio rises after each passage but is later reduced.

For $\alpha = 0.14$, similar behavior is observed except that permanent deformation occurs. A phase diagram is displayed in Figure 5.22. The distance of a point from the origin is the aspect ratio and the angle with respect to the X -axis is the orientation relative to the instantaneous strain axis, the equilibrium being situated on a 45°

line. The initial condition lies on the unit circle at arbitrary orientation, however, an infinitesimal time later it becomes aligned with the strain direction and begins nutating. The solid circles mark points at which the radius is a minimum; the points of maximum rate of change of strain slightly precede these. Overshoot followed by relaxation to a cycle of higher aspect ratios consistently occurs in the vicinity of these points.

Next we investigated whether this behavior is exhibited by contour dynamics. Figure 5.23 depicts successive instants during a single passage. The net increase in the aspect ratio of the passing vortex is evident at the last instant. Also noticeable is a region of large curvature where a wisp later forms leading to breakdown of the simulation. Aspect ratios are shown as circles in Figure 5.24. Overshoot and excitation to higher aspect ratio are present and satisfactorily follow the prediction of the elliptic model (dashed line). We cannot state with certitude that subsequent wisp formation will not significantly diminish the excitation. In §4.2.5 it was observed that, for finite cores, deviations from the elliptic model are manifested as slow reduction of aspect ratio via wisp formation. It was conjectured that this is an analog of the Love (1893) instability that occurs in the axisymmetric case at aspect ratios less than 3 due to parametric excitation by the straining field of the vortex itself. It is believed that this phenomenon occurs here with the induced strain also playing a significant role.

The transition from nutation to rotation at higher aspect ratios causes larger acoustic amplitudes in the second half of the passage as shown in Figure 5.25. The efficiency of the radiation is $\eta = 15.02M^5$, larger than in the $\alpha = 0.1$ case in which the vortex always nutates. In both cases, the second vortex rotates with small eccentricity. If it is assumed that during the period of weak strain at the end of the passage each core is rotating independently, then Equation (4.2.57) can be used to estimate the amplitude. Using mean values of the required quantities at the end of the passage gives an amplitude of 10.8 which is close to the observed value; 85% of the sound comes from the vortex with larger aspect ratio.

Recall that for $\alpha = 0.2$ tearing is observed at the first passage. For $\alpha = 0.18$ the elliptic model predicts tearing at the third passage. The largest strain rate is 40% of the critical tearing value. Figure 5.26 portrays the deformation in the phase plane. The circle for $\lambda = 3$ is the critical value in two-dimensions for *non-elliptic modes* to become unstable in the absence of strain (Love 1893). At the first passage the overshoot grazes this point but settles down to a cycle with $\lambda_{\max} = 2.4$. At the

next passage, there is overshoot followed by undershoot during which the shape becomes nearly circular. The ensuing cycle has a lower $\lambda_{\max} = 2$. Unabated elongation along the strain axis occurs at the third passage (fifth if both vortices are counted). In experiments (Oshima & Asaka 1977; Yamada & Matsui 1978, 1979) the number of successful passages of dye before strong deformation and merging occurs ranges between 1 and 4 (counting both vortices). Successive excitations of the aspect ratio followed by eventual excitation into a regime of elongation may be the process. Asymmetric weakening by diffusion observed by Stanaway, Cantwell & Spalart (1988a) (see §2.9), would also play a role.

The contour dynamics result for $\alpha = 0.18$ is shown in Figure 5.27 with the corresponding aspect ratios in Figure 5.28. The grazing of $\lambda = 3$ predicted by the elliptic model is also realized in the simulation but then the instability to a non-elliptic mode is accompanied by a larger drop in aspect ratio than in the model.

Finally, for completeness, we mention that for $\alpha = 0.16$ the elliptic model again predicted tearing at the third passage. The main differences with the previous case were that at the first passage the aspect ratio peaked at the lower value of 2.25 followed by a cycle with $\lambda_{\max} = 1.75$. However, at the second passage, instead of de-excitation there was excitation to a cycle with $\lambda_{\max} = 3$.

These examples demonstrate that weak strains that fluctuate sufficiently rapidly can excite (or de-excite) permanent elongation. This fact may be used to devise schemes to control the break-up and acoustic emission of vortices in plane and axisymmetric shear layers. Where shrouds may be used, the strain may be induced by bumps in the wall.

5.1.4. *Passage of $\alpha = 0.40$, $\hat{d} = 2$*

Figure 5.29 compares core shapes with the experiment of Oshima, Kambe & Asaka (1975). The elliptic model predicts that for the rear vortex, the critical value for tearing is exceeded at $U_o t / L_o = 3.11$ (roughly frame (b)). The rear vortex is considerably elongated near the symmetry axis and develops an anchor shape as part of it rolls up around the leading vortex. This and other cases ($\alpha = 0.18, \alpha = 0.20$) show that the remnants of tearing protrude towards, or are deposited along, the axis of symmetry. This may explain why, unlike the plane mixing layer, axisymmetric jets do not exhibit phase coherence between velocity traces on the high and low speed sides (Zaman & Hussain 1984). The acoustic signals are given in Figure 5.30.

We end with some studies using the vortex filament method. The method was first tested for the linear vorticity distribution using 316 filaments per vortex. Figure 5.31a compares the filament locations with the contour dynamics result at the final instant. Aside from a small lag in the position, the agreement is very good. The acoustic signal shown in Figure 5.32 (long dashed) also agrees well except for the final dip, a feature also observed for $\alpha = 0.2$. Figures 5.31b and c are two results for a *peaked* distribution having the same circulation and area-effective core size as the linear case. For (b) the core overlap factor f_c defined in §5.B.4 was chosen to be 3, the same as for the linear vorticity case but the resulting flow had 11.1% more energy. For (c), with $f_c = 5.9$ the energy is the same as case (a). The initial vorticities for the two cases are compared in Figure 5.33. The more energetic distribution is more peaked and the corresponding configuration (Figure 5.30b) leads the contour dynamics result. There are no other significant differences from the linear vorticity case. This is unlike the $\alpha = 0.2$ case in which the peaked distribution was more robust and the passage was successful. Figure 5.34 compares the speeds of the vorticity centroids of each ring for the three filament computations and contour dynamics. The peaked distributions have oscillations due to inherent unsteadiness. This unsteadiness is present because, as explained towards the end of Appendix 5.B, the vorticity distribution employed is steady only for small α . The oscillations are greatly magnified in the acoustic signal shown in Figure 5.32. The initial frequency is about 0.39 of the peak vorticity. For the linear vorticity case, the period associated with half the vorticity at the center of the core is 6.29 and corresponds well with the period of the first acoustic oscillation, which is about 6.25.

5.1.5. *Characteristics of jet noise spectra*

The main features of the acoustic signals presented for passage interactions can be summarized as follows. Oscillations occur at a frequency corresponding to half the instantaneous average vorticity. This reflects elliptic mode core nutation and rotation. In cases in which the passage is not successful and one vortex is captured by the other, the combined vortex continues to radiate at the same frequency as exemplified by the filament method continuation of the $\alpha = 0.20$ case. This is analogous to an isolated elliptic vortex ring which has a purely sinusoidal signal at half the vorticity (see §4.2.5). For peaked vorticity distributions the frequency of acoustic oscillations is roughly half the initial peak vorticity. In the case where the passage was successful

($\alpha = 0.1$) the spectrum also had another peak at three times the passing frequency. This is due to the bulk motion of the cores which produces a localized peak about the midpoint of the passage. The precise form of the initial conditions is important: if the shapes are initially in equilibrium with respect to the strain field of the other vortex, the amplitude of the high-frequency part of the signal was substantially reduced. This is probably a rare occurrence, however.

The purpose of this subsection is to document the presence of a frequency equal to half the vorticity in jet noise measurements and the absence of a peak at the passing frequency. We shall focus mainly on the experiments reported in the following series of papers: Zaman & Hussain (1980, 1984), Hussain & Zaman (1980, 1981) and Zaman (1985), which shall be denoted by roman numerals I-V, respectively. The last paper contains acoustic spectra while the rest document other flow characteristics, including the vorticity. The following notation is employed: St_D : Strouhal number based on jet diameter and jet exit velocity, U_e ; Re_j : Reynolds number similarly defined; f_p and f_{jc} denote preferred and jet-column excitation frequencies (Hz), respectively.

In addition to the natural jet, three modes of excitation were employed in the experiments: (i) the shear-layer mode in which several successive pairings of vortices with initial core dimension comparable to the momentum thickness, θ_m take place if the shear-layer is laminar; (ii) the preferred mode ($St_D = 0.3$) in which the shear layer forms vortices with elongated cores (they are rounder with increasing Re_j) which do not pair but undergo azimuthal break-down (The preferred mode is the most frequent occurrence in a natural high speed jet with white background noise (II, IV)); (iii) the jet-column mode (I, III, $St_D = 0.85$) which results in strong vortex pairing of thicker core vortices regardless of the state of the exit boundary layer.

Let us first consider the preferred mode and assume, contrary to the conjecture in Hussain (1983) that the azimuthal breakdown will not significantly contribute to jet noise. This is suggested by the analysis of Michalke (1983) who demonstrated that a large azimuthal coherence length is necessary for sound generation by a monopole ring. We then suppose that internal core dynamics produce sound at a frequency equal to half the peak vorticity so that the Strouhal number is

$$St_D = \frac{(\omega_\phi)_{\max} D}{4\pi U_e}. \quad (5.1.3)$$

Now in IV (Table 2) it is found that the peak phase averaged vorticity scaled on the preferred mode frequency is the same for different Re_j and state of the initial boundary layer even though the size and orientation of the structures changes:

$$\frac{(\omega_\phi)_{\max}}{f_p} = 10.25 \pm 0.95, \quad (5.1.4)$$

where

$$f_p \equiv 0.30 \frac{U_c}{D}. \quad (5.1.5)$$

Substituting (5.1.4) and (5.1.5) into (5.1.3) we get for the acoustic frequency

$$St_D = 0.24 \pm 0.02, \quad (5.1.6)$$

which agrees well with the peak at $St_D = 0.25$ observed for both the high speed natural jet cases as well as those forced in the preferred mode (V: Figures 11, 12, 13b-d, 15, 16).

Let us now turn to the jet-column mode which is represented by the ring passage simulations. The absence of a peak at the passing frequency in the simulation spectra is not without precedent. Moore (1977a, 1977b) has provided a puzzling piece of evidence. Forcing at 0.2% of the jet velocity was applied in the jet-column mode. Pairing of axisymmetric vortex rings was observed via flow visualization at about three diameters downstream of the exit, and an acoustic telescope technique located the acoustic source for all frequencies around the pairing location. Yet a subharmonic was not detectable in the acoustic spectra though it is present in velocity spectra (V). This led some to question the acoustic significance of pairing even when it is present. Imagine that in a simulation, one vortex is created and propagates with its self induced velocity U_o and that the second vortex is created $T_c = \hat{d}L_o/U_o$ later. Then the ratio of the passing period T_p to the creation period is $U_o T_p / \hat{d}L_o$. For the present cases this ratio is about 2.0 so the passing frequency is roughly the subharmonic of the forcing frequency.

More comprehensive data for the jet-column mode is provided in V. It has $Re_j = 60,000$ for which the exit boundary layer is laminar; the level of forcing is 1% of the jet velocity at $St_D = 0.85$. There is periodic vortex pairing with little jitter. Noise spectra are given in V: Figures 7 and 8 at two angles to the jet axis. A small but noticeable subharmonic spike is present. The peak in the spectrum occurs at six times the subharmonic at $St_D = 2.55$. If the shear-layer mode were present it would

contribute at $St_D = 1.5$ and the natural jet spectrum does have such a peak. If the higher frequency peak in the forced case is due to elliptic mode core deformations at half the peak vorticity then one should have

$$\frac{(\omega_\phi)_{\max}}{f_{jc}} = 38.0. \quad (5.1.7)$$

An earlier paper (III) provides phase averaged vorticity contours unfortunately for $Re_j = 32,000$ but with forcing at the same St_D . However it is stated that the ratio of the peak vorticity in the rolled up cores to the peak vorticity in the Blasius boundary layer in the pipe is 0.60. We shall assume that this ratio holds for the experiment at $Re_j = 60,000$ and combine the following facts:

$$(\omega_\phi)_{\max} = 0.60(.4696)^2 \frac{U_e}{\theta_m}, \quad \theta_m/D = 0.004, \quad f_{jc} = \frac{0.85U_e}{D}. \quad (5.1.8)$$

The expressions are 0.60 of the peak vorticity for the Blasius solution, the momentum thickness at the exit from V:Figure 26 and the forcing frequency. One obtains

$$\frac{(\omega_\phi)_{\max}}{f_{jc}} = 38.9, \quad (5.1.9)$$

which agrees very well with (5.1.7).

In conclusion, there is evidence that peaks in measured acoustic spectra correspond to half the peak phase averaged vorticity in both the preferred and jet-column modes; this is consistent with elliptic mode core deformations being the sound source. It is possible that other features such as the breaking of waves on the boundary may also radiate at the same frequency. In the jet-column case this frequency is larger than the pairing frequency.

On the other hand, laminar shear layer mode pairing (e.g. in natural low speed jets) does produce a peak at the pairing frequency. If several stages of pairing take place, as happens under forcing, then subharmonics are also present. For example, V: Figures 13a and 17c-d show two distinct peaks, one at the forcing frequency and another at a frequency six times larger. Zaman believes (and we agree) that part of the noise is internal to the jet facility and that the high frequency peak corresponds to the first stage of pairing. For example for V:Figure 13a, $Re_j = 120,000$ which implies from V:Figure 2a that $\theta_m/D = 0.003$. The roll-up frequency corresponds to $St_{\theta_m} = 0.012$ so that the subharmonic is at $St_D = 2.0$ which is close to the high

frequency peak at $St_D = 2.3$. In these low-speed cases even high amplitude preferred mode forcing up to 1.25% of the jet velocity does not eliminate the high frequency peak suggesting that shear layer mode pairing is still present.

The current study has not addressed interaction of vortex rings that are closely spaced, have thin cores and hence result in nearly two-dimensional interactions that are characteristic of shear layer mode pairing. Investigation of this region of the parameter space is planned and preliminary results indicate that because of local two-dimensionality the angular velocity of the line joining the centers of the vortices is constant resulting in one period of a nearly sinusoidal signal for the overall motion (Dyson's model). This is analogous to the acoustic signal that Moore's elliptic core vortex ring produces in half a rotation. On the other hand, recall that for jet-column like interactions Dyson's model produces a localized peak at the midpoint of the passage. When core deformation effects are included via the elliptic model it is found that the spectrum shows a peak only at the passing frequency provided the passage period is comparable to the period of core deformations. This occurs for initial conditions in which the core size and separation distance are comparable. Whether this parameter range is correct for the shear-layer mode is one of the questions that will be addressed.

Finally, we would like to mention the important and intriguing phenomenon of broadband amplification which is one of the chief objectives of Zaman's paper (V). Jets forced in the jet-column mode show a significant (up to 8dB) noise increase over the unforced jet at all frequencies and angles. Very low threshold levels of forcing are required; these levels certainly exist in jet engines. There is now considerable experimental evidence that this noise is associated with vortex pairing. The question remaining is what aspects of pairing are important. We have seen that internal core dynamics, especially the elliptic mode, can radiate. However, in the jet-column mode, slow azimuthal variations also occur and they may be important. In this regard the recent unpublished work of Möhring reported briefly by Müller & Obermeier (1988) on the sound radiation by a vortex filament distorted azimuthally in the shape of an ellipse may be relevant. From Fohl & Turner (1975, Equation 1) the frequency of the elliptic azimuthal mode for a thin isolated ring is

$$\frac{\omega_e}{\bar{\omega}_\phi} = \frac{\sqrt{3}}{2} \alpha^2 \left[\log \left(\frac{8}{\alpha} \right) - \frac{1}{4} \right], \quad (5.1.10)$$

and therefore dependent on the core size. At present therefore we are unable to connect it to measurements in circular jets. Nevertheless, the importance of core distortions relative to azimuthal ones needs to be studied.

5.2. Collision cases

5.2.1. Collision of $\alpha = 0.20$, $\hat{d} = 8$

This case has the thinnest cores among the collision examples considered. The shapes of the cores (at equal time intervals except the last) are shown in Figure 5.35 along with the trajectory of vorticity centroids. The shape at the final instant is magnified in Figure 5.36a and compared with the two-dimensional steadily translating pair (dotted) first calculated by Sadovskii (1971).^{*} The agreement is very good.

Assume that in their subsequent motion the cores retain the shape of the Sadovskii pair while increasing in radius and shrinking in area. If the core dimensions and inter-centroid separation are small in comparison with the radius, the rate of stretching $\dot{\bar{\sigma}}$ of the centroid will be the speed of the 2-D state provided by Saffman and Tanveer (1982)

$$\dot{\bar{\sigma}} = \sqrt{\frac{\Gamma^2}{37.11S(t)}}, \quad (5.2.1)$$

where $S(t)$ is the cross-sectional area of one member of the pair. Substituting $\Gamma = \mathcal{A}\bar{\sigma}S$ where \mathcal{A} is the constant of proportionality for the linear variation of vorticity inside the vortices, we obtain

$$\frac{\dot{\bar{\sigma}}}{\bar{\sigma}^{1/2}} = \sqrt{\frac{\Gamma\mathcal{A}}{37.11}} = \text{constant}, \quad (5.2.2)$$

so that $\bar{\omega}_\phi \sim \bar{\sigma} \sim t^2$. Equation (5.2.2) allows one to check whether the dynamics at the last instant are consistent with a stretching 2-D shape. Figure 5.37 plots

^{*} We are indebted to Prof. D.I. Pullin for pointing out this reference. Several have independently worked on steadily translating two-dimensional pairs and their contributions should also be acknowledged. Deem & Zabusky (1978) conjectured the existence of a continuous family of solutions and calculated one intermediate member. Pierrehumbert (1980) calculated several members and, independently but with erroneous cusps at the symmetry plane, the touching pair obtained by Sadovskii (1971). The error was noted by Pierrehumbert (1981) in a corrigendum. A more complete analysis of the shape near the symmetry plane was performed by Saffman & Tanveer (1982) who also provide a more accurate recomputation. Wu, Overman & Zabusky (1984) performed a local analysis and carefully calculated and documented the shapes.

the evolution of the quantity $\dot{\bar{\sigma}}/\bar{\sigma}^{1/2}$ during the simulation with Equation (5.2.2) as the dashed line. The curve seems to asymptote to the presumed behavior. At this point, one may suspect that the cores will continue to maintain a constant shape while stretching and shrinking in area. However, this violates energy conservation. Using formulae derived in Appendix 5.A the energy was computed at several points along the *assumed* motion. The computed points in Figure 5.38 show that the energy increases linearly with $\bar{\sigma}$ if the core remains unaltered.

This behavior can also be argued as follows. The kinetic energy (with density set to unity) for an axisymmetric distribution of vorticity is (see Lamb 1932, §162)

$$E = \pi \int \psi \omega_\phi dx d\sigma, \quad (5.2.3)$$

where $\psi(x, \sigma)$ is the Stokes streamfunction

$$\psi(x, \sigma) = \int \omega_\phi(x', \sigma') \mathcal{G}(x, \sigma; x', \sigma') dx' d\sigma'. \quad (5.2.4)$$

Assuming that the vortex pair is slender and expanding the Green's function \mathcal{G} (given in Equation (4.1.13)) in terms of the small parameter

$$\epsilon = \frac{\Delta}{2(\sigma\sigma')^{1/2}}, \quad \Delta = (x - x')^2 + (\sigma - \sigma')^2, \quad (5.2.5)$$

and discarding terms which vanish upon integration for a symmetric x -independent vorticity distribution gives

$$\psi(x, \sigma) = -\frac{1}{2\pi} \int \omega_\phi(\sigma') (\sigma\sigma')^{1/2} [\log \Delta + \mathcal{O}(\epsilon^2, \epsilon^2 \log \epsilon)] dx' d\sigma'. \quad (5.2.6)$$

Consider the contribution ψ_1 from the left half and write

$$\sigma' = \bar{\sigma}(1 - \epsilon''), \quad \epsilon'' = \frac{\bar{\sigma} - \sigma'}{\bar{\sigma}}. \quad (5.2.7)$$

Since ψ is to be evaluated inside the core for the evaluation of the energy $\mathcal{O}(\epsilon) = \mathcal{O}(\epsilon'') = \mathcal{O}(\epsilon')$, where ϵ' is the ratio of core size to radius. Then,

$$\psi_1(x, \sigma) = -\frac{\mathcal{A}\bar{\sigma}}{2\pi} (\sigma\bar{\sigma})^{1/2} \int_1 \left\{ \log \Delta - \frac{3}{2}\epsilon'' \log \Delta + \mathcal{O}(\epsilon'^2, \epsilon'^2 \log \epsilon') \right\} dx' d\sigma'. \quad (5.2.8)$$

The second term in the integrand vanishes if the cores are symmetric in σ about $\bar{\sigma}$. The resulting expression for ψ with error of relative order ϵ'^2 will be used later, but for now we shall be content to replace σ by $\bar{\sigma}$ thereby incurring errors of $\mathcal{O}(\epsilon')$:

$$\psi(x, \sigma) = \bar{\sigma}\Psi(x, \sigma)(1 + \mathcal{O}(\epsilon')), \quad (5.2.9)$$

where Ψ is the streamfunction of a two-dimensional pair with uniform vorticity $\pm \mathcal{A}\bar{\sigma}$. At the expense of introducing additional terms of $\mathcal{O}(\epsilon')$, (5.2.3) becomes

$$E = (1 + \mathcal{O}(\epsilon')) \pi \bar{\sigma} \int (\pm \mathcal{A}\bar{\sigma}) \Psi(x, \sigma) dx d\sigma. \quad (5.2.10)$$

The energy (per unit span) contained in a large circle of radius ρ for a two-dimensional pair with vorticity $\pm \mathcal{A}\bar{\sigma}$ is (Batchelor 1973, p. 529)

$$E_{2-D} = \frac{1}{2} \int (\pm \mathcal{A}\bar{\sigma}) \Psi(x, \sigma) dx d\sigma + \frac{\Gamma^2}{4\pi} \log \rho. \quad (5.2.11)$$

The second term is zero for a vortex pair and comparing with (5.2.10) we have

$$E = 2\pi \bar{\sigma} E_{2-D} (1 + \mathcal{O}(\epsilon')) = 0.128\pi \bar{\sigma} \Gamma_1^2 (1 + \mathcal{O}(\epsilon')), \quad (5.2.12)$$

the last equality being obtained from the value of E_{2-D} given by Pierrehumbert (1980 Table 1). This simple result that the energy is the two-dimensional energy per unit span times the circumference of the ring is true only when the total circulation is zero. Equation (5.2.12) gives the dashed line in Figure 5.38 and agrees very well with the computed values.

The cores must change shape as they stretch in order to conserve energy. A glimpse into how this takes place was obtained by adding node points and continuing the calculation until accuracy began to degrade. Figure 5.36*b* shows that a narrow tail is shed but the head retains the shape of the 2-D pair.

At this point one must wonder why the cores attain the shape of the Sadovskii pair. A possible explanation suggested by the spring-mass analogy (§1.4) is that, since thin core vortices approach each other very slowly compared to their rotation rate, the shapes remain in equilibrium with the induced field of the other vortex. Furthermore, when the separation is smaller than the radius, the flow is nearly two-dimensional locally, and we might expect the cores to evolve as 2-D equilibrium pairs. To check this, Figure 5.39 plots the shapes (solid) for instants when the separation to radius ratio is ≤ 0.6 and local two-dimensionality should begin to hold. The shapes were rescaled to have the same x centroid. The dashed shapes are 2-D pairs from Figure 4*a* in Wu, Overman & Zabusky (1984). The shapes at the last two instants are slightly flatter, otherwise the agreement is very good.

If varying time in thin axisymmetric collisions corresponds to varying the parameter that characterizes the family of 2-D steady pairs* then careful consideration of the axisymmetric collision might lead one to a mapping that links the 2-D steady shapes. We now describe a partial attempt in this direction that also suggests a mechanism for the tail formation.

We retained $\mathcal{O}(\epsilon^2)$ terms in (5.2.8) to obtain the leading order velocity field without introducing $\mathcal{O}(1)$ errors in differentiation:

$$u_x = \frac{1}{\sigma} \frac{\partial \psi}{\partial \sigma} = \frac{\bar{\sigma}^{\frac{1}{2}}}{\sigma^{\frac{1}{2}}} \left(\frac{\partial \Psi}{\partial \sigma} + \frac{\Psi}{2\sigma} (1 + \mathcal{O}(\epsilon)) \right), \quad (5.2.13a)$$

$$u_\sigma = -\frac{1}{\sigma} \frac{\partial \psi}{\partial x} = \frac{\bar{\sigma}^{\frac{1}{2}}}{\sigma^{\frac{1}{2}}} \frac{\partial \Psi}{\partial x} + \mathcal{O}\left(\frac{\Psi}{\bar{\sigma}} \epsilon\right). \quad (5.2.13b)$$

Note that we have reverted to ϵ , the ratio of separation to radius as the small parameter here. Now if the successive cross-sections are 2-D translating pairs, then on their boundary $\Psi = \Psi_o(t) - xV_o(t)$, where V_o is the speed of translation of the 2-D pair. Substituting this into (5.2.13) and replacing σ by $\bar{\sigma}$, which introduces terms of $\mathcal{O}(\epsilon')$, gives for the evolution of the boundary:

$$\frac{dx}{dt} = (u_x)_{2-D} + \frac{\Psi_o(t) - xV_o(t)}{2\bar{\sigma}} (1 + \mathcal{O}(\epsilon) + \mathcal{O}(\epsilon')), \quad (5.2.14a)$$

$$\frac{d\sigma}{dt} = (u_\sigma)_{2-D} (1 + \mathcal{O}(\epsilon')) + \mathcal{O}\left(\frac{\Psi}{\sigma} \epsilon\right). \quad (5.2.14b)$$

The two-dimensional velocity rigidly translates the cross-sections in σ . The second term in (a) causes them to rigidly approach at a decreasing velocity, because both $\bar{\sigma}$ is increasing and $\Psi_o(t)$ is tending to zero as the cores touch. The third term serves to preserve volume by uniform axial compression. The hypothesis is that the axial compression leads to tail-shedding in a manner similar to the tail formation of a compressed Hill's spherical vortex (Moffatt & Moore 1978, Pozrikidis 1986). When a stagnation region is formed, the perturbation due to compression is swept to the rear, amplifies and is ejected by the straining flow.

* We are reminded, perhaps inappropriately, of the fact that time evolving solutions of the KdV equation correspond to a one parameter family of potentials that satisfy a steady Schrödinger equation after one identifies time with the parameter. The KdV equation has the property of "elasticity" that solitary waves return to their original shape when they separate after collisions or when one overtakes another. This type of elastic behavior is similar to what we observed for the passage of thin rings. For fatter cores the interactions are inelastic and the analogy with KdV breaks down. Rather, the features are then closer to those of non-integrable wave equations in which solitary wave interactions lead to the production of smaller scales.

Equation (5.2.14) does not completely link all the 2-D translating pairs. If one applies it starting at the limit of circular cores, the succeeding shapes are ellipses. When (5.2.14) becomes valid at separations smaller than the radius, the cores have already been deformed by higher order effects not accounted for in these equations.

An alternate means of conserving energy in the presence of stretching would be for the cores to flatten without forming a tail. The shape constant 0.128 in Equation (5.2.12) reflects the aspect ratio of the core and scales inversely with it. For example the energy of two rectangular layers of width $2h$ and radial extent ℓ containing uniform vorticity of opposite sign is

$$E = \frac{2\pi}{3} \left(\frac{h}{\ell} \right) \bar{\sigma} \Gamma_1^2 \quad (5.2.15)$$

under the assumption of local two-dimensionality. Energy can be conserved if $h/l \sim (\bar{\sigma})^{-1}$. However, the simulation suggests that the cores do not become sheet-like but eject a tail with a head that remains tube-like. It should be emphasized that only self-stretching can cause core distortion i.e., if the stretching of the pair were induced by other vortices the increase of self-energy would merely reflect transfer of energy to the pair.

In summary, the formation of the tail may be viewed in two ways: i) as a means of conserving energy in the presence of stretching, or ii) as a response of the Sadvskii pair when subjected, because of axisymmetry, to axial compression.

5.2.2. Collision of $\alpha = 0.5, \hat{d} = 8$

Figure 5.40 shows the motion at equal time intervals except for the last instant. The dotted line is the trajectory of the vorticity centroids. The arrowhead follows a particle on the surface to convey the relative time scales for translation and rotation. A thin tail has been formed in the last snapshot; Figure 5.41 gives an enlarged view. The shape of the head is well approximated by the Sadvskii pair (dotted). Subsequently the calculation breaks down as segments near the collision plane become longer than the distance between opposing node points.

Figure 5.42 shows that the stretching rate (solid) is smaller than the prediction of Dyson's model (long dashed) and peaks at the value for the Sadvskii shape but then decreases due to tail formation. An estimate for the rate of circulation deposited into the tail and the accompanying decrease in stretching rate can be made by assuming that it is sufficiently flat that each half carries finite circulation but that the tail's self-

and interaction energy with the head can be neglected i.e., only the head contributes to the energy. This will hold only until the head has not depleted a substantial portion of its vorticity. The assumptions are justified by modeling the tail as two adjacent layers of width $2h$ and radial extent ℓ containing uniform shears of opposite sense with zero velocity outside, neglecting terms of $\mathcal{O}(h/\ell)$, and assuming local two-dimensionality. The self energy is $\mathcal{O}(h/\ell)$ according to (5.2.15). To estimate the energy for the induced field of the head interacting with the tail, assume that the layers are embedded in a stagnation point flow that represents the influence of the head. The strain rate on the collision plane scales as

$$e \sim \frac{V_o \delta_s^2}{\rho^3}, \quad (5.2.16)$$

where ρ is the distance from the head centroid, δ_s and V_o are the core size and radial velocity ($\sim \Gamma_{\text{head}}/\delta_s$) of the head. Then the interaction energy is

$$E \sim \Gamma_{\text{head}} \Gamma_{\text{tail}} \bar{\sigma} \left(\frac{h}{\ell} \right)^2, \quad (5.2.17)$$

which can be neglected. If the head always maintains the shape of the Sadovskii pair the total energy is

$$E = 0.128\pi \bar{\sigma}_{\text{head}} \Gamma_{\text{head}}^2, \quad (5.2.18)$$

which when substituted into (5.2.1) gives

$$\frac{1}{C \bar{\sigma}_{\text{head}}^{\frac{1}{2}}} \frac{d\bar{\sigma}_{\text{head}}}{dt} = 1; \quad C = 0.206 \sqrt{\mathcal{A} E^{\frac{1}{2}}}. \quad (5.2.19)$$

This represents stretching at the rate $\bar{\sigma}_{\text{head}} \sim t^{\frac{4}{3}}$ which is slightly slower than the t^2 behavior for an invariant shape and the asymptotic result for Dyson's model (§4.1.3). Figure 5.43 shows that the quantity on the left hand side of (5.2.19), determined by the node point with largest radius, asymptotes to unity when the tail is mature but clearly a long time simulation is needed to better verify the estimate. From (5.2.18) the circulation of the head decreases as

$$\Gamma_{\text{head}} \sim \bar{\sigma}_{\text{head}}^{-\frac{1}{2}} \sim t^{-\frac{2}{3}}. \quad (5.2.20)$$

5.2.3. Collision of $\alpha = 1.0, \hat{d} = 10$

Figure 5.44 shows successive instants during this collision. The core rotation is slow compared to translation: at $U_o t/L_o = 4.44$ after the rings have travelled several

radii, a particle has made only about $3/4$ -revolutions. At (d) the core shapes are roughly rectangular with aspect ratio 5.04 which is greater than the value 3:1 for a Sadovskii pair. Then as a means of forming such a state with smaller aspect ratio, the core begins to "fill-out" as in (e). At (h) a head of smaller aspect ratio has been formed. It is connected to a long flattened tail by a thin umbilical. Figure 5.45 is a magnified view of the head and umbilical. The head is fit well by the Sadovskii eddy (dotted line). The location of the vorticity centroid (plus sign) shows that roughly half the circulation resides in the tail. Owing to the considerable straining of the vortex boundaries near the collision plane and on the umbilical the total number of node points increased from 600 to 1972. Loss of accuracy began a few time steps prior to the last instant shown. This manifested itself as sharply increasing errors in the invariants. Nevertheless, the total change in the volume of vortical fluid was only $-.034\%$.

At present, one can only conjecture about what may happen subsequently. Due to its larger vorticity, the head will evolve rapidly compared to the tail. The head and tail will continue to separate and their mutual interaction will diminish and each will evolve independently. From previous reasoning, we know that the head cannot stretch and shrink in cross-sectional area while retaining its circulation. It may continually deposit vorticity in the umbilical below it. Changes in the shape of the tail will occur relatively slowly. Its shape is a higher aspect ratio version of state (e) so it may form a smaller head and leave yet another tail. The entire process may repeat *ad infinitum*.

The concept "inelasticity of the collision", used by workers dealing with one-dimensional solitary waves may apply to vortex ring interactions. It refers to the relative amount of small scale production of some conserved quantity that occurs when two solitary waves interact to form two smaller solitons and debris. The fact that collisions of thicker cores result in a larger relative volume of fluid in the tail means that the inelasticity is greater. This is analogous to solitary wave collisions of the RLW equation studied by Lewis & Tjon (1979) in which the inelasticity is greater for larger amplitude, faster moving solitons. They observed that the solitary waves disintegrate into a hierarchical procession of solitary waves in order of decreasing size. The analogy would be strengthened, for example, if the speculation that a hierarchy of Sadovskii eddies forms could be shown to be true. We are indebted to Prof. N.J. Zabusky for pointing out the possible connection with inelastic solitons.

We now present comparisons with the flow visualizations of Oshima (1978a). Since her discussion focussed on the azimuthal instabilities of the rings as they collided rather than on core deformations, we present the visualization photographs and discuss them from the latter point of view. Vortex rings of several initial speeds were collided. The case with the fastest speed results in a clear head-tail structure. The faster rings undergo larger core deformation. The reason is as follows. The speeds were varied by increasing the d.c. current applied to a loudspeaker diaphragm. This increased its displacement and hence led to a thicker core (see for example Equation 3.3b in Saffman (1978) which shows that the core size varies as the $2/3$ power of the stroke length in a piston-orifice apparatus). Figure 5.46 shows the smoke visualization pictures. The Reynolds number based on initial translation velocity and orifice diameter is about 1100. The upper row (U) shows, at successive instants, the meridional plane illuminated by a sheet of light. The lower row (L) is an oblique view 30° to the plane of collision. In U(b) a head with a long tail similar to the contour dynamics result of Figure 5.44h is seen. In L(b) this appears as a concentration of smoke around the periphery of the flattened rings. In L(c) the head has pinched-off and moves independently of the tail. Probably due to asymmetry in the initial conditions U(c) shows that it moves at an angle from the collision plane. The tail also fails to remain planar. Nevertheless axisymmetry is not broken until L(d) where the head has short waves around the circumference. Concentration of dye is seen at the periphery of the tail; this may indicate the formation of another head.

The head-tail structure also occurs in a plane of symmetry in three-dimensional symmetric collisions, for example in experiments on two vortex rings fired at an angle by Schatzle (1987) and in numerical simulations of two rectilinear tubes perturbed by bending them into sine waves. (M.V. Melander 1988, private communication). However, this plane of symmetry is subject to an out of plane strain not present in the axisymmetric case.

We conclude this case with a presentation of the evolution of the energy spectrum and its rate of change (the transfer spectrum) computed as described in Appendix 5.A. Figure 5.47 shows transfer spectra at the instants depicted in Figure 5.44. The trailing oscillations at the last instant are due to insufficient resolution. There is a forward cascade with the wavenumber of peak input drifting towards smaller scale.

Subsequent to (d), peaks diminish and the transfer extends out both towards large and small κ . Closer examination reveals that up to $U_0 t / L_0 = 3.70$ the largest scales

lose energy but thereafter there is a slight inverse cascade. This is also indicated by a change in slope of the square of the acoustic source function which depends on the behavior at small κ (Appendix 5.A).

Figure 5.48 shows spectra of the total energy and the sum of the self-energies, their difference being the interaction terms. For small κ the interaction spectrum is negative but at a value of κ that increases with time it becomes slightly positive and oscillates in sign. The interaction energy is present at scales approaching and larger than the vortex separation distance; at these scales the dipolar nature of the vorticity comes into play. The second vortex causes the velocity to decay faster at large distances, hence, the interaction spectrum is negative. At smaller scales the self spectra dominate. Notice the initial decrease and subsequent increase in the energy at large scales consistent with the behavior of the acoustic source function. The κ^2 and κ^4 ranges at large scales are well known and correspond to flows with and without net impulse (Appendix 5.A). The κ^{-4} at large κ reflects the jump in vorticity at the vortex surface. Due to the forward cascade an intermediate $\kappa^{\frac{2}{3}}$ range develops in the total energy. In the same range, the self spectrum develops a $\kappa^{-\frac{5}{3}}$. Three remarks are in order: First, despite the decrease with time in transfer at each κ these ranges may still represent a transient. Second, as pointed out by A. Wray, the $\kappa^{-\frac{5}{3}}$ in the self-energy would be a useful fact only if the interaction spectrum in this range vanishes in a non-independent ensemble of collisions. Third, the appearance of non-integer powers is due to the combined presence of the tube-like head and sheet-like tail. For example for the self-energy, a slender tube-like core has a κ^{-1} range at scales between the core size and radius (Appendix 5.A). On the other hand an infinitesimal sheet produces κ^{-2} (Townsend 1951). For the total energy, just the dipolar head has a κ^1 range and the present combination with a tail produces $\kappa^{\frac{2}{3}}$.

The evolution of the self and total energies is shown in Figure 5.49. Note the slight increase in the computed energy at the last instant. The reason for this is explained following Equation (5.A.16).

5.2.4. Acoustics of collisions

We now discuss sound generation in the collision cases. Figure 5.50 is a normalized version of Figure 17a in Kambe & Minota (1983, hereafter KM). The solid line is the experimental signal averaged over several realizations; it peaks at a value of 0.5 and then dips to -0.8 . The dashed line shows KMs best prediction with Dyson's model,

obtained with $\alpha = 0.3$. The dip is not predicted and the curve asymptotes to a constant. The lack of agreement in the final stages led KM to propose that the dip is due to viscosity. After modeling its effects they obtained the dotted curve which overpredicts the minimum. The Reynolds number based on initial ring radius and initial translational velocity is 2.1×10^4 .

Our results show that the dip can be accounted for by inviscid core deformation alone. Figure 5.51 shows the calculated result (dotted line) for $\alpha = 0.50$ compared with the experimental result of the previous figure. Both the maximum and minimum are well predicted, but the final peak is not obtained. The instants at which the signal attains a maximum and minimum are labeled A and B in this figure. These instants are also labeled in Figure 5.40 and mark the interval during which the core changes orientation. This is also demonstrated in Figure 5.52 which plots the orientation angle of the fit ellipse. The present case is beyond the range of validity of the elliptic model. Nevertheless, its prediction is included as the chain dashed line. The critical strain rate is exceeded and the cores elongate indefinitely resulting in a sharp drop in the signal.

This case provides the best overall agreement for the *average* over several experimental realizations. The signatures of individual realizations contain fluctuations. From Figure 3 in Kambe (1986) one sees that they are not reproducible and averaging filters them. We believe that they arise from high frequency core dynamics. The irreproducibility of the signals is perhaps due to the sensitivity to initial conditions for thin cores suggested by the numerical results below. For the thick core case presented, high frequencies are absent which accounts for the good agreement with the average. The core size to radius ratio of the experimental vortex is very likely smaller than the value (0.5) used in the simulation. Using Dyson's model KM find that using $\alpha = 0.3$ produces the best fit to the peak in the pressure wave. The smaller core size is also seen in shadowgraph photographs (Kambe & Murakami 1979). This motivates us to consider a thinner core.

Figure 5.53 shows that the acoustic signal for $\alpha = 0.2$ contains amplifying oscillations. Figure 3 in Kambe (1986) shows that measured fluctuation r.m.s. becomes larger as the cores approach.

Figure 5.54 shows the oscillations at early times. The contour dynamics signal shows the presence of two frequencies. A Fourier decomposition of its deviation from Dyson's model during the first five periods has a fundamental with period 0.43

and amplitude 0.025 and a first harmonic with amplitude 0.015. The two modes reflect small propagating waves on the contour of the form $e^{im(\beta - \bar{c}t)}$ where β is the azimuthal coordinate with respect to an origin at the centroid of the contour and \bar{c} is the (angular) phase velocity. For such corrugations on a 2-D circular patch of constant vorticity with radius δ , \bar{c} has been worked out by Kelvin (1880b, see Lamb §158):

$$\bar{c} = \frac{(m-1)}{2m} \frac{\Gamma}{\pi\delta^2}. \quad (5.2.21)$$

We will consider Equation (5.2.21) valid for the present case since the core is slender. Of course in the present situation the perturbations are evolving in the presence of strain but Equation (3.17) in Moore & Saffman (1971) shows that for weak strains the frequency is close to the unstrained natural frequency. The acoustic frequency produced by each mode is $m\bar{c}$; for $m = 2$ (elliptic mode) and $m = 3$ this predicts the observed frequencies extremely well.

From Figure 5.54 we see that elliptic model fails to reproduce the amplitude of the $m = 2$ mode. This is due to a slight inaccuracy in the shape of the steady vortex computed by Norbury. The inherent unsteadiness in Norbury's solution was verified by running an isolated vortex. It was found to radiate with an amplitude consistent with that observed for the $m = 2$ mode.

Given that the initial oscillations are due to slight unsteadiness not caused by strain, it is natural to wonder about the extent to which the character of the subsequent large amplitude oscillations is determined by them. To answer this we performed another simulation using the asymptotic solution of Fraenkel (1972) as the initial shapes. The pattern of the initial oscillations is shown as the dotted curve in Figure 5.54. Their amplitude is smaller than for the Norbury vortex indicating that the asymptotic solution is a closer approximation to the steady shape. The harmonic is stronger than the fundamental, their respective amplitudes being 0.015 and 0.003. Figure 5.55 compares the acoustics at a later stage in the collision. The differences reflect the differences at early times, namely, the Fraenkel vortex produces twice the number of peaks of smaller amplitude due to initial dominance of the harmonic. The frequencies increase due to stretching and their value agree well with $m\bar{c}$.

We conclude therefore that for thin core collisions the acoustic signal is sensitive to the precise form of the initial conditions; initial deviations from the steady shape are amplified by the continually increasing strain rate.

Figure 5.56 shows the calculated acoustic signal for the case of thickest cores ($\alpha = 1.0$). Kambe's experimental result (solid) has been included as a reference, with time origin shifted to make the zero crossings coincide. The feature near the end of the calculated result is due to the beginning of inaccuracy mentioned previously. The letters indicate the corresponding frames of Figure 5.44. Compared to thinner core cases the peak and minimum are broader with slightly larger values, and high frequency oscillations are absent due to the long eddy turnover time. The formation of the head and the elongation of the tail do not produce special features in the signal.

Appendix 5.A. Calculation of the energy and its spectrum

5.A.1. Introduction

This describes how the energy spectra and total energies presented in this chapter were computed. At the end, spectra of representative members of the Norbury-Fraenkel family are presented. At present they remain curiosities but we hope that they will be useful in designing physical models of turbulence in which known vortex solutions are the kinematic constituents. One of the emerging challenges is to represent information about physical structure gained from numerical simulations in statistical models. Some steps in this direction have already been taken. In 1943, Synge & Lin used a model consisting of a superposition of Hill's spherical vortices with random position, strength and orientation. As Saffman (1981*b*) points out, their model resulted in the correct prediction of the asymptotic behavior of the longitudinal correlation for large separations, a result not obtainable from statistical considerations alone. In 1951, Townsend showed that the representation of dissipation scale eddies in isotropic turbulence in terms of a random superposition of vortex sheets in which vorticity stretching is balanced by diffusion resulted in an energy spectrum that was in closer agreement with experiment than an alternative model in which vortex tubes were employed. Chou & Huang (1975) extended the work of Synge & Lin to include viscous vortex rings and obtained the correct decay law for the energy. Lundgren (1982) obtained an inertial range spectrum from a model employing stretching and diffusing spiral sheets. His model is dynamic and provides a plausible mechanism for the energy cascade. In the arena of inhomogeneous flows Perry, Henbest & Chong (1986) modelled the wall region of a turbulent boundary layer in terms of a hierarchy of Λ shaped vortices in different stages of stretching.

In the course of the derivation a calculable expression for the velocity transform will be obtained. This is the only piece of information about the flow that is required to compute, according to the theory of Kambe & Mya Oo (1981), the scattered sound field when a plane acoustic wave is incident on a localized steadily translating region of vorticity. For unsteady motions an additional time transform needs to be performed. They provide approximate numerical results for scattering by a steadily moving vortex ring with thin core. Howe (1983) obtained an exact expression in the limit when the incident wave has long wavelength in which case the core structure does not matter. The present formulae may be used in more general cases.

5.A.2. Derivation

The total energy per unit density is the following integral over the flow domain (which is assumed unbounded):

$$E = \frac{1}{2} \int \mathbf{u}^2(\mathbf{x}) d\mathbf{x}. \quad (5.A.1)$$

By Parseval's relation this is also

$$E = \frac{1}{2} \frac{1}{(2\pi)^3} \int \hat{\mathbf{u}}^2(\mathbf{k}) d\mathbf{k}, \quad (5.A.2)$$

where the hat denotes the complex Fourier transform. In our case, the vorticity is a simple specified function for all time and the boundary of its support is specified at every instant. Hence the goal is to express (5.A.2) in terms of line integrals about the boundaries. One begins by writing the integrand in (5.A.2) in terms of the vorticity. The transform of the relation $\nabla^2 \mathbf{u} = -\nabla \times \boldsymbol{\omega}$ is

$$k^2 \hat{\mathbf{u}} = i\mathbf{k} \times \hat{\boldsymbol{\omega}}, \quad (5.A.3)$$

and, as a consequence of the divergence free property of the vorticity, its transform is orthogonal to the wave vector so that

$$\hat{\mathbf{u}}^2(\mathbf{k}) = \frac{\hat{\boldsymbol{\omega}}^2}{k^2}. \quad (5.A.4)$$

Substituting this into (5.A.2) and performing the integration in spherical coordinates in wave space (k, ϑ_k, ϕ_k) one has

$$E = \int_0^\infty E(k) dk, \quad (5.A.5)$$

$$E(k) = \frac{1}{2} \frac{1}{(2\pi)^3} \int_0^{2\pi} d\phi_k \int_0^\pi d\vartheta_k \hat{\boldsymbol{\omega}}^2(\mathbf{k}) \sin \vartheta_k. \quad (5.A.6)$$

$E(k)$ is the radial energy spectrum function and $E(k) dk$ represents the contribution to the total energy from a spherical shell with radius k and thickness dk .

Next we obtain the Fourier transform of the vorticity:

$$\hat{\omega}(\mathbf{k}) = \int_{\mathcal{D}} e^{-i\mathbf{k}\cdot\mathbf{x}} \omega(\mathbf{x}) d\mathbf{x}, \quad (5.A.7)$$

where \mathcal{D} is the vorticity containing region. Before evaluating this integral for an axisymmetric vorticity distribution $\omega = (0, 0, \omega_\phi(x, \sigma))$ it is necessary to fix the orientation of wave space relative to physical space. The most convenient choice is to align the Cartesian axes in the two systems. One may then define cylindrical coordinates (x_k, σ_k, ϕ_k) in wave space in a manner analogous to those in physical space. Then (5.A.7) becomes

$$\hat{\omega}(\mathbf{k}) = \int_0^{2\pi} d\phi \int_{CS} \sigma \left[-\omega_\phi(x, \sigma) \sin \phi \hat{\mathbf{y}} + \omega_\phi(x, \sigma) \cos \phi \hat{\mathbf{z}} \right] \times e^{-i[xz_k + \sigma\sigma_k \cos(\phi - \phi_k)]} dx d\sigma. \quad (5.A.8)$$

Here CS denotes the cross-section of the vortex rings in a meridional plane. The integral in the azimuthal direction is obtained by introducing $\tilde{\phi} = \phi - \phi_k$ as one can integrate over any period, in particular $\tilde{\phi} \in [0, 2\pi]$. The integrand has parts that are symmetric and antisymmetric about $\tilde{\phi} = \pi$. The second part vanishes upon integration and the first can be expressed in terms of a Bessel function (Gradshteyn & Ryzhik 3.915.2):

$$\hat{\omega}(\mathbf{k}) = -2\pi i \hat{\phi}_k \int_{CS} \sigma \omega_\phi(x, \sigma) J_1(\sigma\sigma_k) e^{-izx_k} dx d\sigma. \quad (5.A.9)$$

The Fourier transform of the vorticity is also axisymmetric and azimuthal. For our case, CS consists of several regions $(CS)_j$ in each of which $\omega_\phi(x, \sigma) = \mathcal{A}_j \sigma$. The area integrals in (5.A.9) can then be reduced to line integrals via Green's theorem in the plane. In spherical coordinates (k, ϑ_k, ϕ_k) defined by

$$x_k = k \cos \vartheta_k, \quad \sigma_k = k \sin \vartheta_k, \quad (5.A.10)$$

the result is

$$\hat{\omega}_{\phi_k}(k, \vartheta_k) = 2\pi \sum_j S_j, \quad (5.A.11)$$

$$S_j = \frac{\mathcal{A}_j}{k \cos \vartheta_k} \oint_{C_j} \sigma^2(\xi) J_1(\sigma(\xi) k \sin \vartheta_k) e^{-ikz(\xi) \cos \vartheta_k} \frac{\partial \sigma}{\partial \xi} d\xi,$$

where ξ parametrizes the contour. When $\vartheta = \pi/2$ the integrand becomes independent of x , the integral vanishes, the above expression is indeterminate and has the value

$$\begin{aligned}\widehat{\omega}_{\phi_k}\left(k, \frac{\pi}{2}\right) &= 2\pi \sum_j \mathcal{S}'_j, \\ \mathcal{S}'_j &= -iA_j \oint_{c_j} \sigma^2(\xi)x(\xi)J_1(\sigma(\xi)k)\frac{\partial\sigma}{\partial\xi}d\xi.\end{aligned}\tag{5.A.12}$$

Note that the real part of $\widehat{\omega}_{\phi_k}$ is antisymmetric about $\vartheta_k = \pi/2$ and the imaginary part is symmetric. Consequently, the integrand in (5.A.6) is symmetric and can be integrated over a hemisphere:

$$E(k) = \sum_{ij} E_{ij}(k), \quad E_{ij}(k) = \int_0^{\frac{\pi}{2}} d\vartheta_k \sin \vartheta_k \mathcal{S}_i \mathcal{S}_j^*, \tag{5.A.13}$$

where the asterisk denotes complex conjugation and \mathcal{S}' should be used at $\vartheta_k = \pi/2$. Integration and summation were interchanged because we wish to retain the identities of individual contributions to the spectrum. We shall refer to terms $E_{ij}(k)$ ($i = j$) as self-spectra and $E_{ij}(k) + E_{ji}(k)$ ($i \neq j$) as interaction spectra.

5.A.3. Numerical implementation

Line integrals were evaluated by interpolating linearly between node points and using two point Gauss quadrature for each segment. We chose $\Delta\xi = 1$ along each segment. The integrand becomes highly oscillatory for large k and, to have a sufficient number of quadrature points between zero crossings, one must place a limit on the largest k for which the spectrum is computed. This limit can be estimated as follows. The local period between zero crossings of the integrand at some point $\xi = \xi_1$ can be approximated as

$$T_s = \frac{2\pi}{kl_\sigma \cos \vartheta_k \pm kl_x \sin \vartheta_k}, \tag{5.A.14}$$

where l_x and l_σ are the x and σ components of the vector directed along the segment containing ξ_1 . This was based on a Taylor series expansion to linear order of the phase function in the exponential term and the behavior of J_1 for large argument. In the worst case

$$T_s = \frac{2\pi}{kl_{\max}}, \tag{5.A.15}$$

where l_{\max} is the length of the longest segment. Requiring at least one segment between zero crossings implies

$$k \leq \frac{2\pi}{l_{\max}}. \quad (5.A.16)$$

Spectra were computed at 257 equispaced points in $\log_{10} k$ up to the full decade containing this limit and then integrated using Romberg quadrature with 8 subdivisions to obtain the self and interaction energies. The fact that the limit (5.A.16) was not strictly observed resulted in some spurious oscillations at large k but the spectrum had decreased by several decades and the oscillations are too small to cause significant error in the total energy, with the exception of the last point in Figure 5.49. The integral over co-latitude was computed similarly with the same number of points.

Transfer spectra and transfer rates defined by

$$T(k) = \frac{\partial E(k)}{\partial t}, \quad T_{ij}(k) = \frac{\partial E_{ij}(k)}{\partial t}, \quad T_{ij} = \frac{\partial E_{ij}}{\partial t} \quad (5.A.17)$$

were calculated by differencing across one time step.

For single and two identical rings, the graphs are made dimensionless as follows:

$$\kappa = kD_o, \quad \hat{E}(\kappa) = \frac{E(k)}{\mathcal{A}^2 D_o^8}, \quad \hat{E} = \frac{E}{\mathcal{A}^2 D_o^8}, \quad \hat{T}(\kappa) = \frac{T(k)}{|\mathcal{A}|^3 D_o^9}, \quad (5.A.18)$$

where D_o is the initial mean toroidal diameter.

5.A.4. Asymptotic behavior of the spectrum

The spectrum at low k reflects the far-field behavior of the velocity field which in turn depends on overall properties of the vorticity rather than its detailed structure. So one expects to be able to construct a power series for $E(k)$ valid at sufficiently small k in which the coefficients depend on successively higher moments of the vorticity distribution. Define these moments as

$$m_{ij} = \int \sigma^i x^j \omega_\phi(x, \sigma) dx d\sigma. \quad (5.A.19)$$

The Bessel function $J_1(\mu)$ has the following expansion about $\mu = 0$

$$J_1(\mu) = \frac{1}{2}\mu \sum_{j=0}^{\infty} \frac{\left(-\frac{1}{4}\mu^2\right)^j}{j!(j+1)!}. \quad (5.A.20)$$

Substituting this into (5.A.9) and using (5.A.6) leads to the desired result. Omitting the algebraic details, which were performed using MACSYMA, we quote the result.

$$\begin{aligned}
E(k) = & \frac{1}{6} m_{20}^2 k^2 - \frac{1}{30} (m_{20} m_{40} + m_{20} m_{22} - m_{21}^2) k^4 \\
& + \frac{1}{1680} (2m_{20} m_{60} + 4m_{20} m_{42} - 8m_{21} m_{41} + 3m_{40}^2 + 4m_{22} m_{40} \\
& + 2m_{20} m_{24} - 8m_{21} m_{23} + 6m_{22}^2) k^6 + \mathcal{O}(k^8).
\end{aligned} \tag{5.A.21}$$

A similar expansion for the velocity transform of a patch of inhomogeneous turbulence has been given by Phillips (1956). The moment m_{20} in the coefficient of the leading term is proportional to the conserved impulse P (with unit density):

$$m_{20} = \frac{P}{\pi}. \tag{5.A.22}$$

For symmetric collisions of vortex rings, the impulse as well as all other moments with even index j vanish. In this case the leading behavior is

$$E(k) = \frac{1}{30} m_{21}^2 k^4. \tag{5.A.23}$$

It is interesting to note that m_{21} is the acoustic source function $Q(t)$ defined in §4.2.5, hence the largest scales are not invariant as the flow evolves.

Similarly, the leading behavior for large k may be obtained by using the method of stationary phase together with the expansion of J_1 for large arguments. The result is an oscillating function that decays as k^{-4} . The coefficient is a complicated function of the curvature of the contour at the stationary points to which no physical interpretation could be given.

5.A.5. Spectra of the Norbury-Fraenkel vortices

For the results provided here contours were represented by 600 segments. As a check $\widehat{E}(\kappa)$ was computed for Hill's vortex and its integral was found to be $\widehat{E} = 0.0797825$. The exact energy is $\widehat{E} = 8/315\pi = 0.0797865\dots$. Figure 5.57 shows spectra for $\alpha = 0.1$ (solid) and $\alpha = 0.6$ (dashed). The slopes for small and large κ are as predicted by the asymptotic expressions. The scale associated with the peak in the spectra (the integral scale) is the toroidal radius. For $\alpha = 0.1$ there is an intermediate k^{-1} region between the scales of the radius and core size. For a core of zero thickness this range persists as $\kappa \rightarrow \infty$ (see Leonard 1985, Figure 12). For scales

smaller than the core radius, the spectra decay as k^{-4} which is characteristic of the jump in vorticity at the boundary.

Appendix 5.B. Implementation of the vortex filament to axisymmetric flow

This appendix describes the specialization of the vortex filament method to axisymmetric flow. It was used in the body of the chapter to study interactions of vortex rings with peaked vorticity distributions that are more representative of those observed experimentally (see for example the experiments of Sullivan, Widnall & Ezekiel 1973). The method described as scheme ‘C’ in Leonard (1980) is used. The presentation is divided into four parts. First, a review of the ideas behind the vortex filament method is provided followed by the equations of filament motion for the axisymmetric case. The third subsection describes the computation of the acoustic signal and diagnostics of accuracy. Finally, the procedures used to discretize the initial vorticity field will be presented.

5.B.1. *The vortex filament method*

Following the approach in two-dimensions of representing the vorticity as a superposition of “blobs” (Chorin & Bernard 1973), Leonard (1980) suggested that in three-dimensions the vorticity could be approximated by a superposition of filaments, each filament being a continuous superposition of blobs about a space curve $\mathbf{r}(\xi)$:

$$\boldsymbol{\omega}(\mathbf{x}, t) = \sum_{i=1}^L \Gamma_i \int_{C_i} \gamma[|\mathbf{x} - \mathbf{r}_i|, \delta_i] \frac{\partial \mathbf{r}_i}{\partial \xi} d\xi, \quad \int \gamma(\mathbf{y}) d\mathbf{y} = 1. \quad (5.B.1)$$

The resulting vorticity is divergence-free if the C_i are closed curves. Here γ is the core function. In keeping with all 3-D applications to date, it has been chosen to be spherically symmetric* and characterized by δ_i , the core size. In the axisymmetric case, δ_i does not vary along the filament. For the 3-D case it is argued that core size variations would lead to waves traveling along the vortex tube which would smooth out any variations. This argument is plausible because for thin cores, the waves are much faster than the filament motion. In some applications this may not be true. For example Siggia & Pumar (1987) argue that for their case filament dynamics are more rapid and so they allow non-uniform cores. Also, to show that the method conserves

* For an exception in 2-D see Teng (1982).

energy and impulse one needs uniform δ_j . The representation of waves in the filament model is a problem that should receive more attention in the future.

The equation giving the velocity in terms of the vorticity for an unbounded domain is the Biot-Savart law.

$$\mathbf{u}(\mathbf{x}, t) = -\frac{1}{4\pi} \int \frac{(\mathbf{x} - \mathbf{x}') \times \boldsymbol{\omega}(\mathbf{x}', t)}{|\mathbf{x} - \mathbf{x}'|^3} d\mathbf{x}'. \quad (5.B.2)$$

Next, substitute (5.B.1) into (5.B.2), define $\mathbf{y} = \mathbf{x}' - \mathbf{r}_i$ and perform the \mathbf{y} integral in spherical coordinates choosing $\mathbf{x} - \mathbf{r}_i$ to be aligned with the polar direction. Then with the aid of the integrals (Bierens de Haan 1939, Table 67, Items 10 & 11):

$$\int_0^\pi \frac{\sin \vartheta d\vartheta}{(1 - 2\mu \cos \vartheta + \mu^2)^{3/2}} = \begin{cases} \frac{2}{1-\mu^2} & \mu^2 < 1 \\ \frac{2}{\mu(\mu^2-1)} & \mu^2 > 1 \end{cases} \quad (5.B.3)$$

$$\int_0^\pi \frac{\sin \vartheta \cos \vartheta d\vartheta}{(1 - 2\mu \cos \vartheta + \mu^2)^{3/2}} = \begin{cases} \frac{2\mu}{1-\mu^2} & \mu^2 < 1 \\ \frac{2}{\mu^2(\mu^2-1)} & \mu^2 > 1 \end{cases}$$

one obtains

$$\mathbf{u}(\mathbf{x}, t) = -\frac{1}{4\pi} \sum_{i=1}^L \Gamma_i \int_{C_i} \frac{(\mathbf{x} - \mathbf{r}_i) \times \frac{\partial \mathbf{r}_i}{\partial \xi} q(|\mathbf{x} - \mathbf{r}_i|, \delta_i)}{|\mathbf{x} - \mathbf{r}_i|^3} d\xi, \quad (5.B.4)$$

$$q(r, \delta) = 4\pi \int_0^r t^2 \gamma(t, \delta) dt, \quad q(\infty) = 1.$$

One usually first chooses a $q(r, \delta)$ that is computationally convenient and/or reproduces a known exact solution and, from it, infers the core function γ . In the present study we used (Leonard 1980, pp. 308–309)

$$q(r, \delta) = [1 + \alpha_o \delta^2 / r^2]^{-3/2}, \quad (5.B.5)$$

which implies from the second of (5.B.4) that

$$\gamma(r, \delta) = \frac{3\alpha_o \delta^2}{4\pi} (r^2 + \alpha_o \delta^2)^{-5/2}. \quad (5.B.6)$$

Here α_o is a free parameter. The choice $\alpha_o = 0.413$ reproduces both the exact long-wavelength dynamics of small waves on a rectilinear vortex as well as the speed of translation of a thin vortex ring. This gives reason to hope that the method may be more general. The value of α_o is pertinent only when a single filament is employed to represent a vortex tube; we intend to use a swarm of filaments, nevertheless, this choice of α_o is retained.

So far the discussion has been purely kinematic and the errors introduced are those associated with interpolation of a given vorticity field by a superposition of blobs. The dynamics is expressed by the Helmholtz theorems that vortex lines are convected with the local velocity field given by (5.B.4) and that the circulation is constant. In general the local velocity would distort each blob from the assumed structure but the only degrees of freedom the method allows are the shapes of the space curves and $\delta_i(t)$. How should one make the best of this limitation? One may argue that as an increasing number of filaments is used to represent a continuous vorticity distribution the total deformation of the filament cores is reduced, hence one may convect each filament by the velocity induced on the space curve. With (5.B.5) for q this results in the so-called Moore-Rosenhead scheme (Leonard 1985). An alternate procedure (Scheme 'D' in Leonard 1980) regards each point on the space curves as the vorticity centroid of a blob and as such it is convected by the γ weighted average of \mathbf{u} around the point. The resulting rule for convecting filaments reads

$$\frac{\partial \mathbf{r}_i(\xi, t)}{\partial t} = -\frac{1}{4\pi} \sum_{j=1}^L \Gamma_j \int_{C_j} \frac{(\mathbf{r}_i - \mathbf{r}_j) \times \frac{\partial \mathbf{r}_j}{\partial \xi'} s(|\mathbf{r}_i - \mathbf{r}_j|, \delta_i, \delta_j)}{|\mathbf{r}_i - \mathbf{r}_j|^3} d\xi', \quad (5.B.7)$$

For our purposes it suffices to say that s is symmetric in δ_i and δ_j . For the precise form of s in terms of γ the reader should consult Leonard (1980); the form is not computationally convenient and perhaps for this reason it has never been implemented to the author's knowledge. The scheme has the nice properties that it conserves impulse and angular impulse of the \mathbf{u} field constructed by (5.B.4) using an *arbitrary* spherically symmetric γ . The reason for the arbitrariness is that both these quantities are independent of γ . The symmetry of s in δ_i and δ_j is alone sufficient for these conservation properties to hold. If the core sizes are held constant in time then scheme 'D' also conserves energy of the \mathbf{u} field with the actual γ , but for this property symmetry alone is not enough.

Scheme 'C' is a compromise between Moore-Rosenhead and 'D' in that filaments are convected as in (5.B.7) but with s chosen merely to be the symmetrized version of q , i. e.,

$$s(y, \delta_i, \delta_j) = q(y, \sqrt{1/2(\delta_i^2 + \delta_j^2)}). \quad (5.B.8)$$

Conservation of impulse and angular impulse are guaranteed. If volume conservation is imposed for each filament i. e.

$$\delta_i^2(t) \mathcal{L}_i(t) = \text{constant}, \quad (5.B.9)$$

where $\mathcal{L}_i(t)$ is the total length of the filament, then the scheme conserves energy provided the cores have negligible overlap, a condition not satisfied by the present calculations. For this reason we considered it essential to monitor the energy of the \mathbf{u} field. We describe its calculation in §5.B.3. For a vortex tube represented by a single filament, Equation (5.B.9) represents vorticity stretching.

In conclusion, using (5.B.7) with q given by (5.B.5), the scheme used to advance the filaments reads

$$\frac{\partial \mathbf{r}_i(\xi, t)}{\partial t} = -\frac{1}{4\pi} \sum_{j=1}^L \Gamma_j \int_{C_j} \frac{(\mathbf{r}_i - \mathbf{r}_j) \times \frac{\partial \mathbf{r}_j}{\partial \xi'}}{[|\mathbf{r}_i - \mathbf{r}_j|^2 + \frac{1}{2}\alpha_o(\delta_i^2 + \delta_j^2)]^{3/2}} d\xi', \quad (5.B.10)$$

with core dynamics given by (5.B.9).

5.B.2. Equations of filament motion for the axisymmetric case

Equation (5.B.10) is particularly convenient in the axisymmetric case because the resulting equations of motion are the same as for Dyson's (1893) model (see §4.1.1) except that the argument of the elliptic integrals is slightly different and a separate term for the self-induced translation is not required since (5.B.7) is well defined when $i = j$. Dropping bars but otherwise using the same notation as §4.1.1 the equations of motion for the axial and radial coordinates of the circular filaments are

$$\begin{aligned} \frac{dx_i}{dt} &= \sum_j u(x_i, \sigma_i; x_j, \sigma_j), \\ \frac{d\sigma_i}{dt} &= \sum_j v(x_i, \sigma_i; x_j, \sigma_j), \end{aligned} \quad (5.B.11)$$

where u and v are as given in Equation (4.1.3) with only the quantity A redefined as

$$A = (x_i - x_j)^2 + \sigma_i^2 + \sigma_j^2 - 2\sigma_i\sigma_j + \frac{1}{2}\alpha_o(\delta_i^2 + \delta_j^2). \quad (5.B.12)$$

5.B.3. Diagnostics

(i) *Calculation of the total energy.* To compute the energy, we follow the same procedure as that used for contour dynamics, namely, determine and then integrate the radial spectrum of the energy. Much of the development is from the unpublished notes of A. Leonard (undated) which were intended to assert the energy conservation

conditions stated previously. In addition Equation (5.B.16) below was used by Degani & Leonard (1976 unpublished, see Figure 13 in Leonard 1985) to calculate the energy spectrum of a patch of free turbulence simulated using vortex filaments. In their study, it was remarkable that with only a small number of filaments the experimentally measured spectrum for low Reynolds number homogeneous turbulence was reproduced.

From (5.A.6) the radial spectrum can be computed from the Fourier transform of the vorticity which for the filament representation (5.B.1) is

$$\hat{\omega}(\mathbf{k}) = \sum_i \Gamma_i \int_{C_i} e^{-i\mathbf{k}\cdot\mathbf{r}} \frac{\partial \mathbf{r}_i}{\partial \xi} \hat{G}_i(\mathbf{k}) d\xi, \quad (5.B.13)$$

where $\hat{G}_i(\mathbf{k})$ is the transform of the core function $\gamma(\mathbf{y})$. For spherically symmetric γ it reduces to the sine transform

$$\hat{G}_i(k) = 4\pi \int_0^\infty y^2 \gamma(y, \delta_i) \frac{\sin ky}{ky} dy. \quad (5.B.14)$$

The integral over the spherical shell was performed by aligning \mathbf{k} with the polar direction in spherical \mathbf{y} coordinates. For the core function given by (5.B.6) the sine transform is tabulated (Erdélyi, *Tables of Integral Transforms*, p. 67, Item 37):

$$\hat{G}_i(k) = a_i k K_1(a_i k), \quad a_i = \sqrt{\alpha_o} \delta_i, \quad (5.B.15)$$

where K_1 is the modified Bessel function of the second kind. Substituting (5.B.13) into (5.A.6) gives

$$\begin{aligned} E(k) &= \frac{1}{4\pi^2} \sum_{i,j} \Gamma_i \Gamma_j \hat{G}_i(k) \hat{G}_j(k) H_{ij}(k), \\ H_{ij}(k) &= \int_{C_i} \int_{C_j} \frac{\sin k\Delta(\xi, \xi')}{k\Delta(\xi, \xi')} \frac{\partial \mathbf{r}_i}{\partial \xi} \cdot \frac{\partial \mathbf{r}_j}{\partial \xi'} d\xi d\xi', \\ \Delta(\xi, \xi') &= |\mathbf{r}_i(\xi) - \mathbf{r}_j(\xi')|. \end{aligned} \quad (5.B.16)$$

The required integral over the spherical shell was obtained by aligning $\Delta \equiv \mathbf{r}_i - \mathbf{r}_j$ with the polar direction. This expression gives the energy spectrum for any configuration of filaments. The large k asymptote may be obtained by applying the method of stationary phase. It says that the dominant contribution to the double line integral arises from pairs of points ξ, ξ' which extremize $\Delta(\xi, \xi')$, i.e., points of local closest and farthest approach. This contribution is proportional to k^{-2} and largest for close points at which the second derivatives of $\Delta(\xi, \xi')$ are small and the vorticity parallel (or

anti-parallel). If one considers, in addition, scales smaller than the core sizes at such points ($ka(\xi), ka(\xi') \gg 1$) then, using the asymptotic form of the Bessel function, the contribution to the spectrum from such points is proportional to $k^{-1}e^{-k(a(\xi)+a(\xi'))}$. Recall that for a vortex ring with a point core, the asymptote is $\sim k^{-1}$ without the exponential cut-off.

To obtain the total energy, (5.B.16) can be integrated exactly from $k = 0$ to $k = \infty$ (Erdélyi, *Tables of Integral Transforms*, p. 107, Item 61):

$$E = \frac{3}{64} \sum_{i,j} \frac{\Gamma_i \Gamma_j}{\sqrt{a_i a_j}} \int_{C_i} \int_{C_j} \frac{P_{1/2}^{-1}(\mu)}{\sqrt{\mu^2 - 1}} \frac{\partial \mathbf{r}_i}{\partial \xi} \cdot \frac{\partial \mathbf{r}_j}{\partial \xi'} d\xi d\xi',$$

$$\mu = \frac{\Delta^2(\xi, \xi') + a_i^2 + a_j^2}{2a_i a_j}.$$
(5.B.17)

$P_{1/2}^{-1}$ is a Legendre function of the toroidal variety. Fortunately, to compute it an integral representation exists (Erdélyi, *Higher Transcendental Functions*, vol. 1, p. 156, item 7) which allows it to be expressed in terms of complete elliptic integrals:

$$P_{1/2}^{-1}(\mu) = \frac{4}{3\pi\mu^* \sqrt{\mu + \mu^*}} [\mu(\mu + \mu^*)E(\bar{r}) - K(\bar{r})],$$

$$\mu^* = \sqrt{\mu^2 - 1}, \quad \bar{r} = \sqrt{\frac{2\mu^*}{\mu + \mu^*}}.$$
(5.B.18)

For the axisymmetric case (5.B.17) reduces to

$$E = \frac{3\pi}{16} \sum_{i,j} \frac{\Gamma_i \Gamma_j \sigma_i \sigma_j}{\sqrt{a_i a_j}} \int_0^\pi \frac{P_{1/2}^{-1}(\mu)}{\mu^*} \cos \phi d\phi,$$

$$\mu = \frac{(x_i - x_j)^2 + \sigma_i^2 + \sigma_j^2 + a_i^2 + a_j^2 - 2\sigma_i \sigma_j \cos \phi}{2a_i a_j}.$$
(5.B.19)

The integrand is indeterminate when $\phi = 0$ and $i = j$ but using the integral representation of the Legendre function one finds its value to be $1/2$.

In the numerical implementation, the double sum was done first, making use of symmetry in i and j , then the integral was computed using the Romberg method with seven sub-divisions (129 points). For the $\alpha = 0.2$ passage case (linear vorticity) the energy monotonically increased by 0.2% of its initial value during the simulation. A third of this occurred between frames (e) and (f) of Figure 5.14. For $\alpha = 0.4$, $\Delta E = .18\%$ (linear vorticity case), 0.37% (peaked vorticity; over-energetic case) and 1.1% (peaked vorticity; matched energy).

(ii) *Calculation of the vorticity.* Contour plots of the vorticity were generated by calculating the vorticity as follows. Substituting the core function (5.B.6) into (5.B.1) gives for the axisymmetric case

$$\omega_\phi(\mathbf{x}, \sigma) = \frac{3\alpha_o}{4\pi} \sum_i \Gamma_i \sigma_i \delta_i^2 \int_0^{2\pi} \frac{\cos \phi d\phi}{(A - B \cos \phi)^{5/2}}, \quad (5.B.20)$$

$$A = (\mathbf{x} - \mathbf{x}_i)^2 + \sigma^2 + \sigma_i^2 + \alpha_o \delta_i^2, \quad B = 2\sigma\sigma_i.$$

This integral has been worked out earlier in (4.2.30) in connection with the elliptic model.

(iii) *Calculation of the impulse.* Substitute the vorticity representation (5.B.1) into $\mathbf{P} = \frac{1}{2} \int (\mathbf{x} \times \boldsymbol{\omega}) d\mathbf{x}$, the definition of the linear impulse (with density set to unity, Batchelor 1973, p. 519). Then let $\mathbf{y} = \mathbf{x} - \mathbf{r}_i$ and note that $\int \gamma(\mathbf{y}) d\mathbf{y} = 1$ and $\int_{C_i} \partial \mathbf{r}_i / \partial \xi d\xi = 0$. The result is

$$\mathbf{P} = \frac{1}{2} \sum_i \Gamma_i \int_{C_i} \left(\mathbf{r}_i \times \frac{\partial \mathbf{r}_i}{\partial \xi} \right) d\xi. \quad (5.B.21)$$

Thus the impulse is independent of the core function. The magnitude $|\mathbf{r}_i \times d\mathbf{r}_i|$ of the integrand is twice the area of the right triangle made by \mathbf{r}_i and $d\mathbf{r}_i$ so the integral is twice the signed area $\int_{C_i} n dS$ enclosed by the filament. Therefore, for a system of coaxial circular filaments

$$\mathbf{P} = \pi \sum_i \Gamma_i \sigma_i^2 \hat{\mathbf{x}}. \quad (5.B.22)$$

In all the runs presented, the relative change of total impulse was less than 10^{-8} . The angular impulse is zero for axisymmetric swirl-free flow.

(iv) *Calculation of the acoustic source function.* According to Möhring's (1978) theory of vortex sound, the far-field acoustic pressure for an acoustically compact three-dimensional region of vorticity is

$$p_a(\mathbf{x}, t) = \frac{\rho_o}{c_o^2} \frac{x_i x_j}{r^3} \frac{d^3}{dt^3} Q_{ij}(t - r/c_o), \quad (5.B.23a)$$

$$Q_{ij}(t) = \frac{1}{12\pi} \int x_i (\mathbf{x} \times \boldsymbol{\omega})_j d\mathbf{x},$$

where ρ_o and c_o are the density and speed of sound in the undisturbed medium and the summation convention is being employed. The evaluation of Q_{ij} proceeds along

similar lines as the impulse except that one has to also note that $\int \mathbf{y}\gamma(\mathbf{y}) d\mathbf{y} = 0$ for a spherically symmetric γ . The result is

$$Q_{ij}(t) = \frac{1}{12\pi} \sum_{\alpha} \Gamma_{\alpha} \int_{C_{\alpha}} r_i^{\alpha} \left(\mathbf{r}^{\alpha} \times \frac{\partial \mathbf{r}^{\alpha}}{\partial \xi} \right)_j d\xi, \quad (5.B.23b)$$

which also does not depend on the core function. For the axisymmetric case,

$$Q_{ij}(t) = \frac{1}{12} \begin{pmatrix} 2 & & \\ & -1 & \\ & & -1 \end{pmatrix} Q(t), \quad Q(t) = \sum_{\alpha} \Gamma_{\alpha} x_{\alpha} \sigma_{\alpha}^2. \quad (5.B.24)$$

Inserting this into (5.B.23a) gives for the far-field acoustic pressure in polar coordinates

$$p_a(r, \vartheta, t) = \frac{\rho_0}{4rc_0^2} (\cos^2 \vartheta - 1/3) Q'''(t - r/c_0). \quad (5.B.25)$$

5.B.4. Initial discretization of the vorticity field

We are currently equipped to start with four types of vortex rings: Hill's spherical vortex, those members of the Norbury-Fraenkel family for which Norbury (1973) provides Fourier coefficients of the shape, elliptic cross-sections whose behavior has been studied by Moore (1980) in the limit of thin cores, and the steadily translating rings with a peaked vorticity distribution obtained by Fraenkel (1972) to first order in core thickness. For all these cases the vorticity is confined and to discretize it into filaments the vorticity region is divided into cells and a vortex filament having the circulation of the cell is placed at the vorticity centroid of the cell. The core size δ_i of the filament is chosen to be some 'overlap' factor f_c times the area-effective radius of the cell. The overlap factor was chosen to give a good approximation to the desired initial vorticity distribution. Too small values resulted in distinct peaks around each filament and for large values the vorticity was less confined and its discontinuities were smeared.

We now describe in turn how the cells were arranged for each of the four cases.

(i) *Hill's spherical vortex.* P. Spalart at NASA Ames suggested that in order that filaments not be wasted each cell should be chosen to have the same circulation. This was feasible for Hill's vortex because of the closed form description of the shape and vorticity distribution. First the semi-circular cross-section is divided into a specified number of horizontal layers each having the same circulation, then each layer

is divided into specified number of cells with the same circulation. The cells along the edges are not approximated to be rectangular; their exact shape is accounted for. The edge cells may have different types of shapes which are unknown *a priori* so one guesses the type, determines where the vertical boundary must fall in order to obtain a certain circulation, and checks that the guess was correct. For some cell types the circulation of the cell is a transcendental function of the location of the vertical side so Newton-Raphson iteration is needed to locate it. A typical discretization is shown in Figure 5.58.

(ii) *Norbury-Fraenkel vortices*. In this case a simpler procedure was employed because of the complicated description of the core shape. All cells including those on the edge are rectangular and roughly identical. Trapezoidal edge cells were not used because their strength would be consistently under approximated. First we specify the maximum number of cells in the axial and radial directions. Then the limit box which surrounds the core is determined by iteration and cell dimensions Δx and $\Delta \sigma$ are calculated from the extent of the box. Finally, we consider a succession of radial slices, determine the radial extent of the vortex at the midpoint of each slice by iteration and slightly adjust $\Delta \sigma$ in order to fit an integer number of cells in the slice. The discretization for the $\alpha = 0.20$ passage case considered in this chapter is shown in Figure 5.59. The resulting vorticity distribution contours are shown in Figure 5.60 and the distribution along the central radial slice compared with the desired distribution is shown in Figure 5.61. An identical discretization procedure was used for elliptic cores.

(iii) *Fraenkel's (1972, pp. 128-130) peaked vorticity cores*. In the above cases, the vorticity is a linear function of the distance from the symmetry axis. For the present case it is specified, as explained below, by a certain mapping of a two-dimensional circular vortex with concentric circular streamlines. Like the Norbury-Fraenkel vortices this is a family of steadily translating rings but solutions are known only to first order in α , the ratio of core to toroidal radius. In order to study interactions of rings with peaked vorticity distributions that are more realistic we could have used any distribution, not necessarily one that was steady in isolation. Our choice was motivated by a desire to minimize secondary effects caused by inherent unsteadiness such as formation of spiral arms during an initial transient.

Of all the possible inviscid vortex ring solutions with a peaked vorticity that might qualify as being "realistic" is there one that might be preferred when small

(but non-negligible) viscosity is present? This is a difficult question. Leith (1984) found that the two-dimensional analog of Fraenkel's solution yields a local minimum of the enstrophy within the class of radially symmetric vortices with fixed circulation and energy. The idea is that vortices reach a steady state by internal re-organization and production of small scales i.e. via an enstrophy cascade. Such initial transients are often observed in experiments and numerical calculations. The shed vorticity carries enstrophy but very little energy to small scales where it is dissipated by viscosity. McWilliams (1984) hypothesized that in the presence of a small amount of damping some integrals of the non-dissipative motion (in this case the energy) are subjected to a far lower rate of decay than others such as the enstrophy. This is called the selective decay hypothesis and some numerical evidence in its favor has been provided by McWilliams (1984) and Basdevant *et al* (1984). In the latter study, *pairs* which had very nearly the structure of the Batchelor (1973, p. 535) pair, which has the same vorticity-streamfunction relation as Leith's minimum enstrophy solution were formed in a wake; however, it remains to be seen whether Batchelor's solution is in fact a minimum enstrophy pair.

We now briefly describe Fraenkel's solution. One can think of steady rings as perturbations of two-dimensional vortices with circular streamlines; the core size to radius ratio α is the expansion parameter. To zeroth order, the two-dimensional solution is unmodified; at first order, the streamlines remain circular but become non-concentric; to second order, the core becomes more elongated in the axial direction because at each cross-section it feels the strain of neighboring curved portions of the ring. Consider first the zeroth order two-dimensional solution. The condition for steadiness is that the vorticity be some function of its corresponding streamfunction. The simplest choice, which leads to the Rankine vortex, is to assume that this function is a constant inside the vortex. A peaked vorticity results at the next level of difficulty i.e. a linear function:

$$\omega_z(\varrho, \beta) = \begin{cases} k^2(\Psi_i(\varrho) - \Psi_0) & 0 \leq \varrho \leq 1; \\ 0 & \varrho > 1. \end{cases} \quad (5.B.26)$$

For convenience the radial extent of the vortex has been normalized so that it occupies the unit disk. Note that polar coordinates (ϱ, β) are used. The streamfunction Ψ_i in the interior satisfies

$$\nabla^2 \Psi_i = \frac{d^2 \Psi_i}{d\varrho^2} + \frac{1}{\varrho} \frac{d\Psi_i}{d\varrho} = -k^2(\Psi_i - \Psi_0), \quad (5.B.27)$$

whose solution is $\Psi_i(\varrho) = C_1 J_0(k\varrho) + \Psi_0$. On the boundary of the vortex let Ψ assume the constant value $C_1(J_0(k) - 1)$. Then $\Psi_i(\varrho) = C_1(J_0(k\varrho) - 1)$. If the circulation is set to π , the streamfunction in the exterior of the vortex is $\Psi_e = (1/2) \log \varrho + C_1(J_0(k) - 1)$ to ensure continuity of Ψ across the boundary. The tangential velocity $\partial\Psi/\partial\varrho$ at the boundary must also match for the two solutions and this determines the value of C_1 . The final solution is

$$\Psi_i(\varrho) = \frac{1}{2kJ_1(k)} \{J_0(k\varrho) - 1\} \quad 0 \leq \varrho \leq 1, \quad (5.B.28)$$

and the corresponding vorticity is

$$\omega_z(s) = \frac{k}{2J_1(k)} J_0(k\varrho) \quad 0 \leq \varrho \leq 1. \quad (5.B.29)$$

The peakiness of the vorticity distribution is characterized by k . If $k = 0$ then the vorticity is constant and if $k = j_{0,1} \approx 2.405$ the first root of J_0 , then the vorticity is peaked at the origin and falls to zero at the boundary. This is the case that was simulated. Intermediate values of k result in less sharply peaked distributions which are discontinuous at the boundary. For $k > j_{0,1}$ the vorticity changes sign.

Now from this two-dimensional solution, Fraenkel defines a vortex ring solution

$$\frac{\omega_\phi(\hat{\varrho}, \hat{\beta})}{\sigma} = \frac{\Gamma}{\pi\alpha^2 L_o^3} \omega_z(\varrho), \quad (5.B.30)$$

$\hat{\varrho}$ is given by the following mapping to $\mathcal{O}(\alpha)$

$$\hat{\varrho} = \delta(\varrho + \alpha Q_1(\varrho)) \cos \beta, \quad \hat{\beta} = \beta. \quad (5.B.31)$$

Here $\hat{\varrho}$ and $\hat{\beta}$ are polar coordinates centered on the cross-section of the core of the vortex ring, $\hat{\beta}$ being measured counterclockwise from the point on the cross-section having the greatest radius, δ is the core radius and $Q_1(\varrho)$ is an expression given in Fraenkel (1972); we shall not repeat it here.

In the discretization algorithm the unit disk is first divided into cells. This proceeds by first dividing the radial direction into a specified number of annular strips N_{st} . Up to a certain radius the radial spacing is uniform but thereafter geometric clustering is used in order to minimize smearing of the derivative discontinuity of the vorticity. Two parameters specify the clustering: the clustering factor r_c and the number of strips in the clustered region, N_c . Each strip is then divided in the angular

direction, the number of cells being chosen to make the cell aspect ratios approximately unity. A filament is then placed at the centroid of vorticity in the mapped image of each cell and assigned its circulation. The cell pattern on the unit disk for the $\alpha = 0.2$ passage case presented in the chapter is shown in Figure 5.62. The parameters used were $N_s = 10$, $N_c = 6$, $r_c = 0.80$. This resulted in 513 filaments per vortex. The resulting vorticity contours are presented in Figure 5.63, note that they are nearly circular but non-concentric. For thick cores Fraenkel's solution is outside its range of validity and the mapping (5.B.31) is no longer onto. For such cases, in particular the $\alpha = 0.4$ passage, only the zeroth order term in (5.B.31) is retained and this accounts for the inherent unsteadiness observed in the motion of the centroid.

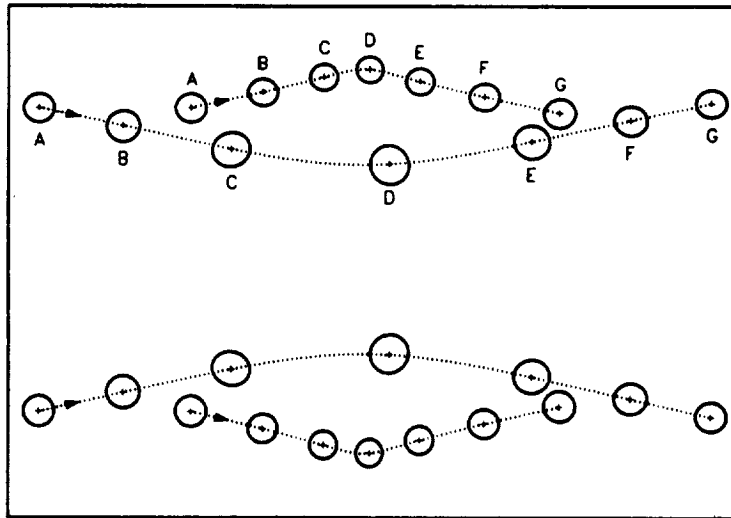


FIGURE 5.1. Core shapes at equal time intervals for the passage of $\alpha = 0.1, \hat{d} = 1$, trajectory of vorticity centroids; +, vorticity centroids. $U_0 t / L_0$: A, 0; B, 0.41; C, 0.82; D, 1.22; E, 1.63; F, 2.04; G, 2.45.

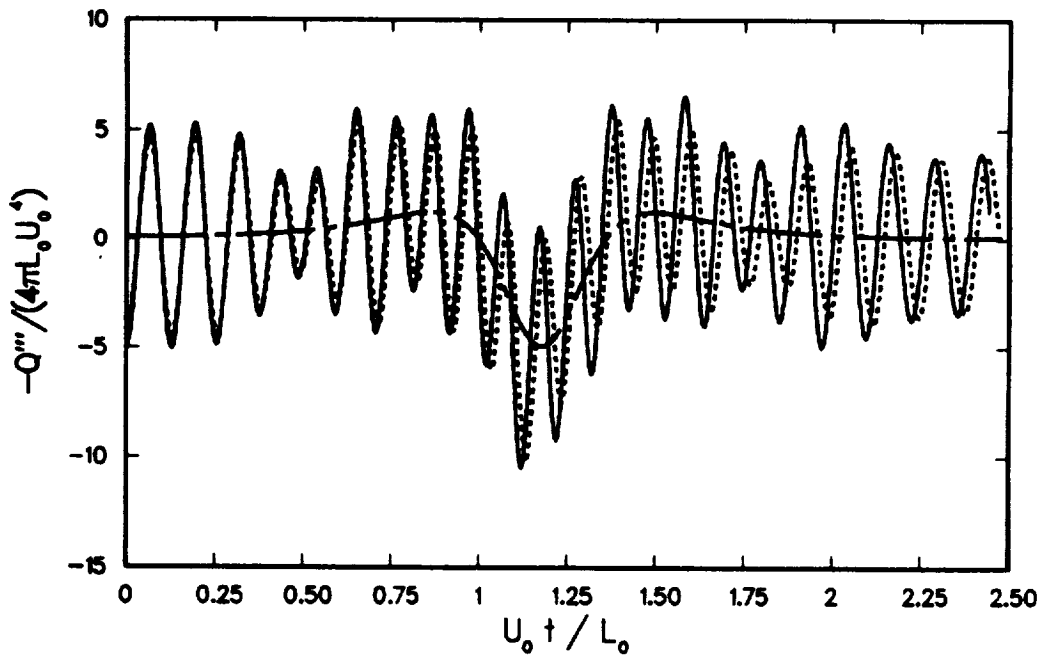


FIGURE 5.2. Normalized acoustic signal for the passage of $\alpha = 0.1, \hat{d} = 1$. —, contour dynamics; ----, elliptic model; - · - ·, Dyson's model.

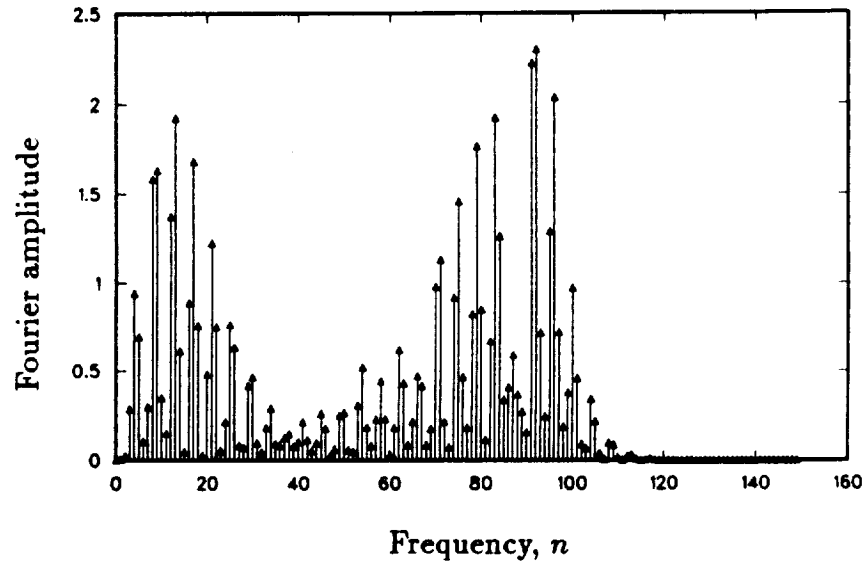


FIGURE 5.3. Fourier amplitudes of the acoustic signal for four passage periods ($\alpha = 0.1, \hat{d} = 1$, elliptic model).

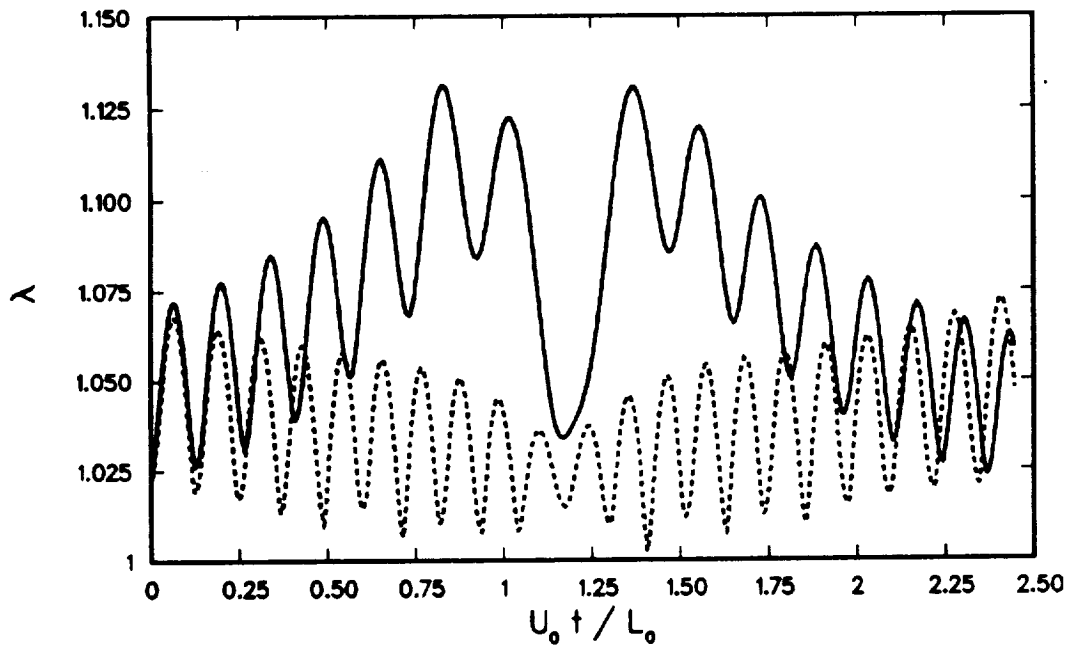


FIGURE 5.4. Evolution of aspect ratios (contour dynamics) for the passage of $\alpha = 0.1, \hat{d} = 1$. —, initially rear vortex; ----, initially leading vortex.

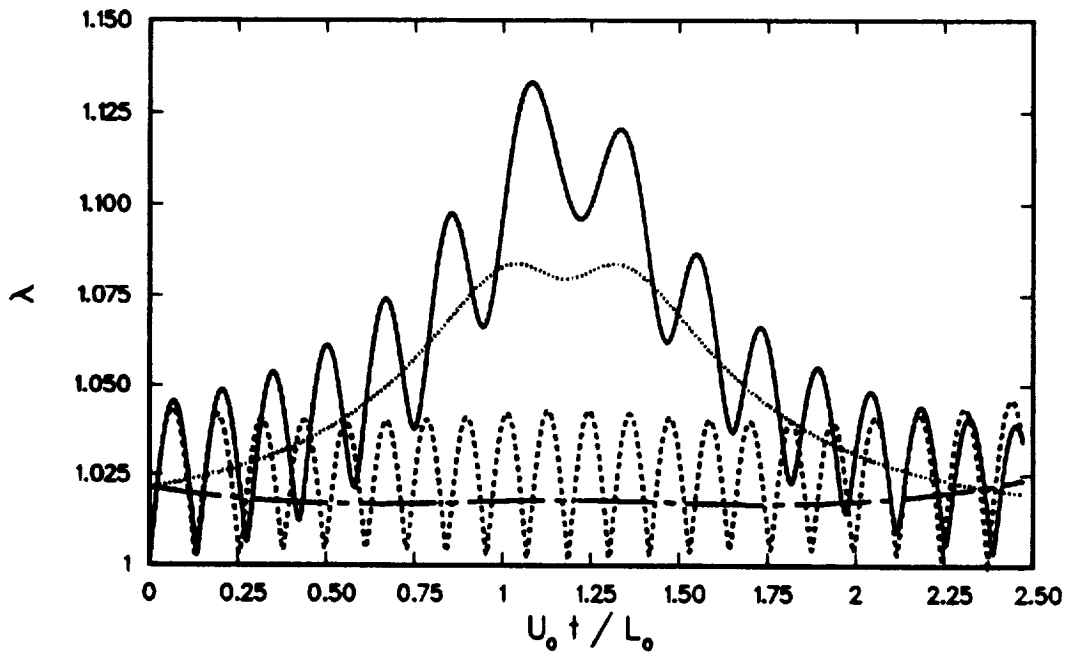


FIGURE 5.5. Aspect ratios (elliptic model) for the passage of $\alpha = 0.1, \hat{d} = 1$. —, initially rear vortex; ----, initially leading vortex; ·····, stable equilibrium for the initially rear vortex; - · - ·, stable equilibrium for the initially leading vortex.

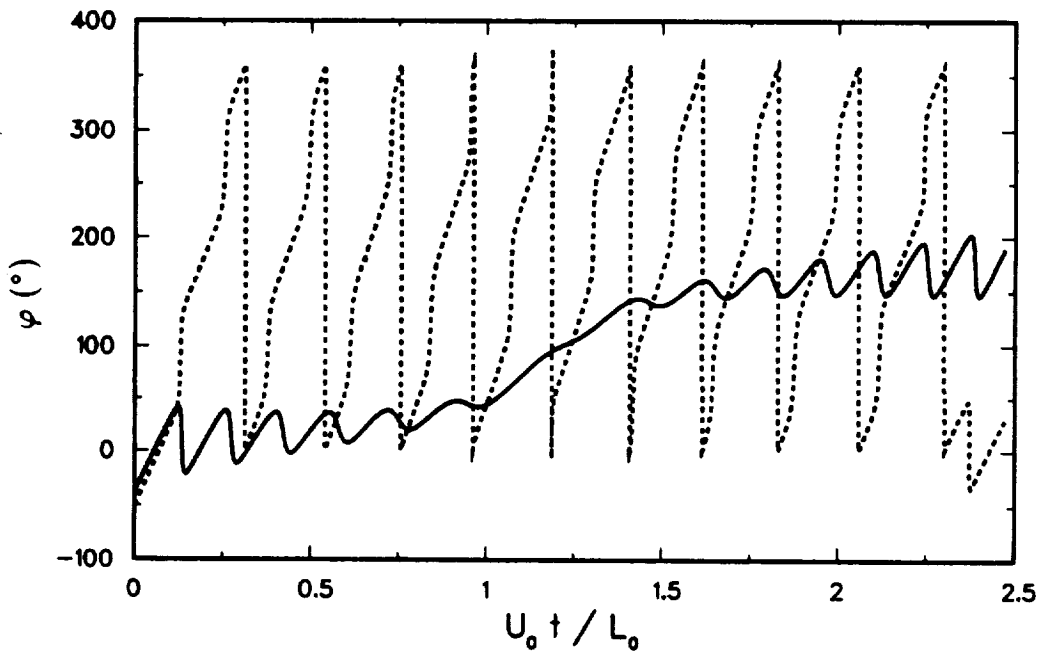


FIGURE 5.6. Orientation angle (elliptic model) for the passage of $\alpha = 0.1, \hat{d} = 1$. —, initially rear vortex; ----, initially leading vortex.

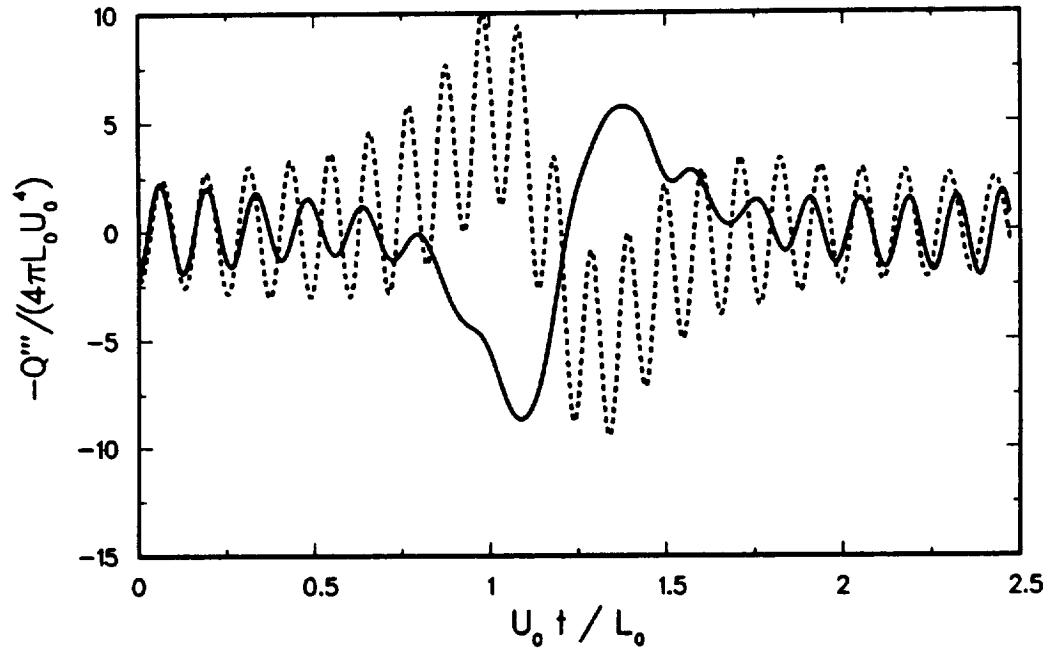


FIGURE 5.7. Contributions to the acoustic signal for the passage of $\alpha = 0.1, \hat{d} = 1$ (elliptic model). —, initially rear vortex (nutating); ----, initially leading vortex (rotating).

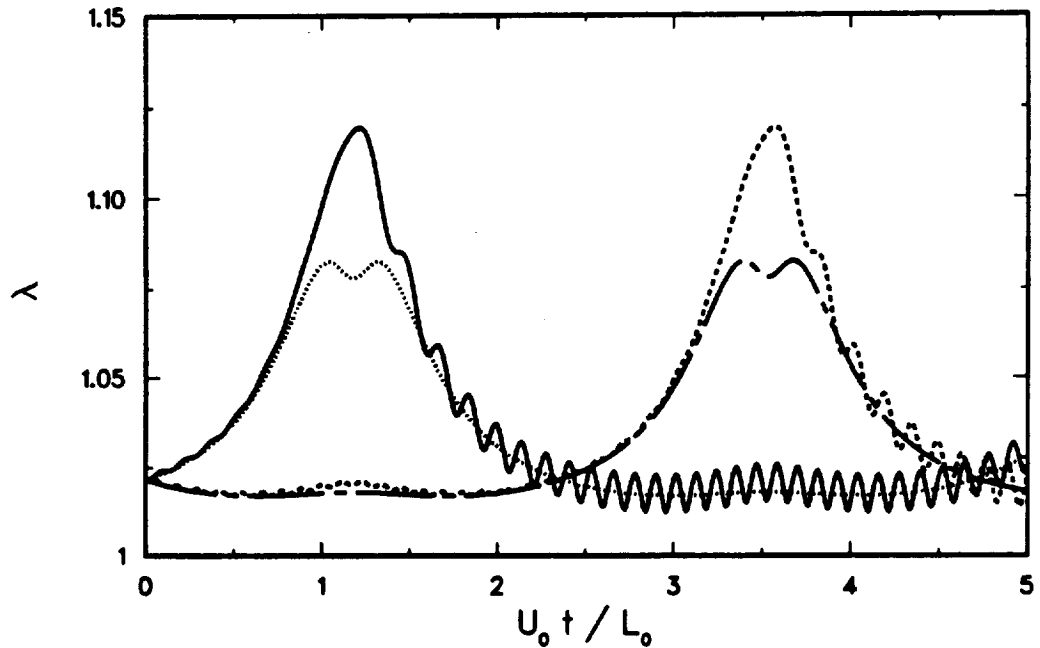


FIGURE 5.8. Aspect ratios (elliptic model) for two passages of $\alpha = 0.1, \hat{d} = 1$ with equilibrium initial conditions.. —, initially rear vortex; ----, initially leading vortex; - · - · - , stable equilibrium for the initially rear vortex; - - - - , stable equilibrium for the initially leading vortex.

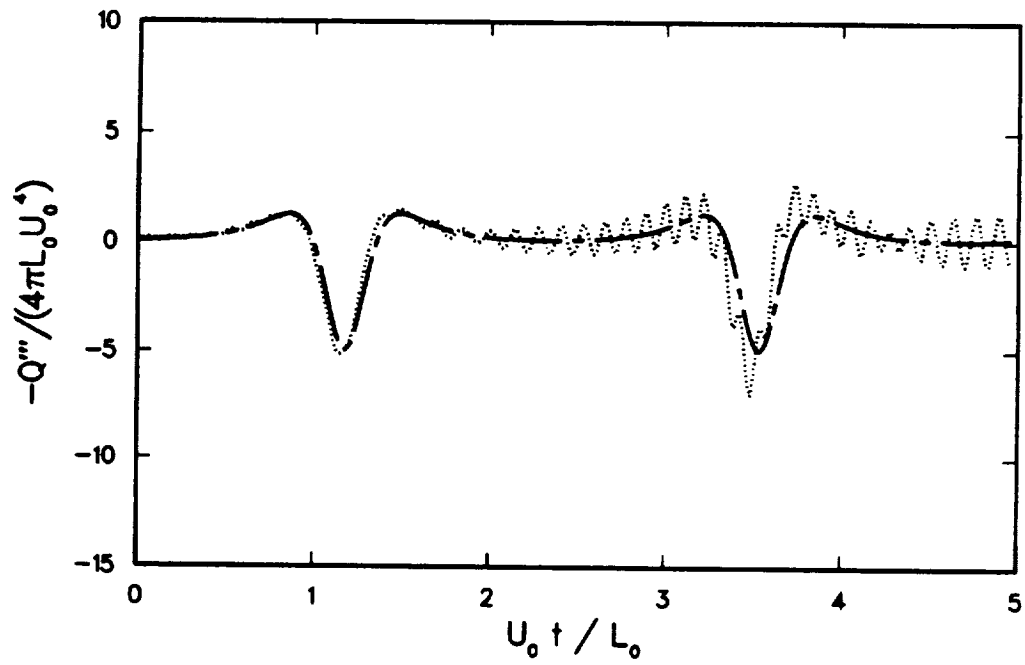


FIGURE 5.9. Acoustic signal (elliptic model) for two passages of $\alpha = 0.1, \hat{d} = 1$ with equilibrium initial conditions., elliptic model; ----, Dyson's model.

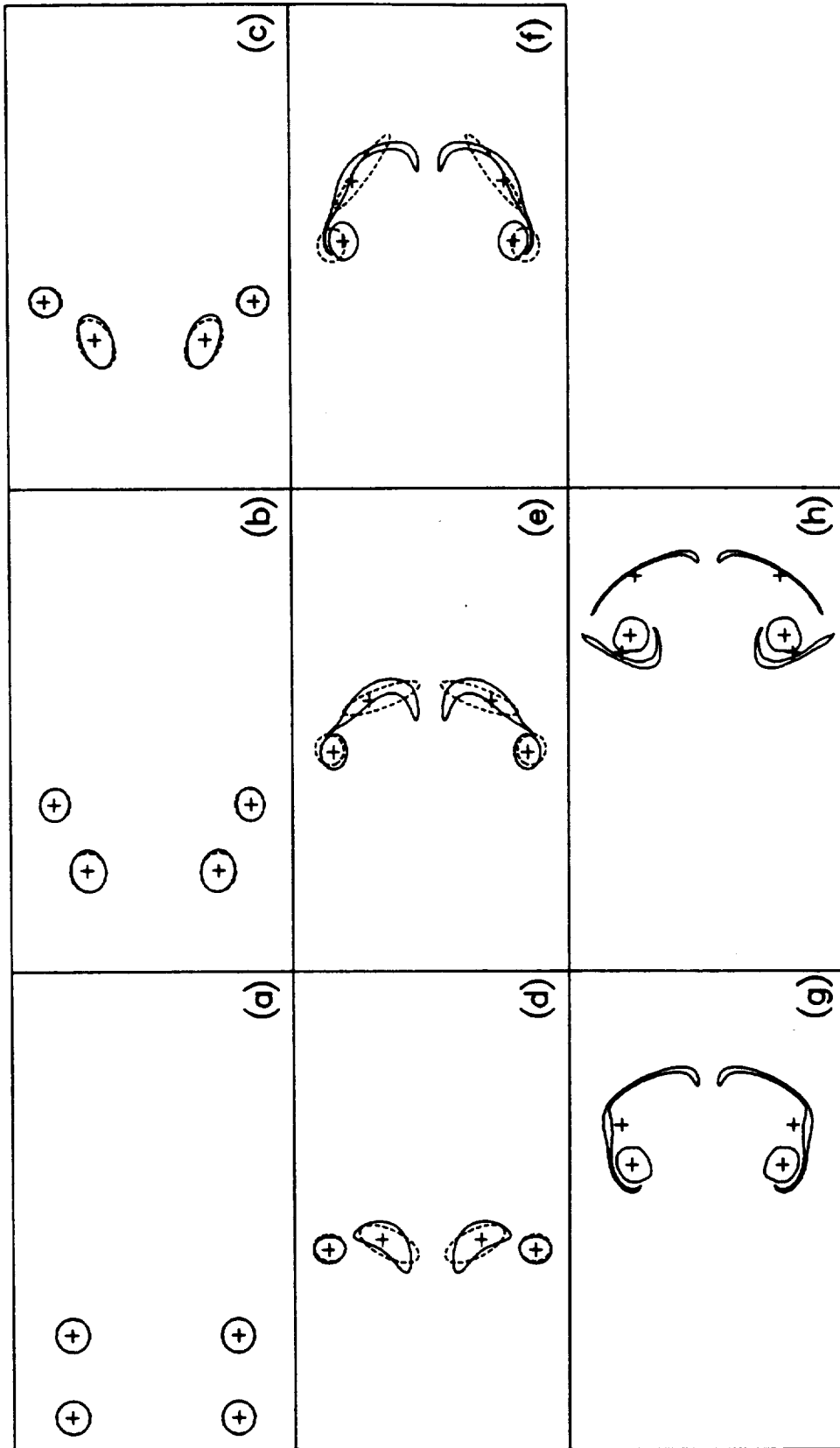


FIGURE 5.10. Core shapes for the passage of $\alpha = 0.2$, $\hat{d} = 1$. —, contour dynamics; , elliptic model; +, vorticity centroids. U_{ot}/L_o : (a) 0; (b) 0.54; (c) 0.81; (d) 1.08; (e) 1.35; (f) 1.62; (g) 1.89; (h) 2.15.

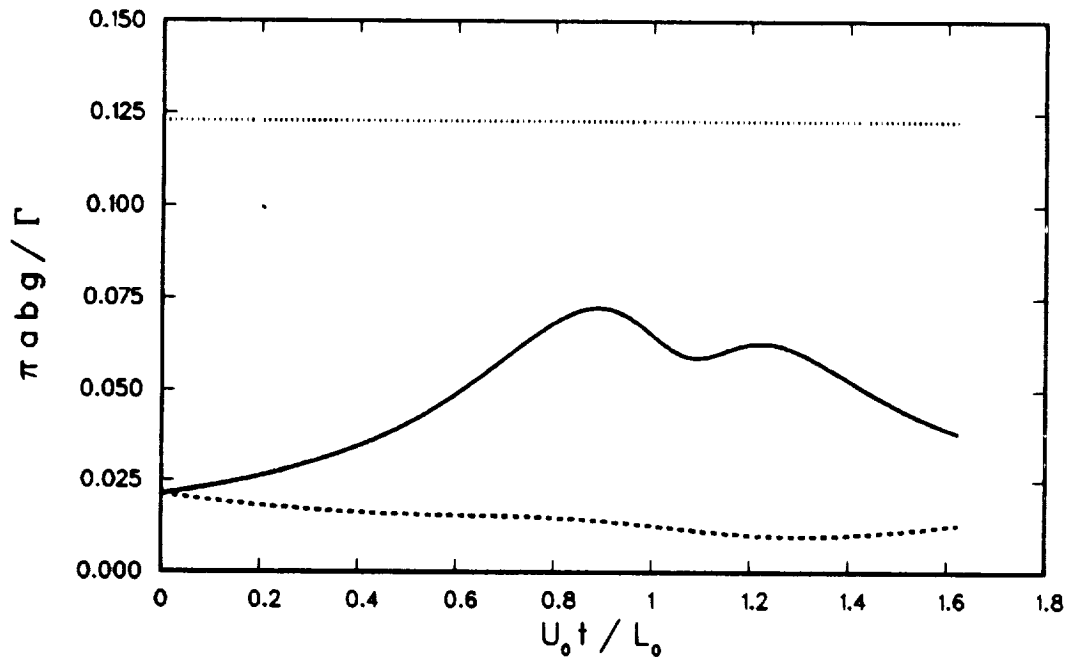


FIGURE 5.11. Ratio of composite strain rate to vorticity at the centroid for the passage of $\alpha = 0.2, \hat{d} = 1$ (elliptic model). —, initially rear vortex; ----, initially leading vortex; ·····, critical value for the disappearance of the regime of rotation for fixed strain.

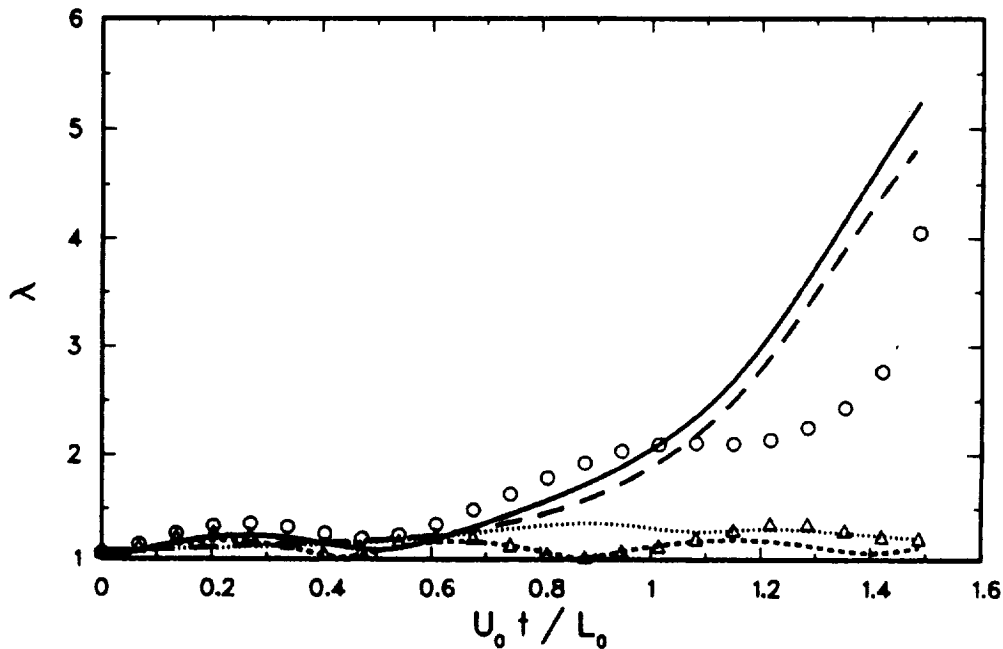


FIGURE 5.12. Aspect ratios for the passage of $\alpha = 0.2, \hat{d} = 1$. O, contour dynamics, initially rear vortex; Δ , contour dynamics, initially leading vortex; —, elliptic model, initially rear vortex; ·····, stable equilibrium, initially rear vortex; ----, elliptic model, initially leading vortex; - - - -, elliptic model with equilibrium initial conditions, initially rear vortex.

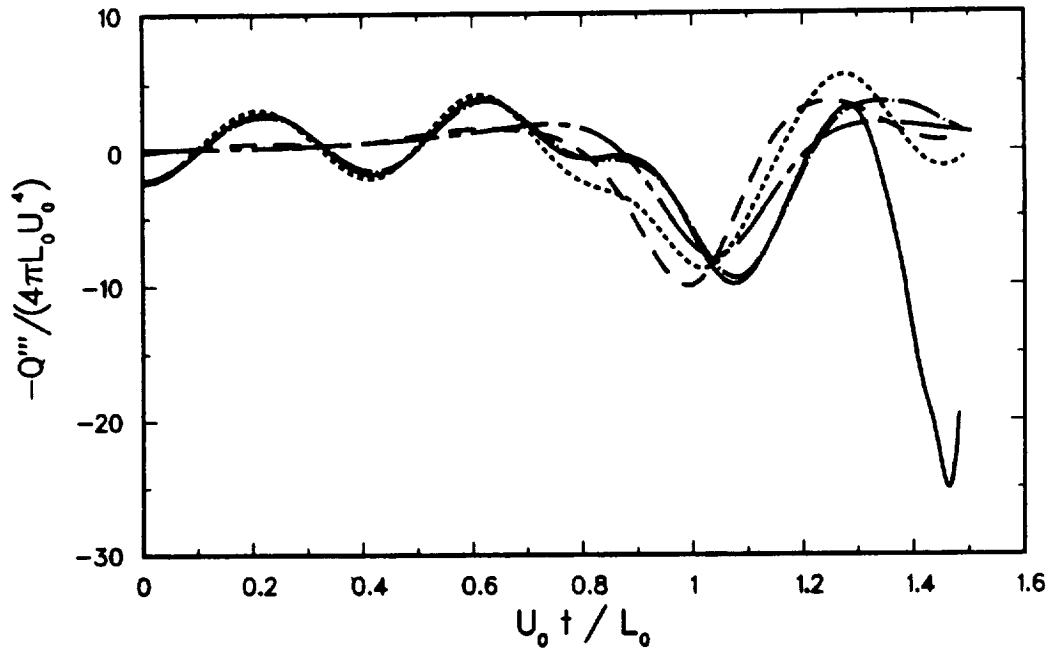


FIGURE 5.13. Acoustic signal for the passage of $\alpha = 0.2, \hat{d} = 1$. —, contour dynamics; ----, elliptic model; -·-·-, elliptic model with equilibrium initial conditions; ····, Dyson's model; — — —, filament method.

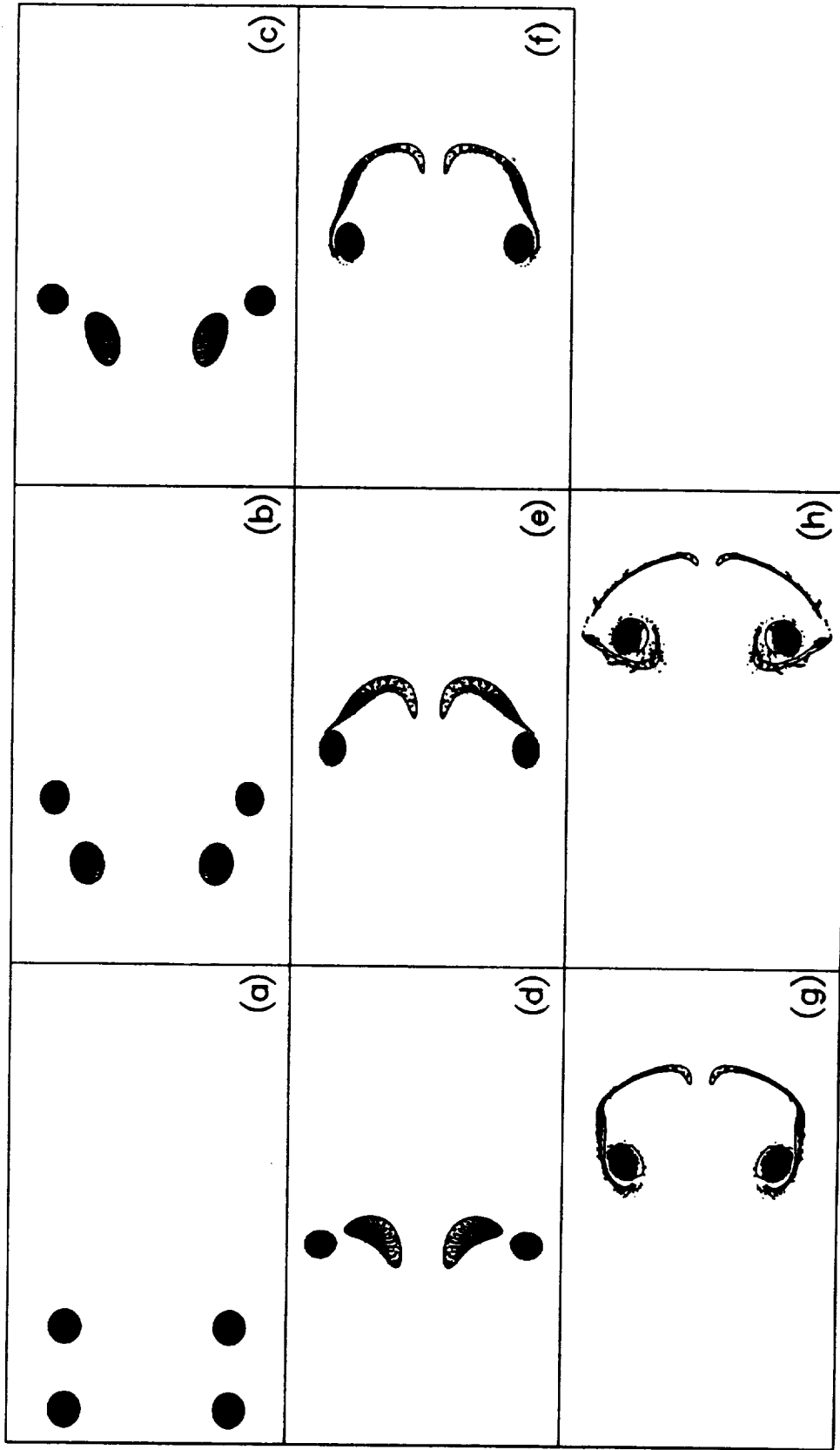


FIGURE 5.14. Filament method passage of $\alpha = 0.2, \hat{d} = 1$ compared with the contours of Figure 5.10 at the same instants.

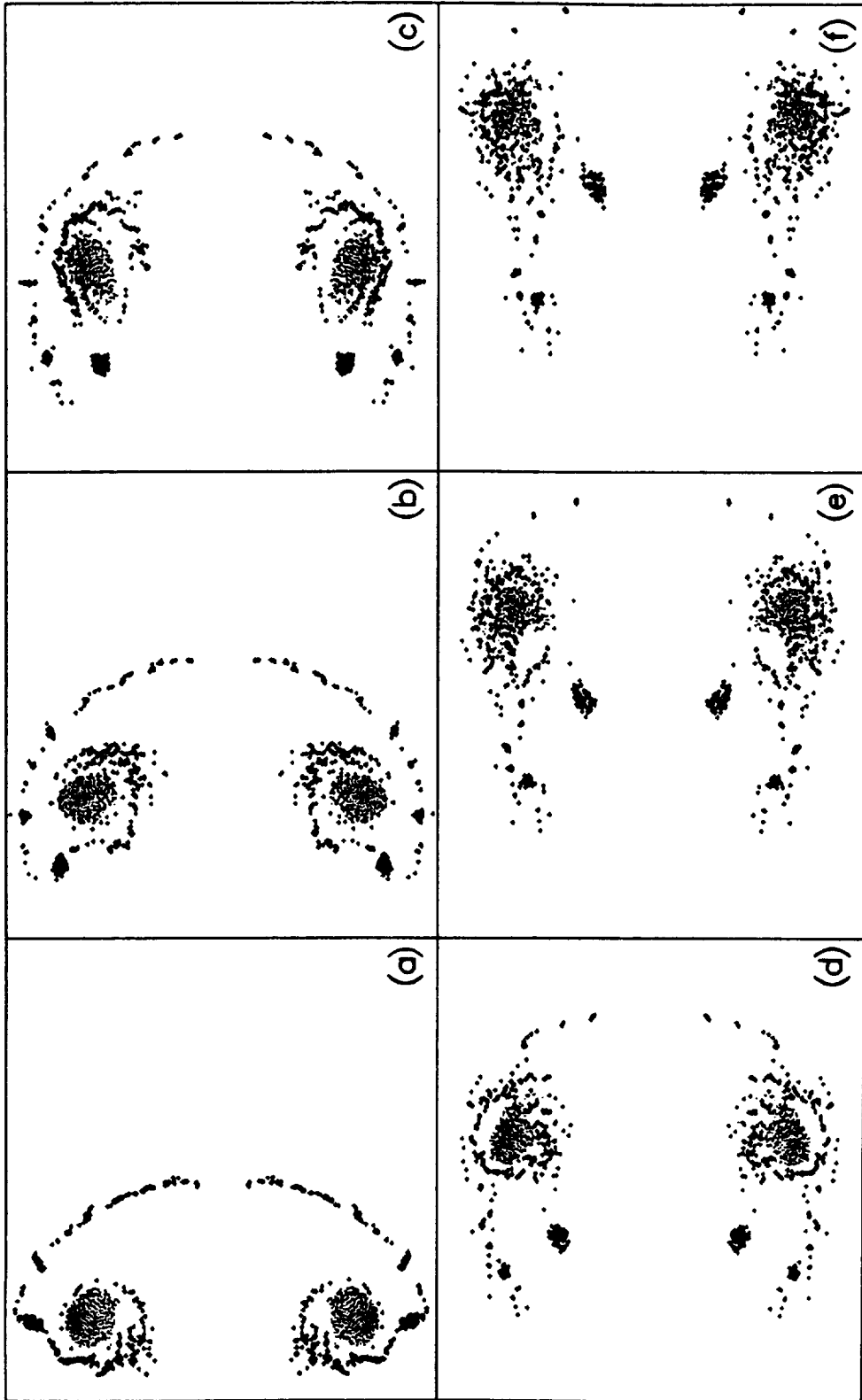


FIGURE 5.15. Continuation of filament method passage of $\alpha = 0.2, \hat{d} = 1$ from the previous figure. $U_0 t/L_0$: (a) 2.16; (b) 2.43; (c) 2.70; (d) 2.98; (e) 3.25; (f) 3.38. Filaments from the initially rear vortex are distinguished by larger plus signs.

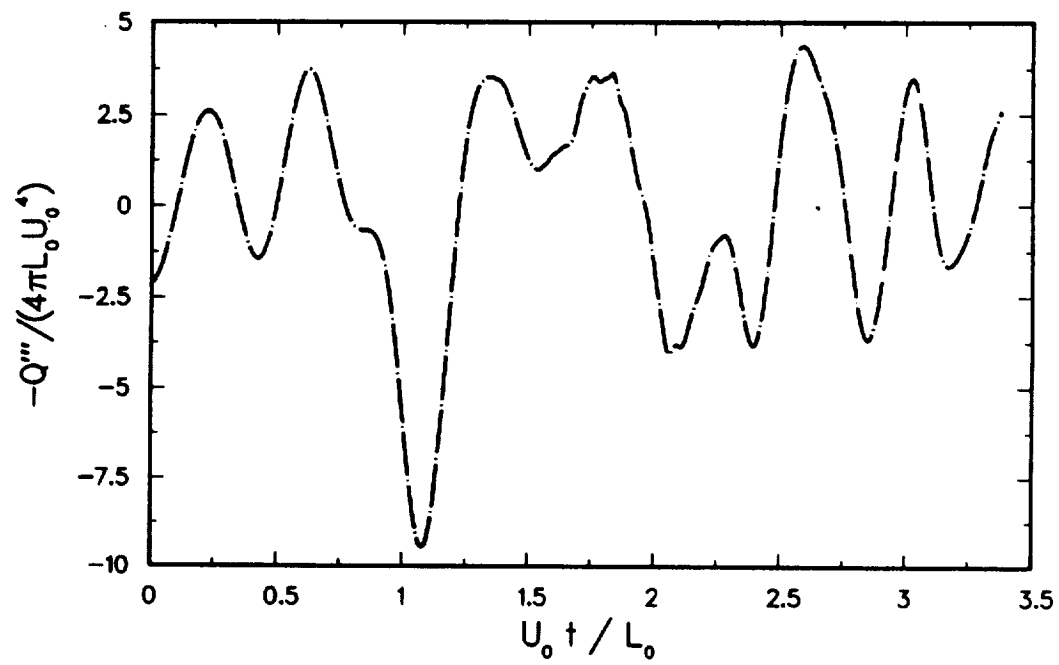


FIGURE 5.16. Acoustic signal for the entire filament calculation for passage of $\alpha = 0.2, \hat{d} = 1$.

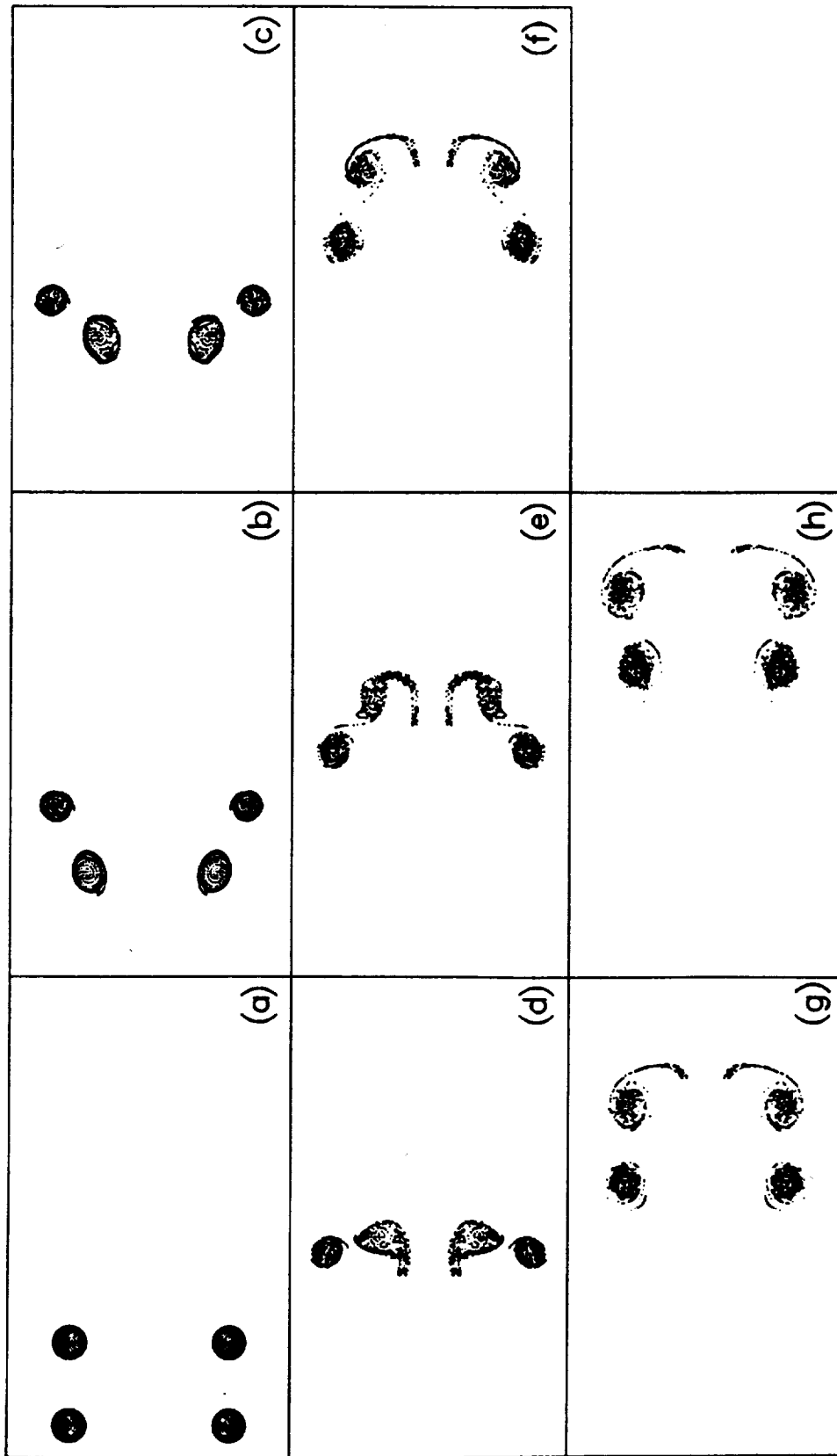


FIGURE 5.17. Filament method passage of $\alpha = 0.2, \hat{d} = 1$ (peaked vorticity). $U_0 t / L_0$: (a) 0; (b) 0.587; (c) 0.881; (d) 1.18; (e) 1.47; (f) 1.76; (g) 2.10; (h) 2.35.

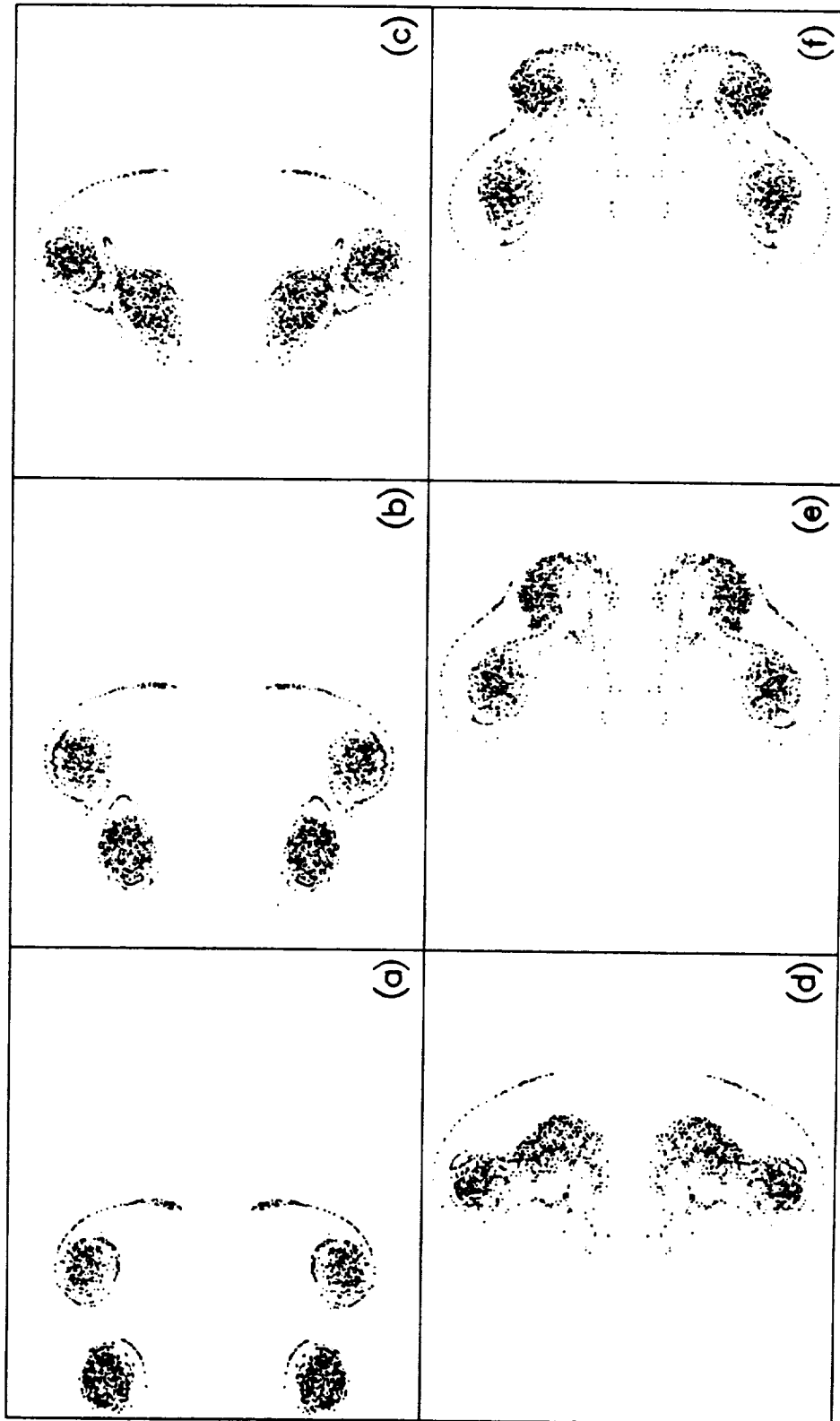


FIGURE 5.18. Continuation of filament method passage of $\alpha = 0.2, \bar{d} = 1$ from the previous figure. $U_0 t / L_0$: (a) 2.35; (b) 2.64; (c) 2.94; (d) 3.23; (e) 3.52; (f) 3.67.

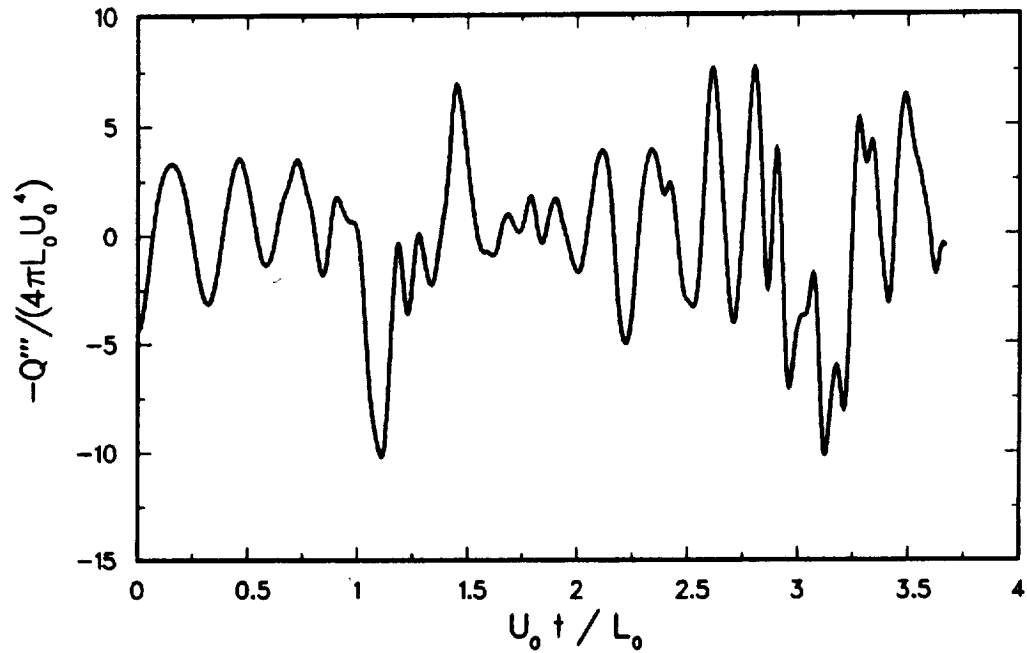


FIGURE 5.19. Acoustic signal for filament method passage of $\alpha = 0.2$, $\hat{d} = 1$ (peaked vorticity).

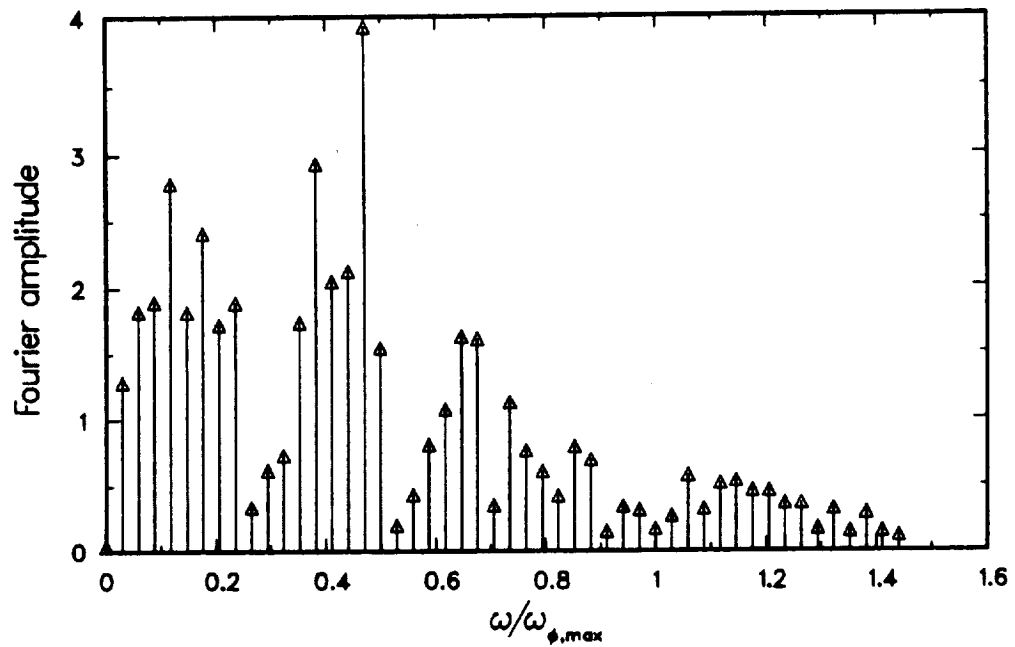


FIGURE 5.20. Fourier amplitudes for the acoustic signal in Figure 5.19. The horizontal axis is the circular frequency normalized by the initial peak vorticity.

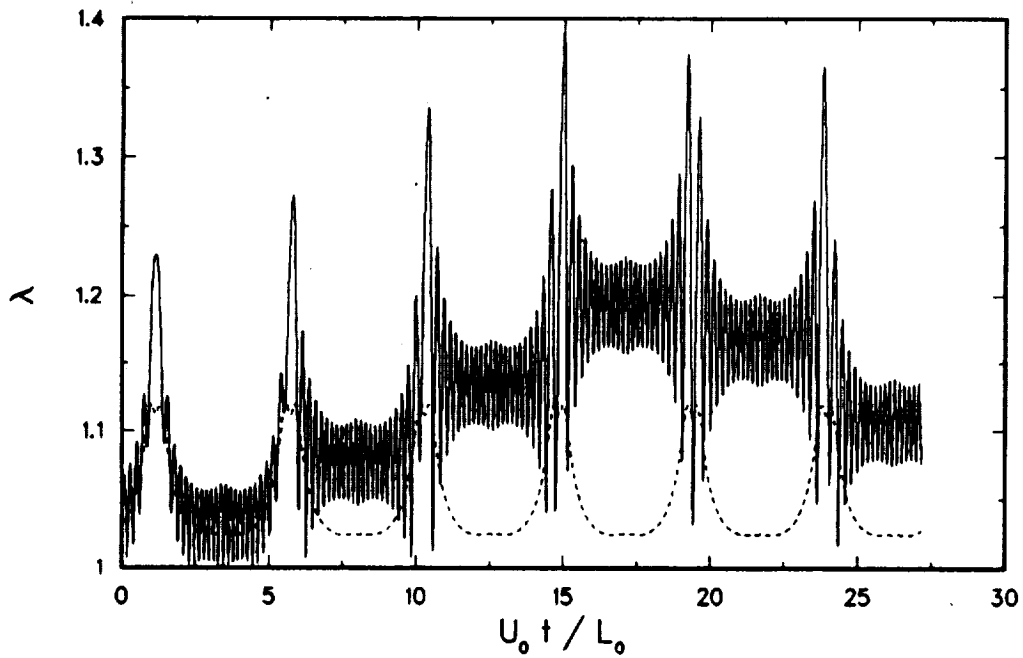


FIGURE 5.21. —, aspect ratio (elliptic model) for the rear vortex in the passage of $\alpha = 0.12, \hat{d} = 1$; ----, stable equilibrium.

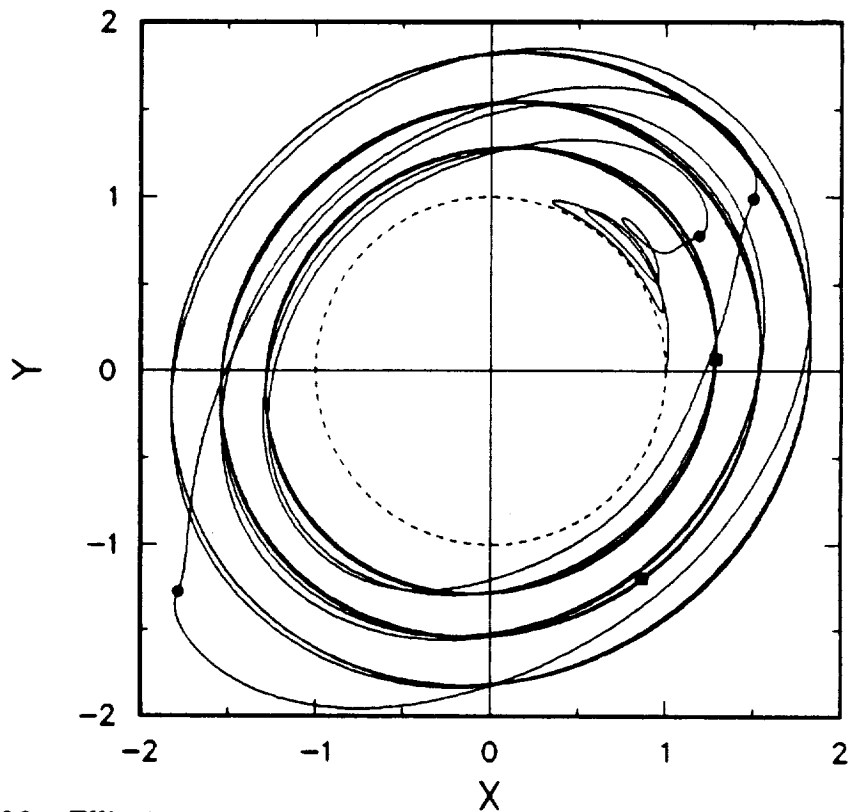


FIGURE 5.22. Elliptic model phase plane trajectory of the initially rear vortex in the passage of $\alpha = 0.14, \hat{d} = 1$. ●, points of minimum radial centroid; ■, points of maximum radial centroid.

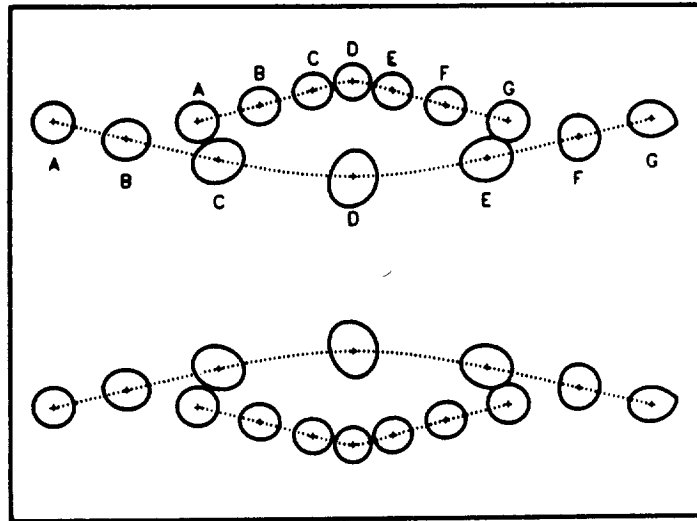


FIGURE 5.23. Core shapes at equal time intervals for the passage of $\alpha = 0.14$, $\hat{d} = 1$, trajectory of vorticity centroids; +, vorticity centroids. $U_0 t / L_0$: A, 0; B, 0.37; C, 0.74; D, 1.11; E, 1.48; F, 1.85; G, 2.22.

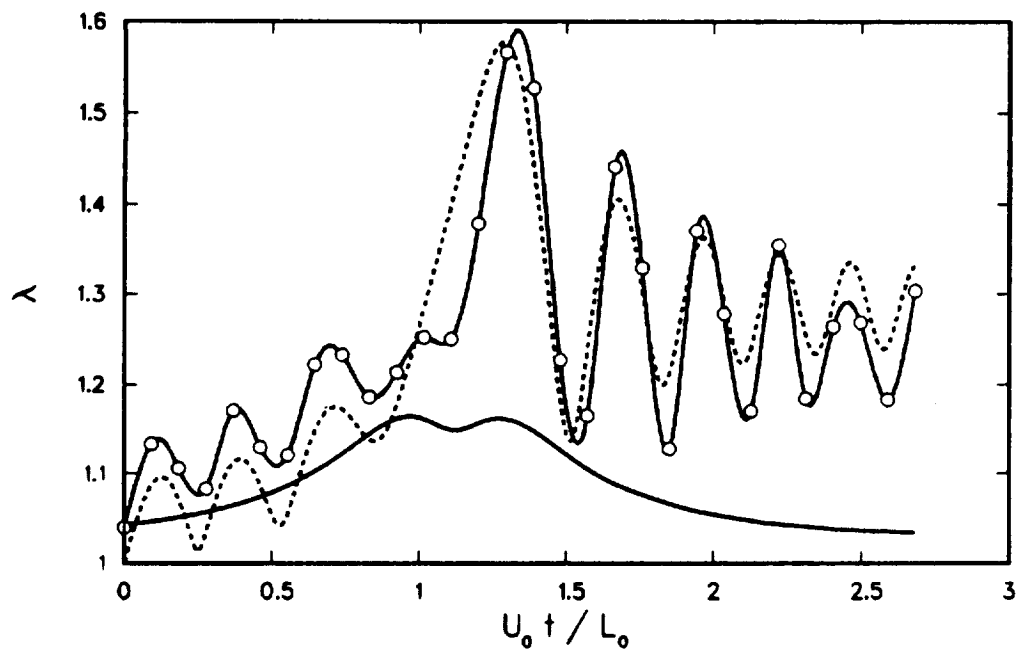


FIGURE 5.24. Aspect ratio of the initially rear vortex for the passage of $\alpha = 0.14$, $\hat{d} = 1$. -O-, contour dynamics; ----, elliptic model; —, stable equilibrium.

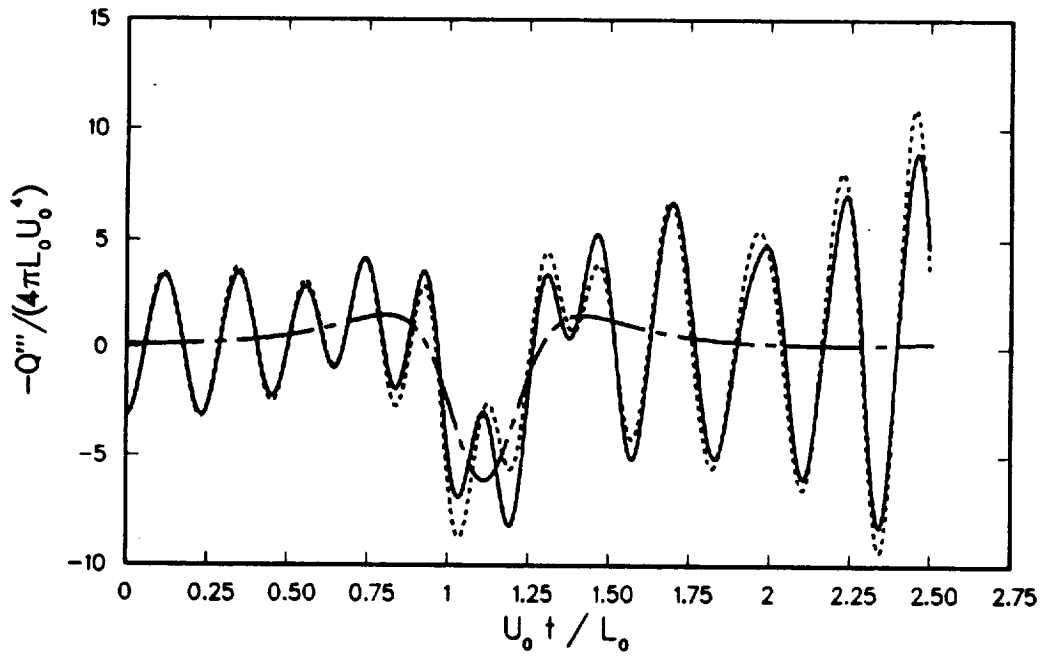


FIGURE 5.25. Acoustic radiation for the passage of $\alpha = 0.14, \hat{d} = 1$. —, contour dynamics; ----, elliptic model; -·-·, Dyson's model.

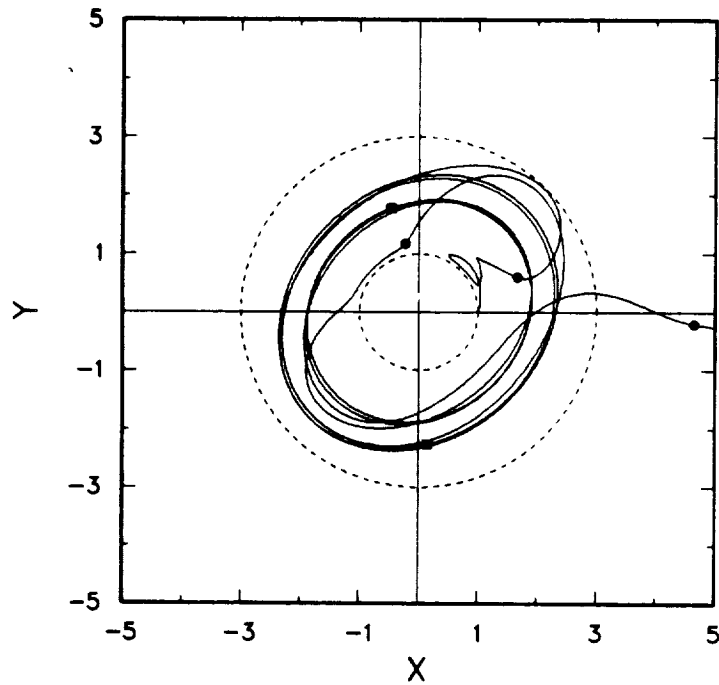


FIGURE 5.26. Elliptic model phase plane trajectory of the initially rear vortex for passage of $\alpha = 0.18, \hat{d} = 1$. ●, ■, points of minimum and maximum radial centroid, respectively.

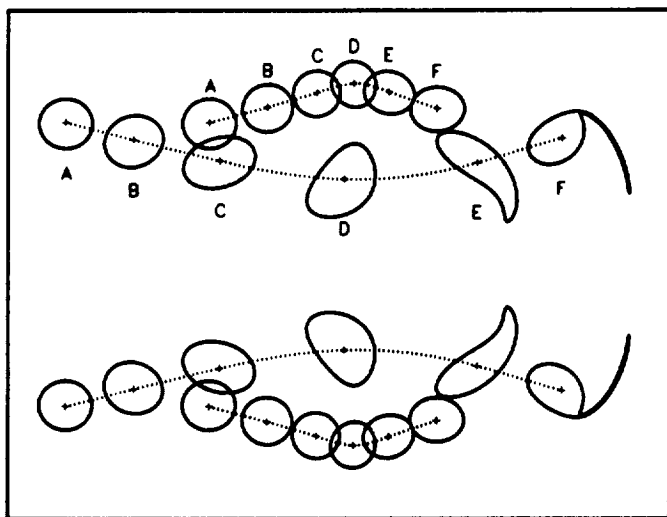


FIGURE 5.27. Core shapes at equal time intervals for the passage of $\alpha = 0.18, \hat{d} = 1$, trajectory of vorticity centroids; +, vorticity centroids. $U_0 t / L_0$: A, 0; B, 0.34; C, 0.68; D, 1.02; E, 1.37; F, 1.71.

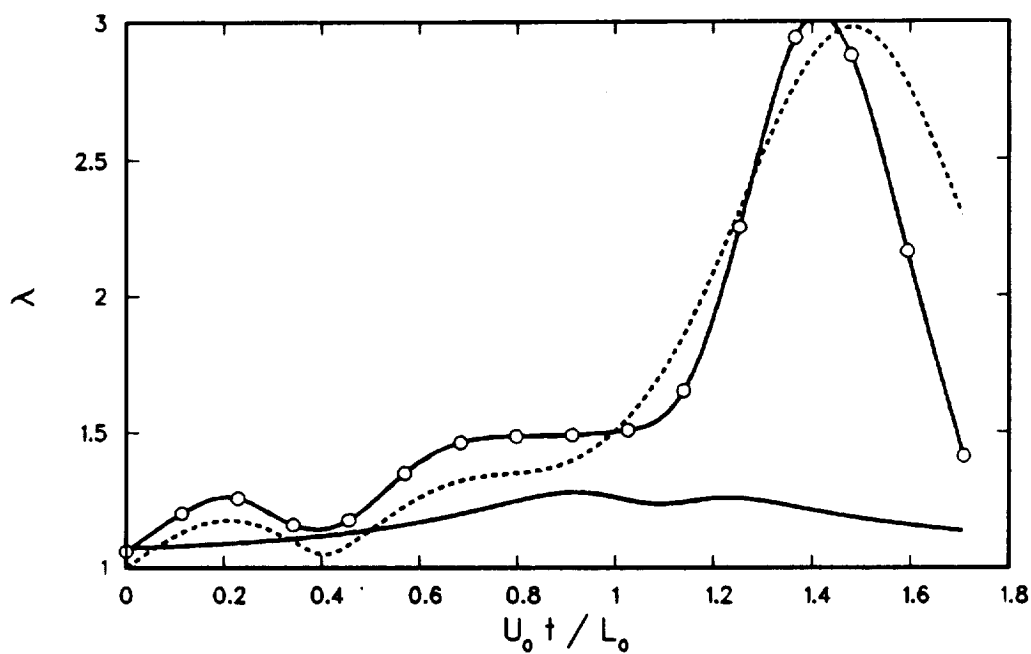


FIGURE 5.28. Aspect ratios for the passage of $\alpha = 0.18, \hat{d} = 1$. -O-, contour dynamics; ----, elliptic model; —, stable equilibrium.

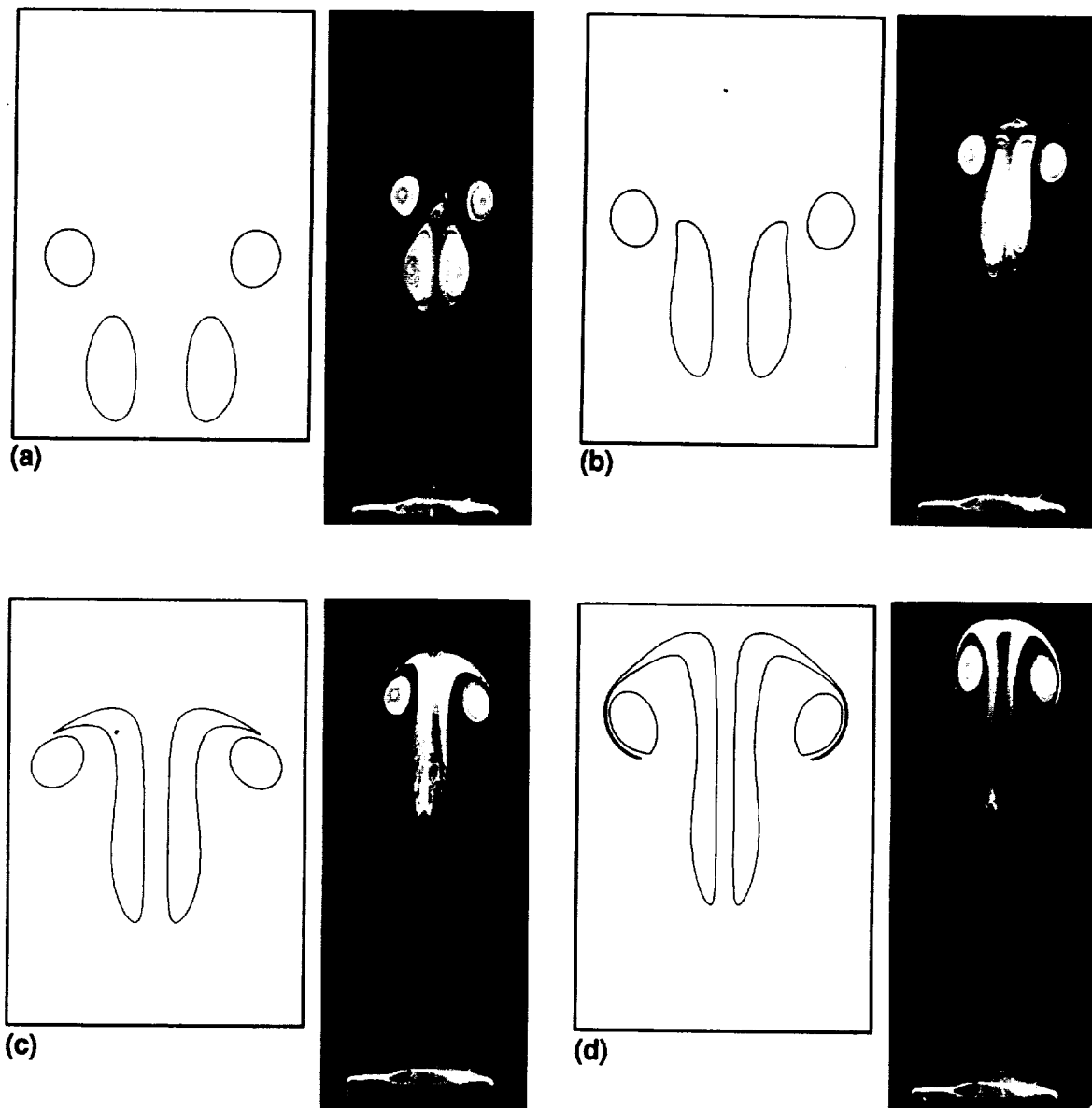


FIGURE 5.29. $\alpha = 0.40$ passage. U_{ot}/L_o : (a) 2.32; (b) 3.16; (c) 3.58; (d) 4.22. The photographs are from Oshima, Kambe & Asaka (1975). *Reproduced with permission.*

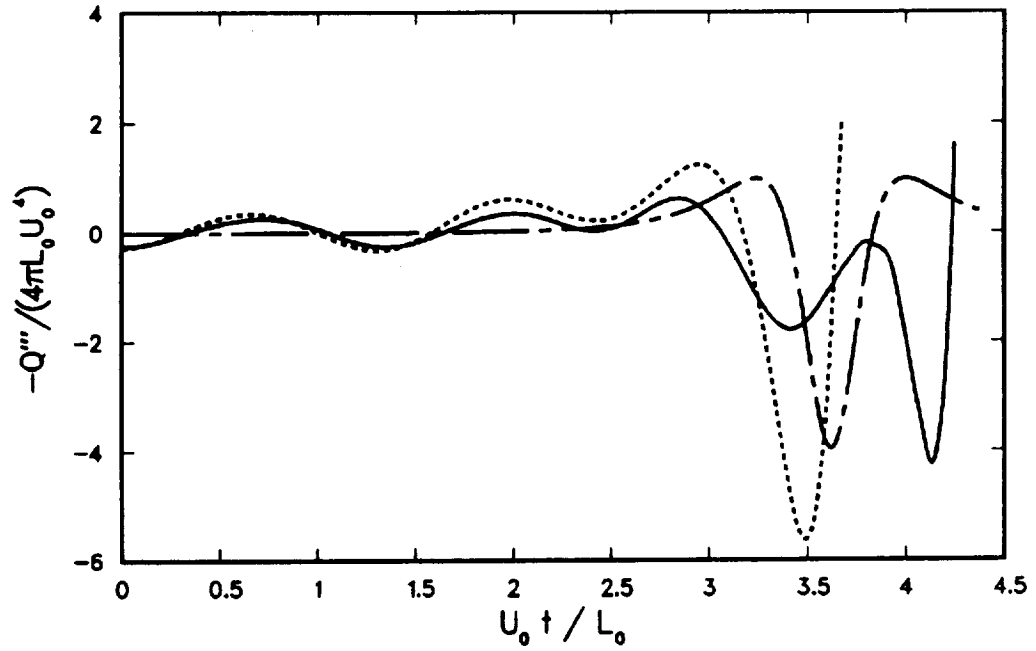


FIGURE 5.30. Comparison of the normalized acoustic signal for the passage of $\alpha = 0.4$, $\hat{d} = 2$. —, contour dynamics; ----, elliptic model; -·-·, Dyson's model.

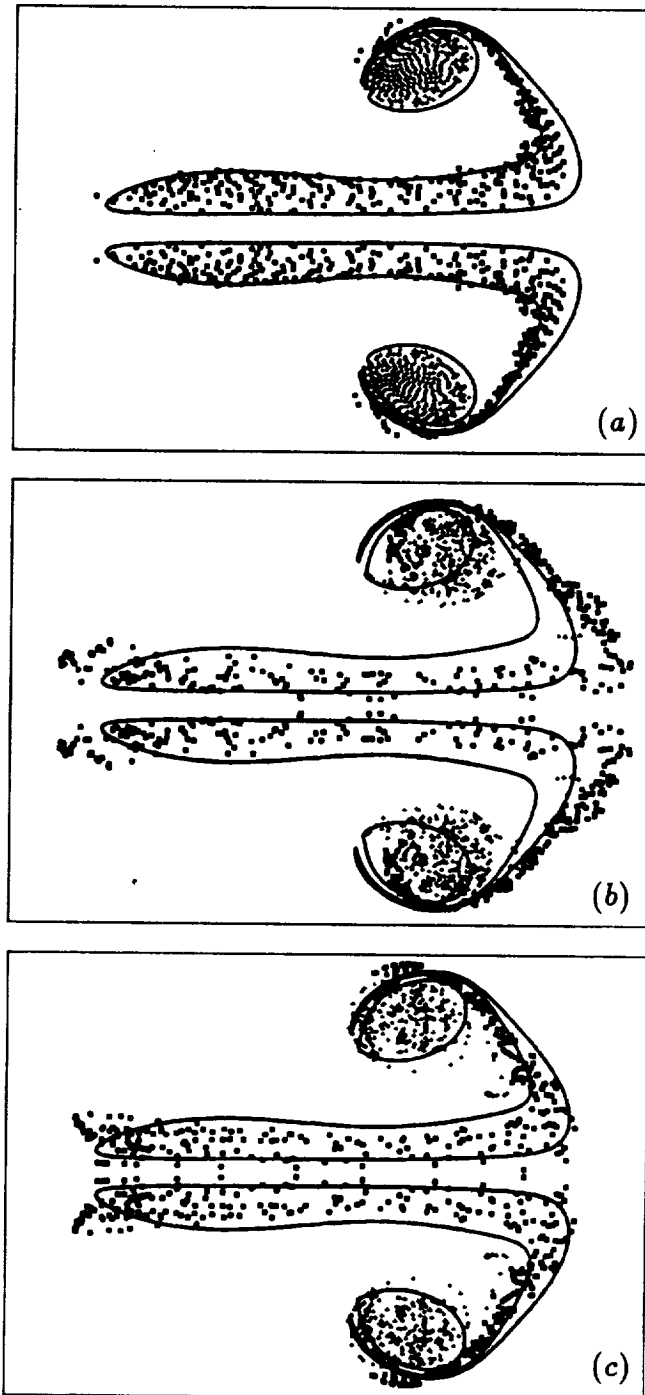


FIGURE 5.31. $\alpha = 0.4$ passage, $\hat{d} = 2$. Comparison of filament method and contour dynamics. (a) Linear vorticity; (b) Peaked over-energetic vorticity; (c) Peaked vorticity with energy matched to (a). ■, +, filaments from the initially rear and front vortices, respectively.

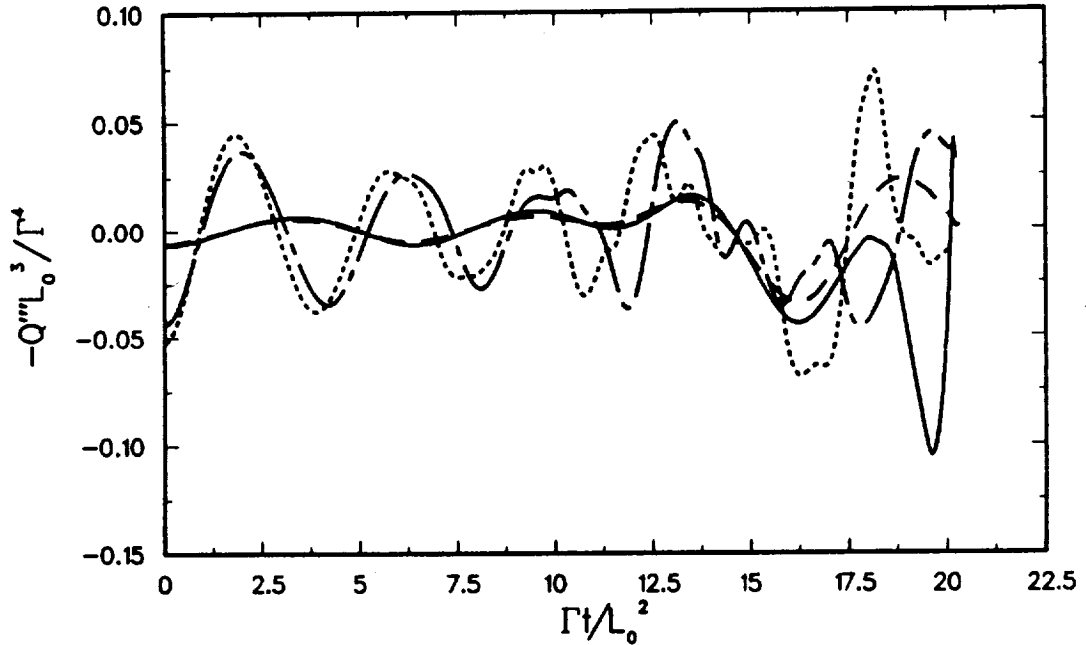


FIGURE 5.32. Comparison of the acoustic signal from vortex filament passage cases and contour dynamics ($\alpha = 0.4, \hat{d} = 2$). —, contour dynamics; ----, filaments, linear vorticity; ····, filaments, peaked over-energetic vorticity; -·-·, filaments, peaked vorticity, energy matched with linear vorticity.

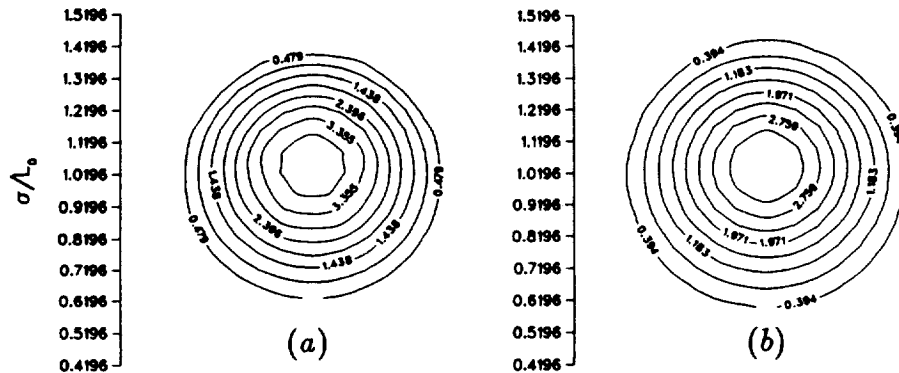


FIGURE 5.33. Initial vorticity normalized by Γ/L_0^2 for the two peaked vorticity passage cases ($\alpha = 0.4, \hat{d} = 2$). (a) Over-energetic; (b) Energy matched to the linear vorticity case.

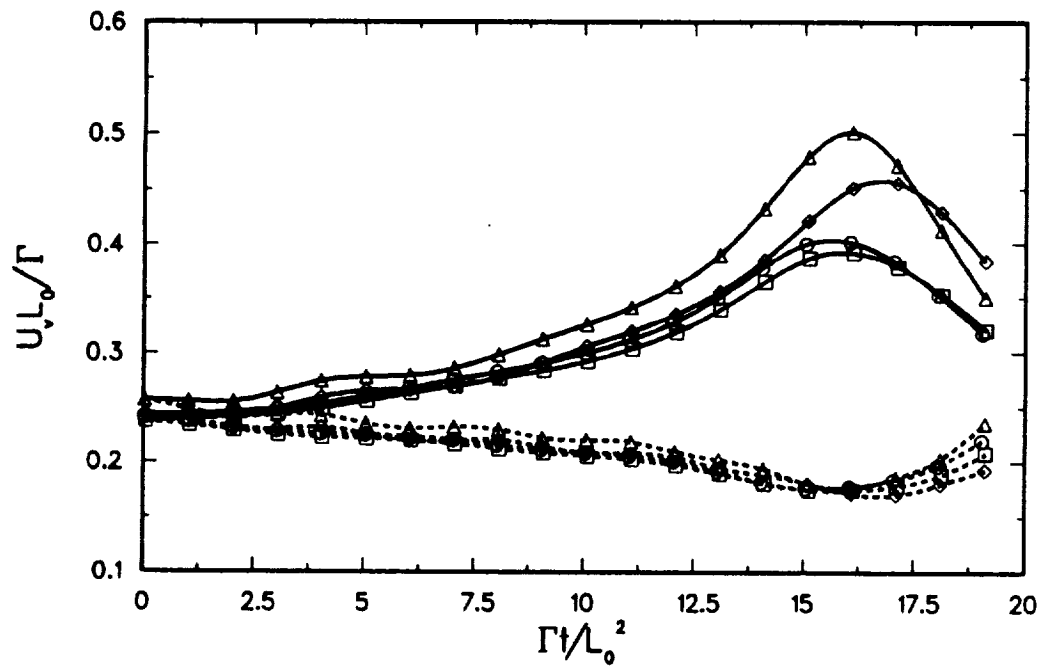


FIGURE 5.34. Speed of the vorticity centroid for the passage of $\alpha = 0.4$, $\hat{d} = 2$. —, initially rear vortex; ----, initially leading vortex; \circ , contour dynamics; \square , filament method (linear vorticity); \triangle , filament method (peaked over-energetic vorticity); \diamond , filament method (peaked vorticity, matched energy).

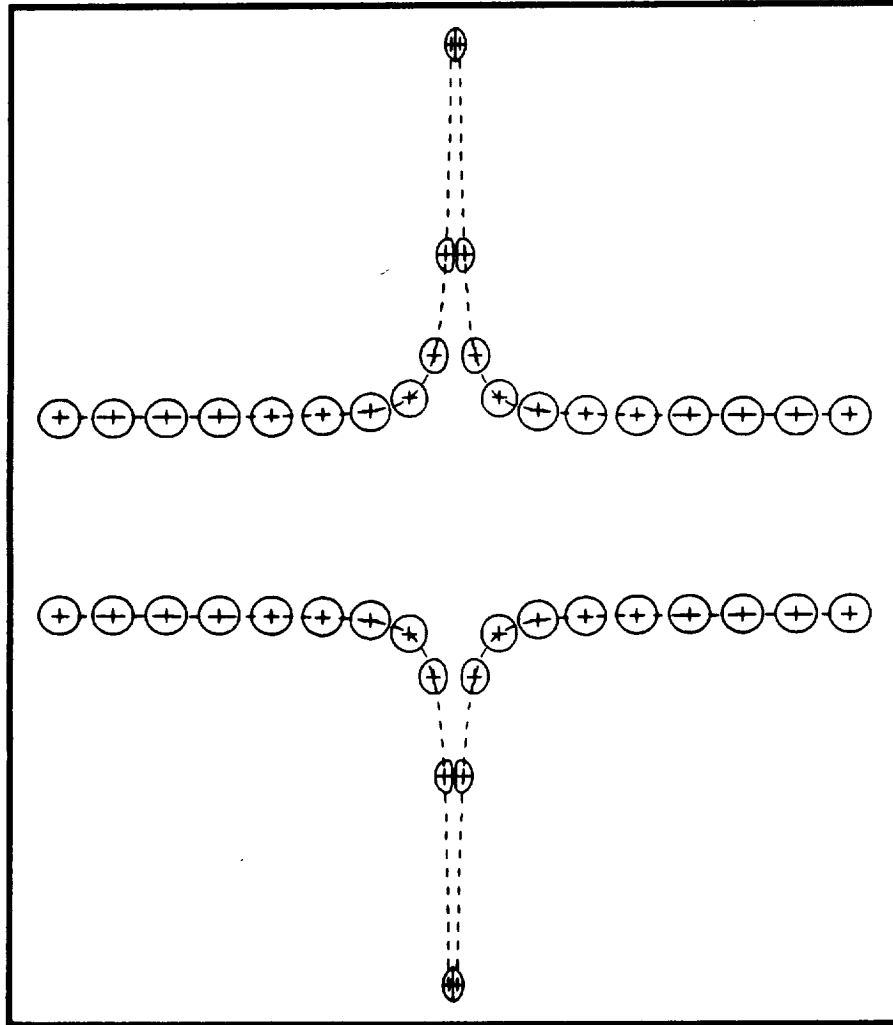


FIGURE 5.35. Core shapes for the collision of $\alpha = 0.2$, $\hat{d} = 8$. At equal time intervals except for the last instant. $U_{ot}/L_o = 0, 0.54, 1.09, 1.63, 2.17, 2.72, 3.26, 3.80, 4.35, 4.89, 5.57$. +, vorticity centroids; ----, trajectory of vorticity centroids.

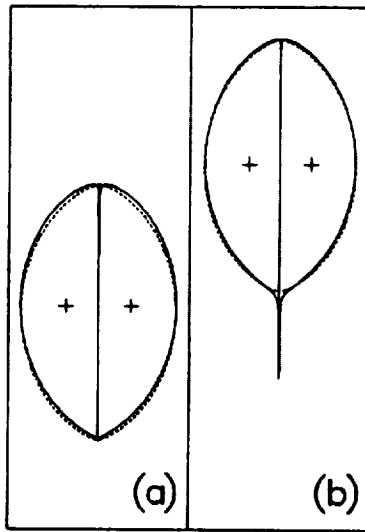


FIGURE 5.36. (a) Shape at $U_0 t / L_0 = 5.57$ magnified from the previous figure; (b) $U_0 t / L_0 = 5.62$. —, computed; ·····, Sadovskii (1971) pair; +, vorticity centroids.

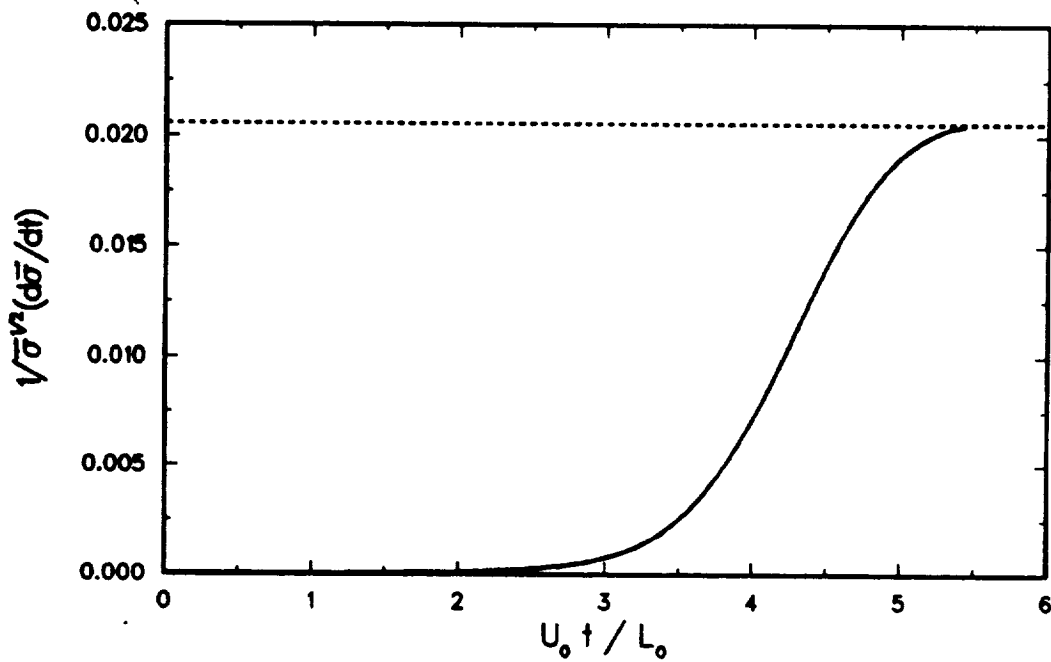


FIGURE 5.37. Rate of the radial shape centroid scaled on $\bar{\sigma}^{-1/2}$. —, simulation; ----, based on a core shape in the form of a Sadovskii (1971) pair.

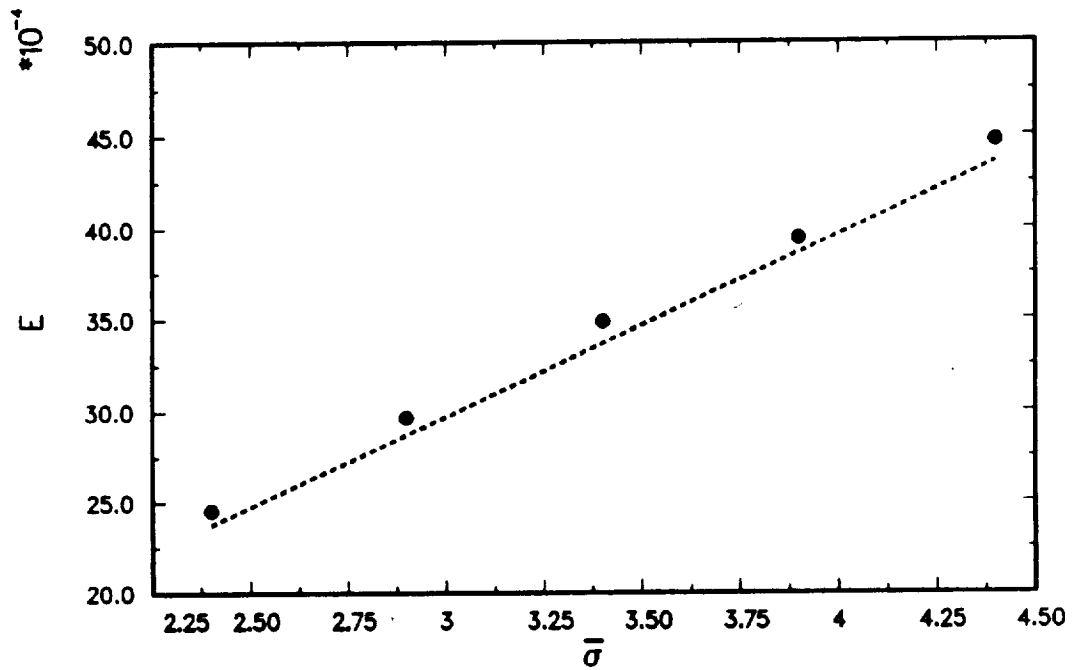


FIGURE 5.38. Energies of states progressively stretched from the configuration at $U_{ot}/L_o = 5.57$ for the collision of $\alpha = 0.2, \hat{d} = 8$. ●, computed; ----, based on a core having the shape of the 2-D translating pair.

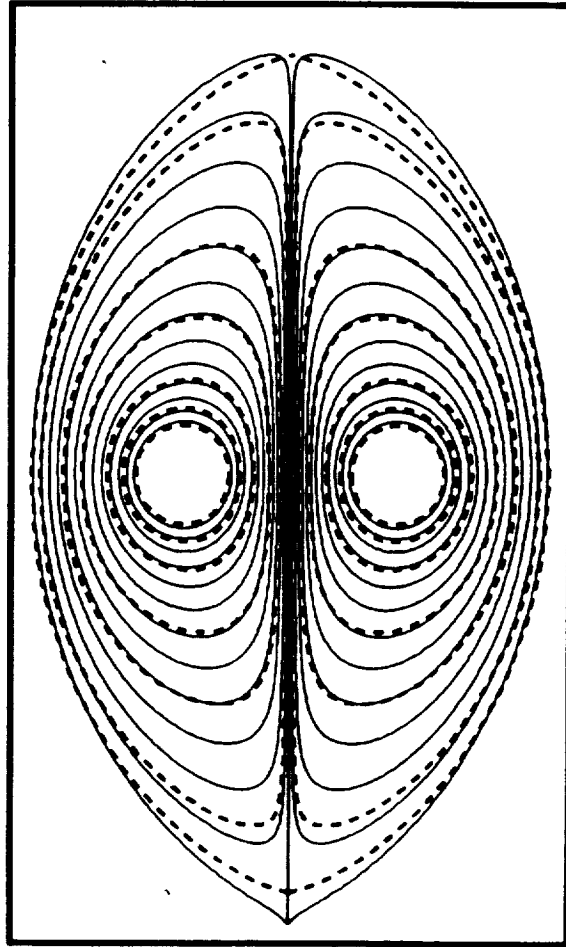


FIGURE 5.39. Rescaled core shapes (solid) for the collision of $\alpha = 0.2, \hat{d} = 8$. $U_o t / L_o = 3.94-5.57$ at equal intervals. ----, two-dimensional translating pairs numbered 6-11 and 13 in Figure 4a of Wu *et al.* (1984).

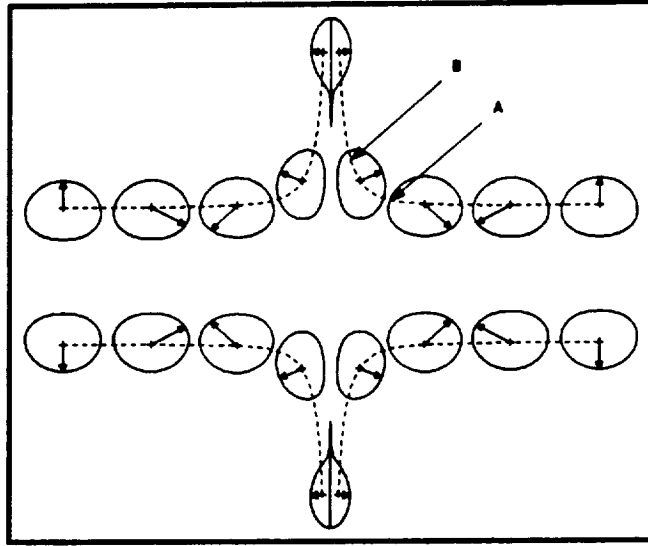


FIGURE 5.40. Core shapes for the collision of $\alpha = 0.5$, $\hat{d} = 8$. At equal time intervals except for the last instant. $U_0 t / L_0 = 0, 1.33, 2.67, 4.00, 5.49$. The arrowhead tracks a particle in its motion around the boundary. Only between the last two instants is the rotation larger than 2π . +, vorticity centroids; A, B, points of maximum and minimum, respectively, in the acoustic signal shown in Figure 5.51.

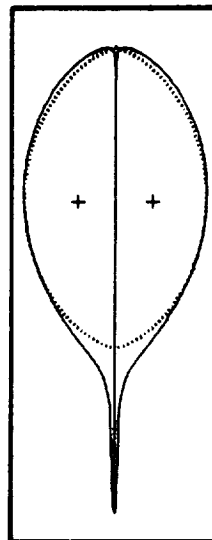


FIGURE 5.41. Shape at $U_0 t / L_0 = 5.49$ magnified from the previous figure. —, computed shape; , Sadvskii (1971) pair.

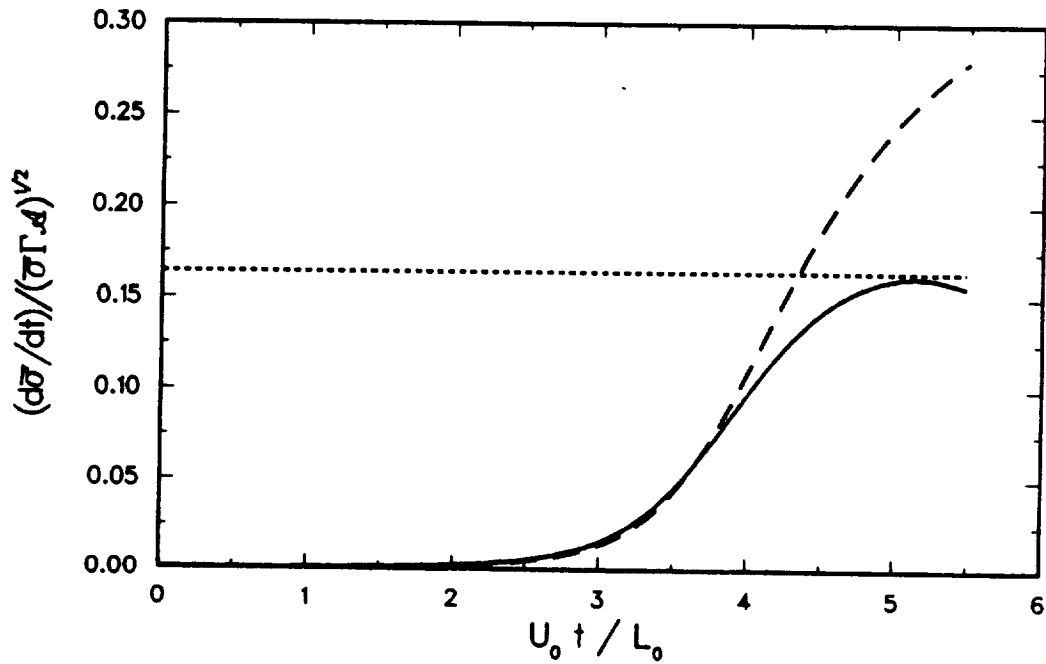


FIGURE 5.42. Rate of stretching of the centroid for the collision of $\alpha = 0.5$. —, contour dynamics; ----, based on a core having the shape of the Sadovskii (1971) pair; - · - ·, Dyson's model.

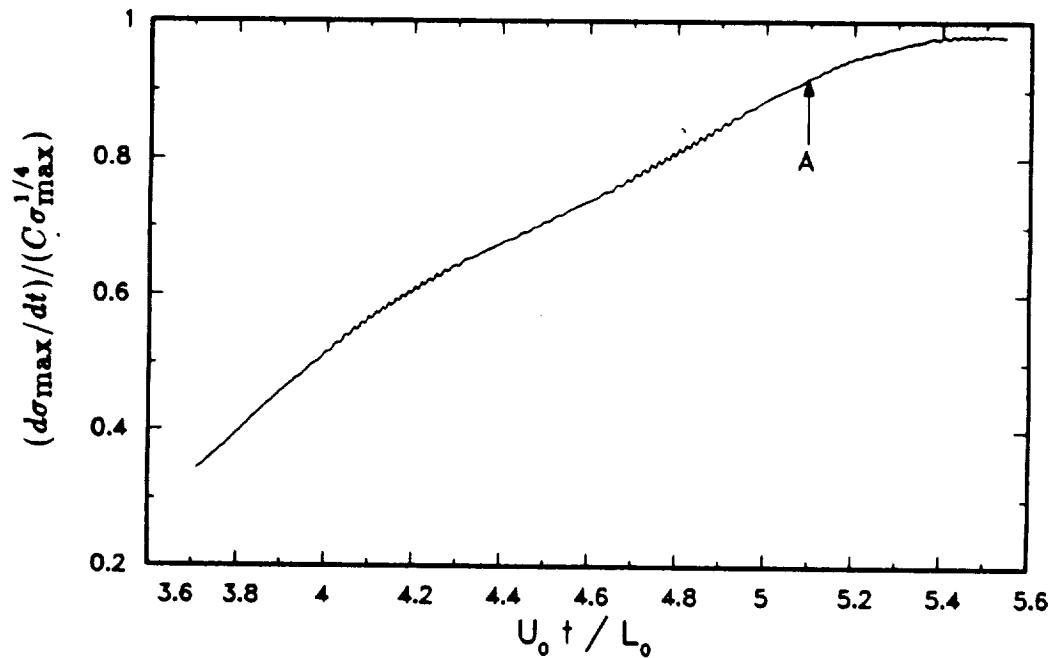


FIGURE 5.43. Rate of stretching of the head for the collision of $\alpha = 0.5$ as determined by the node point with maximum radius. Unity corresponds to the estimate (5.3.19). The point 'A' marks the inception of tail formation as determined by the appearance of a change of sign in curvature along the contour. The oscillations are due to different node points being at the maximum radius.

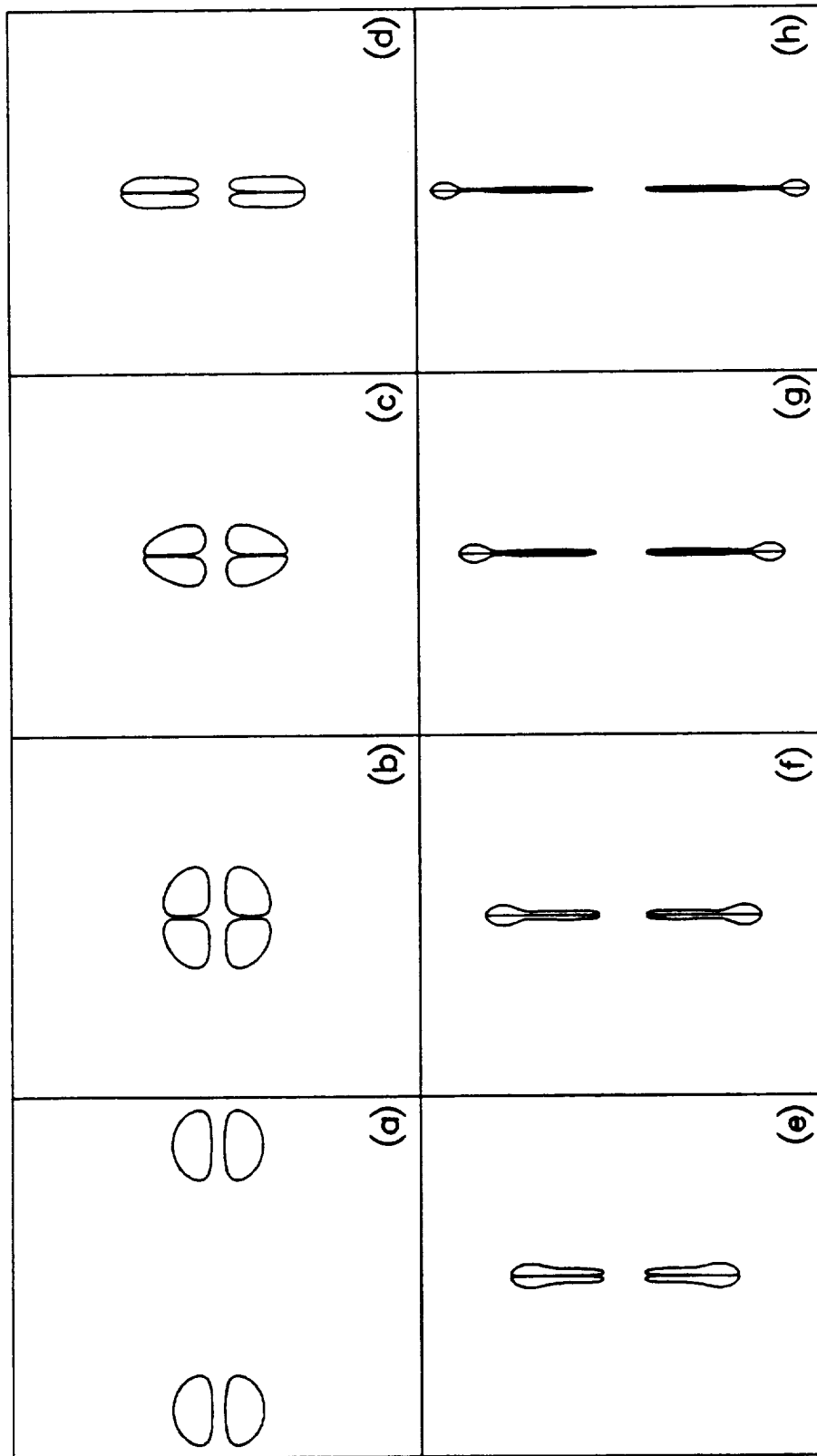


FIGURE 5.44. Core shapes for the collision of $\alpha = 1.0$, $\hat{d} = 10$. +, vorticity centroids. $U_0 t / L_0$: (a) 0; (b) 4.44; (c) 5.18; (d) 5.92; (e) 5.67; (f) 7.41; (g) 8.15; (h) 8.89.

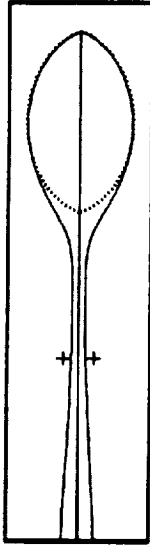


FIGURE 5.45. Magnified portion of the shape at $U_0 t/L_0 = 8.89$ from the previous figure. —, computed shape; ·····, 2-D limiting translating pair; +, vorticity centroid.

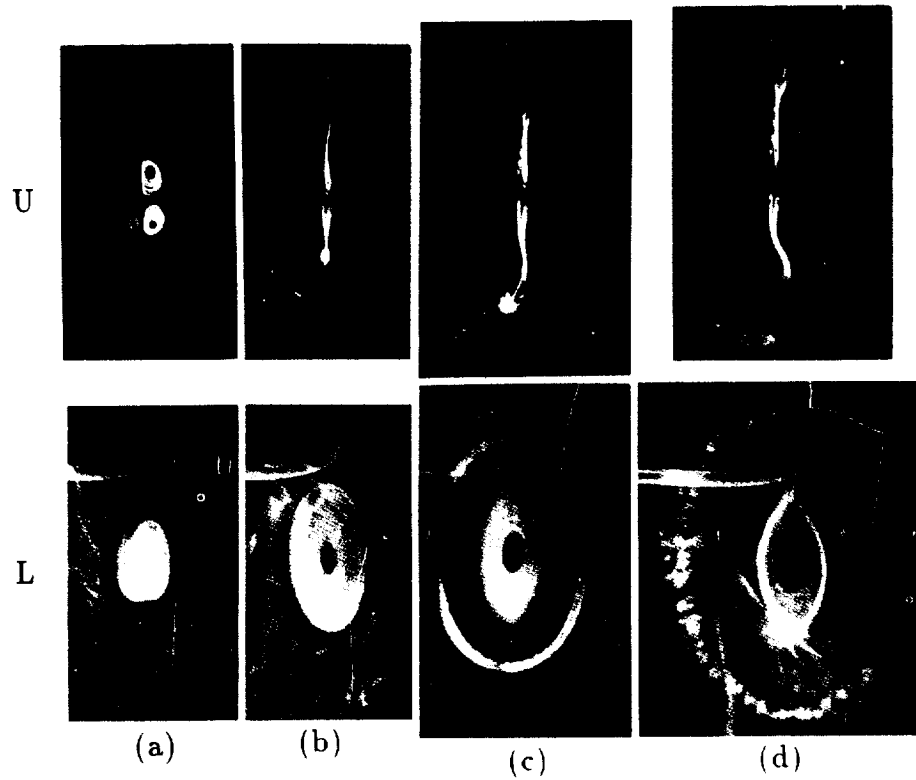


FIGURE 5.46. Smoke visualization of the collision of two vortex rings by Oshima (1978a). U, upper series which show a meridional plane illuminated by a sheet of light; L, lower series which is an oblique view at 30° from plane of collision. *Reproduced with permission.*

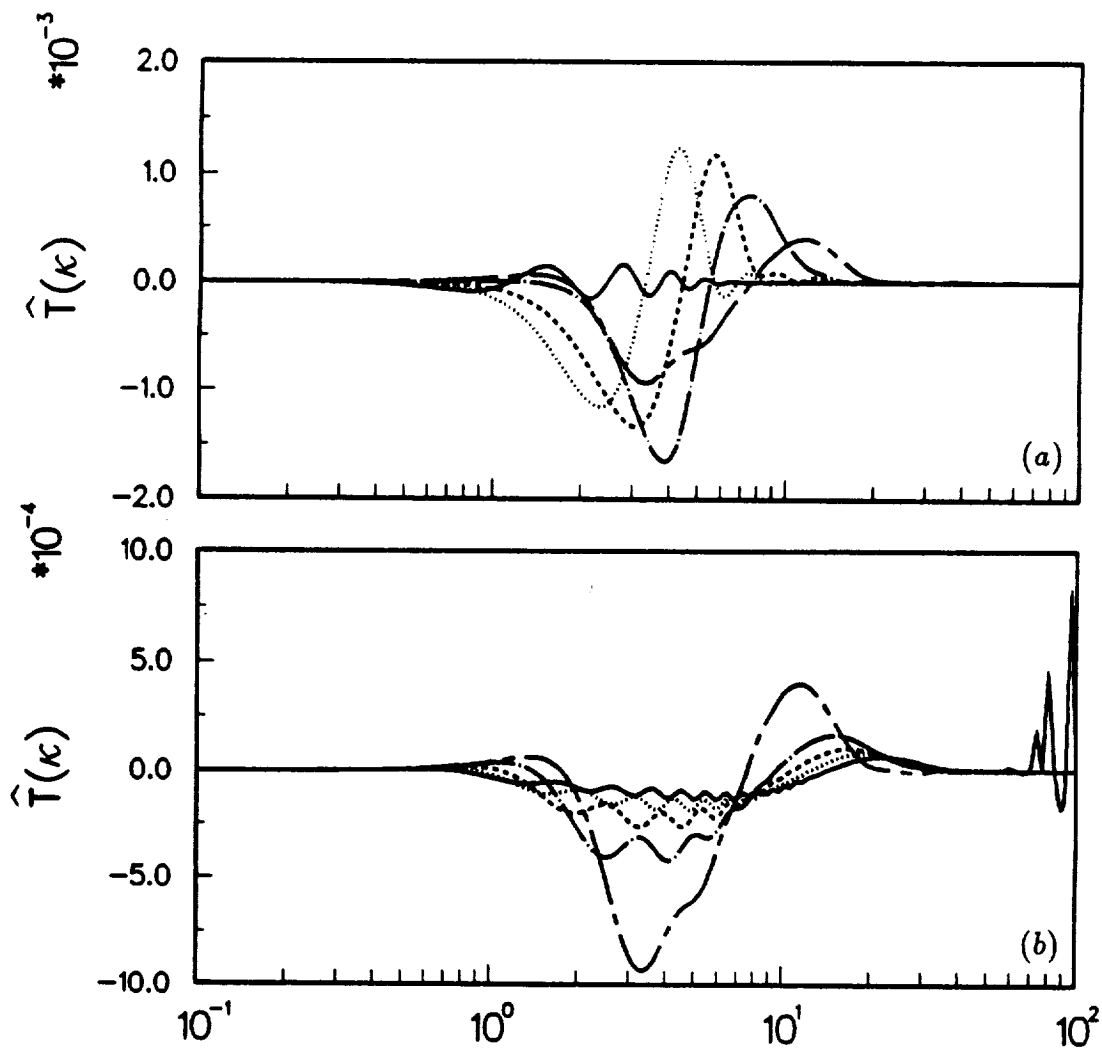


FIGURE 5.47. Transfer spectra for $\alpha = 1.0$ collision. $U_0 t / L_0$ or letters corresponding to Figure 5.44 are: (a): —, (a); ·····, 3.70; - - - - , (b); — · — ·, (c); — — — —, (d); (b): — — — —, (d); — · — ·, (e); - - - - , (f); ·····, (g); —, (h). Note that the ordinate values are multiplied 10^{-3} and 10^{-4} not the axis title.

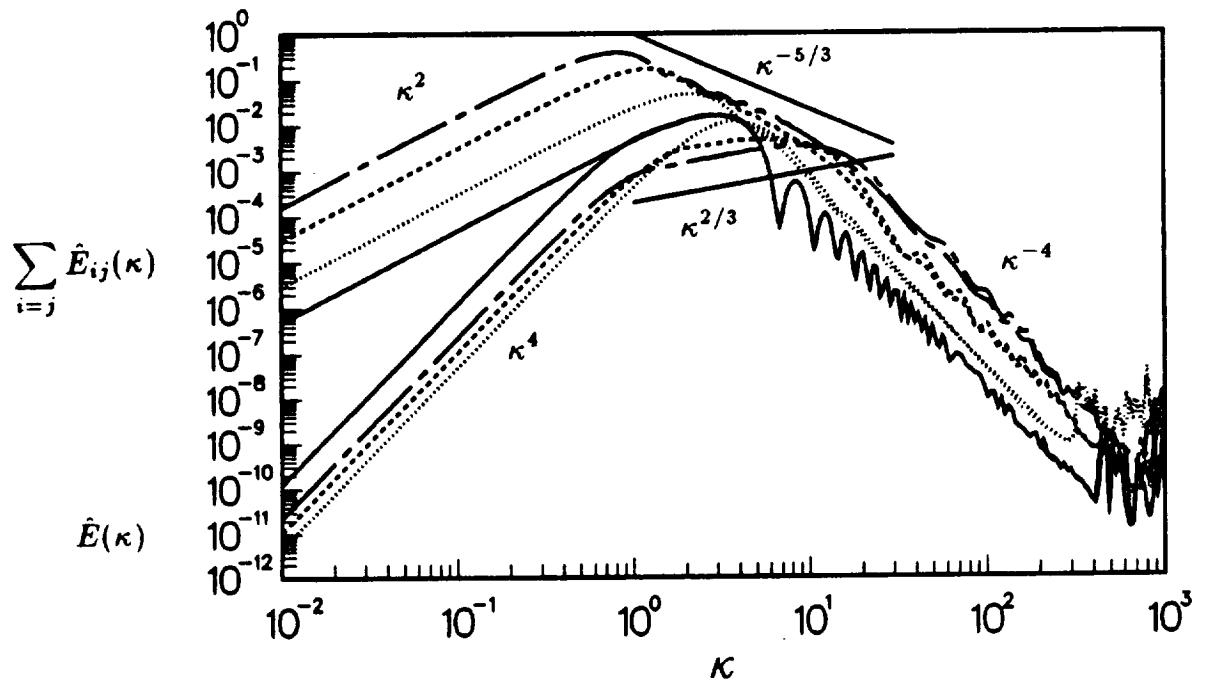


FIGURE 5.48. Spectra of the total energy and sum of self-energies for selected frames in Figure 5.44: —, (a); ·····, (c); - - -, (e); — — —, (g).

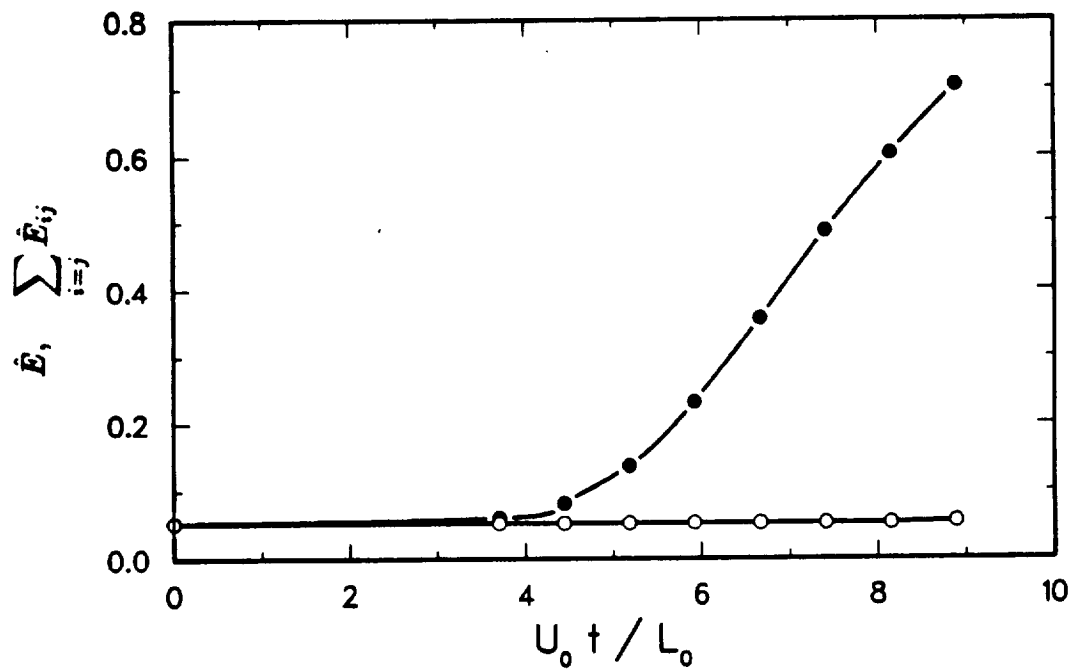


FIGURE 5.49. Energy for $\alpha = 1.0$ collision. O, total; ●, sum of self-energies.

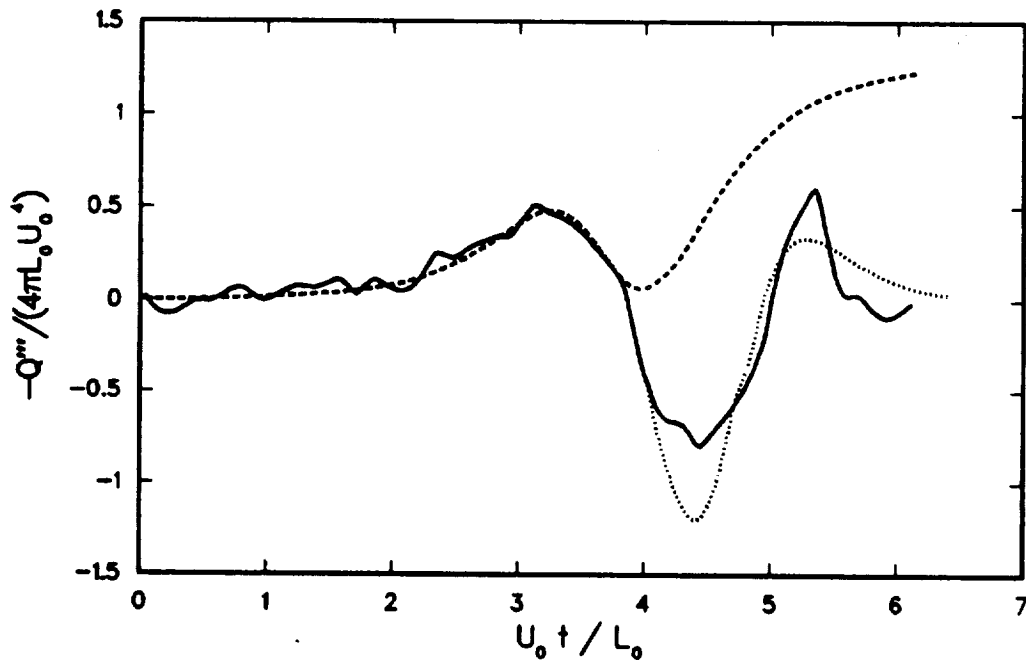


FIGURE 5.50. Normalized version of Figure 17a in Kambe and Minota (1983). —, experiment; ----, Dyson's model with $\delta_o/L_o = 0.3$; ·····, viscous model.

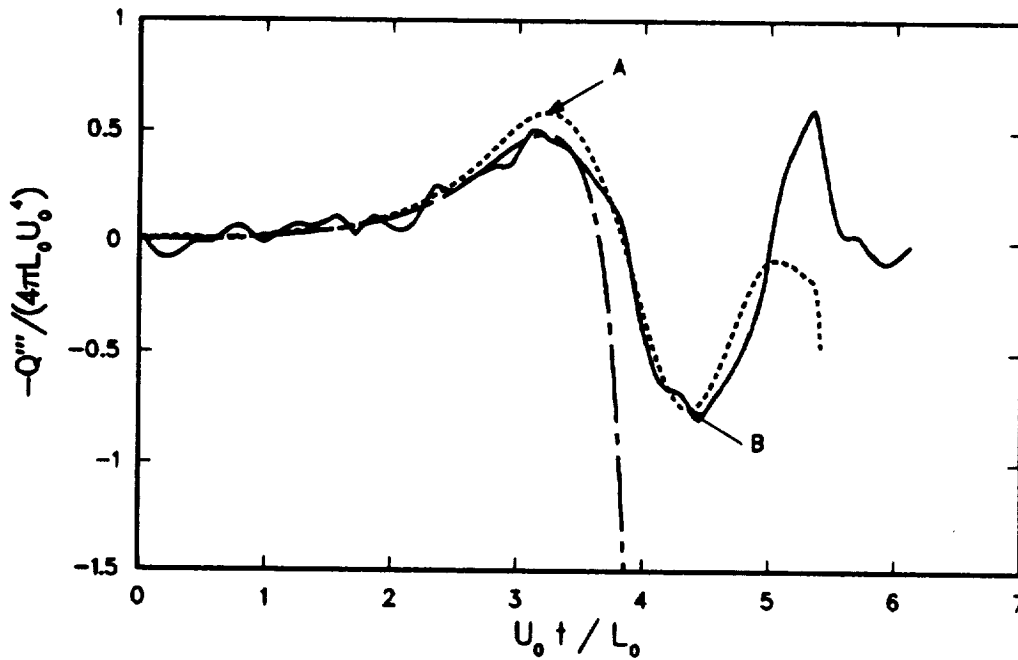


FIGURE 5.51. Acoustic signal for the collision of $\alpha = 0.5$, $\hat{d} = 8$. —, experiment of Kambe and Minota (1983) from the previous figure; ----, contour dynamics; —·—·, elliptic model. The letters A and B refer to the correspondingly labeled points in Figure 5.40.

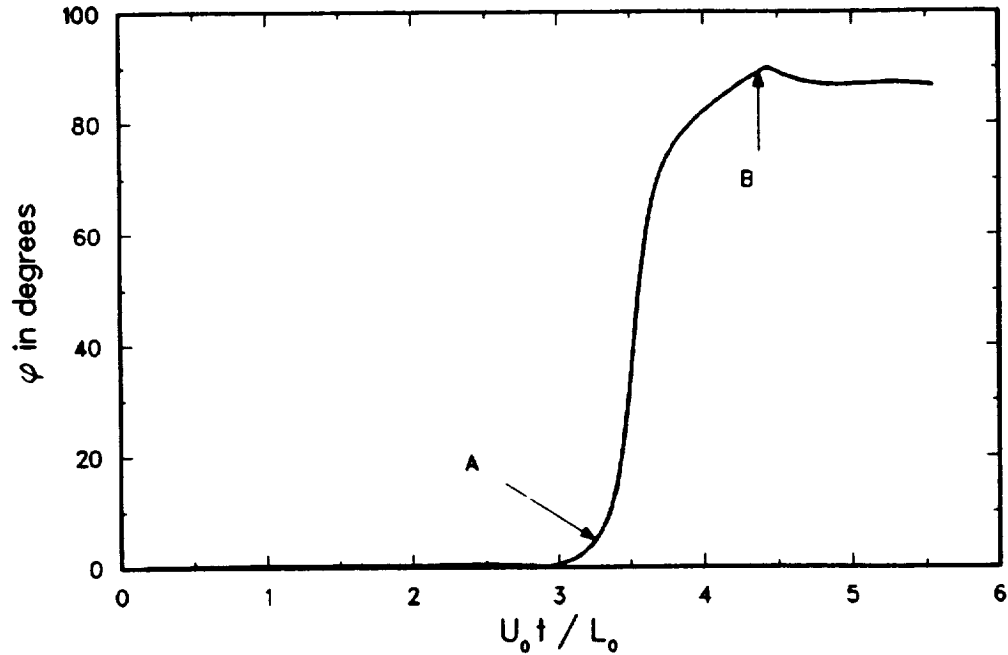


FIGURE 5.52. Orientation angle of the ellipse fitted to the moments of the core shape for the collision of $\alpha = 0.5, \hat{d} = 8$. The instants labeled A and B correspond to those in Figures 5.40 and 5.51.

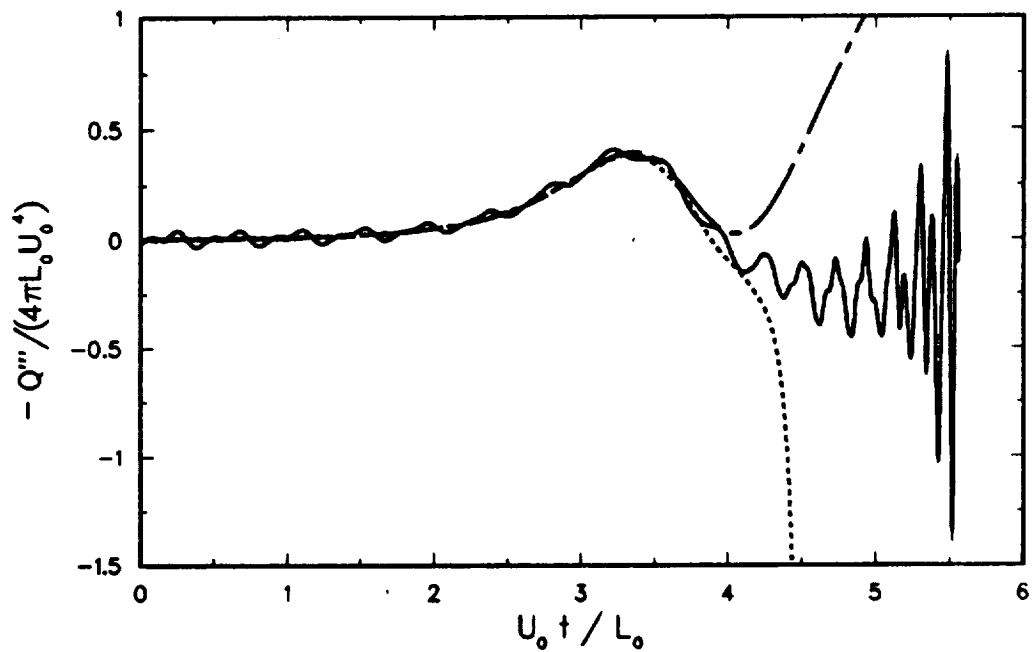


FIGURE 5.53. Acoustic signal for the collision of $\alpha = 0.2, \hat{d} = 8$. —, contour dynamics; ----, elliptic model; - · - ·, Dyson's model.

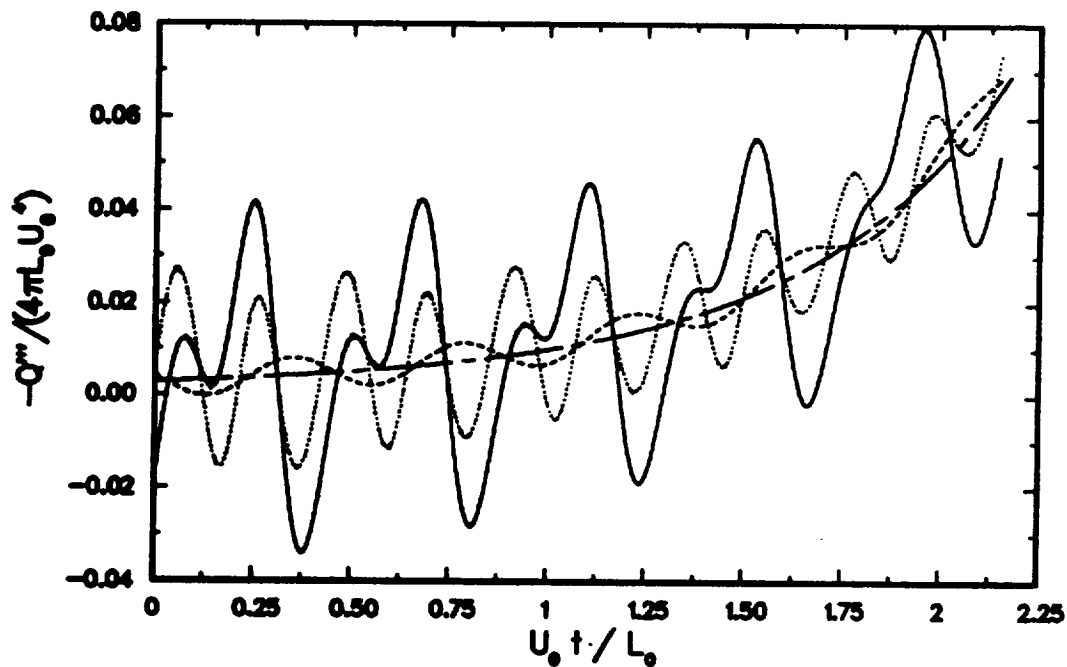


FIGURE 5.54. Acoustic signal at early times for the collision of $\alpha = 0.2$, $\hat{d} = 8$. —, using Norbury's (1973) computed shape as the initial condition; ----, elliptic model with initially circular cores; -·-·, Dyson's model; ·····, using the asymptotic solution of Fraenkel (1972) to obtain the initial shape.

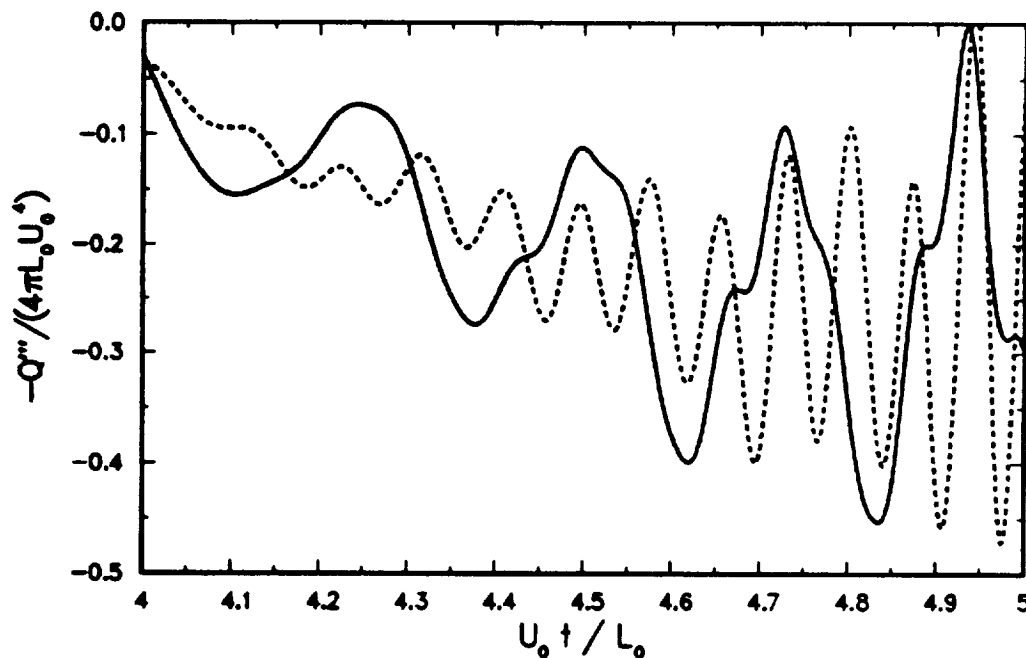


FIGURE 5.55. Acoustic signal in a later time interval for the collision of $\alpha = 0.2$, $\hat{d} = 8$. —, using Norbury's (1973) computed shape as the initial condition; ·····, using the asymptotic solution of Fraenkel (1972) for the initial shape.

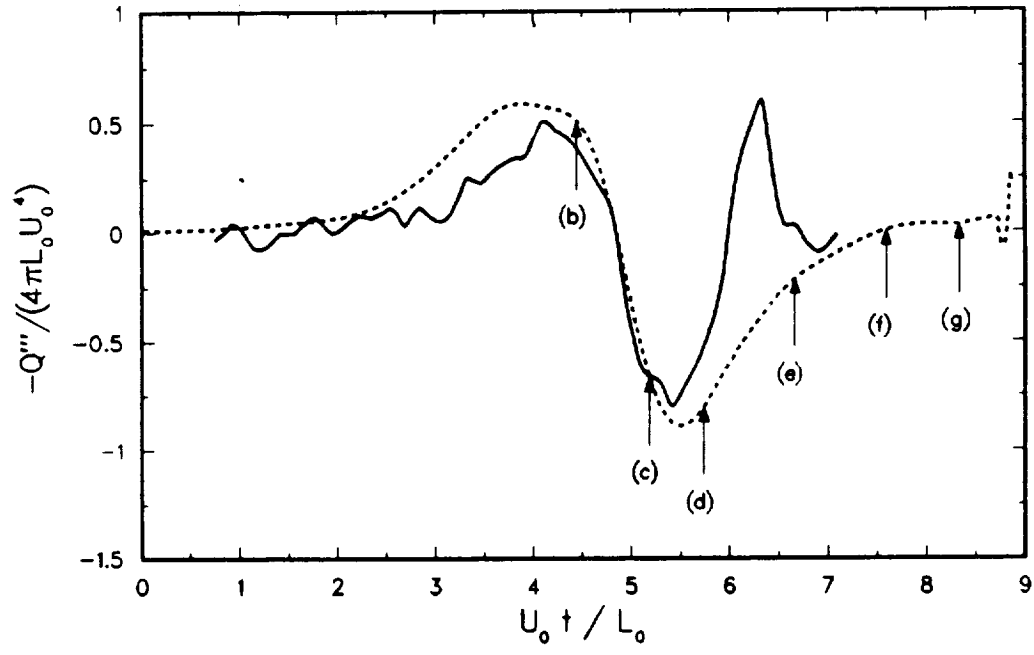


FIGURE 5.56. Acoustic signal for the collision of $\alpha = 1.0, \hat{d} = 10$. ----, contour dynamics; —, experiment of Kambe and Minota (1983) for reference. Letters indicate frames in Figure 5.44.

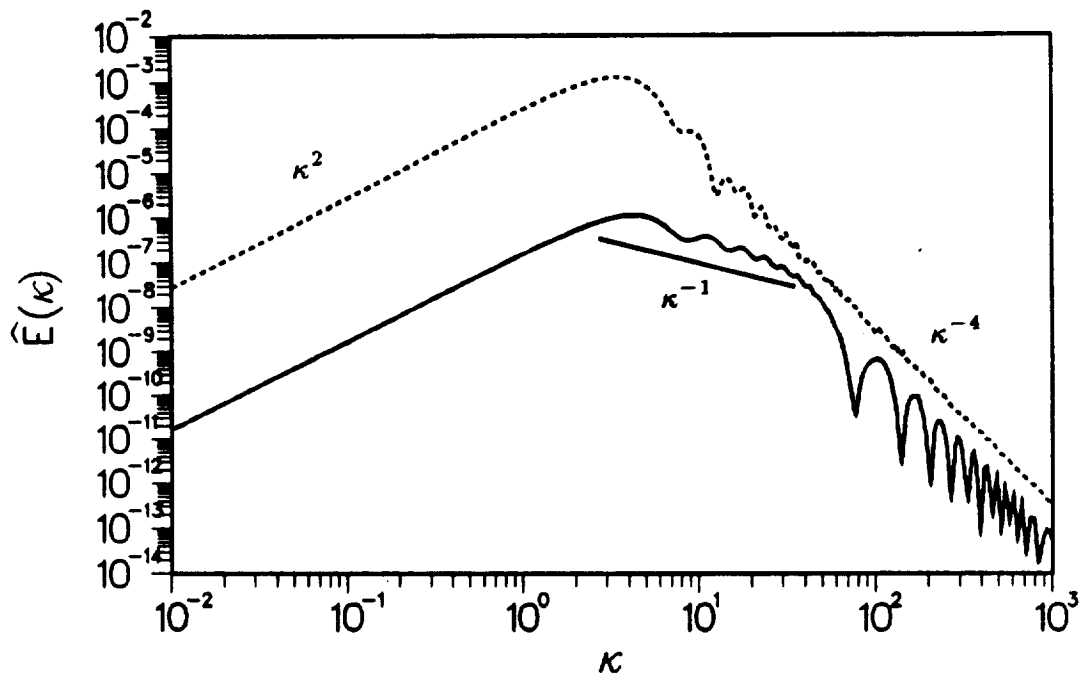


FIGURE 5.57. Energy spectra for two members of the Norbury-Fraenkel family. —, $\alpha = 0.1$; ----, $\alpha = 0.6$.

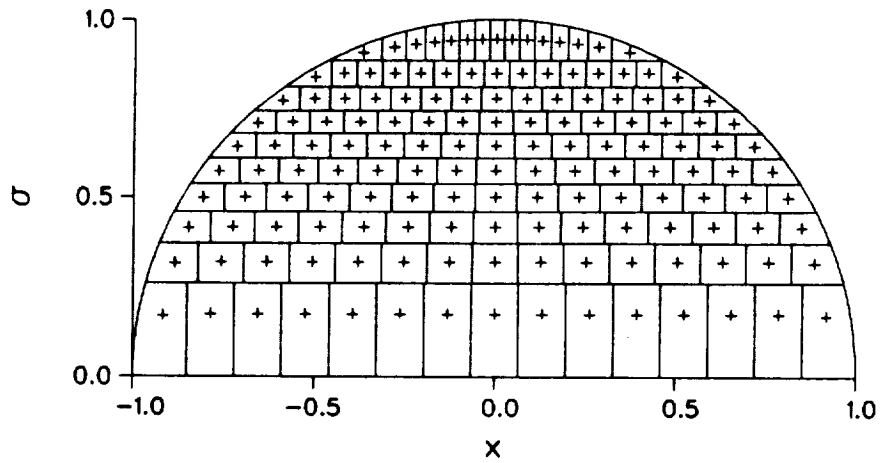


FIGURE 5.58. Cell discretization of Hill's spherical vortex.

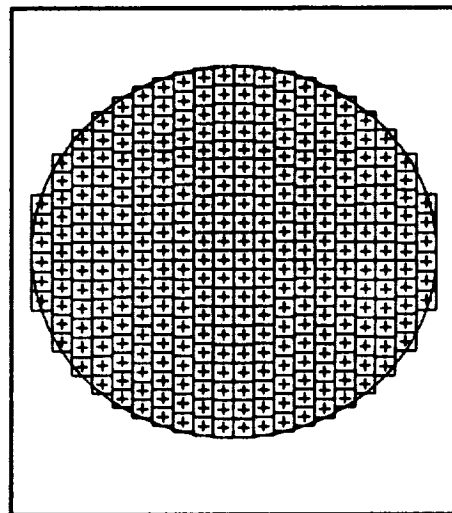


FIGURE 5.59. Cell discretization for the $\alpha = 0.2$ Norbury-Fraenkel vortex used for the passage interaction of §5.1.2.

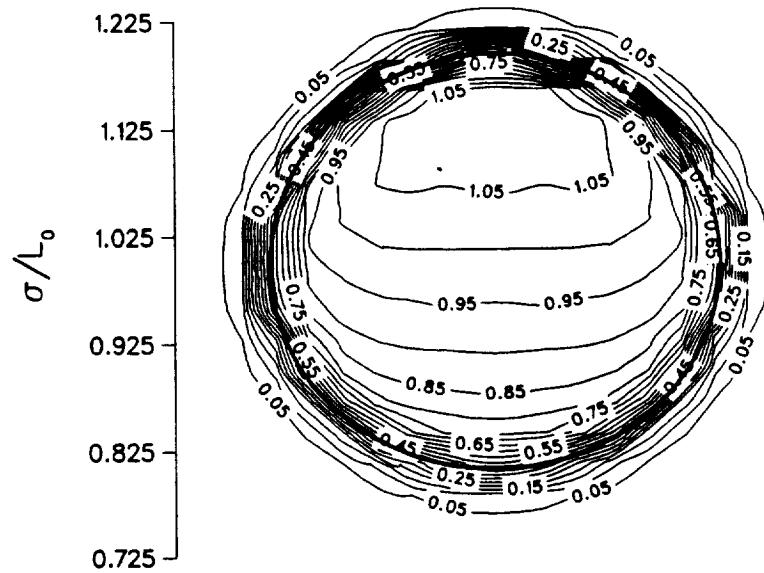


FIGURE 5.60. Contours of normalized vorticity ($\omega_\phi / (\mathcal{A}L_0)$) for the discretization of the previous figure and using a core overlap factor, $f_c = 3$. The thick solid line is the exact core boundary.

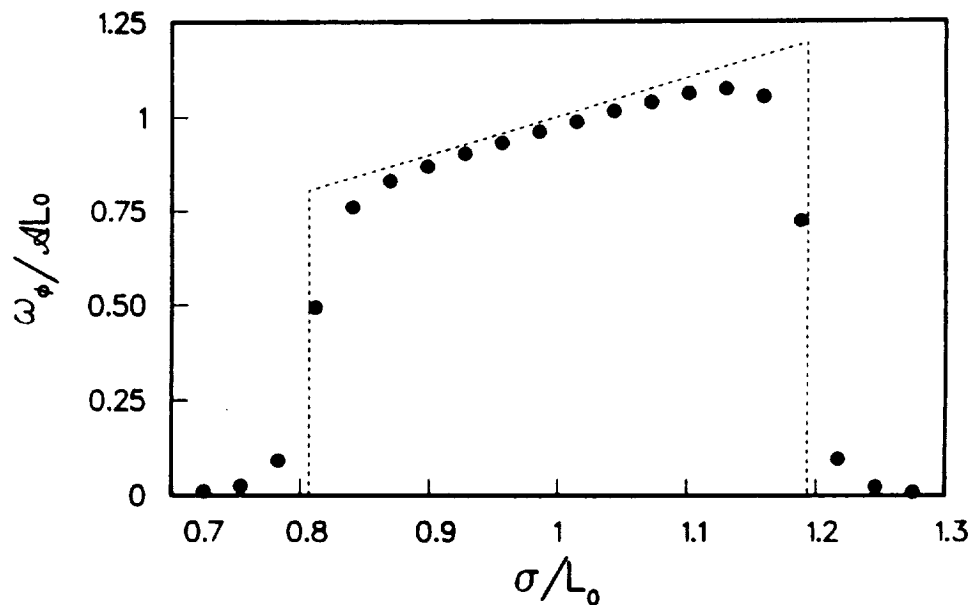


FIGURE 5.61. ●, vorticity distribution along the central radial slice for the previous figure; ----, desired distribution.

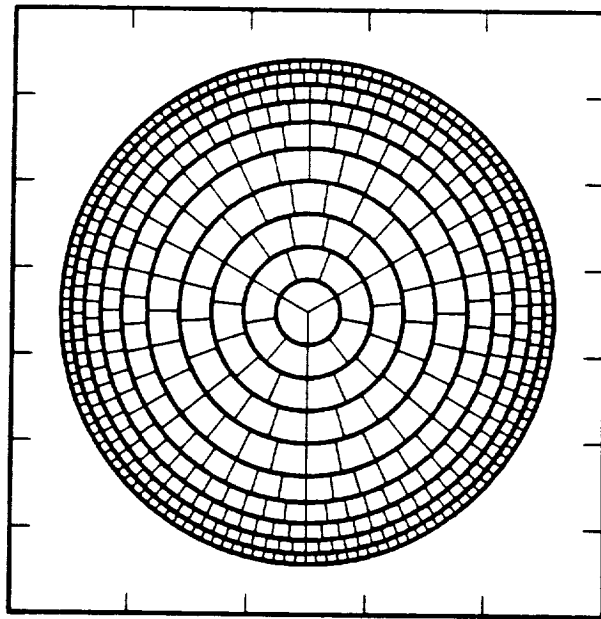


FIGURE 5.62. Cell discretization of the unit disk for Fraenkel's (1972) peaked vorticity solution ($\alpha = 0.2$).

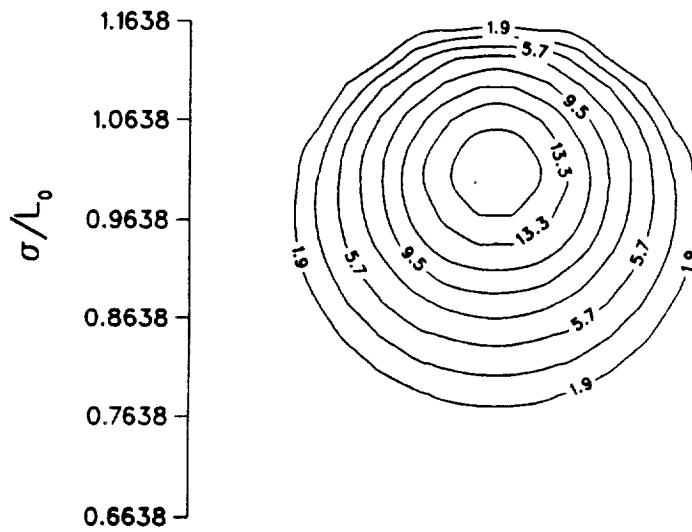


FIGURE 5.63. Contours of $\omega_\phi L_0^2/\Gamma$ corresponding to the discretization of the previous figure and using a core overlap factor of $f_c = 3$.

PARTICLE MOTIONS DUE TO UNSTEADY VORTEX RINGS

6.1. Introduction

Applying some notions from dynamical systems theory, this chapter considers the motion of particles in the irrotational portions of unsteady time periodic vortex ring flows.

The aim is to understand the features observed when tracer is experimentally used to visualize such flows. The study focuses on two situations. The first is that of the "turbulent vortex ring", a term sometimes used only as a label when the motion of a tracer appears chaotic. It will be shown that some of the features observed experimentally may be produced by simple inviscid, periodic unsteadiness of the vortex core. These include puffiness and striations in the tracer, a trailing wake, and the entrainment of fluid from a patch of dye placed in the path of an initially unmarked vortex ring. Axisymmetric unsteadiness in which the cross-section of the core of the ring is elliptical and rotates at constant angular velocity is considered. Qualitative agreement with experiment does not necessarily mean that a sufficient explanation has been offered. The boundary of the core may have an arbitrary number of waves or there may be azimuthal waves of the type reviewed in §2.10. Sallet & Widmayer (1974) have indeed measured irregular hot-wire signals for turbulent rings. We only wish to suggest that relatively simple unsteady models may be fruitful in elucidating large scale aspects of the mixing.

The second situation is that of two leapfrogging rings. In Chapter 5 contour dynamics results corresponded well with flow visualization experiments. In those experiments, a tracer is injected into the shear layer at the lip so that aside from Schmidt number effects there is little ambiguity between vorticity and tracer. But, what happens if tracer is injected not only into the shear layer emitted from the orifice but also into the non-vortical fluid outside the cores? The vorticity may induce tracer particle motions in the irrotational region which can be easily confused as being associated with the vorticity. We will provide an instance from the experimental literature concerning leapfrogging rings where this appears to be the case. It will be

suggested that the descriptions which have been applied to these photographs ought to be reconsidered.

In the next section the necessary background material from dynamical systems theory is canvassed. In §6.3 a survey is made of those papers employing tools from dynamical systems theory to understand particle motions and mixing. The results are contained in §6.4. Three cases of perfectly periodic vortex dynamics are dealt with. The first considers vortex rings with elliptical cross-section and is meant to address flow visualization observations of “turbulent vortex rings,” however, it may be useful in understanding aspects of fluid engulfment in the initial stages of pairing when two neighboring rings co-rotate and also after the merging when an elongated core is formed. The second set of cases was an outgrowth of the need to understand the presence of islands of non-chaotic particle motion embedded in a region of chaotic motion which were observed for the first case and the extent to which they persist under the presence of disturbances on the core. Because the flow in the vicinity of the core is locally two-dimensional we approach this question by considering Kirchhoff’s two-dimensional elliptic vortex and superimpose neutrally stable waves on the boundary of the core (Love 1893). The final case addresses leapfrogging rings. Dyson’s (1893) model is applied to study particle motions for a case from Chapter 5. The case chosen is one for which contour dynamics showed the core deformations to be weak and hence Dyson’s model to be a good approximation.

6.2. Terminology

The purpose of this section is to acquaint the reader with the terminology of this chapter. A more comprehensive treatment of dynamical systems theory can be found in a number of books on the subject. Below, some basic concepts are extracted from Guckenheimer & Holmes (1983). A good descriptive and less technical book is by Thompson & Stewart (1986).

Consider the equations governing the motion of particles in a three-dimensional unsteady flow:

$$\begin{aligned}\dot{x} &= u(x, y, z, t), \\ \dot{y} &= v(x, y, z, t), \\ \dot{z} &= w(x, y, z, t),\end{aligned}\tag{6.2.1a}$$

with

$$(x(0), y(0), z(0)) = (x_o, y_o, z_o). \quad (6.2.1b)$$

The solution may be thought of as a curve in (x, y, z) space (the phase space) parametrized by time. The curves for different (x_o, y_o, z_o) may intersect albeit only at different t . However, in the geometric approach one would like the solution curves to be such that we can talk about surfaces containing the solution curves. It is better to introduce time as an extra direction in the phase space. For this purpose (6.2.1) is written as an *autonomous* system (with right hand side not explicitly dependent on time) at the expense of increasing the dimension of the phase space by one:

$$\begin{aligned} \dot{x} &= u(x, y, z, \bar{\phi}), \\ \dot{y} &= v(x, y, z, \bar{\phi}), \\ \dot{z} &= w(x, y, z, \bar{\phi}), \\ \dot{\bar{\phi}} &= 1 \end{aligned} \quad (6.2.2)$$

The solution is represented by curves in $(x, y, z, \bar{\phi})$ space which do not intersect. Note that if the velocity field is time periodic with period 2π say, then it is sufficient to define $\bar{\phi}$ to be modulo 2π to guarantee that trajectories do not intersect. To see this, assume that two trajectories coincide at the point $x_1, y_1, z_1, (\bar{\phi} \bmod 2\pi)_1$ in the phase space. If the velocity field is time periodic then the trajectories must continue to coincide for both time running forward and backward.

To compress the notation, consider the general case of an n -degree of freedom autonomous system

$$\dot{x} = f(x), \quad x \in R^n. \quad (6.2.3)$$

To say that x belongs to cartesian space is general enough for our purposes. In some situations in fluid mechanics, we may want to consider particle motions on a curved streamsurface, for example a torus in an axisymmetric flow with swirl. However, points on the surface may be described by a transformation to cartesian coordinates.

Discrete maps are an important class of dynamical systems. They may be studied in their own right or they may arise from a continuous dynamical system. For example the cases to be presented have periodic unsteadiness and we shall be concerned with how particles are mapped in successive periods. Such a map is a special case of a

Poincaré map. Hence after integrating (6.2.3) from period i to $i+1$, either numerically or exactly we obtain

$$x^{i+1} = g(x^i), \quad x \in R^n. \quad (6.2.4)$$

A map produced from a continuous system in this way will have one less degree of freedom. Given initial conditions $x(0) = x_0$ for (6.2.3) and $x^0 = x_0$ for (6.2.4), the resulting solution curve for (6.2.3) and discrete set of points for (6.2.4) in the phase space is called an *orbit*. The *fixed points* or *equilibria* \bar{x} of (6.2.3) and (6.2.4) are defined respectively by

$$f(\bar{x}) = 0; \quad (6.2.5a)$$

$$g(\bar{x}) - \bar{x} = 0. \quad (6.2.5b)$$

The particle path equations (6.2.2) have no fixed points but, if the flow is time periodic, it may have periodic particle paths which are the fixed points of the Poincaré map. The systems linearized about the fixed points are

$$\dot{\xi} = A\xi; \quad (6.2.6a)$$

$$\xi^{i+1} = B\xi^i, \quad (6.2.6b)$$

where A and B are constant $n \times n$ matrices with elements

$$a_{jk} = \left. \frac{\partial f_j}{\partial x_k} \right|_{x=\bar{x}}, \quad (6.2.7)$$

$$b_{jk} = \left. \frac{\partial g_j}{\partial x_k} \right|_{x=\bar{x}}.$$

The linearized systems lead to the notion of *eigenspaces*. For the continuous system divide the generalized eigenvectors* of A into three groups, having eigenvalues with real parts positive, negative and zero, respectively. Each group spans a subset of R^n , referred to as the stable, unstable and center eigenspaces, denoted as E^s , E^u and E^c , respectively. For maps, these eigenspaces are constructed from the generalized eigenvectors of B associated with eigenvalues having modulus > 1 , < 1 and $= 1$, respectively. A fixed point having no eigenvalue with zero real part in the case of a continuous system or having no eigenvalue with unit modulus in the case of a map is called *hyperbolic*.

* The qualifier 'generalized' is needed when A does not possess a linearly independent set of eigenvectors. For further discussion consult, for example, the textbook by Franklin (1968) under the index entry of 'principal vector.'

The Hartman-Grobman theorem (Guckenheimer & Holmes, p. 13) says that near a *hyperbolic* fixed point the orbits of the linearized and full system are qualitatively similar. In particular they can be deformed to each other in a continuous, invertible and one-to-one fashion. As an illustration consider two-dimensional separated flow above a no-slip wall as shown in Figure 6.1. The entire wall consists of fixed points. The only non-zero element of the Jacobian matrix at the wall is $\partial u/\partial y$ which itself vanishes at the separation point S . The Jacobian matrix is already in Jordan form, has two zero eigenvalues and the eigenvectors span the center eigenspace which consists of the entire half plane. Because no fixed point is hyperbolic it is understandable from the Hartman-Grobman theorem that near the separation point, streamlines for a linear shear cannot be deformed to the actual streamlines.

An important property of the eigenspaces is that each is an *invariant subspace* for the linearized system; that is to say an orbit on each set remains there always for $-\infty < t < \infty$ for (6.2.6a) and $-\infty < i < \infty$ for (6.2.6b). This is so because the general solution of (6.2.6a) is

$$\xi(t) = \sum_{j=1}^n c_j P_j(t) V_j, \quad (6.2.8)$$

where $P_j(t)$ are polynomials with unit coefficients such that $P_j(0) = 1$ and V_j are the generalized eigenvectors. One sees that if at the initial instant ξ lies on a space spanned by a subset of the V_j , then it does so always.

For hyperbolic fixed points the stable and unstable manifolds of \bar{x} denoted as $W^s(\bar{x})$ and $W^u(\bar{x})$, respectively, are non-linear extensions of the eigenspaces. The manifolds contain information about fluid transport and the results to be presented suggest that certain blobs of fluid near the unstable manifold are drawn out along it and acquire its structure implying that it may be useful for numerical flow visualization. The conventional approach to numerical flow visualization is to follow the trajectories of arbitrary clusters of particles. This has the disadvantage that it is expensive to place particles with sufficient resolution wherever dye is located initially. One usually starts with a judiciously selected blob but this does not yield a global picture.

One begins by defining the manifolds locally in some region \mathcal{U} (not necessarily small) containing \bar{x} . $W_{loc}^s(\bar{x})$ is the set of all orbits in \mathcal{U} which tend to \bar{x} as $t \rightarrow \infty$ and never leave \mathcal{U} for $t \geq 0$. Similarly $W_{loc}^u(\bar{x})$ is the set of all orbits in \mathcal{U} which tend to \bar{x}

as $t \rightarrow -\infty$ and never leave \mathcal{U} for $t \leq 0$. This definition is general and does not refer to the eigenspaces but the stable manifold theorem for continuous systems as well as maps asserts that for a hyperbolic fixed point $W_{loc}^s(\bar{x})$ and $W_{loc}^u(\bar{x})$ exist, are tangent to $E^s(\bar{x})$ and $E^u(\bar{x})$ at \bar{x} and have the same dimensions n_s and n_u . In either case, the global $W^u(\bar{x})$ is then defined constructively by letting the local unstable manifold flow forward under the dynamical system. Similarly, the global stable manifold is constructed by letting the corresponding local manifold flow backward in time. By construction, the manifolds are invariant subspaces; they always contain the same fluid particles.

To illustrate these definitions consider first the separated flow example of Figure 6.1. The only fixed point having an unstable manifold is S and the manifold is the streamline emanating from it. Because S is not hyperbolic the unstable manifold bears no connection to the eigenspaces.

Next consider a vortex ring in a reference frame traveling with the ring. For a sufficiently thin core the streamlines in a meridional plane look like those in Figure 6.2a. There is a hyperbolic fixed point \bar{x} , a saddle. The stable and unstable manifolds of \bar{x} coincide in the loop connecting the saddle to itself. Such a loop is called a *homoclinic orbit* and \bar{x} is called a homoclinic point. As the core size increases to some value, there occurs a change in the topology of the flow. Then there exist two saddles on the symmetry axis as sketched in Figure 6.2b (Batchelor 1967, p. 525).

The dividing streamline is both the unstable manifold of F (excluding the point R) and the stable manifold of R (excluding the point F). Connections such \overline{RF} and the dividing streamline which join two saddles are called *heteroclinic orbits* and together they form a heteroclinic cycle. In the present case the unstable and stable manifolds of the forward and rear stagnation points coincide. This situation is highly exceptional; if the ring were slightly disturbed, the body of fluid carried with it would leak. This will manifest itself as a splitting of the manifolds. In the early seventies several papers motivated their study of vortex rings by suggesting that vortex rings could be used to transport chimney wastes to high altitudes. We should be thankful that the scheme was never implemented.

The final concept which is needed is that of the “*horseshoe*” map introduced by Smale (see Guckenheimer & Holmes, pp. 230–235). It essentially defines chaos. From the structure of the stable and unstable manifolds to be presented in §6.4, it will be observed that certain fluid blobs undergo repeated stretching and folding. The

horseshoe map is an idealized representation of this process. The Smale-Birkhoff test for chaos establishes an equivalence between the behavior of the idealized map and what happens in more complicated dynamical systems. It asserts that the behavior of the horseshoe occurs if the stable and unstable manifolds of a hyperbolic fixed point intersect transversely at a point other than the fixed point. A *transversal* intersection requires that together the tangent spaces of the manifolds at the point of intersection have the same dimension as the phase space. Thus two space curves cannot intersect transversely because their tangents at the point of intersection can at most span a plane. The Smale-Birkhoff test implies that two-dimensional steady flow cannot be chaotic because the manifolds also being trajectories of individual particles cannot intersect transversely. The horseshoe map serves to provide an intuitive appreciation for how continual stretching and folding of fluid blobs results in Lagrangian chaos.

The horseshoe map takes a unit square, stretches it vertically by a factor μ and compresses it horizontally by a factor λ . The resulting rectangle is folded (it then looks like a horseshoe from where its name derives) and placed over the original square so that the folded region lies outside the square (see Figure 6.3).

The map models a fluid blob that after having undergone stretching and folding intersects its shape at an earlier instant. We are interested in those particles, call them Λ , which remain in the square for all iterations i , $-\infty \leq i \leq \infty$. How these particles behave under repeated applications of the map will give us a feel for one notion of chaos. To obtain Λ perform k iterations of the map on the square and ask: what points have remained in the square for the previous k iterations and will continue to remain in the square for the next k iterations. Then take the limit as $k \rightarrow \infty$.

Suppose that the map is applied once. The intersection of the \cap shaped image with the square forms two vertical strips of length λ ($< 1/2$) and height unity. If we undo the folding and stretching we see that the vertical strips come from two horizontal strips of length unity and height μ^{-1} ($< 1/2$). Thus, after one iteration, all points of the original square except those lying in the horizontal strips fall out of the square. Next, consider applying the map again, this time to the two vertical strips. The only points in the strips that will survive in the square will be their intersection with the two horizontal strips. This forms four rectangles of length λ and height μ^{-1} . The result of actually applying the map is four vertical strips of length λ^2 and height unity. Undoing the folding and stretching twice, one sees that these came

from four horizontal strips of length unity and height μ^{-2} . Thus, after two iterations, only those points lying in these strips survive in the square. So if we now consider applying the map twice again to the four vertical strips the surviving points will be intersection of the four horizontal and vertical strips. Carrying out the argument inductively, we see that after k iterations the part of the original square remaining in the square consists of 2^k horizontal strips of length unity and height μ^{-k} and its image will be 2^k vertical strips of length λ^k and height unity. The points which will survive the next k iterations will be their intersection which is 4^k rectangles with dimensions λ^k and μ^{-k} . As $k \rightarrow \infty$, this set has an infinite number of points with total area

$$S_\Lambda = \lim_{k \rightarrow \infty} \left(\frac{4\lambda}{\mu} \right)^k = 0. \quad (6.2.9)$$

Even though Λ is a set of points with zero area, the dynamics of a point x in Λ influences a point y in its vicinity until y falls out of the unit square. The closer y is to x , the longer will y participate in the dynamics of x . For more complicated systems one thinks of several rectangles undergoing the horseshoe map. After a particle falls out of one rectangle it may enter another. These rectangles are said to form a *Markov partition*.

There are three types of dynamics that points on Λ undergo. First, there are a countably infinite number of periodic orbits. Second, Λ has an (uncountably) infinite number of aperiodic orbits. These orbits are such that if one kept track of whether the successive iterates of a point x in Λ ended up on the top half of the square or the bottom using the symbols 1 and 0, the symbol sequence would be random, akin to a coin toss. Finally, there is at least one orbit whose history of being in the top or bottom half of the square will be identical to the history of every other orbit in Λ for an arbitrarily long number of iterations. If a map possesses the last property it is said to be *mixing* a concept which differs from the fluid mechanical connotations of the term. If one defines a distance between points on Λ in terms of how closely their 1 and 0 sequences match (i.e. thinking of the sequence as a binary number) then we would say that there is at least one orbit which comes arbitrarily close to every point in Λ . Such an orbit is called *dense* on Λ .

6.3. Literature Survey

Even though dynamical systems theory has been in existence since the 1890s beginning with Poincaré, its application to the study of particle motions in fluid mechanics has come very recently undoubtedly because of the computer. Whereas our principal motivation is to interpret flow visualization experiments, there are a number of secondary reasons for undertaking this line of inquiry. Dye concentration is only one example of a scalar variable that satisfies a convection-diffusion equation without entering into the momentum equation. For example vortical motions having time scales long compared to the time scale of an external strain imposed by the geometry or by stronger vortices are approximately passive. This approximation is made in rapid distortion theory. It is conceivable that techniques from dynamical systems theory combined with rapid distortion theory might be useful in understanding the behavior of weak vorticity in general fluctuating velocity fields. Other examples of passive scalars include temperature (with small differences) and functions $f(\mathbf{x}, t)$ such that $f = 0$ defines an evolving material surface. Knowledge of the motion of a material surface is required to predict a diffusion controlled reaction at an interface separating two species. Leonard, Rom-Kedar & Wiggins (1987) show that the rate of reaction product formed at a point on the interface is completely determined by the history of the local stretching up until reacted layers overlap.

The flows which have been studied to date have been either three-dimensional steady flows periodic in three directions or two-dimensional flows with periodic unsteadiness. The periodicity makes these problems amenable to study through the use of Poincaré maps.

In the first category is the work of Dombre *et al.* (1986) and the references cited therein. They studied an exact solution of the steady three-dimensional Euler equations

$$\mathbf{u} \times \boldsymbol{\omega} = \nabla \widetilde{H}, \quad (6.3.1)$$

where $\widetilde{H} = p/\rho + \frac{1}{2}\mathbf{u}^2$, is the Bernoulli function. Where \widetilde{H} is not constant, the streamlines lie on the level surfaces of \widetilde{H} . Hence, the complexity of particle trajectories is limited by the complexity of \widetilde{H} . On the other hand trajectories are not constrained if \widetilde{H} is a constant in some region of R^3 . One class of flows satisfying this condition are the so-called ABC flows in which

$$\boldsymbol{\omega} = \lambda \mathbf{u}, \quad (6.3.2)$$

with $\lambda = \text{constant}$ everywhere and the flow periodic in three directions.

For two-dimensional time periodic flows, the investigations fall into three categories: (i) kinematic models, (ii) forced Stokes flow, (iii) point vortices forced by an unsteady potential flow.

(i) *Kinematic models.* Aref (1984) produced a model of stirring in a cylindrical enclosure which utilized two "blinking" point vortices together with their images. They are placed at fixed locations and each is turned on for half a period. The particle path equations are integrated analytically over one period. The resulting discrete map can be iterated forward thousands of iterations with small numerical error. Khakhar, Rising & Ottino (1986) performed additional analysis and computations for the blinking vortex model. They computed the Lyapunov exponent which is a long-time average of local stretching of material lines. They also introduced another model system in which a uniform strain followed by a rotation dependent on distance from the origin is applied during one period.

(ii) *Forced Stokes flow.* The studies in this category underscore the purely kinematic nature of chaotic particle paths and the fact that mixing is possible even in creeping flows (as is well known to anyone who has mixed paints). Chien, Rising & Ottino (1986) experimentally studied Stokes flow in a cavity driven by moving belts located at the top and bottom boundaries. They found efficient mixing for the case in which the belts are driven one at a time in opposite directions. The rate of mixing was optimum at a particular ratio of forcing period to the recirculation time of the eddy. They experimentally verified the presence of the horseshoe map. Aref & Balachandar (1986) and independently Chaiken *et al.* (1987) investigated Stokes flow between two eccentric cylinders which are alternately rotated. An analytical solution is available for the velocity field. In the former paper, several programs for the forcing are treated. In the latter paper, each cylinder rotates with constant angular velocity during its motion; both co-rotating and counter-rotating cases were considered. The essential features were captured by a simple kinematic model employing a combination of "twist" maps. The map has been extensively studied in the dynamical systems literature. The twist map applies a radially symmetric angular displacement to each point by an amount that is a non-linear function of the distance from the origin. The action of each cylinder is modelled by a twist map about the center of each cylinder. In Chaiken *et al.* (1986) striking comparisons of computations with dye visualization experiments are presented.

(iii) *Point vortices with forcing by an unsteady potential flow.* In an effort to study a solution to the Euler equations, Rom-Kedar, Leonard & Wiggins (1988, hereafter RLW) studied particle motions generated by a pair of translating point vortices subjected to a time-periodic straining flow about their common center. This type of perturbation approximates the effect of a channel with wavy walls through which the vortex pair propagates. In the absence of the perturbation the pair is enclosed by an elliptical dividing streamline which separates fluid trapped around the vortices from that flowing past them. When the perturbation is applied fluid is exchanged between the two regions. The Melnikov theory (see Guckenheimer & Holmes) which is valid for small perturbations was used to calculate such quantities as the width of the mixing zone, a band about the unperturbed dividing streamline in which the exchange occurs, and the area of fluid entrained and detrained during each period. The theory predicted that these quantities are optimized at a particular value of the ratio of forcing period to the time it takes for the pair to translate an amount equal to their separation length. Surprisingly, the theory predicted that, to linear order in the forcing amplitude, mixing would disappear altogether at a finite value of this parameter. The predictions of the theory were confirmed numerically by computing the manifolds of the fixed points using the full equations. They studied the question of how rapidly particle density decreases from some initial value in an oval region surrounding the pair. Such questions are important in practice. For example, Winterfeld (1965) measured the decrease in concentration in the wake of a blunt based cone initially seeded with smoke. Such devices are used to stabilize flames in jet combustion chambers and afterburners. The turbulent recirculation zone serves as a heat source to the main flame.

In any case, RLW symbolically analyze the intersection of the stable and unstable manifolds and reduce the problem to that of determining: given a large number of particles entrained at period zero, how many of these remain after n periods. The entrained fluid is a definite and relatively small region, hence, the computational task is much simpler.

Finally, to end the literature survey we would like to mention that flows evolving in a self-similar fashion in time, can be made steady by applying time dependent transformations. Cantwell (1986) has been pursuing this approach and has applied it, among other things, to a diffusing Stokes vortex ring and unsteady jets with point sources of momentum.

The present work differs from previous work in the following respects:

(i) We take up the suggestion of Khakhar, Rising & Ottino (1986) that "Future studies might focus on the dynamics of flows specified by an internal parameter, perhaps the Reynolds number, in which changes in the parameter result in changes in flow kinematics and thus the mixing." To this end we consider solutions of the Euler equations which are inherently unsteady; no external forcing is applied. The time scale of the unsteadiness relative to the time scale of the overall vortex motions which governs the strength of mixing are determined internally i.e. according to the Euler equations.

(ii) Vortex patches rather than point vortices are considered.

(iii) There are prices to be paid for these features. First, the solutions considered are valid only in some asymptotic limit. For each case, the restrictions will be specified later. Second, the expressions for the velocity field in two of the three cases are complex and expensive to compute; in one case numerical approximation is needed.

6.4. Results

The first example is that of a single unsteady vortex ring. We consider the solution due to Moore (1980) in which the core is an ellipse with semi-major and minor axes lengths a and b and mean toroidal radius L_o when the major axis is aligned with the symmetry axis. If a/L_o is small, the dynamics are locally two-dimensional and the core rotates at the constant angular velocity of Kirchhoff's elliptic vortex (Lamb 1932, §159). This core motion causes the translational velocity to oscillate once every half-rotation of the major axis. These oscillations occur about an average velocity given by Kelvin's formula (§2.7) with the core size replaced by the arithmetic average of a and b . The radial centroid oscillates similarly. The complete equations describing the motion of the core are (4.2.38)–(4.2.40). In §4.2.5 deviations from Moore's solution for thick cores were considered and it was shown that strain due to curvature caused the aspect ratio to pulsate as well as to decrease secularly. Thus, for fat cores the results of this chapter apply for only a few periods. The velocity field due to the elliptical core ring will approximate that due to two vortex rings in the process of merging.

In order to track particles, one needs the velocity field. However, in Moore's study it was necessary to know only the zeroth order streamfunction in the vicinity of the

core and the corresponding velocities have $\mathcal{O}(1)$ errors. In the present calculations we obtain the velocities everywhere numerically from the contour dynamics equations. Thus the core dynamics follows an asymptotic result whereas the velocity field is unapproximated.

The Poincaré map is defined using the period of the velocity field which is half the period of rotation of the major axis; phase zero is taken when the major axis is parallel to the symmetry axis. Each period consisted of 25 fourth-order Runge-Kutta steps. The unstable manifold is computed by first locating, using secant iterations, the forward hyperbolic fixed point F of the Poincaré map lying on the symmetry axis. See Figure 6.5. Next, the direction of the unstable eigenvector is estimated by forward mapping a particle near the fixed point. This defines two end-points of a segment. Many points are placed on the segment and iterated forward to build the manifold. The fact that the initial segment does not lie exactly on the manifold poses no practical problems. Since neighboring points converge to the manifold from both sides, initial errors are quickly diminished. This was checked by deliberately introducing large errors into the initial angle of the segment and comparing with the shape of the manifold without the errors. The stable manifold of the rear fixed point is obtained by symmetry. If time were reversed, the vortex would rotate in a clockwise direction and R would be the front hyperbolic point and a similar procedure would yield its unstable manifold symmetric to the first one. With time restored to its original course this becomes the stable manifold of R .

Figure 6.4 shows the unstable manifold for $\alpha' \equiv (a + b)/(2L_o) = 0.20$ and an aspect ratio $\lambda \equiv a/b = 2$. Figure 6.5 shows a limited portion of both manifolds. The unstable manifold of F begins as non-oscillatory but meanders about the stable manifold of R in the rear of the ring. The stable manifold of R begins as oscillatory in the front of the ring and becomes non-oscillatory in the rear. The square symbols mark some intersection points. Because the manifolds intersect the Smale-Birkhoff test implies that a horseshoe type of chaos is present. A particle started on one manifold ends up somewhere else on the same manifold after one period. Hence intersection points get mapped to intersection points. It was checked that the first point (nearest F) is mapped to the third, the second to the fourth, etc. Therefore the lobe denoted as A_o is mapped to A_1 and so on. All the lobes must have the same volume and this was verified. After the sixth period, fluid in A_o is engulfed into the oval shaped region O consisting of the non-oscillating halves of the two manifolds.

For convenience we shall refer to a lobe such as A_6 as the entrance lobe. Similarly B_0 is “detained” after the fifth period. A lobe such as B_5 shall be referred to as the exit lobe. Thus in every period the region O picks up fresh fluid in exchange for old fluid over a limited portion of the boundary. Figure 6.6 plots the volume exchanged during the time that the vortex travels one diameter as a function of the ellipticity $\epsilon_e \equiv (a - b)/(a + b)$. The parameter ϵ_e is the amplitude of the centroid oscillations in Moore’s solution. The largest value of ϵ_e shown corresponds to an aspect ratio of 2. The solid circles are for a core size to radius ratio $\alpha' = 0.150$ and the solid squares are for $\alpha' = 0.125$. According to the linearized theory due to Melnikov (Guckenheimer & Holmes) valid for small perturbations about the steady state, the amplitude of the manifold oscillations is linear in the perturbation amplitude ϵ_e . In the present cases, the linear behavior persists up to quite large values of the ellipticity. Note that the time that it takes to travel one diameter is independent of ϵ_e hence the ordinate scaling does not affect the linearity. Also note the sensitivity of the slope to α' , a slightly thicker core processes fluid much more rapidly.

More intersections of the two manifolds give information about smaller volumes of fluid. Figure 6.7 sketches some manifolds with as many lobes shown as the fineness of a pen would allow in order to illustrate the qualitative behavior implied by the manifolds. Suppose we wished to know how long particles remain with the vortex after they are engulfed. By observing successive maps of the entrance lobe one sees that they are stretched and wound around the vortex and every map after the third has a piece contained in the exit lobe which has been rejected. Consider the shaded sub-regions of the entrance lobe. Those regions, like the stippled and screen-dotted, that happen to be contained in a single lobe of the stable manifold have relatively simple histories. The stippled region is mapped out of O after 4 periods, the screen-dotted after 5. Following their motion backward in time one observes that their shapes are symmetric. Note however that their orientation changes. The solid region is not inside one lobe of the stable manifold but rather very many which are not drawn. It has a more complicated history. Following its motion forward, it intersects a stable manifold lobe that is drawn after four iterations. We identify its middle piece as the first to be rejected in six more iterations. Following it further in time as it intersects more of the drawn stable manifold lobes one is able to identify more portions to be detained in later iterations. Note how the solid region is drawn out along the unstable manifold and begins to reveal its shape.

Figure 6.8*a-b* gives an example of how the horseshoe arises. It depicts iterations (hatched) of a roughly rectangular region (screen-dotted) whose boundaries lie in the stable and unstable sets. Note how the region is bent and after the sixth iteration (Figure 6.8*b*) intersects itself in two strips. In six more iterations, this fluid will intersect the original rectangle in four finer strips contained in the original two and so on. Rectangles which have this property are said to form a *Markov partition* for the Poincaré map. Note again how the rectangle is drawn out along the unstable manifold and more iterations would reveal its finer structure.

Figure 6.9 is a spark-schlieren photograph kindly provided to us by Prof. Sturtevant (same as Sturtevant 1979, Figure 11*d*). It shows a shock-tube generated ring propagating to the left. For later purposes it is important to mention that the compression chamber was 15 cm long and the ring location is $x/D = 2.78$, where D is the pipe diameter. Keep in mind that in a Schlieren image the difference in illumination at a given point from the overall illumination is proportional to the density gradient, normal to a knife edge, integrated over the *entire* length of the test section normal to the photograph. Unfortunately, the direction of the knife edge is not provided. The walls of the tube were cooled to aid in visualization. The vortical core consists of cooled shear layer fluid as well as warm ambient fluid sandwiched between turns of the spiral. As temperature mixes at roughly the same rate as vorticity, the subcore (see §2.3) acquires a smooth temperature distribution. Indeed the fine white line in the center of the core indicates a region of uniform density. The visualization is also aided by the reduced density in the vortical core from compressibility effects. In any case, the vortical core is the dark region and outer undiffused turns of the spiral may also be visible.

We are interested in the streaky pattern in the rear which is described in a later report (Sturtevant 1981). His remarks apply to oblique views of the ring that are of insufficient resolution to allow reproduction here, however, they refer to a realization in which the same generation parameters and visualization technique were used as for the photograph we have presented. We think it is not inappropriate to quote that description in its entirety. Before quoting his description it should be noted that “ring” refers to the entire volume of fluid, vortical and non-vortical (or weakly vortical) carried with the ring.

“By the time the vortex has propagated 40 diameters from the vortex generator the cooled fluid ingested into the ring has mixed completely with warmer fluid

entrained from the outside, but, before this time, a great deal of information about the flow field can be obtained from this method of flow visualization. In the first photograph of Figure 10 ($x/D = 1.7$) the boundary between the vortex ring and the outer fluid is sharply defined. Dark circumferential rings extend around the interface dividing the vortex from the external fluid. These lines are suggestive of a wavy, unstable shear layer at the interface. The column of fluid seen behind the vortex ring at this close-in station is not a wake but is fluid ejected from the shock tube which has not been ingested into the vortex ring. In the second photograph ($x/D = 3.1$) [slightly later than the photograph we have been able to provide] the circumferential lines on the external interface have distorted and have developed a three-dimensional irregularity. The ring now trails a thin wake."

"At $x/D = 4.5$ the flow inside the ring seems to be fully turbulent. Disturbances on the boundary of the ring protrude into the surrounding fluid and, after being convected along the boundary to the rear of the ring, seem to grow almost explosively outward from the rearward surface of the ring. Apparently, this is a mechanism for ejection of fluid into the wake of the vortex ring, because in this photograph, and in subsequent ones, the wake thickens very rapidly. The rapid growth of disturbances on the interface at the rear of the vortex ring appears to be the mechanism not only for ejecting ring fluid into the wake but also for entraining external fluid into the ring, because, after $x/D = 6.0$ mixing within the ring becomes so strong that the photographs rapidly lose their contrast. By $x/D = 6.0$ the spatial distribution of the inhomogeneities within the ring seems to have become relatively homogeneous and isotropic. It is noteworthy that this state of fully developed turbulence is reached just before the instability waves on the core of the ring reach substantial amplitude. Though the relationship between the core instability and the turbulence in the ring is not at all clear, it is certainly apparent from these photographs that substantial three-dimensional random, unsteady motion (turbulence) occurs within the ring *before* there are any signs of the fundamental core instability" (Sturtevant's italics).

Several comments are due. First his description of the interface is consistent with the picture of entrainment and detrainment provided by the unstable manifolds. We do not agree that it is due to a shear-layer instability. Second, wherever turbulence is mentioned, it does not refer to vortical motions but rather chaotic motion of the cold fluid carried with the ring and entrained ambient warm fluid. Third, the distortions

of the interface are described as three-dimensional suggesting that the unsteady vortical motion causing it is also three-dimensional. However this is inconsistent with the fact that it is observed before the Widnall instability. Given that Schlieren visualization presents an integrated view of density gradient, complex axisymmetric stirring of cold and ambient fluid cannot be distinguished from three-dimensional motion even in a 30° oblique view. It is possible that even in its low amplitude stages the Widnall instability is an efficient stirrer. We are not inclined to this view for two reasons. First, in the initial stages the waves are stagnant according to both experiment (Maxworthy 1977) and theory. Second, even when the waves begin to rotate (Maxworthy 1977), short waves have a short range effect on the velocity field. This is suggested by Widnall, Bliss & Tsai (1974) who say that "for short waves, such as are observed on vortex rings, the velocities induced at the core boundary owing to distant perturbations on the ring are negligible; preliminary calculations of the outer potential flow using toroidal co-ordinates indicate that these are of order $1/(N_w R)^2$ as $N_w R \rightarrow \infty$." Here N_w is the number of waves and R is the radius of the ring.

What form of unsteadiness produces the stirring? One possibility is the instability of two-dimensional compressible vortices studied by Broadbent & Moore (1979). They found that a two-dimensional circular patch of uniform vorticity and entropy was unstable to two-dimensional wavy deformations of the boundary, the elliptic mode being the most unstable. The instability is weak; it takes many core rotations for the initial disturbance to undergo an e -fold amplification especially at low Mach numbers based on maximum rotational velocity in the core. Sturtevant mentions that the maximum velocity in the core is near sonic; this allows us to find the growth rate of the elliptic mode from Table 1 of Broadbent & Moore (1979). Then, using Kelvin's speed formula with a core size to radius ratio of 0.10 estimated by Sturtevant we find that in the time that the vortex propagates one ring diameter there are 0.90 e -foldings of the initial disturbance. On the other hand, using Equation 9.2 of Widnall & Tsai (1977), the three-dimensional instability undergoes 1.4 e -foldings but as mentioned earlier its influence would decay more rapidly from the core. Thus one cannot *a priori* discount the presence and influence of the Broadbent & Moore instability.

Figure 12 in Sturtevant (1979) is a photograph of the same case without pre-cooling. Only the naturally occurring reduced density in the vortex core is used for visualization. No streaks are present.

Maxworthy (1974, hereafter M) studied turbulent vortex rings in water with $Re \approx 1 \times 10^4$ based on propagation velocity and toroidal radius. Figure M:3 shows a ring marked with a blob of dye. The blob becomes puffy and its boundary corrugated with ejections similar to those suggested by the unstable manifold. Most of the dye is rejected to a wake and eventually remains only in a thin toroidal core with core to toroidal radius ratio of about 0.1.

In Figure M:4 an undyed ring is pushed through a patch of dye. "The outer region of the moving bubble was immediately filled with dyed fluid, but the core remained clear. As time progressed, a thin skin around the core became dyed but penetration to the centre of the core never seemed to take place, at least during our experiments." The remarks suggest that there is little exchange between the vortical core and surrounding fluid.

In Figure M:5 a weak salt solution was used to mark the bubble and observed using the shadowgraph technique. "The major motions in the outer bubble are of larger scale; they mix environmental with bubble fluid and deposit the majority into a wake. There are, clearly, small scale streaks in the region, but are being convected around and stretched by the large scales, and only show up because of the small diffusion coefficient possessed by the denser salty water."

These observations are also consistent with unsteady motion of a vortical core inducing the entrainment and detrainment.

Unlike the situation we have treated, in the experiments of Maxworthy the vortical core is not completely isolated from the surrounding fluid. We have not addressed slow *permanent* entrainment characterized by growth of the bubble. The rate of growth of bubble volume divided by the surface area times the propagation velocity defines an entrainment coefficient. Maxworthy reports a value of about 0.01 independent of Re . Weak vorticity either diffusing into the bubble or entering it via wisps torn off from the core would become turbulent due to chaotic passive advection. Little whirls are chaotically advected by bigger whirls. It would be very interesting to study, using rapid distortion theory, how the spectrum of the weak vorticity evolves due to chaotic advection. This vorticity is continually being rejected into the wake, resulting in a slow loss of impulse.

The splitting of the manifolds is generic and may also occur in laminar wake cavities in which after a critical Reynolds number, periodic velocity signals are measured. Plate 35 in the book edited by Goldstein (vol. 2, 1965) shows dye visualization

behind a circular disk in such a regime and is suggestive of manifold splitting. The book explains: "When the Reynolds number exceeds the critical value, an oscillating disturbance of the surface of the vortex ring becomes visible, with the result that successive portions of its substance are discharged downstream at regular intervals of time which depend on the rate of flow and the dimensions of the disk."

"In investigating wakes behind various obstacles experimenters have noticed some definite periodicity in the records of the velocity at points behind the obstacle, but have been unable to observe any uniformity or periodicity in the shape of the vorticity discharge." These conflicting observations may again be due to inadequacy of the visualization technique.

One may wonder if, in the numerical example, despite the fluid exchange process, some fluid is permanently carried with the vortex. Figure 6.10 shows that two such regions exist near the core. After half a major axis rotation region 'A' is transported to 'B' and vice-versa. The motion is quasiperiodic and periodic for some exceptional points inside. In a cylindrical coordinate phase space in which the azimuthal direction is chosen to be angle of the ellipse, the motion of particles takes place on tori whose cross-section has been depicted in the figure. These are called KAM tori after the Kolmogorov-Arnold-Moser theorem for perturbed Hamiltonian systems. In the fluid mechanical context the KAM theorem refers to the survival, under small perturbations about steady flow, of such regions near the closed streamlines of the steady flow.

The existence of these regions of trapped fluid near the vortex core can be understood in terms of the streamline pattern of the steadily rotating Kirchhoff elliptic vortex in two-dimensions. This is because the velocity field in the vicinity of the core is locally the same with additional terms in the axisymmetric case that account for self-induction. From the KAM theorem one expects that some of the qualitative features will remain unchanged in the presence of these additional terms. Before presenting some representative streamline patterns we briefly describe how they were obtained.

Lamb (1932, §159) discusses particle paths in the interior of the vortex and finds them to be ellipses (relative to the vortex) geometrically similar to the boundary of the vortex. The interest here is on the exterior flow. Let $z = x + iy$ define fixed

coordinates and let $Z' = X' + iY'$ rotate with the vortex, X' being measured along the major axis which makes an angle φ with the x axis so that

$$z = Z'e^{i\varphi}. \quad (6.4.1)$$

Next define elliptic coordinates

$$Z' = c \cosh \zeta, \quad \zeta = \xi + i\eta, \quad c \equiv \sqrt{a^2 - b^2}. \quad (6.4.2)$$

Lamb provides the streamfunction and from it one can write down the complex potential using the Cauchy-Riemann relations (following Saffman 1979):

$$\Phi = -\frac{i\Gamma}{2\pi} \left(\zeta + \frac{1}{2}e^{-2\zeta} \right). \quad (6.4.3)$$

The corresponding velocity field is

$$u - iv = \frac{d\Phi}{dz} = -\frac{i\Gamma}{\pi c} e^{-\zeta} e^{-i\varphi}. \quad (6.4.4)$$

Figure 6.11a shows the Poincaré section, every half rotation, of particle paths relative to the vortex for a slightly elliptical vortex. If the vortex were circular, particle paths would also be circular but the slight ellipticity creates mounds of fluid on the major axis side that rotate with the vortex. Similar mounds exist for the potential flow of a solid rotating ellipse as shown by Morton (1913). The mound is created about the point in the circular flow where the particle rotation frequency is the same as the vortex rotation frequency. Figure 6.11b shows larger mounds for aspect ratio equal to two.

We are now interested in particle transport in the presence of linearized waves on the boundary of the elliptic vortex. Love (1893) has studied the stability of the waves and a description of how we obtain the particle path equations from his analysis follows.

Since the vorticity distribution is unaltered, the disturbance streamfunction obeys the Laplace equation which is separable in elliptic coordinates and a typical eigenmode (choosing the one that decays at infinity) is

$$\delta\Psi = A_m(t) \cosh m\xi_0 e^{-m(\xi-\xi_0)} \cos m\eta + B_m(t) \sinh m\xi_0 e^{-m(\xi-\xi_0)} \sin m\eta, \quad (6.4.5)$$

where ξ_0 is the value of ξ on the unperturbed boundary. As for the unperturbed ellipse it is convenient to work with complex variables. The velocity potential associated

with (6.4.5) is obtained from the Cauchy-Riemann relations and a complex potential is formed:

$$\delta\Phi(\zeta) = -e^{-m\zeta} e^{m\xi_0} (B_m(t) \sinh m\xi_0 - iA_m(t) \cosh m\xi_0). \quad (6.4.6)$$

Love obtains an expression (preceding his Equation 21) for the amplitudes $A_m(t)$ and $B_m(t)$ after invoking continuity of flow quantities and the dynamical constraint that the boundary is material. It has the solution:

$$\begin{aligned} A_m(t) &= D_1 \sin \bar{\nu}t + D_2 \cos \bar{\nu}t, \\ B_m(t) &= \sqrt{\frac{\bar{\nu}_2}{\bar{\nu}_1}} (D_2 \sin \bar{\nu}t - D_1 \cos \bar{\nu}t), \quad \bar{\nu} = \sqrt{\bar{\nu}_1 \bar{\nu}_2}, \\ \bar{\nu}_{1,2} &= \frac{1}{2} \omega_0 \left[\frac{2m\lambda}{(\lambda+1)^2} - 1 \pm \left(\frac{\lambda-1}{\lambda+1} \right)^m \right], \quad \lambda \equiv \frac{a}{b}, \end{aligned} \quad (6.4.7)$$

where ω_0 is the value of the uniform vorticity. The value of $\bar{\nu}$ determines the stability of a vortex with aspect ratio λ to a given mode m . Love shows that all modes are neutrally stable provided $\lambda < 3$. When $\lambda > 3$ the $m = 3$ mode is the first to become unstable. Neutrally stable modes serve as bifurcation points for finite amplitude periodic solutions and they should be obtained in the future.

The constants that appear in the equation for the complex potential are

$$\beta_{1,2} \equiv \frac{\sinh m\xi_0}{\cosh m\xi_0} e^{m\xi_0}, \quad (6.4.8)$$

and using the definition for ξ_0 they become

$$\beta_{1,2} = \frac{1}{2} \left[\left(\frac{\lambda+1}{\lambda-1} \right)^m \mp 1 \right]. \quad (6.4.9)$$

Hence considering initial conditions such that $D_1 = 0$ and $D_2 = \epsilon$ the perturbation velocity is

$$u - iv = \frac{d(\delta\Phi)/d\zeta}{dz/d\zeta} = \frac{\epsilon m e^{-m\zeta} e^{-i\varphi}}{c \sinh \zeta} \left(\sqrt{\frac{\bar{\nu}_2}{\bar{\nu}_1}} \beta_1 \sin \bar{\nu}t - i\beta_2 \cos \bar{\nu}t \right), \quad (6.4.10)$$

which when added to (6.4.4) gives the equations used to track particles.

Finally, in order make ϵ dimensionless and concrete we relate it to the amplitude of the surface deflection. This is done by determining a confocal ellipse that encloses

the perturbed vortex. Invoking the condition of continuous tangential velocity at the interface, Love (Equation 14) obtains for our initial phase:

$$\delta\xi = \frac{\epsilon h_o^2 m}{\omega_o} e^{m\xi_o} \cos m\eta, \quad h_o^2 \equiv (a^2 \sin^2 \eta + b^2 \cos^2 \eta)^{-1}. \quad (6.4.11)$$

The inequality

$$\delta\xi < \frac{m\epsilon}{b^2\omega_o} e^{m\xi_o}, \quad (6.4.12)$$

defines an enlarged confocal ellipse with major axis $a + \delta a$ containing the perturbation such that for small $\delta\xi$

$$\epsilon_a \equiv \frac{\delta a}{a} = \frac{m\epsilon\lambda}{\omega_o a^2} e^{m\xi_o}. \quad (6.4.13)$$

The perturbation amplitude was specified with ϵ_a .

Consider an $m = 4$ perturbation with $\epsilon_a = 0.10$. Figure 6.12 shows 20 orbits relative to the rotating vortex for 1000 periods which were started on one side of the vortex. Particle paths sufficiently far from the vortex as well as in the inner region of the mounds remain non-chaotic. The outer region of the mound has chaotic orbits which make their way to the opposite side of the vortex. Figure 6.13 is a close-up of the inner mound region and shows two chains of islands. Particles are transported from one island to another in each chain.

Figure 6.14 shows orbits in the mound region for $m = 3$ and $\epsilon_a = 0.10$; they are qualitatively similar to the previous case. An orbit started just outside the outermost torus in Figure 6.14, in the transition region between regular and chaotic motion, is shown in Figure 6.15. The first 961 iterations (dots) are neither completely chaotic nor regular and remain confined to a region that is similar in shape to the outermost torus. Quite rapidly, however, the particle breaks free and begins to explore a larger area. The next 65 iterates are shown surrounded with diamonds. The calculation was run for 3000 iterations and eventually the particle crossed over to the other side of the vortex. The shape of the initial part of the orbit with its linked sausage appearance suggested an island chain with homoclinic points between the islands with split manifolds through which the particle eventually escapes, but we were unable to locate any tori. This behavior is also symptomatic of and may be due to the presence of so-called cantori which act as leaky barriers to particle transport. See MacKay *et al.* (1984) for a brief history. Their existence has been proved for Hamiltonian systems. They are invariant sets which may be thought of as being similar to the first scenario described except that they have zero area. They act as obstructions

to transport across them but like the spaces between island chains through which particles cross, cantori have gaps and hence act as partial two-way barriers.

Finally, using Dyson's (1893) model, the leapfrogging of rings with core size to radius ratio of 0.1 and an initial separation of one radius is studied. This case was studied with contour dynamics in the last chapter. Although Dyson's model fails to predict the acoustic signal it is still a good approximation for the velocity since the cores remain thin and nearly circular and there is no permanent deformation; the maximum aspect ratio was 1.14. Figure 6.16 shows unstable manifolds of the Poincaré map with period equal to one passage at three phases of $\bar{\phi}_o = 3/2\pi, 2\pi$ and 3π (modulo 2π); the circles indicate the vortical core. The flow visualization photographs are from Yamada & Matsui (1978). A cross-section of the flow has been illuminated by a sheet of light. The stretching along the manifold is so rapid that even though 4000 particles were placed on the initial segment, the visual appearance of the manifold as a connected curve disappears after the third forward map of the initial segment. For $\bar{\phi}_o = 2\pi$ the manifold winds back and forth between the two vortices each time passing through the "braid" region.

Even the very fine scale features of the manifold agree remarkably well with the experimental photographs. Maxworthy (1979) has used the photographs together with vorticity diffusion arguments to provide a plausible rendering of the underlying vorticity. For example, the first photograph shows the first passage almost completed, and "thereafter, the latter [the passing vortex] is distorted and wraps around the former and the two rings become one." In referring to the third photograph, Maxworthy says that the passing vortex "has become so distorted that it is barely recognizable", and Yamada & Matsui say that "the core of the first ring was severely deformed and stretched, and it seemed to roll up around that of the second ring..." Maxworthy's guess of the vorticity field underlying the third photograph is sketched as Stage 3 in Figure 1 of his paper and shows the two rings diffused together.

On the other hand, the present result suggests that the observed pattern may be due merely to complex motion of tracer in irrotational or weakly vortical fluid, with vortex cores behaving in a simple, non-deforming and almost classical manner. It is only tracer that appears to deform and roll-up around the leading vortex. We would like to stress three points. First, this interpretation is appropriate only for this experiment in which a smoke wire was stretched across the entire diameter of the orifice, causing smoke to be introduced not only in the emitted shear layer (which would

mark the vorticity aside from Schmidt number effects) but also into non-vortical fluid initially transported with each vortex. This points out that one ought to be careful to ensure that only vortical regions are marked. Second, weak vorticity around the periphery of a core may also become susceptible to passive advection and acquire the structure of the unstable manifold; compare it with the filament calculation for a peaked vorticity distribution shown in Figure 5.18. Third, the question of whether the two rings diffuse together or behave in the simple manner suggested at the Reynolds number of the experiment (1600 based on initial translation speed and orifice diameter), will have to await viscous numerical computations at higher Reynolds number. Stanaway *et al.* (1988a) have utilized a spectral method to simulate a passage interaction with initially Gaussian vorticity distributions. Parameters were chosen to be those of the present inviscid calculation, the core size being defined where the maximum velocity occurs. The Reynolds number based on initial self-induced speed and diameter was 609. They observed that the first passage is successful but, during the second, the passing vortex strongly deforms. A measure of the extent of viscous merging is the level of the highest vorticity contour that surrounds the vorticity peaks of both rings. At roughly the phase of the last Yamada & Matsui photograph and stage 3 as sketched in Maxworthy (1979, Figure 1), this level is 10% of the peak vorticity. Hence, at the Reynolds number of the simulation, neither Maxworthy's nor the classical picture is completely accurate. We hope that simulations at higher Reynolds number will lead to a synthesis of inviscid descriptions and Maxworthy's views about the role of viscous diffusion.

This chapter has presented some examples of chaotic particle motion resulting from unsteadiness of the vorticity. Despite the simplicity of the examples from the Eulerian point of view, they have a very rich and complex structure which has been shown to be relevant to what is observed in the laboratory. Thus we feel that the study of simple inviscid models may be useful for understanding mixing, combustion and dye visualization for more complex shear flows. After observing that certain nearby regions tend to be drawn out along the unstable manifold, we partially understand why smoke should tend to acquire its structure. As a second step, what needs to be shown is that overall stretching rates are positive along (at least some portions of) the manifold.

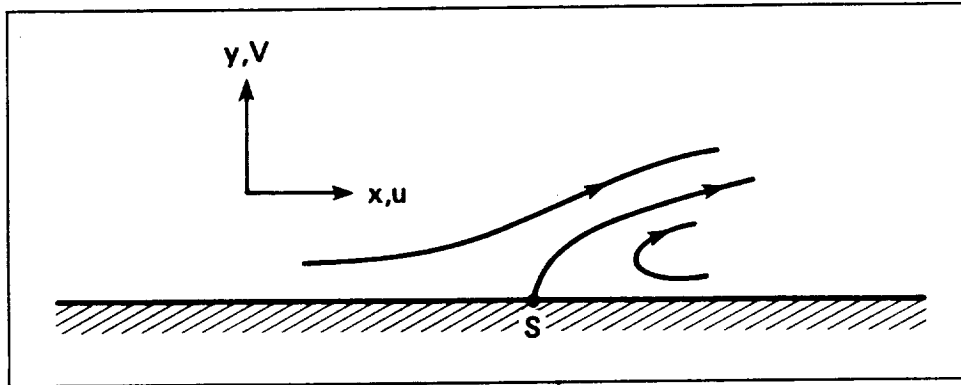


FIGURE 6.1. Streamlines for separated viscous flow over a solid wall.

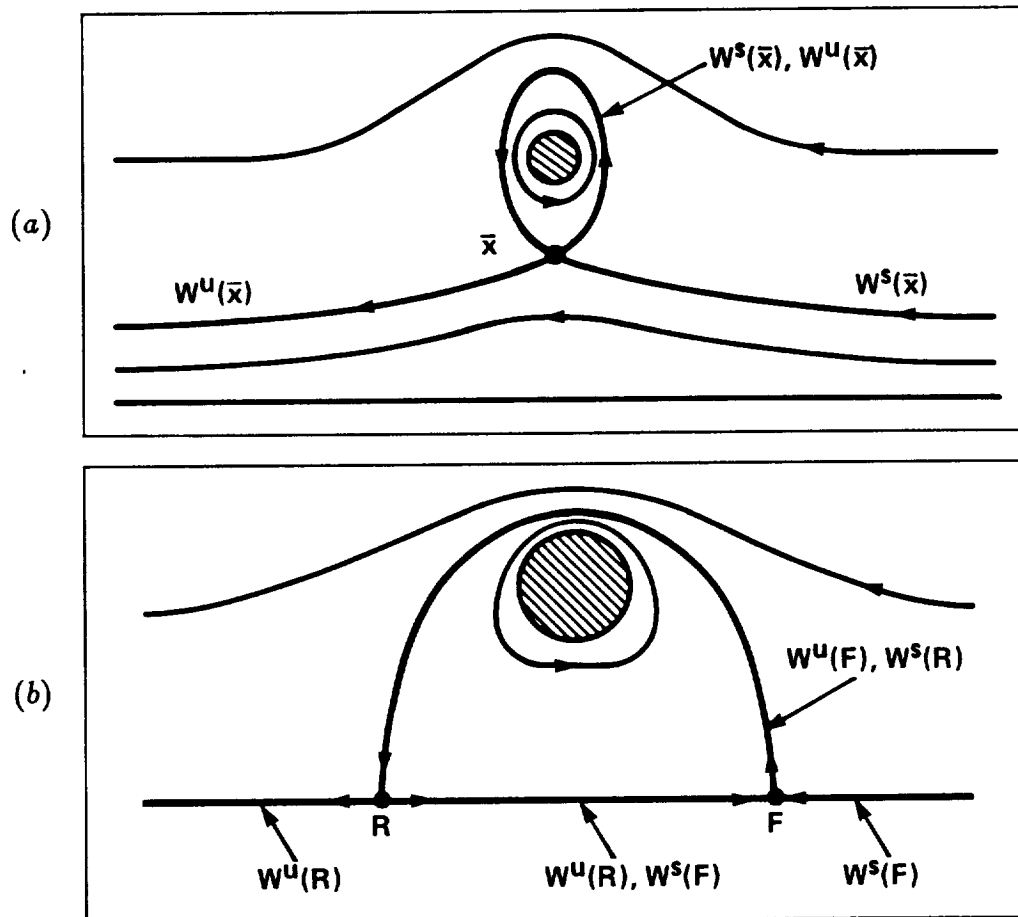


FIGURE 6.2. Sketch of streamlines for steadily translating vortex rings. The hatched region shows the vorticity containing region. (a) is for very thin cores and (b) for thick cores.

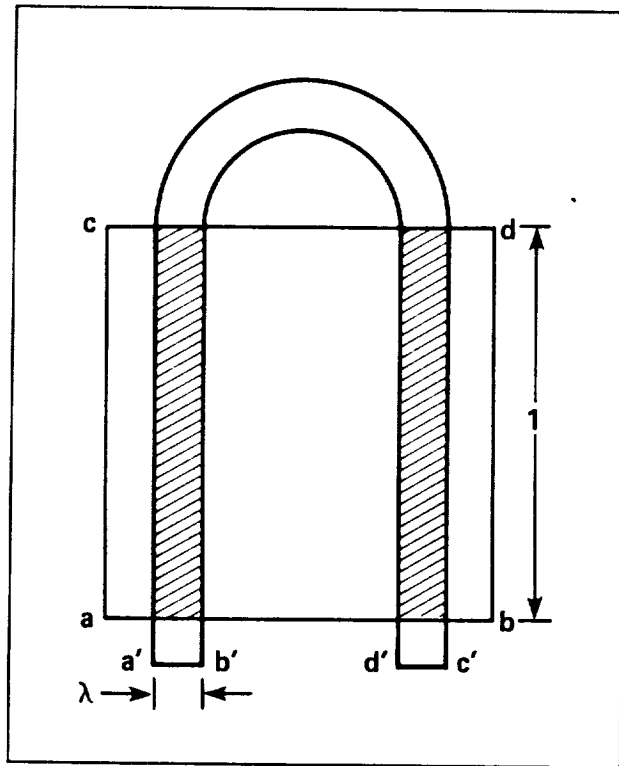


FIGURE 6.3. Smale's horseshoe map.

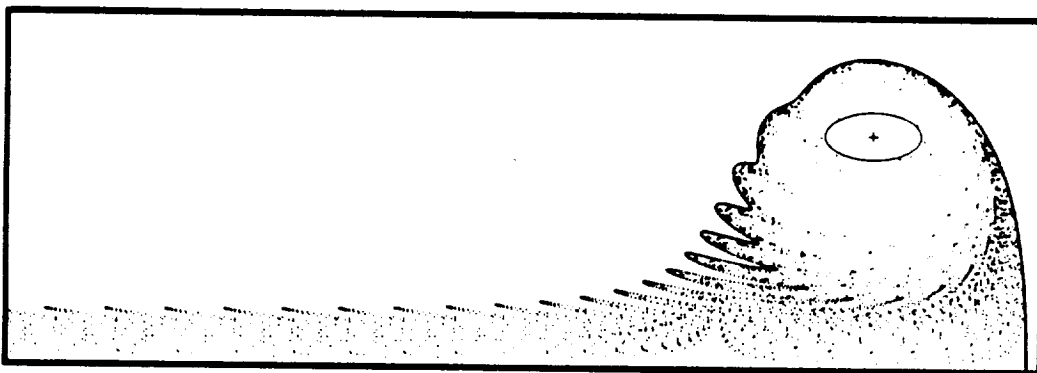


FIGURE 6.4. Unstable manifold of the forward periodic point for an elliptical core ring. $\lambda = 2$, $\alpha' \equiv (a + b)/(2L_o) = 0.15$.

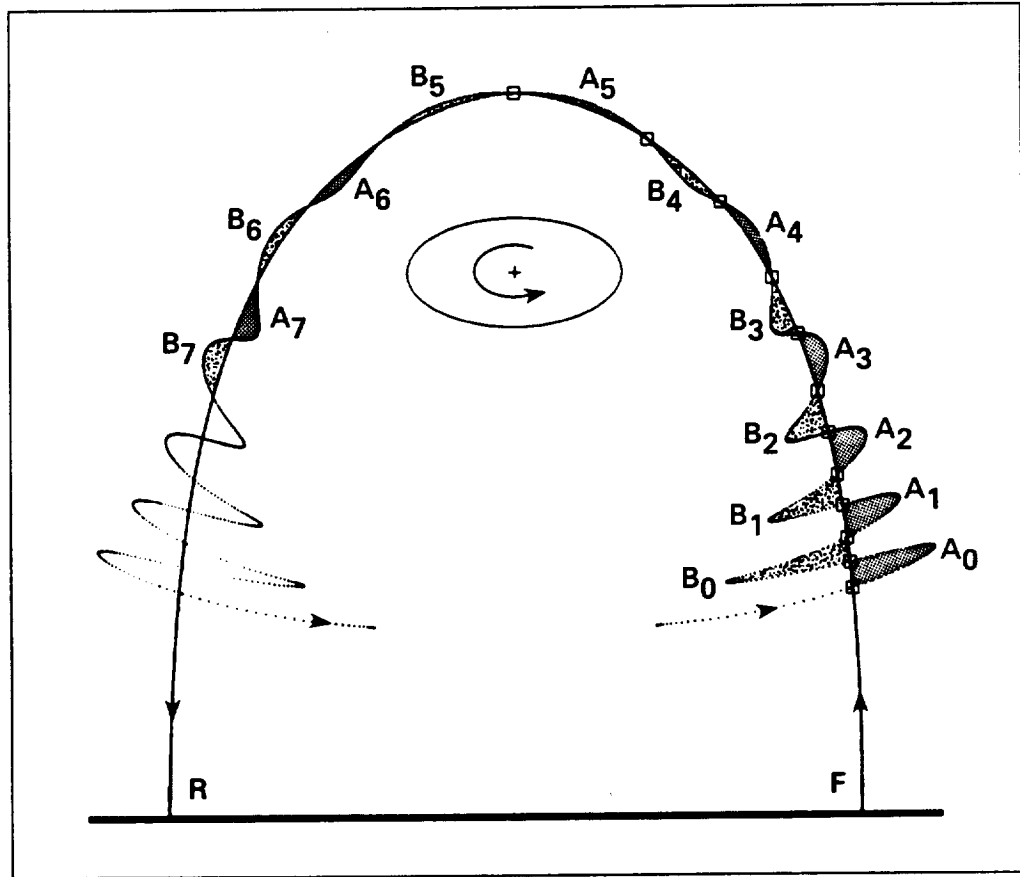


FIGURE 6.5. Abridged portions of the stable and unstable manifolds corresponding to the previous figure illustrating fluid engulfment and rejection.

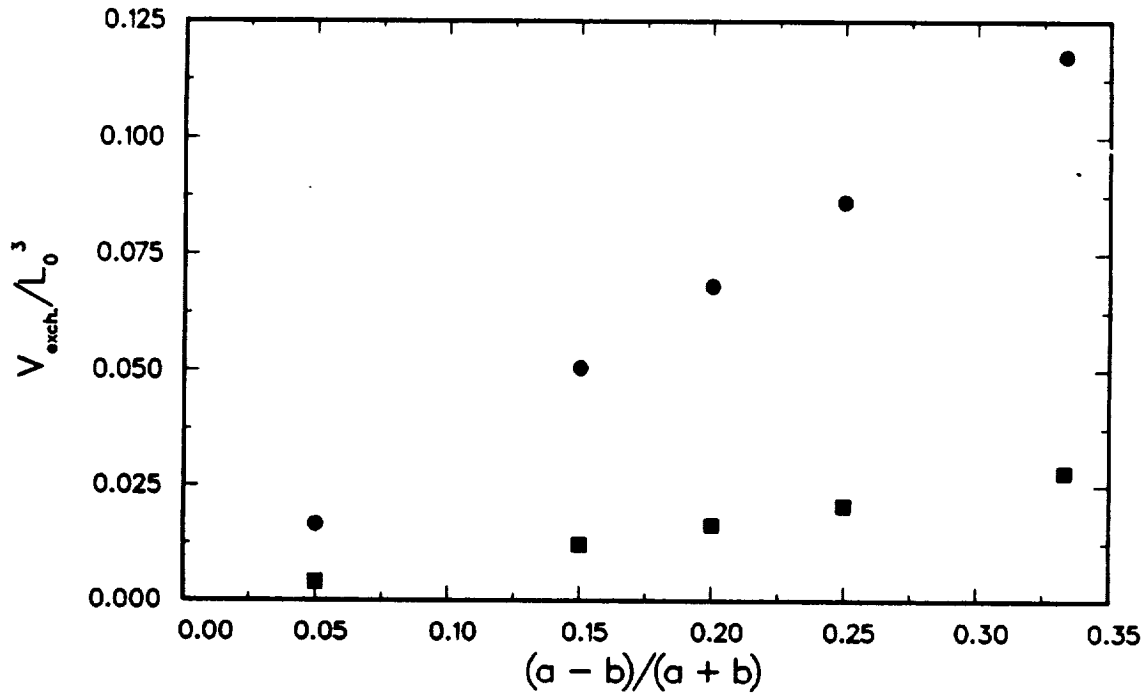


FIGURE 6.6. Volume of fluid exchanged by elliptical core vortex rings per diameter translation as a function of the ellipticity. The volume is scaled using the mean toroidal radius L_0 . \bullet , $\alpha' \equiv (a + b) / (2L_0) = 0.150$; \blacksquare , $\alpha' = 0.125$.

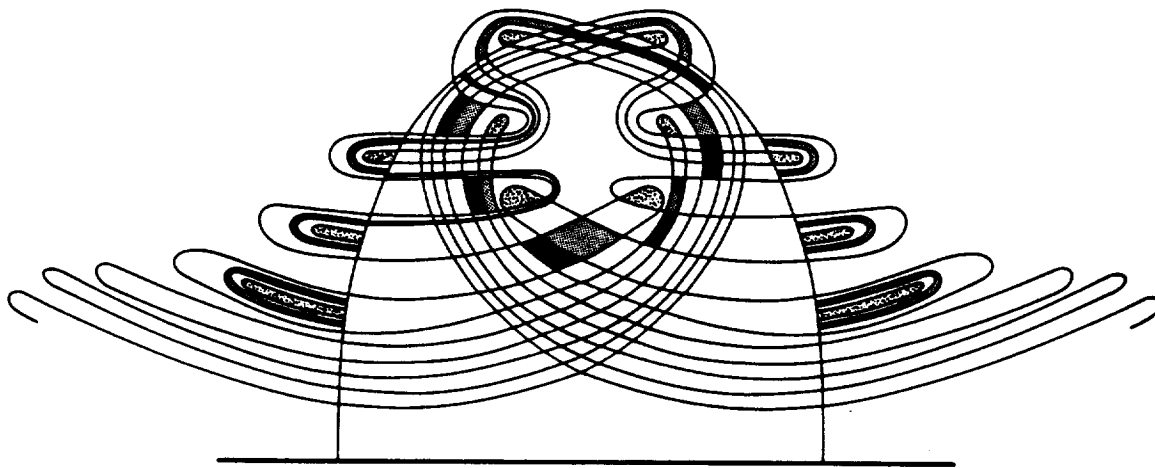


FIGURE 6.7. Motion of selected fluid regions bounded by the manifolds.

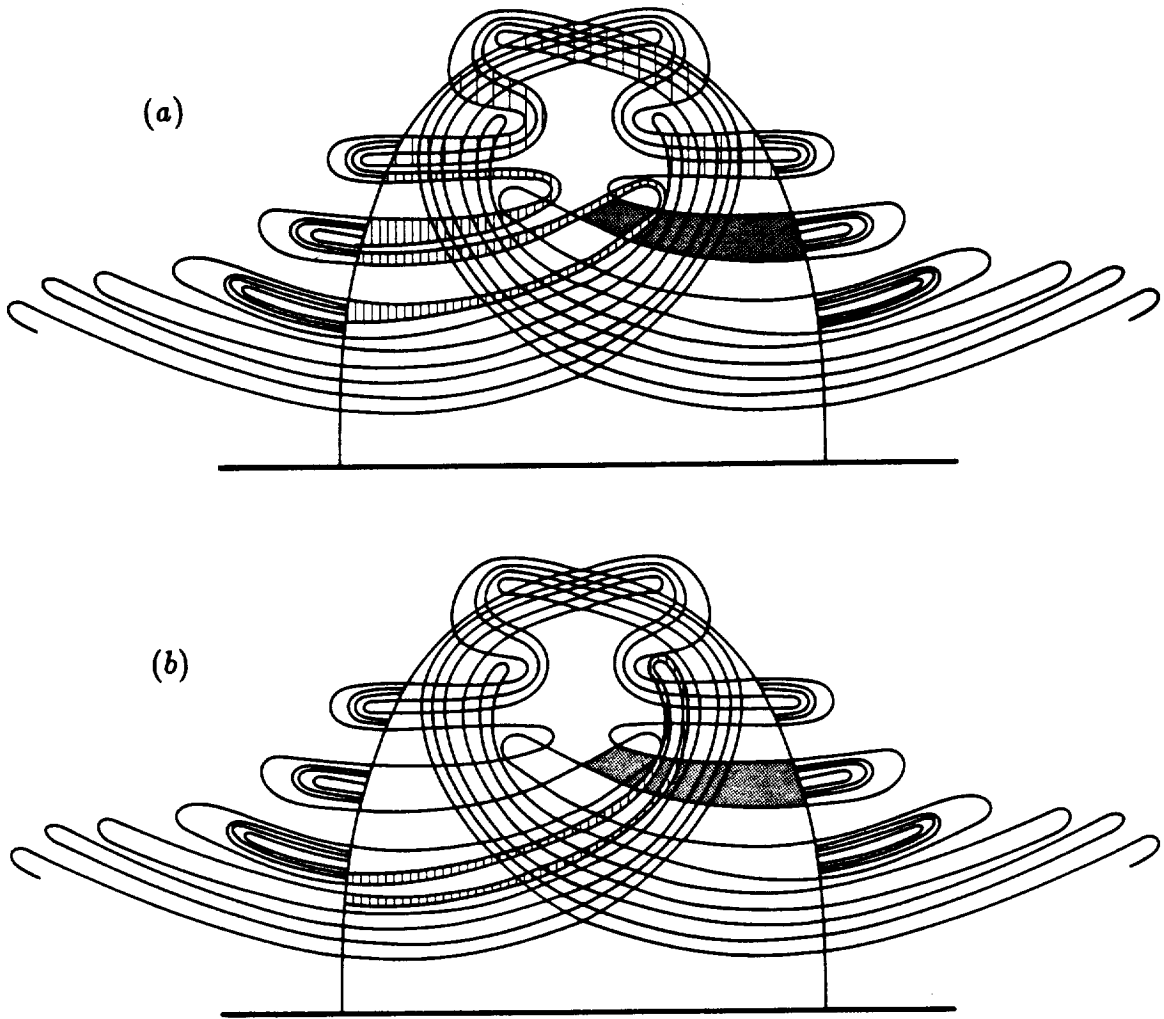


FIGURE 6.8 Sketch of six Poincaré maps of a “rectangle” (screen dotted) leading to the horseshoe map. The iterates are hatched and proceed counterclockwise. (a) shows the first five iterations and (b) the last.

ORIGINAL PAGE
BLACK AND WHITE PHOTOGRAPH

ORIGINAL PAGE IS
OF POOR QUALITY

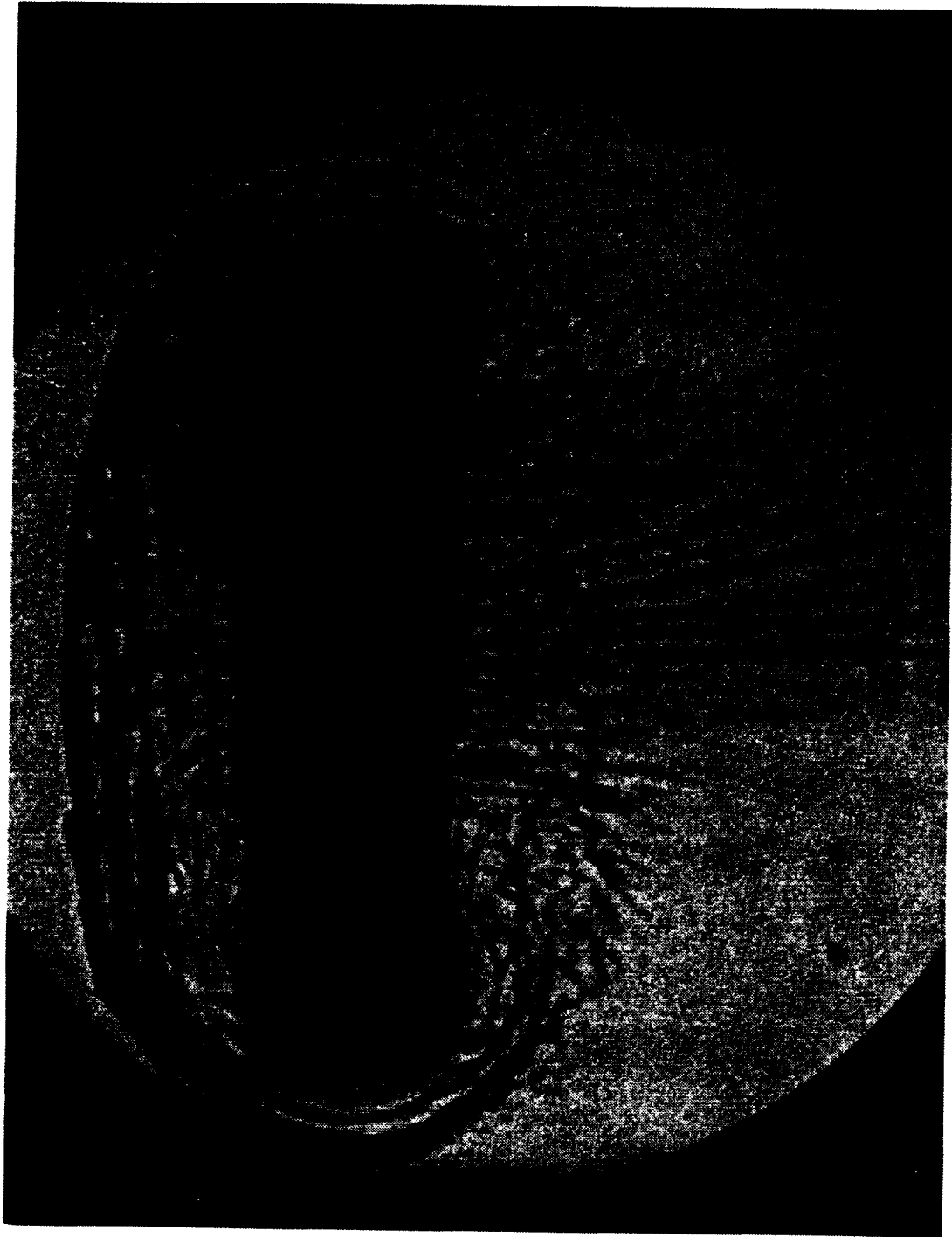


FIGURE 6.9. Schlieren visualization of a shock-tube generated ring propagating to the left. *Courtesy of B. Sturtevant.*

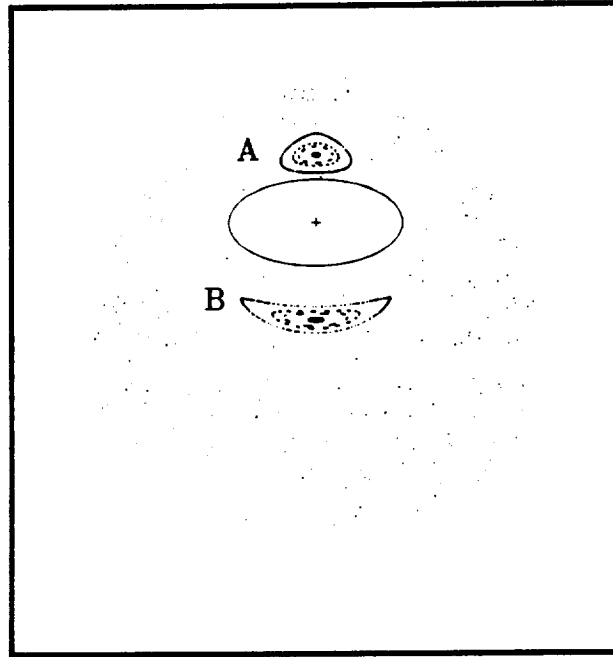


FIGURE 6.10. Poincaré section of regions of fluid permanently carried by an elliptical core ring. $\lambda = 2$, $\alpha' \equiv (a + b)/(2L_0) = 0.15$.

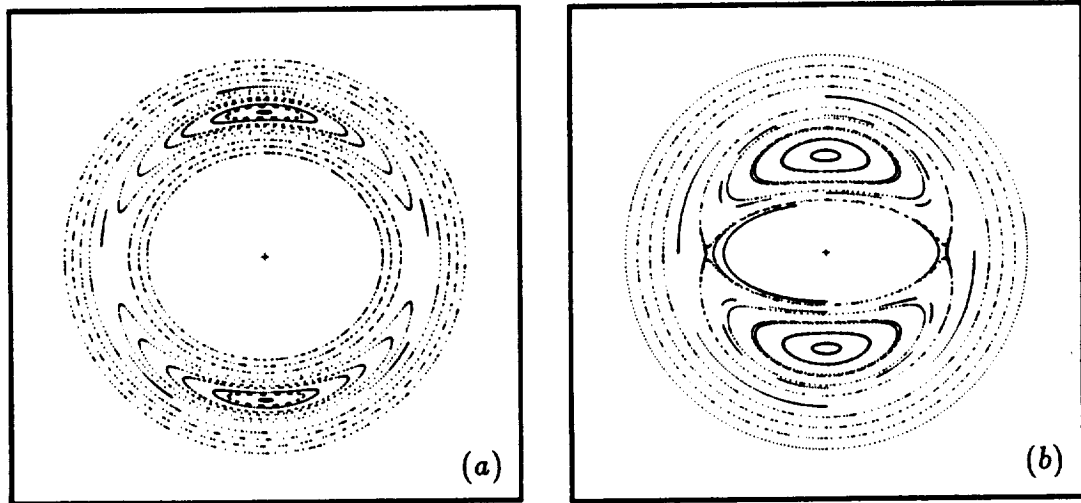


FIGURE 6.11. Poincaré section of particle paths for Kirchhoff's two-dimensional elliptic vortex in a reference frame rotating with the vortex. (a) $\lambda = 1.1$; (b) $\lambda = 2$.

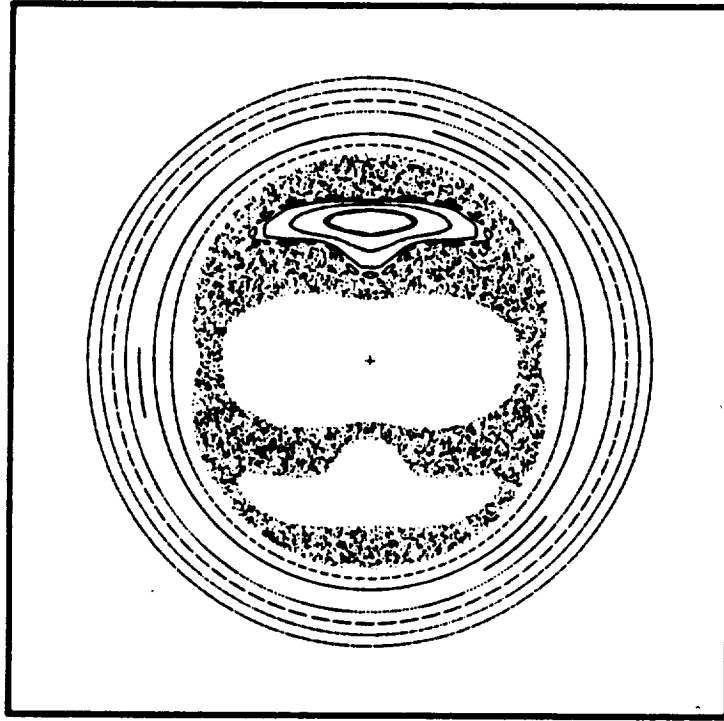


FIGURE 6.12. Poincaré section of particle paths for an elliptic vortex with a propagating wave on the boundary. $m = 4$, $\epsilon_a = 0.1$, $\lambda = 2$, number of periods = 2000. Twenty particles were started on the upper side and are shown relative to a reference frame rotating with the vortex.

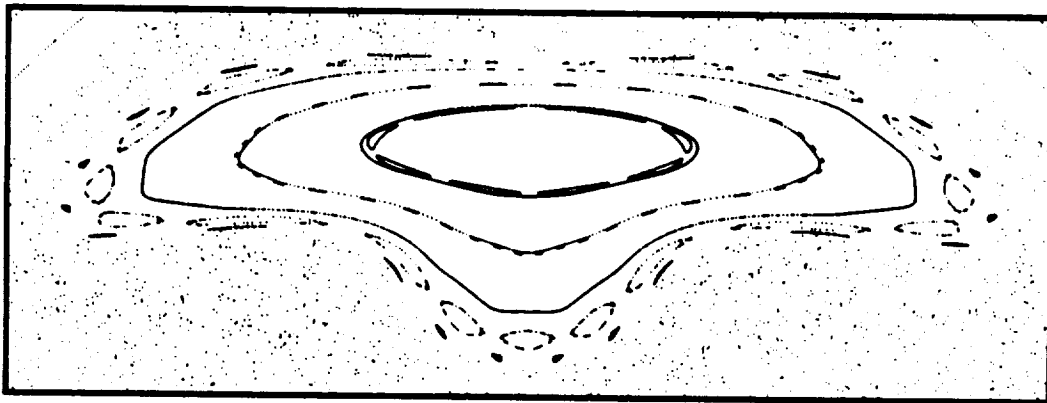


FIGURE 6.13. Close-up of the upper mound region in the previous figure.

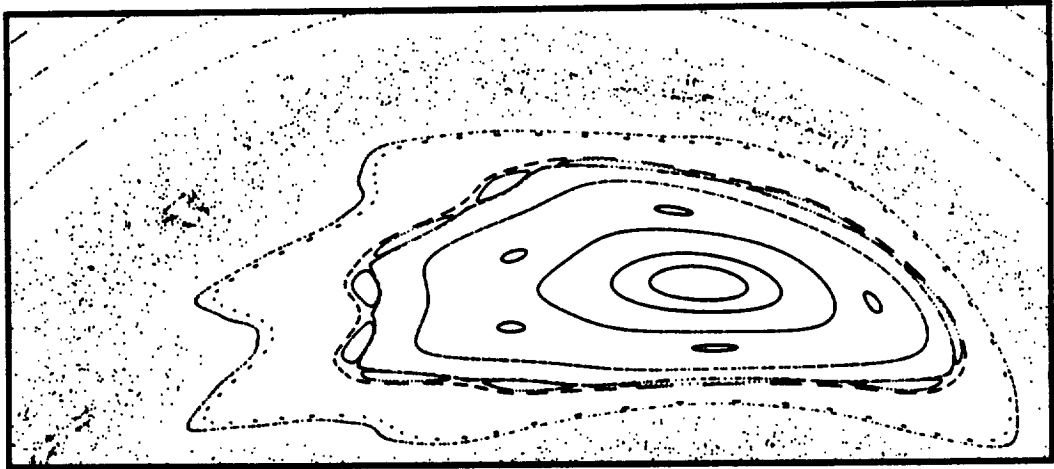


FIGURE 6.14. Poincaré section of particle paths for an elliptic vortex with a propagating wave on the boundary. $m = 3, \epsilon_a = 0.1, \lambda = 2$, number of periods = 2000. Twenty particles were started on the upper side and are shown relative to a reference frame rotating with the vortex. A close-up of the mound region is shown.

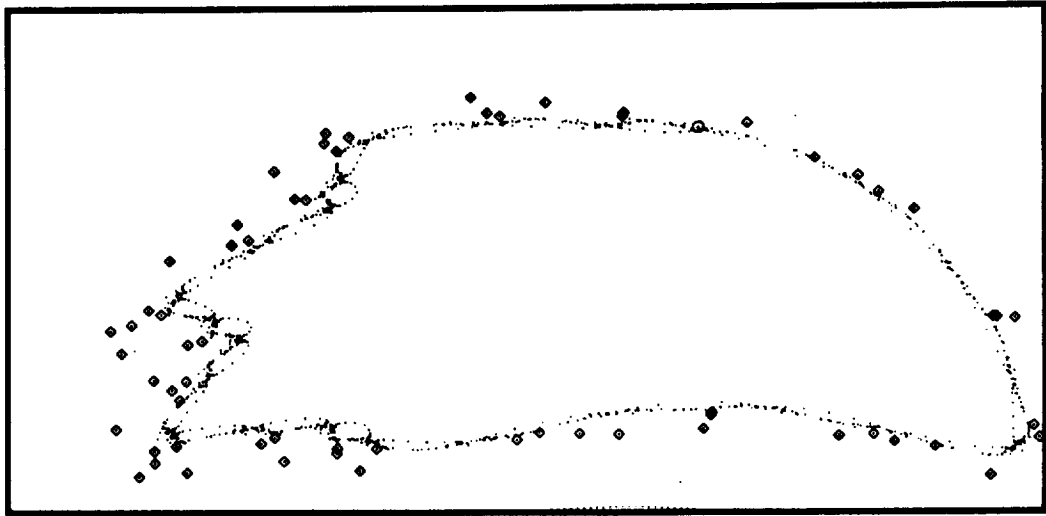


FIGURE 6.15. Same case as the previous figure. Shows one orbit started just outside the outermost torus. Dots represent the first 961 periods and diamonds the next 65.

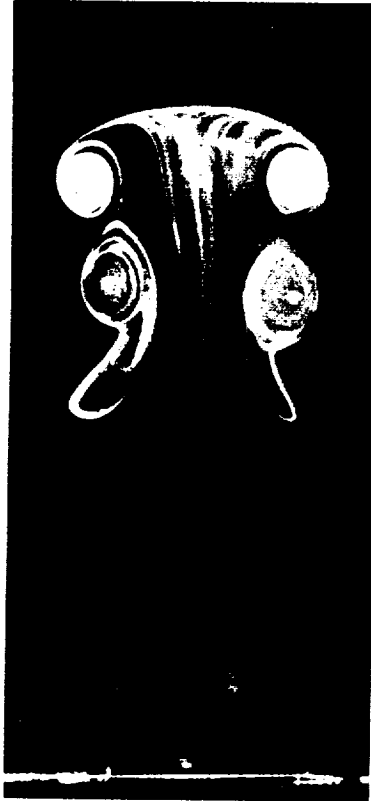
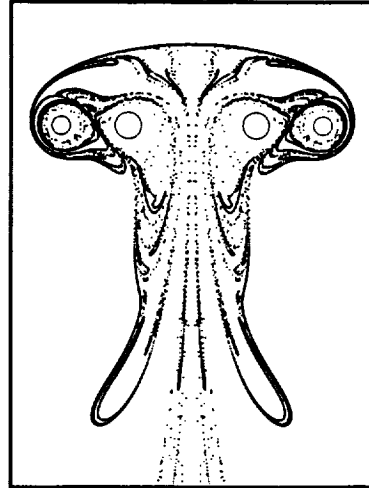
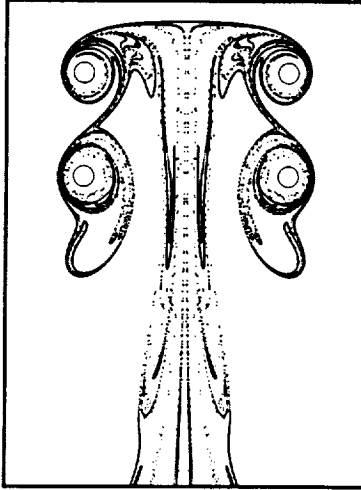
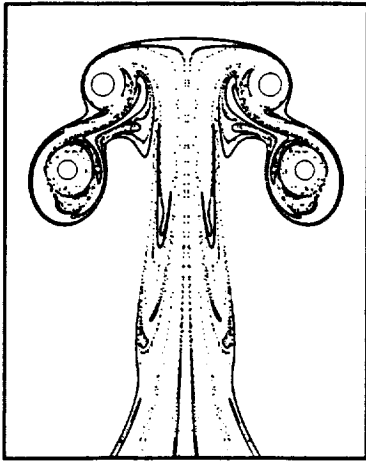


FIGURE 6.16. Unstable manifold at different phases for two leapfrogging rings. Photographs are from Yamada & Matsui (1978). *Reproduced with permission.* Please turn page sideways.

CLOSING REMARKS

7.1. Conclusions

(1) The contour dynamics formulation, developed for two-dimensional regions of uniform vorticity by Zabusky, Hughes & Roberts (1979), was extended to axisymmetric vortex rings in which the azimuthal vorticity varies linearly with respect to distance from the axis of symmetry.

(2) A model for the axisymmetric flows which retains only the elliptic degrees of freedom in the core shape was developed. Six ODEs govern the evolution of the position and shape of each vortex in the model. The classical model due to Dyson (1893) assumes that cores remain circular and therefore implicitly includes only the isotropic compression part of the strain and ignores the plane strain. The elliptic model accounts for the latter. The results of the model were compared with contour dynamics and found to accurately predict whether a passage of two rings would be successful, the overall pattern of core deformation, and the acoustic signal.

(3) The vortex filament method (Leonard 1980) was implemented for axisymmetric flow and tested against the contour dynamics method. It was found to be accurate even for sensitive measures such as the acoustic signal. Inaccuracy occurred at late times when thin sheet-like regions which could not be resolved well developed and a Kelvin-Helmholtz-like clumping of filaments, not present in the contour dynamics simulations occurred.

(4) The vortex filament method enabled the study of the passage of rings with more realistic vorticity distributions that are peaked. The vorticity distribution was found to be less important for cases in which large strains occur. For example, for a case of thin rings, the strain rate was small and the passage successful for a peaked distribution, but unsuccessful for a linear distribution having the same circulation and core size. For a case of thick rings, the strain rate to vorticity ratio was large and the two distributions exhibited the same pattern of deformation.

(5) Möhring's (1978) theory of vortex sound was implemented for the three methods listed above. The theory solves Lighthill's (1956) exact equation (neglecting viscous stresses) for isentropic pressure fluctuations in the far-field by assuming that the vortical region is small compared to the sound wavelength and that kinetic energy is conserved. The usefulness and novelty of Möhring's theory lies in the fact that the acoustic pressure depends on an integral of the vorticity which is easily computed.

The predictions of Möhring's theory combined with contour dynamics was compared against the signal measured by Kambe & Minota (1983) for colliding rings. Except for a final peak, the agreement with the *ensemble averaged* signal was very good for core size to radius ratios of 0.5 and 1.0. In particular, a negative peak not predicted by Dyson's model and which was accounted for by Kambe & Minota using a viscous model is reproduced, suggesting that it is due to inviscid core deformation. The two core sizes simulated are very likely larger than in the experiment. Calculations for a thin core ($\alpha = 0.2$) showed that oscillations are produced when the signal becomes negative. Similar oscillations are present in individual realizations of the experiment but, because they are not reproducible, averaging filters them out. Calculations with two slightly different initial conditions showed that the oscillations are sensitive to the precise form of the initial conditions. Small initial unsteadiness is amplified by the continually increasing strain rate as the rings collide.

(6) Small core deformations were found to be as important to sound generation as bulk motion. In one instance of passage, the total radiated power is 6.8 times larger than that obtained by ignoring core oscillations (Dyson's model). These oscillations radiate significant power at a frequency equal to about half the vorticity. Peaks in laboratory jet noise spectra correspond to half the peak phase averaged vorticity for the preferred and jet-column modes suggesting that axisymmetric core deformation may be an important sound source. The oscillations were found to be sensitive to small changes in initial conditions. If the core shapes were initially chosen to be in equilibrium with respect to the induced strain, the radiated power was significantly reduced.

(7) When cores rotate rapidly compared to how fast they approach, which holds for thin rings, core shapes behave elastically in the sense that they remain near equilibrium with respect to the instantaneous induced field of the other vortex. For instance, in a head-on collision the shapes evolved through the family of two-dimensional

steadily propagating pairs. Similarly, in a passage interaction, the aspect ratio followed the equilibrium value, which relaxed to its initial value when the passage was complete. The motion was therefore nearly periodic. This behavior can be likened to that of a spring mass system; the length of the spring is like the aspect ratio and the value of gravity is analogous to the strain rate imposed by the other vortex. If the value of gravity changes slowly compared to the natural frequency of the system, the extension of the spring behaves quasi-statically. This is the concept of adiabatic invariance in the theory of differential equations with time varying Hamiltonian (Arnol'd 1978, p. 297), and its relevance to elliptic vortices in a strain field has been noted by Neu (1984, p. 2400). It is perhaps of interest to note that from the collision case simulated, it appears to also hold in the infinite degree of freedom case.

(8) For thick core passages, core rotation is slow compared to how rapidly the induced strain changes so that when the strain relaxes, the shape does not. The variation of strain due to the curved geometry is an essential effect that distinguishes the behavior of a pair of like-signed rings and a pair of two-dimensional corotating patches. It accounts for a greater susceptibility to vortex tearing in the former case. For example, one vortex ring captures part of another when the initial ratio of separation to area-effective core radius is 5, whereas in two dimensions convective merging occurs only when this ratio is less than 3.4 (Roberts & Christiansen 1972).

(9) For the collision of thick core rings, the cores initially flatten but subsequently a clumping phenomenon occurs whereby a "head" emerges, which has very nearly the shape of a two-dimensional steadily propagating vortex dipole, trailing a long thin tail. The head-tail structure agrees well with the flow visualization photographs of Oshima (1978a).

(10) When two rings collide, the energetics of the stretching process implies core deformation. In particular, simulations indicated that the formation of thin sheets takes place. In turbulence, a pair of three-dimensional vortex tubes, stretching due to their mutual induction, may generate fine scales for the same reason.

(11) The spectrum of the energy was computed in an effort to understand the relation of wavenumber space behavior to physical space dynamics. A simple vortex ring collision, without a hierarchy of physical scales, exhibited a rich energy spectrum. Energy was transferred out of low and into high wavenumbers. The dipolar head-tail structure of the core resulted in a $k^{2/3}$ range between the scales of the toroidal and

core radius, while the energy of each ring considered in isolation produced a $k^{-5/3}$ intermediate range.

(12) Tools from dynamical systems theory were applied to study the motion of fluid particles for two cases of unsteady time periodic vortex ring motion. In the first case, we have isolated rings of slender elliptic cross-section evolving according to Moore's (1980) solution. This case was intended to address tracer visualizations of "turbulent vortex rings." Turbulent vortex rings are admittedly more complicated. Nevertheless, many features observed in flow visualization are understood by this simple model. These include surface corrugations and fine scale streaks in the blob of tracer, the loss of dye from an initially marked ring, the trailing of a wake and entrainment from a patch of dye placed in the path of an unmarked ring. It therefore appears not necessary to posit the existence a shear layer at the interface through which the entrainment occurs. The view of a turbulent ring as consisting of a small scale turbulence within a core and large scale turbulence in the outer region which entrains and detrains environmental fluid is not the only one consistent with flow visualization. The alternate view is that Biot-Savart induction by the core unsteadiness itself is sufficient.

The second case was the alternate passage of one ring through another. Dyson's (1893) circular core model was applied to a case for which contour dynamics had shown it to be accurate. The structure of the computed unstable manifold agreed remarkably well the smoke photographs of Yamada & Matsui (1978) which appear to depict the deformation of the passing vortex and its wrapping around the front vortex. On the basis of this, a re-evaluation of previous interpretations of these photographs was suggested. The agreement with flow visualization photographs recommends the unstable manifold as a numerical flow visualization tool for other time periodic flows.

(13) Deviations from Moore's (1980) asymptotic solution for an isolated vortex ring having thin elliptic cross-section were studied. The deviations consisted of two parts. The aspect ratio oscillated with an amplitude that can be accounted for by the self-induced strain due to curvature. In addition the aspect ratio underwent a secular decline accompanied by growth of a non-elliptic mode. This is thought to be due to a parametric excitation by the primary periodic motion in the self-induced strain.

7.2. Recommendations for future work

(1) *Studies in two-dimensional contour dynamics with external strain.* The understanding of the behavior of thin core rings would benefit from added knowledge about the behavior of two-dimensional vortex patches subject to weak strains. This is so because, for thin cores the dynamics is locally two-dimensional but with a strain-like curvature correction. Two situations were encountered in this work where added knowledge of two-dimensional dynamics would have been welcome:

a) For the elliptical core vortex ring studied in §4.2.5, a possible mechanism for growth of the non-elliptic mode is parametric excitation. A relevant study in two-dimensions would be the stability of an elliptic vortex undergoing periodic motion on one of Neu's (1984) integral curves to non-elliptic perturbations. The observed instability suggests that the $m = 3$ mode (three waves along the apsidal angle) would be the most unstable one at the strain rate to vorticity ratios and aspect ratios considered.

b) How does the Sadovskii (1971) pair respond to straining? In collisions of thin rings, the cores have the shape of the Sadovskii pair at one instant (§5.2.1) but they cannot maintain this or any constant shape and conserve energy. This necessitates the deposition of vorticity in a thin trailing tail, according to a short time simulation. As a plausible mechanism we saw that the local flow tended to flatten the pair. Just as an initially flattened Hill's spherical vortex sheds a tail and forms again a spherical head (Moffatt & Moore 1978, Pozrikidis 1986), the two-dimensional pair would have a similar response when subjected to the strain due to curvature. i.e., distortions are swept to the rear of the vortex where they accumulate. The validity of this assertion needs to be tested.

(2) *Asymmetric collisions.* We need to study asymmetric collisions, both for cases in which the two vortices bind into a couple and the case where the two vortices separate to infinity.

a) For the case when the rings separate to infinity how is energy and impulse transferred between the vortices? This issue arose after a discussion with Prof. D.W. Moore in which he raised the possibility (suggested to him by T.B. Benjamin) that the final states would be steady. According to Benjamin's variational statement (§2.7.3), steady solutions have maximal energy given a fixed circulation and impulse. Benjamin's conjecture supposes that either there is no net transfer of impulse and energy or that it is just right to produce new maximals. This would be an intriguing

and surprising outcome for thick cores; thin ones may remain in equilibrium. It is more likely that each core will have its internal degrees of freedom excited. Does the resulting vortex then tend to a steady or periodic solution after forming wisps?

b) The Poincaré map was found useful in understanding flow visualization photographs but unfortunately it is limited to time periodic flows. As an extension of the idea, Jung (1986) has introduced the so-called scattering map which is valid when a flow has well defined initial and final states. Asymmetric collisions would be a good arena to test its usefulness. When two vortex rings approach one another, each carries a body of fluid. When they interact they will exchange fluid with each other and with the surroundings.

c) For the RLW equation (Lewis & Tjon 1979) symmetric collisions of solitons form a "resonant" condition in which small scale production is maximized. Do asymmetric collisions lead to lower small scale production than the symmetric collisions considered here?

(3) *Time periodic solutions.* Just as the problem of determining whether a pair of vortices in two dimensions coalesce has been approached by first considering the stability of steady configurations, the question of whether the passage of two vortex rings will lead (after a certain number of cycles) to capture is naturally addressed by considering stability of periodic solutions. The present results are specific to the initial conditions used i.e. cores initially having the shape of the Norbury-Fraenkel rings. Alternative initial conditions were hardly considered. There is no reason to believe that the results are generic. For example, there might be isolated points in the space of initial shapes which even for thick cores, allow a successful periodic passage without permanent deformation. Information about the existence and stability of two-vortex periodic solutions would provide a more global picture. Work in this direction should first be undertaken with the elliptical model of §4.2 and then with axisymmetric contour dynamics. Note that in the limit of thin cores and small separations the solutions would be the two-dimensional corotating pairs. Similarly, more families of time periodic solutions bifurcate from other two-dimensional rotating configurations.

For the foregoing discussion, we are indebted to S.K. Lele for pointing out the possibility of periodic cores in lieu of merely rotating ones.

(4) *Flow control.* The fact that even weak strains can excite or de-excite perturbations on a vortex core suggests a strategy employing a shroud with corrugated walls to break-up or stabilize vortex rings, jet and plane shear layer vortices in order to

control mixing and/or sound generation. A corrugated boundary produces a periodic straining on each vortex. Guidelines about the frequency and amplitude of the strain required to produce a desired result may be obtained from the elliptic model.

(5) *Untangle the manifolds for the passage interactions.* In the passage interaction, why does the unstable manifold bear such a striking resemblance to smoke photographs? To address this, the Lyapunov exponents of trajectories along the unstable manifold need to be computed to see if fluid is on average drawn out along it. The manifold was presented without much understanding of what it said about the motion of fluid parcels. The manifold needs to be calculated with adaptive resolution, untangled (i.e. its topology understood) and the successive mappings of fluid volumes needs to be studied in the manner of the elliptic ring case. This is needed to understanding the fluid engulfment process during vortex pairing in jets.

(6) *Role of axisymmetric core deformation in jet noise.* If the phenomena of broadband suppression and amplification are to be understood a more thorough study, than that provided here needs to be undertaken. Vortex spacings and core sizes should be chosen to mimic the shear-layer and jet-column modes (J. Bridges, private communication). The effect of initial conditions should be studied; as we have seen, they can have a large effect.

It would be of interest to experimentally verify whether axisymmetric deformed rings are efficient noise sources compared to azimuthal modes of small azimuthal wavenumber, the higher wavenumber Widnall instability and the breakdown that follows it. In the laboratory passage of one ring through another, is there a high frequency component of large amplitude present as suggested by the results in §5.1?

(7) *Long time simulations.* Two cases offer the possibility of realizing the scenario of vortices grinding down to a hierarchy of physical scales, each one a coherent state. First, a flattened Hill's vortex returns to a Hill's vortex by shedding a tail. Because the tail is a just a more flattened version of the initial state it may form another Hill's vortex and so on. Second, two colliding vortex rings flatten and then form a shape that is very nearly the limiting equilibrium shape for a translating pair of uniform vortices. We conjectured that an infinity of such states with a range of sizes may form. Long time simulations are needed to verify this. If true, it would be a most interesting cascade mechanism.

REFERENCES

- ACTON, E. 1980 A modelling of large eddies in an axisymmetric jet. *J. Fluid Mech.* **98**, 1-31.
- AITON, E.J. 1972 *The Vortex Theory of Planetary Motions*. MacDonald: London.
- ALLEN, G.A. JR. 1984 Transition and mixing in axisymmetric jets and vortex rings. Dept. of Aero. & Astro., Stanford Univ. SUDAAR Report 541 Also ALLEN, G.A. JR., Ph.D. thesis.
- AREF, H. 1983 Integrable, chaotic, and turbulent vortex motion in two-dimensional flows. *Ann. Rev. Fluid Mech.* **15**, 345-389.
- AREF, H. 1984 Stirring by chaotic advection. *J. Fluid Mech.* **143**, 1-21.
- AREF, H. & BALANCHANDAR, S. 1986 Chaotic advection in a Stokes flow. *Phys. Fluids* **29**, 3515-3521.
- ARNOL'D, V.I. 1965 Conditions for nonlinear stability of stationary plane curvilinear flows of an ideal fluid. *Soviet Math.-Doklady.* **6**, 773-777.
- ARNOL'D, V.I. 1978 *Mathematical Methods in Classical Mechanics*. Springer Verlag: New-York, Heidelberg, Berlin.
- BAKER, G.R. 1980 A test of the method of Fink & Soh for following vortex-sheet motion. *J. Fluid Mech.* **100**, 209-220.
- BASDEVANT, C., COUDER, Y. & SADOURNY, R. 1984 Vortices and vortex-couples in two-dimensional turbulence, or, Long-lived couples are Batchelor's couples. In *Lecture Notes in Physics*, vol. 230, pp. 327-346, Springer Verlag: New-York, Heidelberg, Berlin.
- BATCHELOR, G.K. 1956 A proposal concerning laminar wakes behind bluff bodies at large Reynolds number. *J. Fluid Mech.* **1**, 388-398.
- BATCHELOR, G.K. 1967 *An Introduction to Fluid Dynamics*. Cambridge University Press: Cambridge, England.
- BATCHELOR, G.K. 1973 *An Introduction to Fluid Dynamics*. First paperback edition. Cambridge University Press: Cambridge, England.
- BATISHCHEV, V.A. & SRUBSHCHIK, L.S. 1971 Diffusion of a spherical Hill vortex with vanishing viscosity. *Soviet Physics-Doklady.* **16**, 286-288.
- BENDER, C.M. & ORSZAG, S.A. 1978 *Advanced Mathematical Methods for Scientists and Engineers*. McGraw-Hill.
- BENJAMIN, T.B. 1962 Theory of the vortex breakdown phenomenon. *J. Fluid Mech.* **14**, 593-629.

- BENJAMIN, T.B. 1976 The alliance of practical and analytical insights into the non-linear problems of fluid mechanics. In *Applications of Methods of Functional Analysis to Problems in Mechanics* (ed. P. Germain & B. Nayroles), Lecture Notes in Mathematics, vol. 503, pp. 8–28, Springer Verlag: New-York, Heidelberg, Berlin.
- BERGER, M.S. & FRAENKEL, L.E. 1975 Global free boundary problems and the calculus of variations in the large. In *Applications of Methods of Functional Analysis to Problems in Mechanics* (ed. P. Germain & B. Nayroles), Lecture Notes in Mathematics, vol. 503, pp. 186–192, Springer Verlag: New-York, Heidelberg, Berlin.
- BIERENS DE HAAN, D. 1939 *Nouvelles Tables d'Integrales Définies*. G. E. Stechert & Co: New York.
- BLISS, D.B. 1973 The dynamics of flows with high concentrations of vorticity. Ph.D. thesis, Dept. Aero. & Astro., M.I.T.
- BROADBENT, E.G. & MOORE, D.W. 1979 Acoustic destabilization of vortices. *Phil. Trans. Roy. Soc. London A290*, 353–371.
- BROWN, G.L. & ROSHKO, A. 1974 On density effects and large structure in turbulent mixing layers. *J. Fluid Mech.* **64**, 775–816.
- BUCHWALD, J.D. 1976 Entry under Sir William Thomson in *Dictionary of Scientific Biography*. Charles Scribner's Sons: New York.
- BURBEA, J. 1980 Vortex motions and conformal mappings. In *Nonlinear Evolution Equations and Dynamical Systems* (ed. M. Boiti, F. Pempinelli & G. Soliani), Lecture Notes in Physics, vol. 120, pp. 276–298, Springer Verlag: New-York, Heidelberg, Berlin.
- BURBEA, J. 1981 On patches of uniform vorticity in a plane of irrotational flow. *Arch. Rational Mech. Anal.* **77**, 349–358.
- BURBEA, J. & LANDAU, M. 1982 The Kelvin waves in vortex dynamics and their stability. *J. Comp. Phys.* **45**, 127–156.
- BURBEA, J. 1983 Aerofoil-vortex in a rotational and strained field. *Proc. Roy. Soc. London A390*, 181–189.
- BYRD, P.F. & FRIEDMAN, M.D. 1971 *Handbook of Elliptic Integrals for Scientists and Engineers*. Springer Verlag: New-York, Heidelberg, Berlin.
- CANTWELL, B. 1986 Viscous starting jets. *J. Fluid Mech.* **173**, 159–189.
- CANTWELL, B.J. & ROTT, N. 1988 The decay of a viscous vortex pair. *Phys. Fluids* **31**, 3213–3224.
- CHAIKEN, J., CHEVRAY, R., TABOR, M. & TAN, Q.M. 1986 Experimental study of Lagrangian turbulence in a Stokes flow. *Proc. Roy. Soc. London A408*, 165–174.

- CHAIKEN, J., CHU, C.K., TABOR, M. & TAN, Q.M. 1987 Lagrangian turbulence and spatial complexity in a Stokes flow. *Phys. Fluids* **30**, 687-694.
- CHAMBERLAIN, J.P. & LIU, C.H. 1984 Navier-Stokes calculations for unsteady three-dimensional vortical flows in unbounded domains. A.I.A.A. Paper 84-0418, 22nd Aerospace Sciences Meeting.
- CHAPMAN, D.S. & CRITCHLOW, P.R. 1967 Formation of vortex rings from falling drops. *J. Fluid Mech.* **29**, 177-185.
- CHAHINE, G.L. & GENOUX, P.F. 1983 Collapse of a cavitating vortex ring. *J. Fluids Eng.* **105**, 400-405.
- CHEN, C.-J. & CHANG, L.-M. 1972 Flow patterns of a circular vortex ring with density differences under gravity. *J. Appl. Mech.* vol. 39, No. 4, *Trans. ASME*, vol. 94, Series E, pp. 869-872.
- CHIEN, W.-L., RISING, H. & OTTINO, J.M. 1986 Laminar mixing and chaotic mixing in several cavity flows. *J. Fluid Mech.* **170**, 355-377.
- CHORIN, A.J. & BERNARD, P.S. 1973 Discretization of a vortex sheet, with an example of roll-up. *J. Comp. Phys.* **13**, 423-29.
- CHOU, P.-Y. & HUANG, Y.-N. 1975 On the statistical vorticity structure theory of homogeneous isotropic turbulence. *Scientia Sinica* **18**, 199-222.
- CLARK, A.R. 1979 Ph.D. thesis, Univ. Houston.
- CODY, W.J. 1965 Chebyshev approximations for the complete elliptic integrals K and E . *Math. of Comp.* **19**, 105-112.
- COLES, D. 1965 Transition in circular Couette flow. *J. Fluid Mech.* **21**, 385-425.
- CRIGHTON, D.G. 1980 Jet noise and the effects of jet forcing. In *The Role of Coherent Structures in Modelling Turbulence and Mixing* (ed. J. Jimenez), Lecture Notes in Physics, vol. 136, pp. 340-362, Springer Verlag: New-York, Heidelberg, Berlin.
- CROW, S.C. 1970 Stability theory for a pair of trailing vortices. *A.I.A.A. J.* **8**, 2172-2179.
- DEEM, G.S. & ZABUSKY, N.J. 1978 Vortex waves: Stationary "V states," interactions, recurrence and breaking. *Phys. Rev. Lett.* **40**, 859-862.
- DIDDEN, N. 1977 Untersuchung laminarer instabiler Ringwirbel mittels Laser-Doppler-Anemometrie. Thesis, Univ. of Göttingen.
- DIDDEN, N. 1979 On the formation of vortex rings: Rolling-up and production of circulation. *J. Appl. Mech. and Phys. (ZAMP)* **30**, 101-116.
- DIDDEN, N. 1982 On vortex formation and interaction with solid boundaries. In *Vortex Motion* (ed. H.G. Hornung & E.-A. Müller), pp. 1-17, Friedr. Vieweg. & Sohn: Braunschweig/Wiesbaden.
- DIMOTAKIS, P.E. 1984 Entrainment into a fully developed two-dimensional shear layer. A.I.A.A. Paper 84-0368, 22nd Aerospace Sciences Meeting.

- DOMBRE, T., FRISCH, U., GREENE, J.M., HÉNON, M., MEHR, A. & SOWARD, A.M. 1986 Chaotic streamlines in the ABC flows. *J. Fluid Mech.* **167**, 353–391.
- DRITSCHEL, D.G. 1985 The stability and energetics of corotating uniform vortices. *J. Fluid Mech.* **157**, 95–134.
- DRITSCHEL, D.G. 1986 The non-linear evolution of rotating configurations of uniform vorticity. *J. Fluid Mech.* **172**, 157–182.
- DRITSCHEL, D.G. 1988a Nonlinear stability bounds for inviscid, two-dimensional, parallel or circular flows with monotonic vorticity, and the analogous three-dimensional quasi-geostrophic flows. *J. Fluid Mech.* **191**, 575–582.
- DRITSCHEL, D.G. 1988b Contour surgery: A topological reconnection scheme for extended integrations using contour dynamics. *J. Comp. Phys.* **77** (in press).
- DRITSCHEL, D.G. 1988c Contour dynamics/surgery on the sphere. *J. Comp. Phys.* (in press).
- DRITSCHEL, D.G. 1988d The repeated filamentation of two-dimensional vorticity interfaces. *J. Fluid Mech.* (in press).
- DRITSCHEL, D.G. 1988e On the stabilization of a two-dimensional vortex strip by adverse shear. Preprint.
- DRITSCHEL, D.G. 1988f The existence, stability, and nonlinear evolution of isolated, two-fold symmetric distributions of vorticity in an ideal, two-dimensional fluid. Preprint.
- DURST, F. & SCHÖNUNG, B. 1982 Computations of steady ellipsoidal vortex rings with finite cores. *Computers and Fluids* **10**, 87–93.
- DYSON, F.W. 1893 The potential of an anchor ring.—Part II. *Phil. Trans. Roy. Soc. London* **A184**, 1041–1106.
- ELDER, F.K. & DE HAAS, N. 1952 Experimental study of the formation of a vortex ring at the open end of a cylindrical shock tube. *J. Appl. Phys.* **23**, 1065–1069.
- EYDELAND, A. & TURKINGTON, B. 1988 A numerical study of vortex rings with swirl. Preprint submitted for publication.
- FOHL, T. & TURNER, J.S. 1975 Colliding vortex rings. *Phys. Fluids* **18**, 433–436.
- FORNBERG, B. 1988 Steady viscous flow past a sphere at high Reynolds numbers. *J. Fluid Mech.* **190**, 471–489.
- FRAENKEL, L.E. 1970 On steady vortex rings of small cross-section in an ideal fluid. *Proc. Roy. Soc. London* **A316**, 29–62.
- FRAENKEL, L.E. 1972 Examples of steady vortex rings of small cross-section in an ideal fluid. *J. Fluid Mech.* **51**, 119–135
- FRAENKEL, L.E. & BERGER, M.S. 1974 A global theory of steady vortex rings in an ideal fluid. *Acta Math.* **132**, 13–51.
- FRANKLIN, J.N. 1968 *Matrix Theory*. Prentice-Hall: Englewood Cliffs, New Jersey.

- FRIEDMAN, A. & TURKINGTON, B. 1981 Vortex rings: Existence and asymptotic estimates. *Trans. Am. Math. Soc.* **268**, 1–37.
- GLEZER, A. 1981 An experimental study of a turbulent vortex ring. Ph.D. thesis, Calif. Inst. Tech.
- GOLDSTEIN, S. (ed.) 1965 *Modern Developments in Fluid Dynamics*. Dover.
- GRADSHTEYN, I.S. & RYZHIK, I.M. 1980 *Table of Integrals, Series, and Products*. Academic Press: New York.
- GRAY, A.G. 1914 Notes on Hydrodynamics. II. Determination of translational velocity of a vortex ring of small cross-section. *The Lond., Edin., and Dub. Phil. Mag. and J. of Sci.* **28** (sixth series), 13–18.
- GREENGARD, C. & THOMANN, E. 1988 Vortons and weak solutions to the Euler equations. Preprint submitted for publication.
- GUCKENHEIMER, J. & HOLMES, P. 1983 *Nonlinear Oscillations, Dynamical Systems, and Bifurcations of Vector Fields*. Springer Verlag: New-York, Heidelberg, Berlin.
- GUCKENHEIMER, J. & HOLMES, P. 1983 *Nonlinear Oscillations, Dynamical Systems, and Bifurcations of Vector Fields*. Springer Verlag: New-York, Heidelberg, Berlin.
- HADAMARD, J. 1954 *The Psychology of Invention in the Mathematical Field*. Dover.
- HAMA, F.R. 1962 Progressive deformation of a curved vortex filament by its own induction. *Phys. Fluids* **5**, 1156–1162.
- HARPER, J.F. & MOORE, D.W. 1968 The motion of a spherical liquid drop at high Reynolds number. *J. Fluid Mech.* **32**, 367–391.
- HAVELOCK, T.H. 1931 The stability of motion of rectilinear vortices in ring formation. *The Lond., Edin., and Dub. Phil. Mag. and J. of Sci.* **11** (seventh series), 617–633.
- HEBERT, D.J. 1983 A Hamiltonian–Lagrangian system of vortex boundary curves. *J. Math. Phys.* **24**, 1672–1678.
- HEILBRON, J.L. 1976 Entry under Joseph John Thomson in *Dictionary of Scientific Biography*. Charles Scribner's Sons: New York.
- HELMHOLTZ, H. 1858 Translated in TAIT, P.G. 1867 On integrals of the hydrodynamical equations which express vortex-motion. *The Lond., Edin., and Dub. Phil. Mag. and J. of Sci.* **33** (fourth series), 485–512.
- HICKS, W.M. 1884 On the steady motion and small vibrations of a hollow vortex. *Phil. Trans. Roy. Soc. London* **A175**, 161–195.
- HICKS, W.M. 1885 Researches on the theory of vortex rings.—Part II. *Phil. Trans. Roy. Soc. London* **A176**, 725–780.
- HILL, M.J.M. 1894 On a spherical vortex. *Phil. Trans. Roy. Soc. London* **A185**, 213–245.

- HORNUNG, H.G. 1988 Vorticity generation and secondary flows. A.I.A.A. Paper 88-3751-CP. In *Proc. AIAA/ASME/SIAM/APS First Nat. Fluid Dyn. Cong.*, pp. 566-571.
- HOWE, M.S. 1983 On the scattering of sound by a vortex ring. *J. Sound Vib.* 87, 567-571.
- HUSSAIN, A.K.M.F. 1980 Coherent structures and studies of perturbed and unperturbed jets. In *The Role of Coherent Structures in Modelling Turbulence and Mixing* (ed. J. Jimenez), Lecture Notes in Physics, vol. 136, pp. 252-291, Springer Verlag: New-York, Heidelberg, Berlin.
- HUSSAIN, A.K.M.F. & ZAMAN, K.B.M.Q. 1980 Vortex pairing in a circular jet under controlled excitation. Part 2. Coherent structure dynamics. *J. Fluid Mech.* 101, 493-544.
- HUSSAIN, A.K.M.F. & ZAMAN, K.B.M.Q. 1981 The 'preferred mode' of the axisymmetric jet. *J. Fluid Mech.* 110, 39-71.
- HUSSAIN, A.K.M.F. 1983 Coherent structures—reality and myth. *Phys. Fluids* 26, 2816-2850.
- JACOBS, P.A. & PULLIN, D.I. 1985 Coalescence of stretching vortices. *Phys. Fluids* 28, 1619-1625.
- JAWSON, M.A. & SYMM, G.T. 1977 *Integral Equation Methods in Potential Theory and Elastostatics*. Academic Press: New York.
- JIMENEZ, J. 1986a On the linear stability of the inviscid Kármán vortex street. *J. Fluid Mech.* 178, 177-194.
- JIMENEZ, J. 1986b Linear stability of a non-symmetric Kármán street of small uniform vortices. Preprint.
- JUNG, C. 1986 Poincaré map for scattering states. *J. Phys.* A19, 1345-53.
- KAMBE, T. & OSHIMA, Y. 1975 Generation and decay of viscous vortex rings. *J. Phys. Soc. Japan* 38, 271-280.
- KAMBE, T. & MURAKAMI, T. 1979 Sound generation by head-on collision of two vortex rings. In *Mechanics of Sound Generation in Flows*. (ed. E.-A. Müller), pp. 123-129. Springer Verlag: New-York, Heidelberg, Berlin.
- KAMBE, T. & MYA OO, U 1981 Scattering of sound by a vortex ring. *J. Phys. Soc. Japan* 50, 3507-3516.
- KAMBE, T. & MINOTA, T. 1981 Sound generation from vortex systems. *J. Sound Vib.* 74, 61-72.
- KAMBE, T. & MYA OO, U. 1982 Numerical analysis of an axisymmetric viscous flow. *Memoirs Fac. Engr., Kyushu Univ.* 42, 371-388.
- KAMBE, T. & MINOTA, T. 1983 Acoustic wave radiated by head-on collision of two vortex rings. *Proc. Roy. Soc. London* A386, 277-308.

- KAMBE, T. & MYA OO, U. 1984 An axisymmetric viscous vortex motion and its acoustic emission. *J. Phys. Soc. Japan* **53**, 2263–2273.
- KAMBE, T. 1984 Axisymmetric vortex solution of the Navier-Stokes equation. *J. Phys. Soc. Japan* **53**, 13–15.
- KAMBE, T. 1986 Acoustic emissions by vortex motions. *J. Fluid Mech.* **173**, 643–666.
- KAMM, J.R. 1987 Shape and stability of two-dimensional uniform vorticity regions. Ph.D. thesis, Calif. Inst. Tech.
- KELVIN, LORD (THOMSON, W.) 1867 On vortex atoms. *The Lond., Edin., and Dub. Phil. Mag. and J. of Sci.* **34**, 15–24.
- KELVIN, LORD (THOMSON, W.) 1880a Vortex statics. *The Lond., Edin., and Dub. Phil. Mag. and J. of Sci.* **10** (fifth series), 97–109.
- KELVIN, LORD (THOMSON, W.) 1880b Vibrations of a columnar vortex. *The Lond., Edin., and Dub. Phil. Mag. and J. of Sci.* **10** (fifth series), 155–168.
- KHAKHAR, D.V., RISING, H. & OTTINO, J.M. 1986 Analysis of chaotic mixing in two model systems. *J. Fluid Mech.* **172**, 419–451.
- KIDA, S. 1981 Motion of an elliptic vortex in a uniform shear flow. *J. Phys. Soc. Japan* **50**, 3517–3520.
- KIDA, S. 1982 Stabilizing effect of finite core on Kármán vortex street. *J. Fluid Mech.* **122**, 487–504.
- KIMURA, Y. 1988 Ph.D. thesis, Univ. Tokyo.
- KITAPLIOGLU, C. & KIBENS, V. 1980 Discrete vortex modeling of an axisymmetric jet flowfield. A.I.A.A. Paper 80-1003, 6th Aeroacoustics Conference.
- KOCHIN, N.E., KIBEL', I.A. & ROZE, N.V. 1964 *Theoretical Hydromechanics*, Wiley Interscience.
- KRASNY, R. 1987 Computation of vortex sheet roll-up in the Trefftz plane. Preprint submitted for publication.
- KRUTZSCH, C.-H. 1939 Über eine experimentell beobachtete Erscheinung an Wirbelringen bei ihrer translatorischen Bewegung in wirklichen Flüssigkeiten. *Annalen der Physik* **35**, 497–523.
- KÜCHEMANN, D. 1965 Report on the I.U.T.A.M. symposium on concentrated vortex motions in fluids. *J. Fluid Mech.* **21**, 1–20.
- LAMB, SIR H. 1932 *Hydrodynamics*. Dover.
- LEISS, C. & DIDDEN 1976 *Zeitschrift der angewandte Mathematik und Mechanik* **56**, T206.
- LEITH, C.E. 1984 Minimum enstrophy vortices. *Phys. Fluids* **27**, 1388–1395.
- LEONARD, A. 1980 Vortex methods for flow simulation. *J. Comp. Phys.* **37**, 289–335.

- LEONARD, A. 1985 Computing three-dimensional incompressible flows with vortex elements. *Ann. Rev. Fluid Mech.* **17**, 523-559.
- LEONARD, A., ROM-KEDAR, V. & WIGGINS, S. 1987 Fluid mixing and dynamical systems. To appear in *Nuclear Physics B* as the Proc. of the Chaos 87 Meeting in Monterey.
- LIGHTHILL, M.J. 1952 On sound generated aerodynamically. I. General theory. *Proc. Roy. Soc. London A* **211**, 564-587.
- LILLY, J.C. 1972 *The Center of the Cyclone*. Julian Press: New York.
- LIN, S.J. & CORCOS, G.M. 1984 The mixing layer: deterministic models of a turbulent flow. Part 3. The effect of plane strain on the dynamics of streamwise vortices. *J. Fluid Mech.* **141**, 139-178.
- LEWIS, J.C. & TJON, J.A. 1979 Resonant production of solitons in the RLW equation. *Phys. Lett.* **73A**, 275-279.
- LIN, C.C. 1955 *The Theory of Hydrodynamic Stability*. Cambridge University Press: Cambridge, England.
- LIGHTHILL, M.J. 1966 Dynamics of rotating fluids: a survey. *J. Fluid Mech.* **26**, 411-431.
- LINDMAN, C.F. 1944 *Examen des Nouvelles Tables d'integrales Définies de M. Bierens de Haan*. G. E. Stechert & Co: New York.
- LIU, C.H. & TING, L. 1982 Numerical solution of viscous flow in unbounded fluid. In *Eighth International Conference on Numerical Methods in Fluid Mechanics* (ed. E. Krause), Lecture Notes in Physics, vol. 170, pp. 357-363, Springer Verlag: New-York, Heidelberg, Berlin.
- LOVE, A.E.H. 1893 On the stability of certain vortex motions. *Proc. Lond. Math. Soc.* **25** (first series), 18-42.
- LOVE, A.E.H. 1894 On the motion of paired vortices with a common axis. *Proc. Lond. Math. Soc.* **25** (first series), 185-194.
- LUNDGREN, T.S. 1982 Strained spiral vortex model for turbulent fine structure. *Phys. Fluids* **25**, 2193-2203.
- LUNDGREN, T.S. & ASHURST, W.T. 1988 Area varying waves on curved vortex tubes. *J. Fluid Mech.* (to appear).
- LUGT, H.J. 1983 *Vortex Flow in Nature and Technology*. John Wiley and Sons.
- MACKEY, R.S., MEISS, J.D. & PERCIVAL, I.C. 1984 Transport in Hamiltonian systems. *Physica D* **13**, 55-81.
- MARRIS, A.W. & ASWANI, M.G. 1977 On the general impossibility of controllable axi-symmetric Navier Stokes motions. *Arch. Rational Mech. Anal.* **63**, 107-153.
- MAXWORTHY, T. 1972 The structure and stability of vortex rings. *J. Fluid Mech.* **51**, 15-32.

- MAXWORTHY, T. 1974 Turbulent vortex rings (with an appendix on an extended theory of laminar vortex rings). *J. Fluid Mech.* **64**, 227–239.
- MAXWORTHY, T. 1977 Some experimental studies of vortex rings. *J. Fluid Mech.* **81**, 465–495.
- MAXWORTHY, T. 1979 Comments on “Preliminary study of mutual slip-through of a pair of vortices.” *Phys. Fluids* **22**, 200.
- MCWILLIAMS, J.C. & ZABUSKY, N.J. 1982 Interactions of isolated vortices. I. Modons colliding with modons. *Geophys. Astrophys. Fluid Dyn.* **19**, 207–227.
- MCWILLIAMS, J. 1983 Interactions of isolated vortices. II. Modon generation by monopole collision. *Geophys. Astrophys. Fluid Dyn.* **24**, 1–22.
- MCWILLIAMS, J.C. 1984 The emergence of isolated coherent vortices in turbulent flow. *J. Fluid Mech.* **146**, 21–43.
- MEIRON, D.I., SAFFMAN, P.G. & SCHATZMAN, J.C. 1984 The linear two-dimensional stability of inviscid vortex streets of finite cored vortices. *J. Fluid Mech.* **147**, 187–212.
- MELANDER, M.V., STYCZEK, A.S. & ZABUSKY, N.J. 1984 Elliptically desingularized vortex model for the two-dimensional Euler equations. *Phys. Rev. Lett.* **53**, 1222–1225.
- MELANDER, M.V., ZABUSKY, N.J. & STYCZEK, A.S. 1986 A moment model for vortex interactions of the two-dimensional Euler equations. Part 1. Computational validation of a Hamiltonian elliptical representation. *J. Fluid Mech.* **167**, 95–115.
- MELANDER, M.V., OVERMAN, E.A. II & ZABUSKY, N.J. 1987 Computational vortex dynamics in two and three dimensions. *Appl. Num. Math.* **3**, 59–80.
- MELANDER, M.V., MCWILLIAMS, J.C. & ZABUSKY, N.J. 1987 Axisymmetrization and vorticity gradient intensification of an isolated two-dimensional vortex through intensification. *J. Fluid Mech.* **178**, 137–159.
- MELANDER, M.V. & ZABUSKY, N.J. 1987 Interaction and “apparent” reconnection of 3D vortex tubes via direct numerical simulations. *Fluid Dyn. Res.* **3**, 247–250.
- MELANDER, M.V., ZABUSKY, N.J. & MCWILLIAMS, J.C. 1988 Symmetric vortex merger in two dimensions: Causes and conditions. *J. Fluid Mech.* **195**, 303–340.
- MICHALKE, A. Some remarks on source coherence affecting jet noise. *J. Sound Vib.* **87**, 1–17.
- MINAHEN, C.D. 1983 Hermeneutics of the vortex-structure in symbolist aesthetics: Phenomenology of a symbol as a symbol. Ph.D. thesis, Dept. of French and Italian, Stanford Univ.
- MOFFATT, H.K. 1969 The degree of knottedness of tangled vortex lines. *J. Fluid Mech.* **35**, 117–129.

- MOFFATT, H.K. 1978 *Magnetic Field Generation in Electrically Conducting Fluids*. Cambridge University Press: Cambridge, England.
- MOFFATT, H.K. & MOORE, D.W. 1978 The response of Hill's spherical vortex to a small axisymmetric disturbance. *J. Fluid Mech.* **87**, 749-760.
- MOFFATT, H.K. 1985 Magnetostatic equilibria and analogous Euler flows of arbitrarily complex topology. *J. Fluid Mech.* **159**, 359-378.
- MOFFATT, H.K. 1986 On the existence of localized rotational disturbances which propagate without change of structure in an inviscid fluid. *J. Fluid Mech.* **173**, 289-302.
- MOFFATT, H.K. 1988 Generalised vortex rings with and without swirl. *Fluid Dyn. Res.* **3**, 22-30.
- MÖHRING, W. 1978 On vortex sound at low Mach Number. *J. Fluid Mech.* **85**, 685-691.
- MOORE, C.J. 1977a The role of shear-layer instability waves in jet-exhaust noise. *J. Fluid Mech.* **80**, 321-367.
- MOORE, C.J. 1977b Shear layer instability noise produced by various jet nozzle configurations. In *Mechanics of Sound Generation in Flows* (ed. E.-A. Müller), pp. 48-54. Springer Verlag: New-York, Heidelberg, Berlin.
- MOORE, D.W. & GRIFFITH-JONES, R. 1974 The stability of an expanding circular vortex sheet. *Mathematika* **21**, 128-133.
- MOORE, D.W. & SAFFMAN, P.G. 1971 Structure of a line vortex in an imposed strain. In *Aircraft Turbulence and Wakes* (ed. Olsen, Goldberg & Rogers), pp. 339-354. Plenum.
- MOORE, D.W. & SAFFMAN, P.G. 1972 The motion of a vortex filament with axial flow. *Phil. Trans. Roy. Soc. London A272*, 403-429.
- MOORE, D.W. & SAFFMAN, P.G. 1973 Axial flow in laminar trailing vortices. *Proc. Roy. Soc. London A333*, 491-508.
- MOORE, D.W. & SAFFMAN, P.G. 1974 A note on the stability of a vortex ring of small cross-section. *Proc. Roy. Soc. London A338*, 535-537.
- MOORE, D.W. & SAFFMAN, P.G. 1975a The density of organized vortices in a turbulent mixing layer. *J. Fluid Mech.* **69**, 465-473.
- MOORE, D.W., & SAFFMAN, P.G. 1975b The instability of a straight vortex filament in a strain field. *Proc. Roy. Soc. London A346*, 413-425.
- MOORE, D.W. 1979 Vortex motion. *Inaugural Lect. Imp. Coll. Sci.* **10**, 115-124. Lecture delivered on January 13, 1976.
- MOORE, D.W. 1980 The velocity of a vortex ring with a thin core of elliptical cross-section. *Proc. Roy. Soc. London A370*, 407-415.
- MOORE, D.W. 1985 The effect of compressibility on the speed of propagation of a vortex ring. *Proc. Roy. Soc. London A397*, 87-97.

- MORTON, W.B. 1913 On the displacements of the particles and their paths in some cases of two-dimensional motion of a frictionless liquid. *Proc. Roy. Soc. London* **A89**, 106–124.
- MÜLLER, E.-A. & OBERMEIER, F. 1988 Vortex sound. *Fluid Dyn. Res.* **3**, 43–51.
- NEU, J.C. 1984 The dynamics of a columnar vortex in an imposed strain. *Phys. Fluids* **27**, 2397–2402.
- NORBURY, J. 1972 A steady vortex ring close to Hill's spherical vortex. *J. Fluid Mech.* **72**, 253–284.
- NORBURY, J. 1973 A family of steady vortex rings. *J. Fluid Mech.* **57** 417–431.
- O'BRIEN, V. 1961 Steady spheroidal vortices—more exact solutions to the Navier-Stokes equations. *Q. Appl. Math.* **19**, 163–168.
- OKABE, J. & INOUE, S. 1961 The generation of vortex rings II. *Rep. Res. Inst. Appl. Mech., Kyushu Univ.* **9**, 147–161.
- OSHIMA, Y., KAMBE, T. & ASAKA, S. 1975 Interaction of two vortex rings moving along a common axis of symmetry. *J. Phys. Soc. Japan* **38**, 1159–1166.
- OSHIMA, Y. & ASAKA, S. 1977 Interaction of two vortex rings along parallel axes in air. *J. Phys. Soc. Japan* **42**, 708–713.
- OSHIMA, Y. 1978a Head-on collision of two vortex rings. *J. Phys. Soc. Japan* **44**, 328–331.
- OSHIMA, Y. 1978b The game of passing-through of a pair of vortex rings. *J. Phys. Soc. Japan* **45**, 660–664.
- OVERMAN, E.A. II, & ZABUSKY, N.J. 1982a Coaxial scattering of Euler-equation translating V-states via contour dynamics. *J. Fluid Mech.* **125**, 187–202.
- OVERMAN, E.A. & ZABUSKY, N.J. 1982b Evolution and merger of isolated vortex structures. *Phys. Fluids* **25**, 1297–1305.
- PEREGRINE, D.H. 1981 The fascination of fluid mechanics. *J. Fluid Mech.* **106**, 59–80.
- PERRY, A.E., HENBEST, S. & CHONG, M.S. 1986 A theoretical and experimental study of wall turbulence. *J. Fluid Mech.* **165**, 163–199.
- PHILLIPS, O.M. 1956 The final period of decay of non-homogeneous turbulence. *Proc. Camb. Phil. Soc.* **52**, 135–151.
- PIERREHUMBERT, R.T. 1980 A family of steady, translating vortex pairs with distributed vorticity. *J. Fluid Mech.* **99**, 129–144.
- PIERREHUMBERT, R.T. 1981 Corrigendum, A family of steady, translating vortex pairs with distributed vorticity. *J. Fluid Mech.* **102**, 478.
- PIERREHUMBERT, R.T. & WIDNALL, S.E. 1981 The structure of organized vortices in a free shear layer. *J. Fluid Mech.* **102**, 301–313.

- POCKLINGTON, H.C. 1895 The complete system of periods of a hollow vortex ring. *Phil. Trans. Roy. Soc. London A* **186**, 603-619.
- POZRIKIDIS, C. & HIGDON, J.J.L. 1985 Nonlinear Kelvin-Helmholtz instability of a finite vortex layer. *J. Fluid Mech.* **157**, 225-263.
- POZRIKIDIS, C. 1986 The non-linear instability of Hill's vortex. *J. Fluid Mech.* **168**, 337-367.
- PRENDERGAST, K.H. 1956 The equilibrium of a self-gravitating incompressible fluid sphere with a magnetic field. I. *Astrophys. J.* **123**, 498-507.
- PULLIN, D.I. 1979 Vortex ring formation at tube and orifice openings. *Phys. Fluids* **22**, 401-403.
- PULLIN, D.I. 1981 The nonlinear behaviour of a constant vorticity layer at a wall. *J. Fluid Mech.* **108**, 401-421.
- PULLIN, D.I. & JACOBS, P.A. 1986 Inviscid evolution of stretched vortex arrays. *J. Fluid Mech.* **171**, 377-406.
- PUMIR, A. & KERR, R.M. 1987 Numerical simulation of interacting vortex tubes. *Phys. Rev. Lett.* **58**, 1636-1639.
- RAYFIELD, G.W. & REIF, F. 1963 Evidence for the creation and motion of quantized vortex rings in superfluid helium. *Phys. Rev. Lett.* **11**, 305-308.
- RAYLEIGH, LORD 1945 *Theory of Sound*. Dover.
- REYNOLDS, O. 1876 *Nature*, **14**, 477.
- ROBERTS, P.H. 1972 A Hamiltonian theory for weakly interacting vortices. *Mathematika* **19**, 169-179.
- ROBERTS, K.V. & CHRISTIANSEN, J.P. 1972 Topics in computational fluid mechanics. *Computer Phys. Commun.* **3** (suppl.), 14-32.
- ROBINSON, A.C. & SAFFMAN, P.G. 1984 Three-dimensional stability of an elliptical vortex in a straining field. *J. Fluid Mech.* **142**, 451-466.
- ROGERS, W.B. 1858 On the formation of rotating rings by air and liquids under certain conditions of discharge. *Am. J. Sci. and the Arts* **26** (second series), 246-258.
- ROM-KEDAR, V., LEONARD, A. & WIGGINS, S. 1988 An analytical study of transport, mixing and chaos in an unsteady flow. Preprint submitted for publication.
- ROTT, N. & CANTWELL, B.J. 1988 Asymptotic vortex drift. Preprint submitted for publication.
- SADOVSKII, V.S. 1971 Vortex regions in a potential stream with a jump of Bernoulli's constant at the boundary. *Prikladnaia matematika i mekhanika* **35**, 773-779.
- SAFFMAN, P.G. 1970 The velocity of viscous vortex rings. *Stud. Appl. Math.* **49**, 371-380.

- SAFFMAN, P.G. 1975 On the formation of vortex rings. *Stud. Appl. Math.* **54**, 261-268.
- SAFFMAN, P.G. 1978 The number of waves on unstable vortex rings. *J. Fluid Mech.* **84**, 625-639.
- SAFFMAN, P.G. 1979 The approach of a vortex pair to a plane surface in inviscid fluid. *J. Fluid Mech.* **92**, 497-503.
- SAFFMAN, P.G. & SZETO, R. 1980 Equilibrium shapes of a pair of equal uniform vortices. *Phys. Fluids* **23**, 2339-2342.
- SAFFMAN, P.G. & SZETO, R. 1981 Structure of a linear array of uniform vortices. *Stud. Appl. Math.* **65**, 223-248.
- SAFFMAN, P.G. 1981a Dynamics of vorticity. *J. Fluid Mech.* **106**, 49-58.
- SAFFMAN, P.G. 1981b Coherent structures in turbulent flow. In *The Role of Coherent Structures in Modelling Turbulence and Mixing* (ed. J. Jimenez), Lecture Notes in Physics, vol. 136, pp. 1-9, Springer Verlag: New-York, Heidelberg, Berlin.
- SAFFMAN, P.G. & SCHATZMAN, J.C. 1981 Properties of a vortex street of finite vortices. *SIAM J. Sci. Stat. Comp.* **2**, 285-295.
- SAFFMAN, P.G. & SCHATZMAN, J.C. 1982 Stability of a vortex street of finite vortices. *J. Fluid Mech.* **117**, 171-185.
- SAFFMAN, P.G. 1982 Structure and stability of streets of finite vortices. In *Vortex Motion* (ed. H.G. Hornung & E.-A. Müller), pp. 142-153, Friedr. Vieweg. & Sohn: Braunschweig/Wiesbaden.
- SAFFMAN, P.G. & TANVEER, S. 1982 The touching pair of equal and opposite uniform vortices. *Phys. Fluids* **25**, 1929-1930.
- SAFFMAN, P.G. 1988 The stability of vortex arrays to two- and three-dimensional disturbances. *Fluid Dyn. Res.* **3**, 13-21.
- SALLET, D.W. & WIDMAYER, R.S. 1974 An experimental investigation of laminar and turbulent vortex rings in air. *Z. Flugwiss.* **22**, 207-215.
- SCHATZLE, P.R. 1987 An experimental study of fusion of vortex rings. Ph.D. thesis, Calif. Inst. Tech.
- SHELLEY, M.J. 1985 The motion of vortex layers. *Bull. Am. Phys. Soc.* **30**, 1745.
- SIGGIA, E.D. & PUMIR, A. 1987 Vortex dynamics and the existence of solutions to the Navier-Stokes equations. *Phys. Fluids* **30**, 1606-1626.
- SNOW, J.T. 1978 On inertial instability as related to the multiple-vortex phenomenon. *J. Atmos. Sci.* **35**, 1660-1667
- SOMMERFELD, A. 1950 *Mechanics of Deformable Bodies*. Academic Press: New York.
- SQUIRE, H.B. & WINTER, K.G. 1951 The secondary flow in a cascade of aerofoils in a non-uniform stream. *J. Aero. Sci.* **18**, 271-277.

- STANAWAY, S., CANTWELL, B.J. & SPALART, P.R. 1986 A full simulation of a vortex ring. In *Proc. Ninth Australasian Fluid Mech. Conf.*, Auckland, New Zealand, pp. 362–366. Also, Dept. of Aero. & Astro., Stanford Univ. SUDAAR Report 560.
- STANAWAY, S.K., CANTWELL, B.J. & SPALART, P.R. 1988a A numerical study of viscous vortex rings using a spectral method. NASA TM 101004. Also STANAWAY, S.K., Ph.D. thesis, Dept. of Aero. & Astro., Stanford Univ.
- STANAWAY, S.K., CANTWELL, B.J. & SPALART, P.R. 1988b Navier-Stokes simulations of axisymmetric vortex rings. A.I.A.A. Paper 88-0318, 26th Aerospace Sciences Meeting.
- STUART, J.T. 1967a Hydrodynamic stability of fluid flows. *Inaugural Lect. Imp. Coll. Sci.*, 109–130, Lecture delivered on November 14, 1967.
- STUART, J.T. 1967b On finite amplitude oscillations in laminar mixing layers. *J. Fluid Mech.* **29**, 417–440.
- STURTEVANT, B. & KULKARNY, V. 1978 Dynamics of vortices and shock waves in non-uniform media. AFOSR-TR-78-1403, Available from Defence Technical Information Service, Govt. Accession. No. AD-A060359, Fiche N79-15002.
- STURTEVANT, B. 1979 Dynamics of vortices and shock waves in nonuniform media. AFOSR-TR-79-0898, Available from Defense Technical Information Service, Govt. Accession. No. AD-A072842, Fiche N80-15366.
- STURTEVANT, B. & OSTBO, T. 1979 Dynamics of vortex rings. Project summary in *Caltech. Division of Engineering and Applied Science Report: 1979-80, 1980-81*, p. 5.
- STURTEVANT, B. 1981 Dynamics of turbulent vortex rings. AFOSR-TR-81-0400, Available from Defense Technical Information Service, Govt. Accession. No. AD-A098111, Fiche N81-24027.
- SU, C.H. 1979 Motion of fluid with constant vorticity in a singly connected region. *Phys. Fluids* **22**, 2032–2033.
- SULLIVAN, J.P., WIDNALL, S.E. & EZEKIEL, S. 1973 Study of vortex rings using a laser doppler velocimeter. *A.I.A.A. J.* **11**, 1384–1389.
- SYNGE, J.L. & LIN, C.C. 1943 On a statistical model of isotropic turbulence. *Trans. Roy. Soc. Canada*, 3rd Ser. Sec. III, **37**, 45–79.
- TAIT, P.G. 1867 On integrals of the hydrodynamical equations which express vortex-motion. Transl. of Helmholtz (1858). *The Lond., Edin., and Dub. Phil. Mag. and J. of Sci.* **33** (fourth series), 485–512.
- TANG, Y. 1985 Nonlinear stability of vortex patches. Ph.D. thesis, State Univ. New York at Buffalo.
- TENG, Z.-H. 1982 Elliptic vortex method for incompressible flow at high Reynolds number. *J. Comp. Phys.* **46**, 54–68.

- THOMPSON, J.M.T. & STEWART, H.B. 1986 *Nonlinear Dynamics and Chaos*. John Wiley and Sons.
- THOMSON, J.J. 1883 *A Treatise on the Motion of Vortex Rings*. Macmillan and Co.: London.
- THOMSON, J.J. & NEWALL, H.F. 1885 On the formation of vortex rings by drops falling into liquids, and some allied phenomena. *Proc. Roy. Soc. London A39*, 417-436.
- TOWNSEND, A.A. 1951 On the fine-scale structure of turbulence. *Proc. Roy. Soc. London A208*, 534-542.
- TSAI, C.-Y. & WIDNALL, S.E. 1976 The stability of short waves on a straight vortex filament in weak externally imposed strain field. *J. Fluid Mech.* **73**, 721-733.
- TUNG, C. & TING, L. 1967 Motion and decay of a vortex ring. *Phys. Fluids* **10**, 901.
- TURKINGTON, B. 1986 Vortex rings with swirl: axisymmetric solutions of the Euler equations with nonzero helicity. *SIAM J. Math. Anal.* (to appear).
- VAN DYKE, M. 1982 *An Album of Fluid Motion*. The Parabolic Press: Stanford, Calif.
- VON KÁRMÁN, T. 1967 *The Wind and Beyond*. Little, Brown and Co: Boston, Toronto.
- WALTERS, J.K. & DAVIDSON, J.F. 1963 The initial motion of a gas bubble formed in an inviscid liquid. *J. Fluid Mech.* **17**, 321-336.
- WIDNALL, S.E. & BLISS, D. 1971 Slender body analysis of the motion and stability of a vortex filament containing an axial flow. *J. Fluid Mech.* **50**, 335.
- WIDNALL, S.E., BLISS, D.B. & TSAI, C.-Y. 1974 The instability of short waves on a vortex ring. *J. Fluid Mech.* **66**, 35-47.
- WIDNALL, S.E. & SULLIVAN, J.P. 1973 On the stability of vortex rings. *Proc. Roy. Soc. London A332*, 335-353.
- WIDNALL, S.E. 1975 The structure and dynamics of vortex filaments. *Ann. Rev. Fluid Mech.* **7**, 141-165.
- WIDNALL, S.E. & TSAI, C.-Y. 1977 The instability of the thin vortex ring of constant vorticity. *Phil. Trans. Roy. Soc. London A287*, 273-305.
- WINANT, C.D. & BROWAND, F.K. 1974 Vortex pairing: The mechanism of turbulent mixing-layer growth at moderate Reynolds number. *J. Fluid Mech.* **63**, 237-255.
- WINTERFELD, G. 1965 On processes of turbulent exchange behind flame holders. In *Tenth Symposium on Combustion.*, pp. 1265-1275, The Combustion Institute: Pittsburgh.

- WU, H.M., OVERMAN, E.A. II & ZABUSKY, N.J. 1984 Steady-state solutions of the Euler equations in two dimensions: Rotating and translating V -states with limiting cases I. Numerical algorithms and results. *J. Comp. Phys.* **53**, 42-71.
- YAMADA, H. & MATSUI, T. 1978 Preliminary study of mutual slip-through of a pair of vortices. *Phys. Fluids* **21**, 292-294.
- YAMADA, H. & MATSUI, T. 1979 Mutual slip-through of a pair of vortex rings. *Phys. Fluids* **22**, 1245-1249.
- ZABUSKY, N.J., HUGHES, M.H. & ROBERTS, K.V. 1979 Contour dynamics for the Euler equations in two dimensions. *J. Comp. Phys.* **30**, 96-106.
- ZABUSKY, N.J. 1981 Computational synergetics and mathematical innovation. *J. Comp. Phys.* **43**, 195-249.
- ZABUSKY, N.J. & OVERMAN, E.A. II 1983 Regularization of contour dynamical algorithms. I. Tangential regularization. *J. Comp. Phys.* **52**, 351-373.
- ZAMAN, K.B.M.Q. 1985 Far-field noise of a subsonic jet under controlled excitation. *J. Fluid Mech.* **152**, 83-111.
- ZAMAN, K.B.M.Q. & HUSSAIN, A.K.M.F. 1980 Vortex pairing in a circular jet under controlled excitation. Part 1. General jet response. *J. Fluid Mech.* **101**, 449-491.
- ZAMAN, K.B.M.Q. & HUSSAIN, A.K.M.F. 1984 Natural large-scale structures in the axisymmetric mixing layer. *J. Fluid Mech.* **138**, 325-351.
- ZOU, Q., OVERMAN, E.A. II, WU, H.-M. & ZABUSKY, N.J. 1988 Contour dynamics for the Euler equations: Curvature controlled initial node placement and accuracy. *J. Comp. Phys.* **78**, 350-368.



Report Documentation Page

1. Report No. NASA TM-102257	2. Government Accession No.	3. Recipient's Catalog No.	
4. Title and Subtitle Dynamics of a Class of Vortex Rings		5. Report Date December 1989	
		6. Performing Organization Code	
7. Author(s) Karim Shariff, Anthony Leonard (Calif. Inst. Tech., Pasadena, CA) and Joel H. Ferziger (Stanford Univ., Stanford, CA)		8. Performing Organization Report No. A-90016	
		10. Work Unit No.	
9. Performing Organization Name and Address Ames Research Center Moffett Field, CA 94035-1000		11. Contract or Grant No.	
		13. Type of Report and Period Covered Technical Memorandum	
12. Sponsoring Agency Name and Address National Aeronautics and Space Administration Washington, DC 20546-0001		14. Sponsoring Agency Code	
		15. Supplementary Notes Point of Contact: Karim Shariff, Ames Research Center, MS 202-1, Moffett Field, CA 94035-1000 (415) 604-4728 or FTS 464-4728	
16. Abstract <p>The contour dynamics method is extended to vortex rings with vorticity varying linearly from the symmetry axis. An elliptic core model is also developed to explain some of the basic physics. Passage and collisions of two identical rings are studied focusing on core deformation, sound generation and stirring of fluid elements.</p> <p>With respect to core deformation, not only the strain rate but how rapidly it varies is important and accounts for greater susceptibility to vortex tearing than in two dimensions. For slow strain, as a passage interaction is completed and the strain relaxes, the cores return to their original shape while permanent deformations remain for rapidly varying strain. For collisions, if the strain changes slowly the core shapes migrate through a known family of two-dimensional steady vortex pairs up to the limiting member of the family. Thereafter energy conservation does not allow the cores to maintain a constant shape. For rapidly varying strain, core deformation is severe and a head-tail structure in good agreement with experiments is formed.</p> <p>With respect to sound generation, good agreement with the measured acoustic signal for colliding rings is obtained and a feature previously thought to be due to viscous effects is shown to be an effect of inviscid core deformation alone. For passage interactions, a component of high frequency is present. Evidence for the importance of this noise source in jet noise spectra is provided.</p> <p>Finally, processes of fluid engulfment and rejection for an unsteady vortex ring are studied using the stable and unstable manifolds. The unstable manifold shows excellent agreement with flow visualization experiments for leapfrogging rings suggesting that it may be a good tool for numerical flow visualization in other time periodic flows.</p>			
17. Key Words (Suggested by Author(s)) Vortex rings, Vorticity dynamics, Contour dynamics, Jet noise, Vortex sound, Chaotic advection		18. Distribution Statement Unclassified-Unlimited Subject Category - 34	
19. Security Classif. (of this report) Unclassified	20. Security Classif. (of this page) Unclassified	21. No. of Pages 296	22. Price A13

End date May 23, 1990



